

2

AD-A247 892

**PLASMA BEAM MEASUREMENTS**

J. H. Degnan
D. Dietz
J. L. Holmes
G. F. Kiuttu
D. W. Price
R. J. Richter-Sand
E. L. Ruden
C. R. Sovinec
K. Struve

August 1991

Final Report

DTIC
ELECTE
MAR 26 1992
S B D

APPROVED FOR PUBLIC RELEASE; DISTRIBUTION UNLIMITED.

Weapons Laboratory
Air Force Systems Command
Kirtland Air Force Base, NM 87117-6008

92-07714



This final report was prepared by the Phillips Laboratory (formerly Weapons Laboratory), Kirtland Air Force Base, New Mexico, under Job Order 57971199. The Laboratory Project Officer-in-Charge was Dr James H. Degnan (WSP).

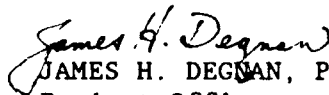
When Government drawings, specifications, or other data are used for any purpose other than in connection with a definitely Government-related procurement, the United States Government incurs no responsibility or any obligation whatsoever. The fact that the Government may have formulated or in any way supplied the said drawings, specifications, or other data, is not to be regarded by implication, or otherwise in any manner construed, as licensing the holder, or any other person or corporation; or as conveying any rights or permission to manufacture, use, or sell any patented invention that may in any way be related thereto.

This report has been authored by employees of the United States Government. Accordingly, the United States Government retains a nonexclusive royalty-free license to publish or reproduce the material contained herein, or allow others to do so, for the United States Government purposes.

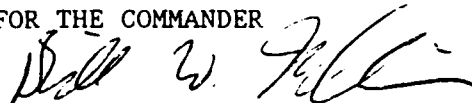
This report has been reviewed by the Public Affairs Office and is releasable to the National Technical Information Service (NTIS). At NTIS, it will be available to the general public, including foreign nationals.

If your address has changed, please notify PL/WSP, Kirtland AFB, NM 87117-6008 to help us maintain a current mailing list.

This report has been reviewed and is approved for publication.


JAMES H. DEGNAN, PhD
Project Officer

FOR THE COMMANDER



BILLY W. MULLINS, Maj, USAF
Chief, High Energy Plasma Division

REPORT DOCUMENTATION PAGE			Form Approved OMB No. 0704-0188	
Public reporting burden for this collection of information is estimated to average 1 hour per response, including the time for reviewing instructions, searching existing data sources, gathering and maintaining the data needed, and completing and reviewing the collection of information. Send comments regarding this burden estimate or any other aspect of this collection of information, including suggestions for reducing this burden, to Washington Headquarters Services, Directorate for Information Operations and Reports, 1215 Jefferson Davis Highway, Suite 1204, Arlington, VA 22202-4302, and to the Office of Management and Budget, Paperwork Reduction Project (0704-0188), Washington, DC 20503.				
1. AGENCY USE ONLY (Leave blank)	2. REPORT DATE August 1991	3. REPORT TYPE AND DATES COVERED Final - January-October 1989		
4. TITLE AND SUBTITLE PLASMA BEAM MEASUREMENTS		5. FUNDING NUMBERS PE: 62601F PR: 5797 TA: 11 WU: 99		
6. AUTHOR(S) J. H. Degnan, D. Dietz, J. L. Holmes, G. F. Kiuttu*, D. W. Price, R. J. Richter-Sand**, E. L. Ruden, C. R. Sovinec, and K. W. Struve		8. PERFORMING ORGANIZATION REPORT NUMBER WL-TR-90-83		
7. PERFORMING ORGANIZATION NAME(S) AND ADDRESS(ES) Weapons Laboratory Kirtland AFB, NM 87117		10. SPONSORING / MONITORING AGENCY REPORT NUMBER		
9. SPONSORING / MONITORING AGENCY NAME(S) AND ADDRESS(ES)		11. SUPPLEMENTARY NOTES *Mission Research Corporation, Albuquerque, NM **North Star, Albuquerque, NM		
12a. DISTRIBUTION / AVAILABILITY STATEMENT Approved for public release; distribution unlimited.		12b. DISTRIBUTION CODE		
13. ABSTRACT (Maximum 200 words) Coaxial plasma gun plasma parameters were determined using a diagnostic array to observe electron density, temperature, luminosity, beam target interactions, target luminosity, magnetic fields and ion species. Diagnostics included He-Ne and CO ₂ laser and 94 GHz microwave interferometry, visible spectrometry using an optical multichannel analyzer, rotating mirror fast framing camera, gated microchannel plate framing cameras, optical vacuum photodiodes, X-ray diodes and inductive magnetic probes. The plasma gun was operated with 126 or 252 μ F, 18 kV discharges with Ar or H gas. For these conditions, 70-80 km/s average plasma velocity and 0.5-2 eV plasma electron temperature were observed. The dominant plasma ionic species was Si ⁺¹ with a quartz insulator; with an alumina insulator, Al ⁺¹ and Al ⁺² were the dominant species. The plasma was self-luminous for 1.5-3 m. Interferometry showed averaged electron densities of 10 ⁺¹⁵ cm ⁻³ . The plasma showed MHD instabilities. Plasma currents were 0.5-1.5 kA. Fast plasma velocities contributed less than 1 percent of the total beam energy.				
14. SUBJECT TERMS Coaxial configurations, High speed photography, Interferometry, luminosity, Magnetic fields, Photodetectors, Plasma devices, Plasmas (physics), Spectrometers			15. NUMBER OF PAGES 180	
17. SECURITY CLASSIFICATION OF REPORT Unclassified			16. PRICE CODE	
18. SECURITY CLASSIFICATION OF THIS PAGE Unclassified		19. SECURITY CLASSIFICATION OF ABSTRACT Unclassified		20. LIMITATION OF ABSTRACT SAR

ACKNOWLEDGEMENTS

We wish to thank Dr Dah Yu Cheng Technology and Services, Sunnyvale, CA and Dr Peter Baum of General Research Corporation, Santa Barbara, CA for professional advice and related contributions. We wish to thank Jeff Reed, Glenn Oliver, and Dave Williams of General Research for assembling and operating the coaxial gun, and for designing, assembling, and operating the capacitor banks and vacuum drift chamber used in this work. We wish to thank Michael Griffin for his advice and support. We also wish to thank Eric Hendren and Jerry Baca of the Weapons Laboratory, and Bill Green, Mike Martin, Wayne Sommars, and Joe Willis of Maxwell Laboratories, Albuquerque, NM for technical and logistics support.



Accession For	
NTIS CNA&I	<input checked="" type="checkbox"/>
DTIC TAB	<input type="checkbox"/>
Unannounced	<input type="checkbox"/>
Justification	
By	
Distribution/	
Availability Codes	
Dist	Avail and/or Special
A-1	

CONTENTS

	<u>Page</u>
INTRODUCTION	1
FAST PHOTOGRAPHY DATA	3
OPTICAL AND VACUUM ULTRAVIOLET PHOTODIODE DATA	31
MAGNETIC FIELD MEASUREMENTS	39
INTERFEROMETRY ON THE WL/GRC EXPERIMENTS	57
OPTICAL SPECTROSCOPY	70
TARGET IMPACT RADIATION CALCULATIONS	112
MAGNETOHYDRODYNAMIC SIMULATIONS OF GRC/CHENG DEFLAGRATION GUN	126
REFERENCES	145
APPENDIX	147

FIGURES

<u>Figure</u>		<u>Page</u>
1.	Cordin camera setup.	4
2.	Cordin rotating mirror camera and time sequence of frames.	5
3.	Cordin photograph, Shot 2505, $z = 5.7$ m, alumina insulator, Ar operation.	6
4.	Cordin photograph, Shot 2506, $z = 5.7$ m, quartz insulator, Ar operation.	7
5.	Cordin 200- μ s streak photograph, Shot 2506.	8
6.	Cordin photograph, Shot 2486, $z = 5.0$ m, Ar operation, Ar puff target.	9
7.	Cordin photograph, Shot 2487, $z = 5.0$ m, Ar operation, Ar puff target.	10
8.	Cordin photograph, Shot 2488, $z = 5.0$ m, Ar operation, no puff target.	11
9.	Cordin photograph, Shot 2492, $z = 5.0$ m, He operation, no puff target.	12
10.	Cordin photograph, Shot 2448, $z = 10$ m, Ar operation, overhead 45-deg view, fresh target.	15
11.	Cordin photograph, Shot 2449, $z = 10$ m, Ar operation, overhead 45-deg view, used target.	16
12.	Cordin photograph, Shot 2538, $z = 10$ m, Ar operation, rear direct view, blow-through target.	17
13.	Cordin 200- μ s streak photograph, Shot 2538.	18
14.	Microchannel plate camera.	20
15.	The MCP camera views.	21
16.	Some MCP photographs of coaxial gun muzzle emission.	22
17.	Some MCP photographs of target, $z = 10$ m, $t = 60$ μ s.	22
18.	Some MCP photographs of self-luminous plasma beams for He, Ar operation, $z = 2$ m, $t = 20$ to 30 μ s.	24
19.	Some MCP photographs suggesting instabilities.	25
20.	Some MCP photographs of beamheads, $z = 2$ m, $t = 20$ μ s.	26

FIGURES (Continued)

<u>Figure</u>		<u>Page</u>
21.	Some MCP photographs of beam in Shot 2505 (alumina insulator) suggesting turbulence, granular structure.	27
22.	The TRW IC camera view (top), frame sequence (lower left), and streak photograph description.	27
23.	The IC framing photographs, Shot 2501, $z = 8$ m, alumina insulator, Ar operation; 1- μ s exposures at 70, 75, 80 μ s after fiducial.	28
24.	The IC framing photographs, Shot 2502, $z = 8$ m, alumina insulator, Ar operation; 1- μ s exposures at 70, 75, 80 μ s after fiducial.	29
25.	The IC camera 10- μ s streak photograph, Shot 2506, quartz insulator, Ar operation.	30
26.	Response functions for bare Al photocathode (XRD) and Si PIN.	32
27.	Optical photodiode signals for Shot 2501; $z = 5, 8$ m, 20 μ s/division; signal peaks at 48, 82 μ s after fiducial suggest velocity ~ 88 km/s.	33
28.	Optical photodiode signals for Shot 2526; $z = 5$ m (plasma beam) and $z = 15$ m (beam - target luminosity); $z = 5$ and 15-m traces at 20 and 50 μ s/division, respectively; signal peaks at 64, 200 μ s past fiducial suggest velocity ~ 74 km/s.	33
29.	Coaxial gun integrated Rogowski coil current signal; 20 μ s/division, peak current ~ 600 kA.	34
30.	Optical photodiode signals showing evidence of fast plasma beam component (precursor); 20 μ s/division; $z = 5$ m; H operation.	35
31.	The XRD traces. $z = 10$ m, observing beam - target luminosity, Shot 2436: 1 V, 20 μ s/division, no magnet. Shot 2451: 1 V, 50 μ s/division, and 0.1 V, 10 μ s/division, no magnet and no inductive isolator. Shots 2460, 2463, and 2466: 1 V, 50 μ s/division, magnet and inductive isolator.	36
32.	Upper trace: XRD signal. Lower trace: photodiode signal. Both traces looking at beam - target luminosity at $z = 10$ m; 2 V, 50 μ s/division; gun current starts ~ 105 μ s; Possible XRD evidence for fast beam component ~ 15 μ s after gun current starts.	38

FIGURES (Continued)

<u>Figure</u>		<u>Page</u>
33.	Correlation of luminosity and magnetic field precursor and main signal responses taken at 5-m station. Both time bases 20 μ s/division.	43
34.	Reversed pair of B_θ probe signals taken at 5-m station. Both time bases 10 μ s/division. Fiber optic coupling of signal.	44
35.	Reversed pair of B_θ probe signals taken at 10-m station. Both time bases 20 μ s/division.	46
36.	Magnetic probe signals taken at 10-m station. Both time bases 20 μ s/division.	47
37.	Correlation of noise signals with large B_θ signal taken at 10-m station. All time bases 20 μ s/division.	48
38.	Sample CO_2 interference signal and calculated \bar{n} taken at 5-m station through center port. 20 kJ bank, Ar plenum.	60
39.	The \bar{n} from HeNe signal at 0.7-m station through center port and port 6.4 cm off-center. 20 kJ bank with Ar plenum.	62
40.	Interferometry results at 5-m station.	63
41.	Beam power.	66
42.	Centered \bar{n} and inferred beam power from HeNe signal at 5 m. The 40 kJ bank with H_2 plenum.	67
43.	The \bar{n} from millimeter wave signal at 5 m.	69
44.	The OMA system configuration block diagram.	71
45.	150 1/mm grating reflection efficiency.	73
46.	1200 1/mm grating reflection efficiency curve.	74
47.	1800 1/mm grating reflection efficiency curve.	75
48.	Silicon intensified tube (SIT) vidicon detector.	76
49.	Detector response function.	77
50.	Typical time-integrated Ar spectrum at 5 m.	80

FIGURES (Continued)

<u>Figure</u>		<u>Page</u>
51.	High-resolution spectrum of the Si II 4s-4p multiplet.	81
52.	High-resolution Si II 4p-5s multiplet.	82
53.	High-resolution H α spectrum.	83
54.	High-resolution H β spectrum.	84
55.	Tangential view at 5 m.	86
56.	Interferometer port (no wall) view, at 5 m.	87
57.	Radial (wall) view at 5 m.	88
58.	Broad-band spectrum at 5 m with alumina insulator.	89
59.	Broad-band Ar load spectrum at 5 m and 80 μ s.	90
60.	Time-integrated broad-band Ar load spectrum at 5 m.	91
61.	Time-integrated broad-band He load spectrum at 5 m.	92
62.	Broad-band Ar load spectrum, 0-10 μ s, 0.3 m.	93
63.	Broad-band H load spectrum, 5-10 μ s, 0.3 m.	94
64.	Time history of electron temperature for LTE model.	96
65.	Scaling of the FWHM of H β with electron density.	98
66.	Grotrian diagram of the Si II system (from Ref. 18).	103
67.	Energy levels for the Si II system (from Ref. 18).	104
68.	Boltzmann plot of CRE calculations for Si II at 5 eV.	105
69.	Temperature history from CRE model assuming $N_E = 10^{16} \text{ cm}^{-3}$.	107
70.	The computational model.	113
71.	Radiation leakage in a 1-D calculation.	115
72.	One-dimensional MHD deflagration.	128
73.	Computation mesh for the neutral gas calculation.	130

FIGURES (Concluded)

<u>Figure</u>		<u>Page</u>
74.	Mass density of neutral gas 60 μ s from valve actuation.	131
75.	Hydrostatic pressure of neutral gas 60 μ s from valve actuation.	131
76.	Problem region for the electrostatic calculation.	133
77.	Equipotential lines.	133
78.	Computation mesh for the MHD calculation.	135
79.	Enclosed current contours from the MHD calculation.	137
80.	Ion number density from the MHD calculation.	138
81.	Fluid velocity from the MHD calculation.	139
82.	Enclosed current 9.5 μ s after breakdown.	141
83.	Temperature contours from the MHD calculation.	142
84.	Ion Larmor radii at 3.5 μ s.	143

TABLES

<u>Table</u>		<u>Page</u>
1.	Calculated equilibrium current (assuming $kT = 1.0$ eV).	53
2.	Calculated Bennett current (assuming $kT_i = kT_e = 1.0$ eV).	55
3.	Interferometric parameters for the WL/GRC experiment.	57
4.	Inferred time integrated plasma beam properties.	65
5.	Grating specifications.	70
6.	Hydrogen ($H^+ - H^0$) relaxation times.	100
7.	Si III $4p^1P^0$ to $4p^3P^0$ state density ratio.	102
8.	Goodness of CRE fit to Si II line intensity data.	106
9.	Ratio of Ar II to Si II for line intensity ratio of 10^{-3} .	108
10.	Cases studied.	123
11.	Luminosity as a function of time.	124
12.	Luminosities for various broad spectral ranges.	125

INTRODUCTION

The High Energy Plasma Division of the Weapons Laboratory (WL/AWX) was tasked to find out the parameters of a plasma beam produced by the General Research Corporation (GRC), Santa Barbara, California, plasma gun. An array of diagnostics was applied to observe electron density, temperature, self-luminosity, target impact luminosity and effect, magnetic field, and ionic species identification. These diagnostics included HeNe and CO₂ laser and 94-GHz microwave interferometers, an Optical Multichannel Analyzer (OMA), a Cordin gas driven rotating mirror framing camera, three Microchannel Plate (MCP) gated framing cameras, optical and X-ray photodiodes, and inductive (loop) magnetic probes.

For 126- μ F, 18-kV discharge through the GRC Cheng gun with 30 psig Ar puff operation, the following plasma beam parameters were observed:

beam mass	~3 to 5 mg
beam kinetic energy	~3.4 to 3.9 kJ
beam momentum	~0.16 N-s
velocity distribution "peak"	~70-80 km/s
electron temperature	~0.5 to 2 eV
dominant ionic species is Si ⁺¹ for quartz insulator use	
	Al ⁺¹ , Al ⁺² for alumina insulator use

Other important results include: The plasma beam was self-luminous over a length ~1.5 to 3 m. Interferometry indicated radial averaged electron densities $\sim 10^{15}$ cm⁻³, consistent with optical spectroscopy data. The plasma beam diameter was approximately half the tube diameter, i.e., ~10 to 12 cm. The beam exhibited magnetohydrodynamic (MHD) like instabilities, and was time correlated with an azimuthal magnetic field consistent with an axial current ~0.5 to 1.5 kA. Faster beam components were sometimes observed, with velocity distributions typically "peaking" ~250 km/s and sometimes extending to >500 km/s. Target impact luminosity suggested that the fast beam component energy was <<1 percent of the main beam component energy. Time resolved target damage observation indicates that it is the slower, main beam component that does damage, e.g., blowing through a 0.7- μ m aluminum (Al) foil.

INTRODUCTION

The High Energy Plasma Division of the Weapons Laboratory (WL/AWX) was tasked to find out the parameters of a plasma beam produced by the General Research Corporation (GRC), Santa Barbara, California, plasma gun. An array of diagnostics was applied to observe electron density, temperature, self-luminosity, target impact luminosity and effect, magnetic field, and ionic species identification. These diagnostics included HeNe and CO₂ laser and 94-GHz microwave interferometers, an Optical Multichannel Analyzer (OMA), a Cordin gas driven rotating mirror framing camera, three Microchannel Plate (MCP) gated framing cameras, optical and X-ray photodiodes, and inductive (loop) magnetic probes.

For 126- μ F, 18-kV discharge through the GRC Cheng gun with 30 psig Ar puff operation, the following plasma beam parameters were observed:

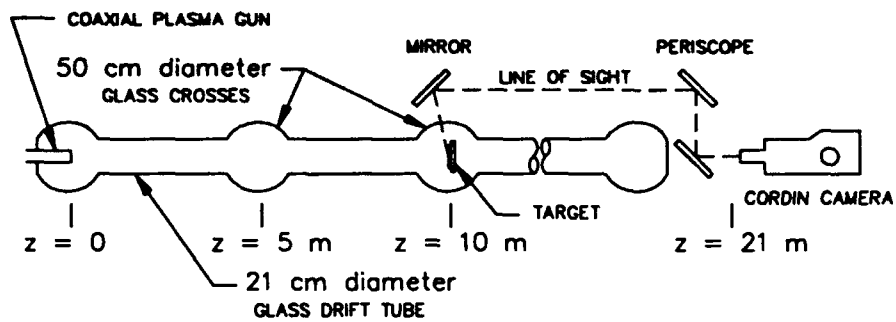
beam mass	-3 to 5 mg
beam kinetic energy	-3.4 to 3.9 kJ
beam momentum	-0.16 N-s
velocity distribution "peak"	-70-80 km/s
electron temperature	-0.5 to 2 eV
dominant ionic species is Si ⁺¹ for quartz insulator use	
	Al ⁺¹ , Al ⁺² for alumina insulator use

Other important results include: The plasma beam was self-luminous over a length -1.5 to 3 m. Interferometry indicated radial averaged electron densities -10¹⁵ cm⁻³, consistent with optical spectroscopy data. The plasma beam diameter was approximately half the tube diameter, i.e., -10 to 12 cm. The beam exhibited magnetohydrodynamic (MHD) like instabilities, and was time correlated with an azimuthal magnetic field consistent with an axial current -0.5 to 1.5 kA. Faster beam components were sometimes observed, with velocity distributions typically "peaking" ~250 km/s and sometimes extending to >500 km/s. Target impact luminosity suggested that the fast beam component energy was <<1 percent of the main beam component energy. Time resolved target damage observation indicates that it is the slower, main beam component that does damage, e.g., blowing through a 0.7- μ m aluminum (Al) foil.

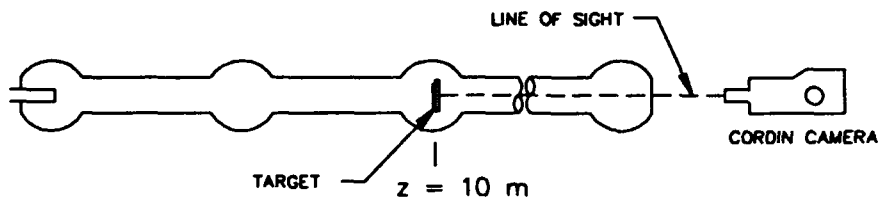
FAST PHOTOGRAPHY DATA

Fast photography data were obtained with three different types of fast cameras: a Cordin model 200 rotating mirror simultaneous framing/streak camera, three MCP tube cameras, and an old TRW Model ID Image Converter (IC) camera with framing and streak heads. The Cordin rotating mirror camera takes 24 frames, 0.7 x 0.9 in, recorded on Polaroid (Type 55 or Type 57) or cut film (Royal X-pan). The Cordin camera speed can be varied from 10,000 to 100 RPS, corresponding to mirror periods of 100 to 10,000 μ s, frame exposure times of 128 ns to 12.8 μ s, and start-to-start framing intervals of 125 ns to 12.5 μ s. At the faster speeds, the pneumatically driven Cordin Beryllium (Be) mirror is driven by Helium (He). At slower speeds, Nitrogen (N) or dry air will suffice. For these experiments, the Cordin was typically operated with dry air, and a mirror period of \sim 6400 μ s, corresponding to a framing interval of \sim 8 μ s, and camera coverage of \sim 192 μ s. For most shots, the mirror period was recorded and was in the range \sim 6250 to \sim 6500 μ s. For those shots in which the Cordin camera was used (almost all of them), the Cordin provided the first trigger. When the mirror reaches a preset speed, a signal (referred to as T_0 pulse) is generated and the Fire Pulse Delay (FPD) begins. The time from the T_0 pulse to first frame time is \sim 0.10 periods. The FPD is adjusted so the luminous event of interest occurs in or after the first frame. For these experiments, the FPD was typically \sim 700 μ s. The FPD signal is 125 V into 50 Ω . The T_0 pulse is 15 V into 10,000 Ω . It is possible to add an integral number of mirror periods to the FPD when long delays are needed, since the Cordin mirror period does not perceptibly change for many tens of periods. For these experiments, that was not necessary. The FPD triggered a fast solenoid operated gas puff valve, which puffed gas into an already charged coaxial plasma gun. The charged gun typically self-break initiated its discharge \sim 80 to 100 μ s after the puff valve was triggered, i.e., \sim 80 to 100 μ s after the FPD signal.

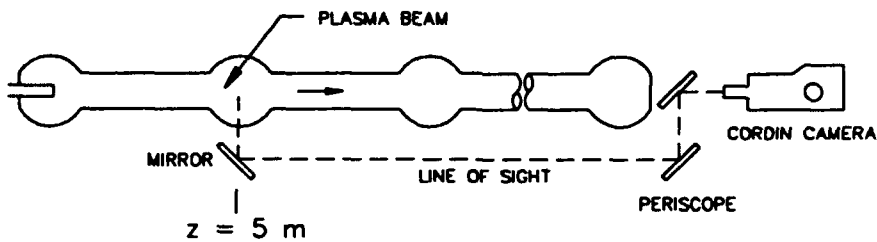
The Cordin camera observation geometry is illustrated in Figure 1 for four different views, two plasma beam target interaction views and two self-luminous beam views. A photograph of the Cordin camera is shown in Figure 2. Eight-microsecond framing and \sim 200- μ s streak photographs of the self-luminous plasma beam are shown in Figures 3 through 9. Figures 3 and 4 show views of



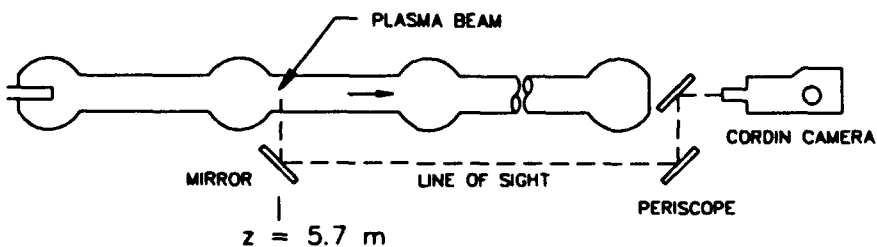
(a) Overhead 45 deg front view of target



(b) Direct rear view of target



(c) Lower 90 deg view of beam at $z = 5 \text{ m}$
(Through spherical "cross")



(d) Lower 90 deg. view of beam at $z = 5.7 \text{ m}$
(Through cylindrical drift tube)

Figure 1. Cordin camera setup.

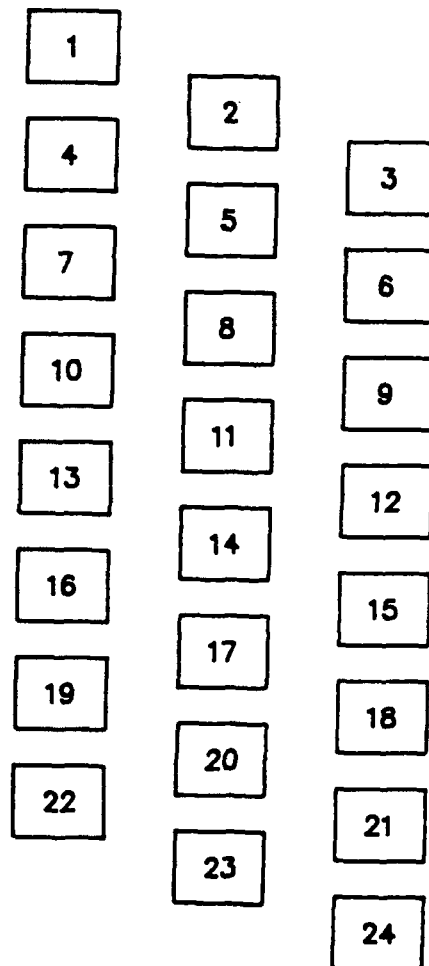
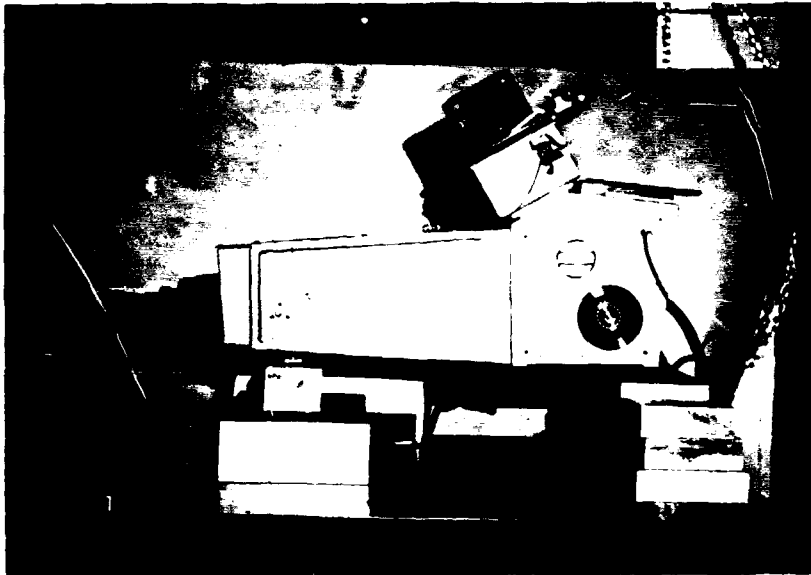


Figure 2. Cordin rotating mirror camera and time sequence of frames.

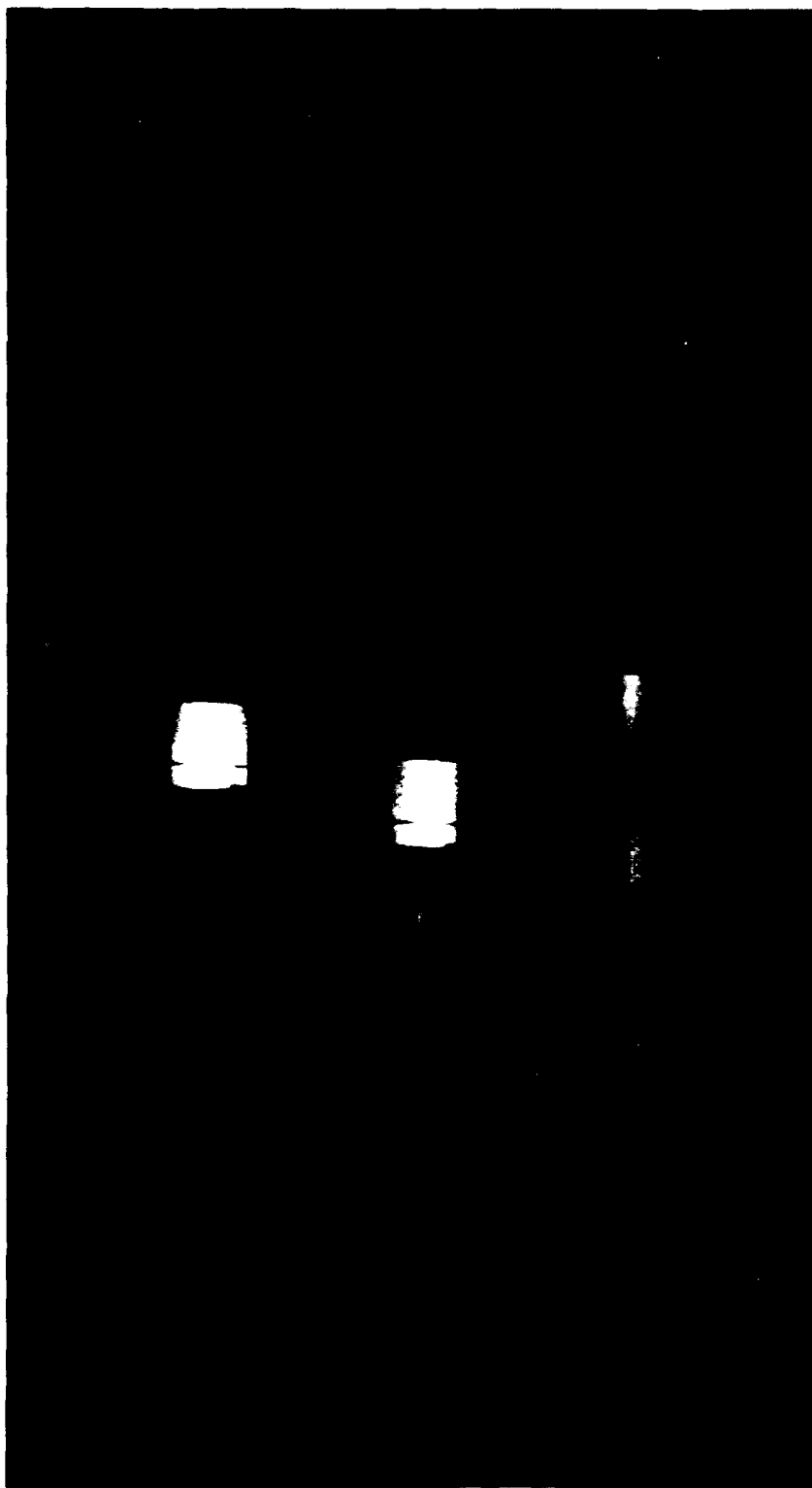


Figure 3. Cordin photograph, Shot 2505, $z = 5.7$ m, alumina insulator, Ar operation.

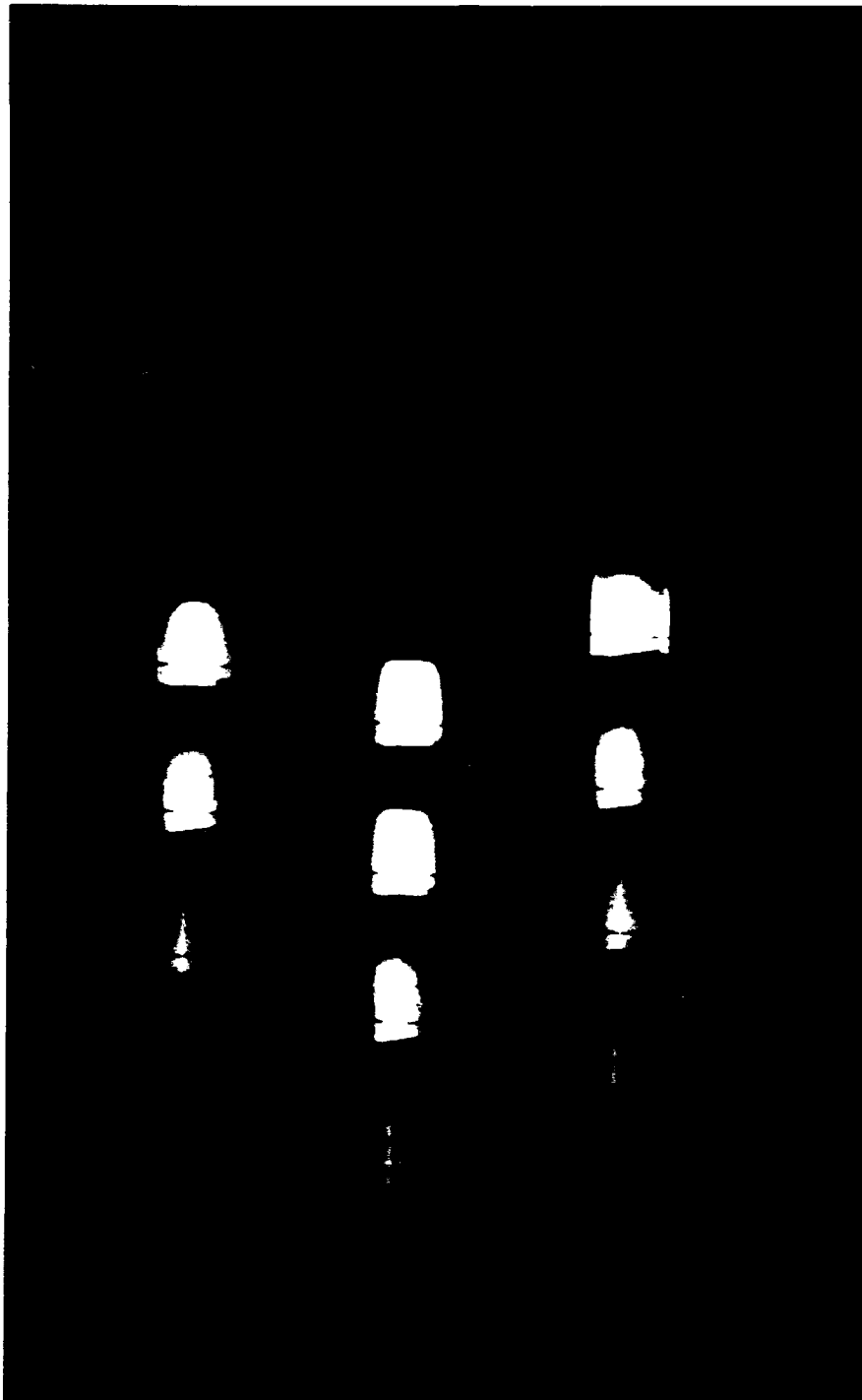


Figure 4. Cordin photograph, Shot 2506, $z = 5.7$ m.
quartz insulator, Ar operation.

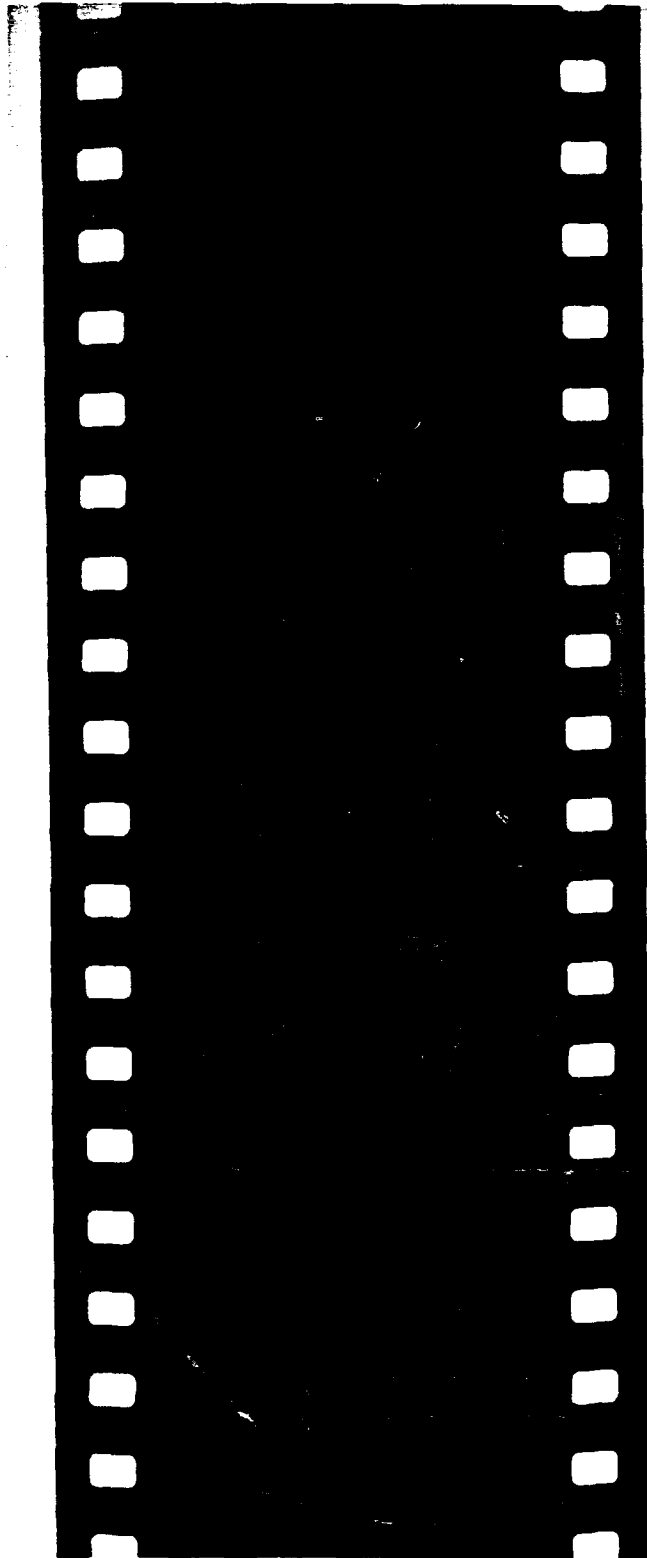


Figure 5. Cordin 200- μ s streak photograph,
Shot 2506.

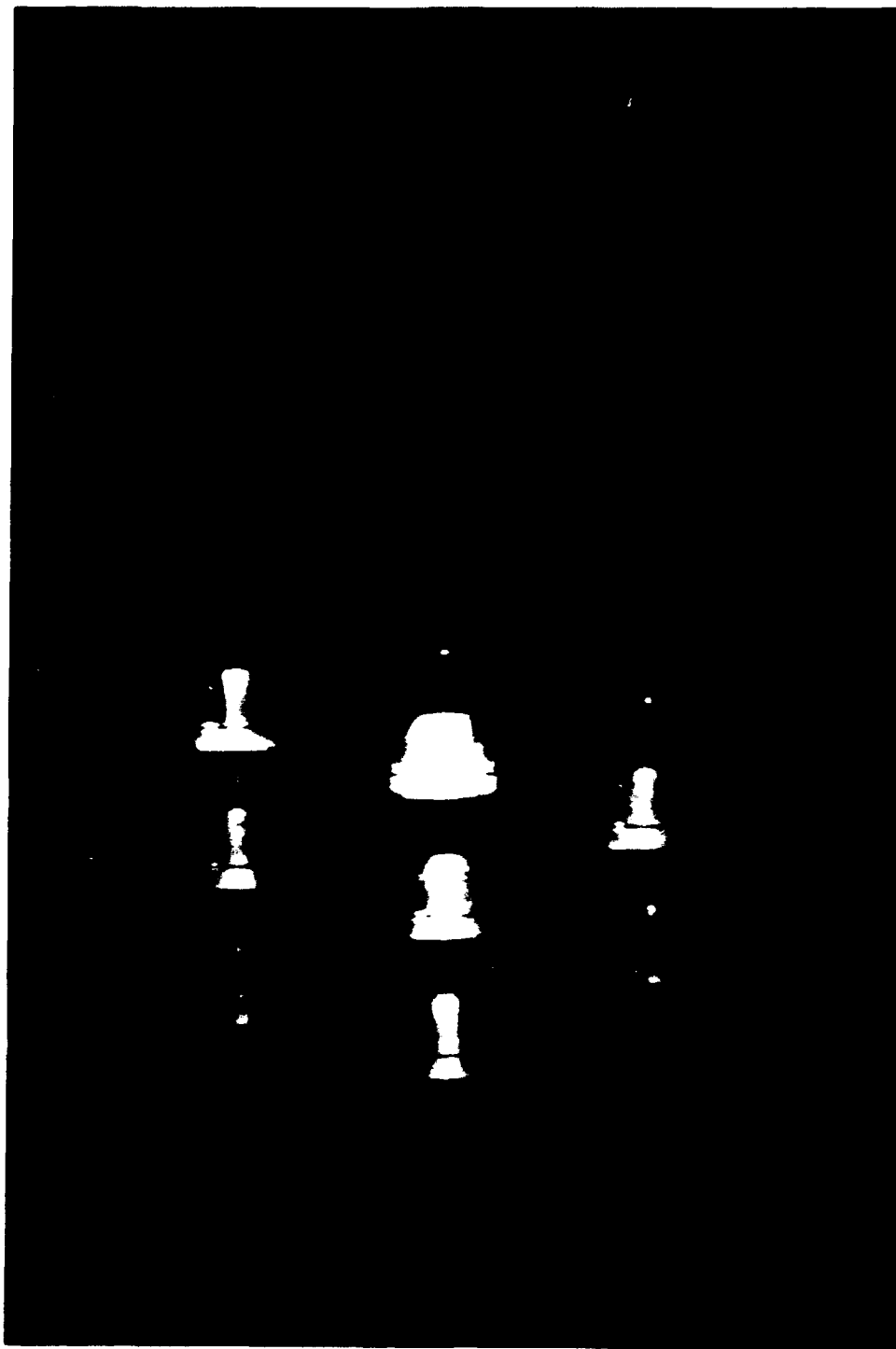


Figure 6. Cordin photograph. Shot 2486, $z = 5.0$ m,
Ar operation, Ar puff target.

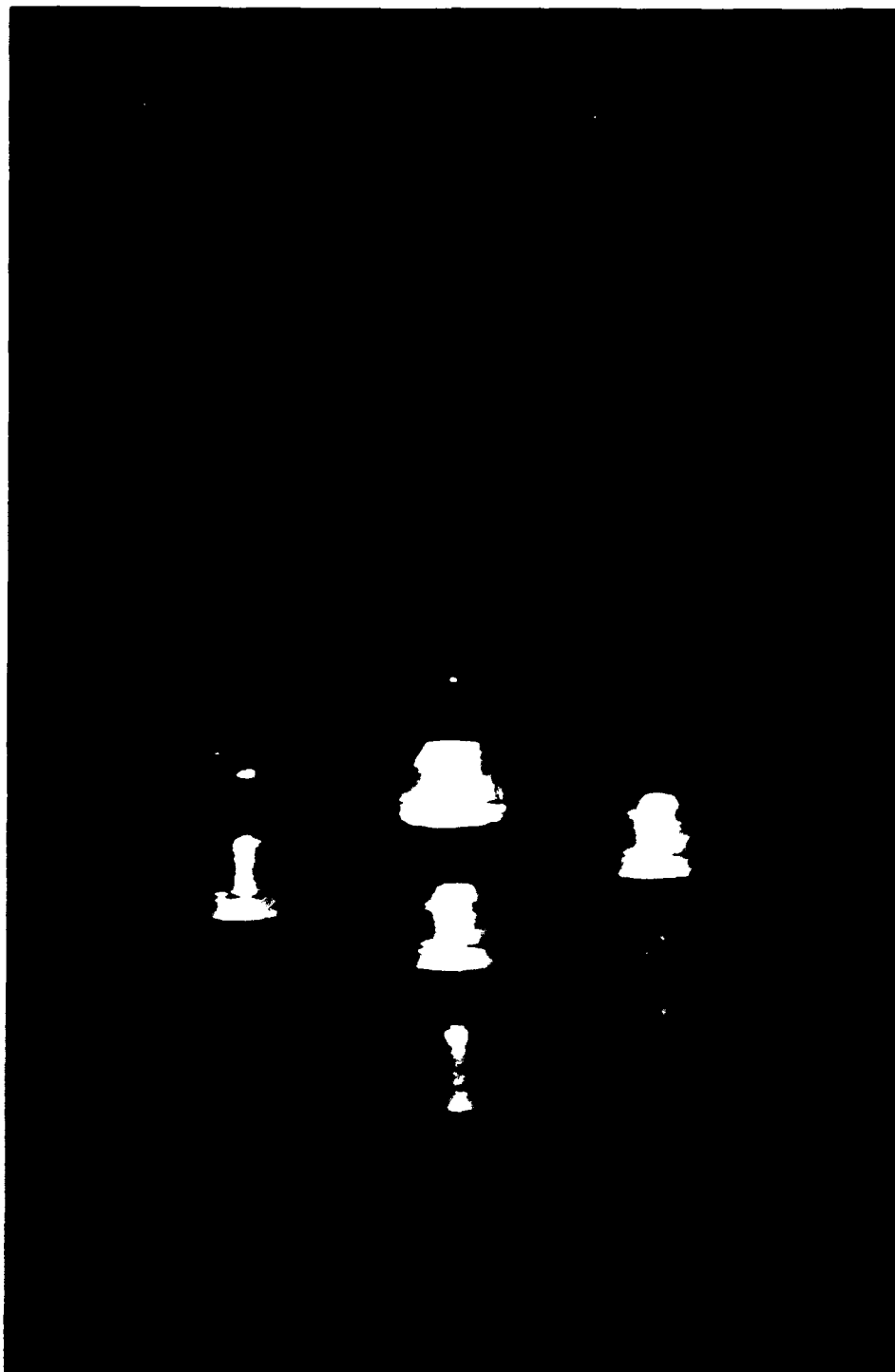
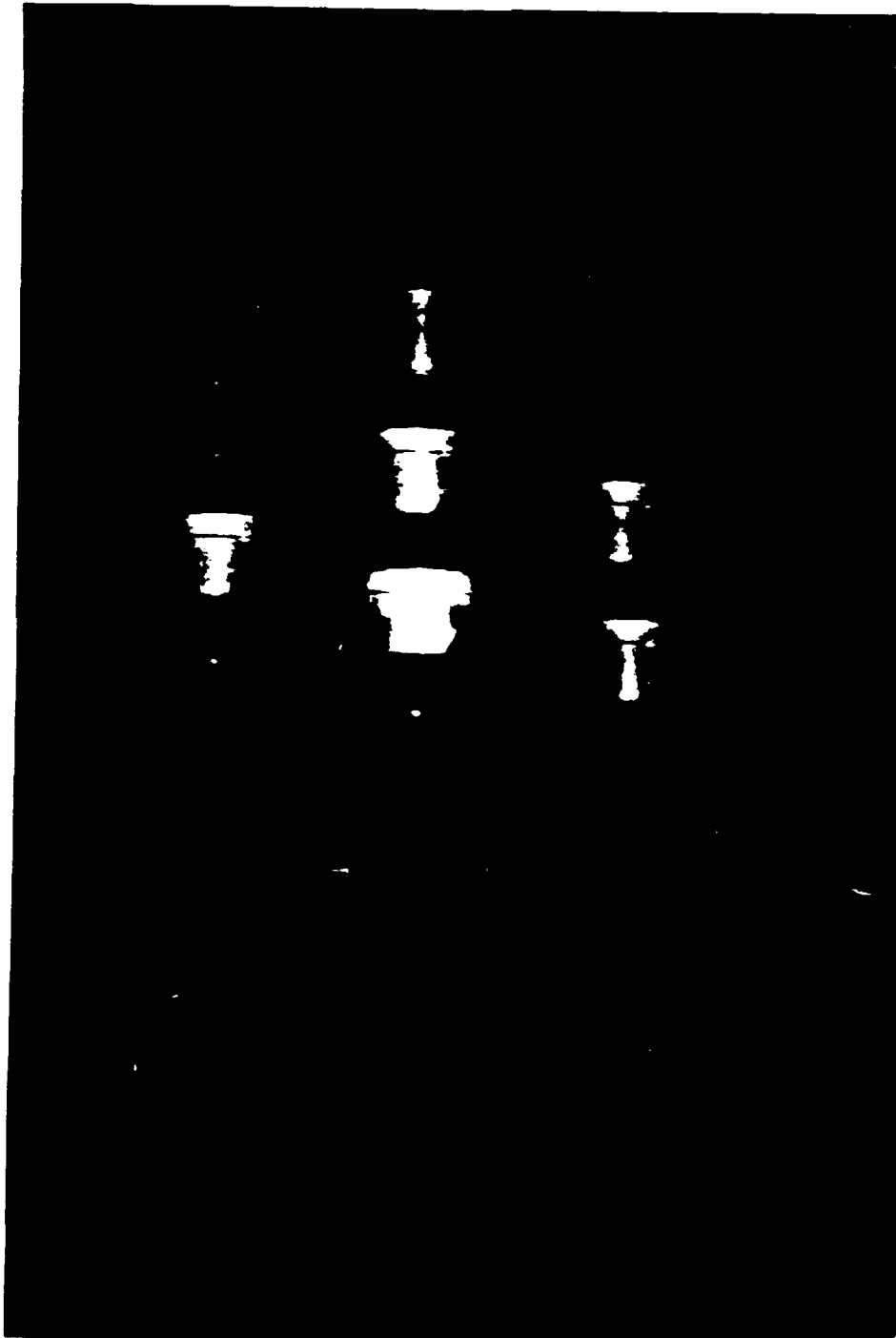


Figure 7. Cordin photograph, Shot 2487, $z = 5.0$ m,
Ar operation, Ar puff target.

operation, no data were
obtained from the operation.



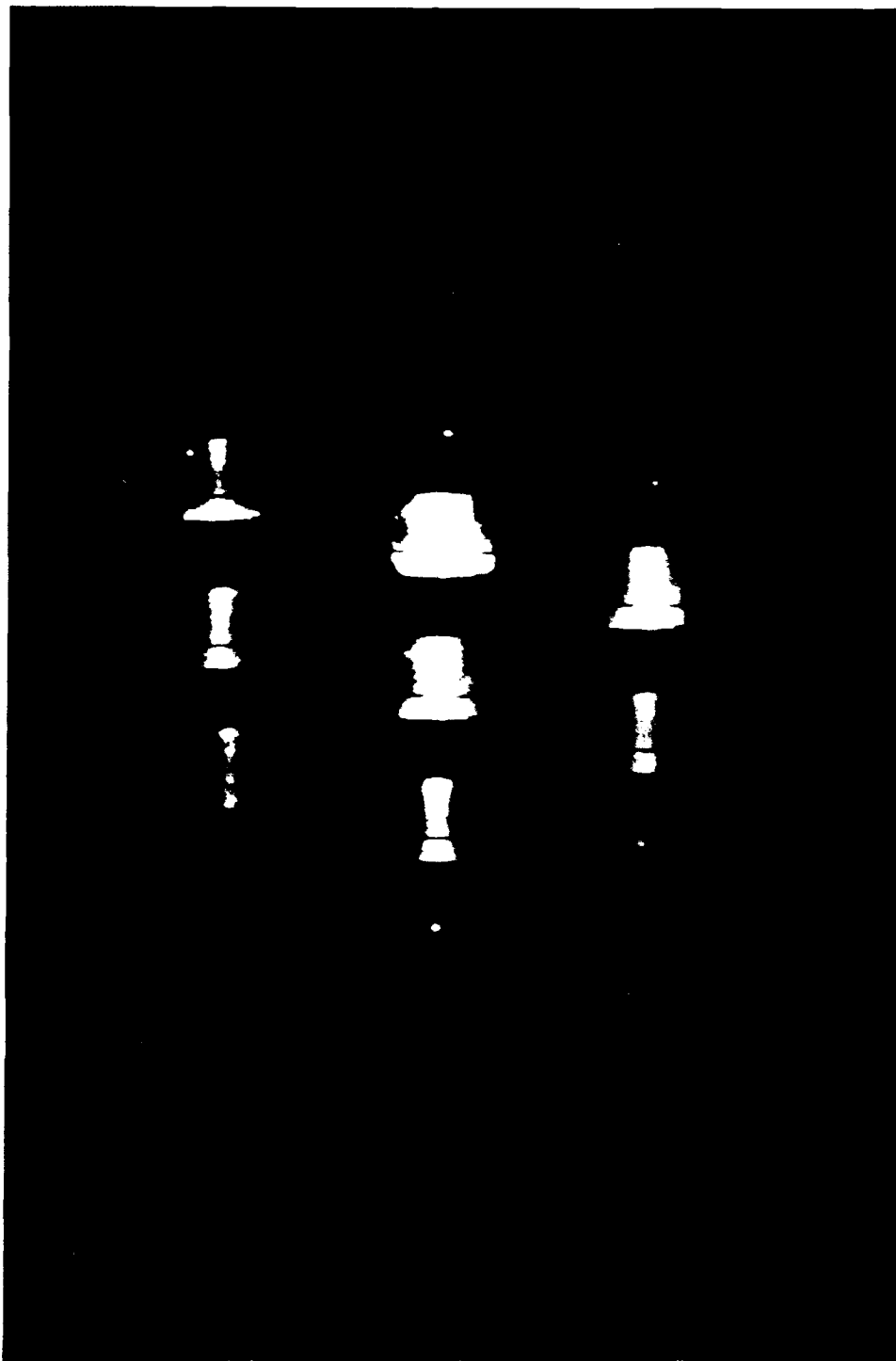


Figure 9. Cordin photograph, Shot 2492, $z = 5.0$ m,
He operation, no puff target.

the beam taken through the 21-cm inner diameter cylindrical glass drift tube (Fig. 1d). These photographs are for Shots 2505 (alumina coaxial gun insulator) and 2506 (quartz coaxial gun insulator). The order of the 24 frames is 8 slanted rows of 3 frames each, starting left to right, top to bottom, as numbered in Figure 2b. In Figure 3, the beam is first evident in frame 9 and remains evident through frame 17. It is brightest in frames 10 and 11. There is faint light in the lower right corners of frames 1 and 2, which is believed to be caused by reflected light from the coaxial gun discharge. This is consistent with the intended relative timing of the Cordin camera and the puff valve firing. The central column frames (2, 5, 8, 11, 14, etc.) are generally brighter than adjacent frames for equal event luminosity. This systematic effect must be considered when interpreting the photographs. Another systematic effect is a very sharp luminous line on the axis of the drift tube for this view. This is an artifact due to reflection from a light source (such as the plasma beam) further from the coaxial gun than the region of the drift tube being photographed. This reflection artifact was generated with a headlight, for example. The true plasma beam is readily evident, superimposed on this line. The dark line transverse to the drift tube axis due to the slit for the simultaneous streak photograph. The time interval between the light from the coaxial gun discharge and the brightest frame (10) is $\sim 72 \mu\text{s}$, corresponding to a peak in the velocity distribution of $7.9 \text{ cm}/\mu\text{s}$ or 79 km/s . (The gun to photographed region distance is 5.7 m .) The beam is off the drift tube axis in some frames, appearing to oscillate around the drift tube axis. The walls of the drift tube are themselves luminous, possibly from reflection and/or return current. As discussed in the section on magnetic probe data, azimuthal magnetic field consistent with axial currents of up to 1.5 kA are observed, coinciding with beam luminosity in space and time. While luminous beam is evident for 9 frames ($72 \mu\text{s}$), the full width half maximum (FWHM) of the apparent luminosity is < 2 frames ($16 \mu\text{s}$), indicating that the bulk of the luminosity of the plasma beam is confined to an axial length of $(\sim 7.9 \text{ cm}/\mu\text{s})(16 \mu\text{s}) = 126 \text{ cm}$, at least for this shot. The diameter of the luminous beam is generally less than or on the order of half the drift tube diameter, or $\sim 10 \text{ cm}$. In Figure 4, the first evidence of beam luminosity is also in frame 9. The beam luminosity persists through frame 20. The exposure is somewhat brighter, and the beam appears better centered than in Figure 3, though a simultaneous streak photograph taken for the same shot

(Fig. 5) suggests some transverse beam wandering. The wall luminosity is most evident in frame 9. It is also evident in the brightest part of the related streak photograph. These photographs (Figs. 3-5) are typical for this view.

Figures 6 through 9 show Cordin photographs of the self-luminous beam viewed through the ~50-cm dia spherical glass "cross" at the "5-m" diagnostic station. Though distorted by the spherical glass, the plasma beam is evident. Figures 6 through 8 are for argon (Ar) coaxial gun operation (Shots 2486, 2487 and 2488); Figure 9 is for He coaxial gun operation (Shot 2492). In Shots 2486 and 2487, an ~3 to 30- μ g Ar gas puff was injected into the 5-m station, to provide a gas puff impact target for the plasma (or possibly neutral) beam. This puff target had no obvious effect on the luminous beam. In Figures 6 through 8, plasma beam luminosity becomes substantial in frame 13 and persists for 8 to 10 additional frames. The luminosity FWHM is perhaps 2 frames (16 μ s) or less. There is a small amount of apparently reflected light in earlier frames. The framing photographs for He operation are similar, but shifted to earlier time (by about 5 frames = 48 μ s). This is due largely to a shorter coaxial gun puff to breakdown delay (58 μ s instead of 98 μ s for Ar).

Figures 10 through 13 show Cordin photographs of plasma beam target interaction. Figures 10 and 11 show 8- μ s framing photographs of a 45-deg overhead front view (Fig. 1a) of a target located 10 m from the coaxial gun. Reflected light from the coaxial gun discharge is evident in frame 8 for Figure 10 (Shot 2448, fresh target), and in frames 7 and 8 for Figure 11 (Shot 2449, used target). Target luminosity peaks in frame 24 for both shots and has become substantial (near peak) in frame 22 for Shot 2448, frame 23 for Shot 2449. If this peak luminosity is interpreted as impact luminosity, the velocity of the main plasma beam component is ~90 km/s for Shot 2448, ~80 km/s for Shot 2449. Preceding target luminosity drops rapidly as time-of-flight (TOF) becomes smaller (as inferred velocity becomes larger). From these photographs, there is no evidence of any impact luminosity from plasma beam with velocity over 200 km/s. For 100-km/s inferred velocity, the luminosity is an order of magnitude below peak.

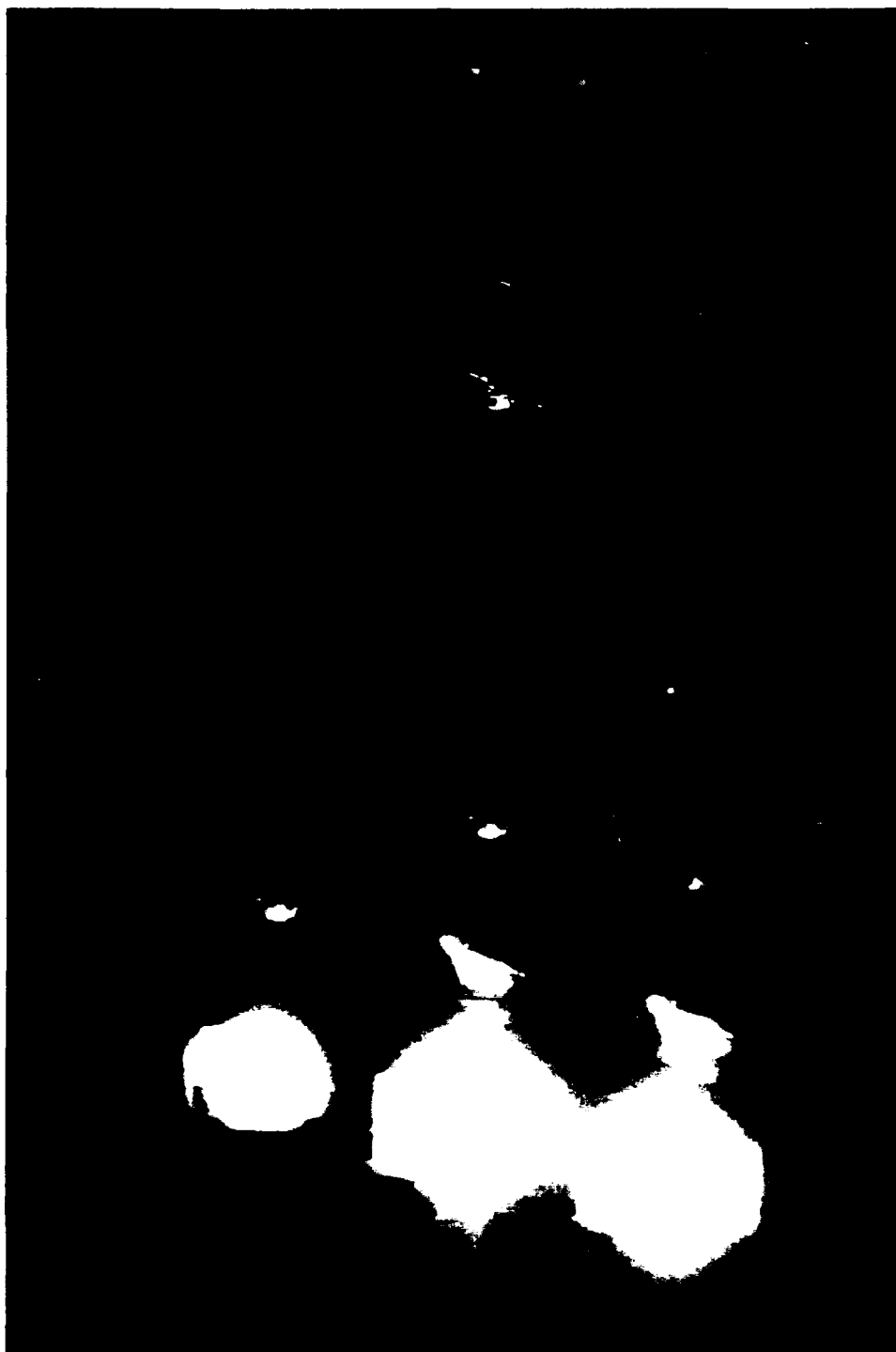


Figure 10. Cordin photograph. Shot 2448, $z = 10$ m,
Ar operation, overhead 45-deg view,
fresh target.

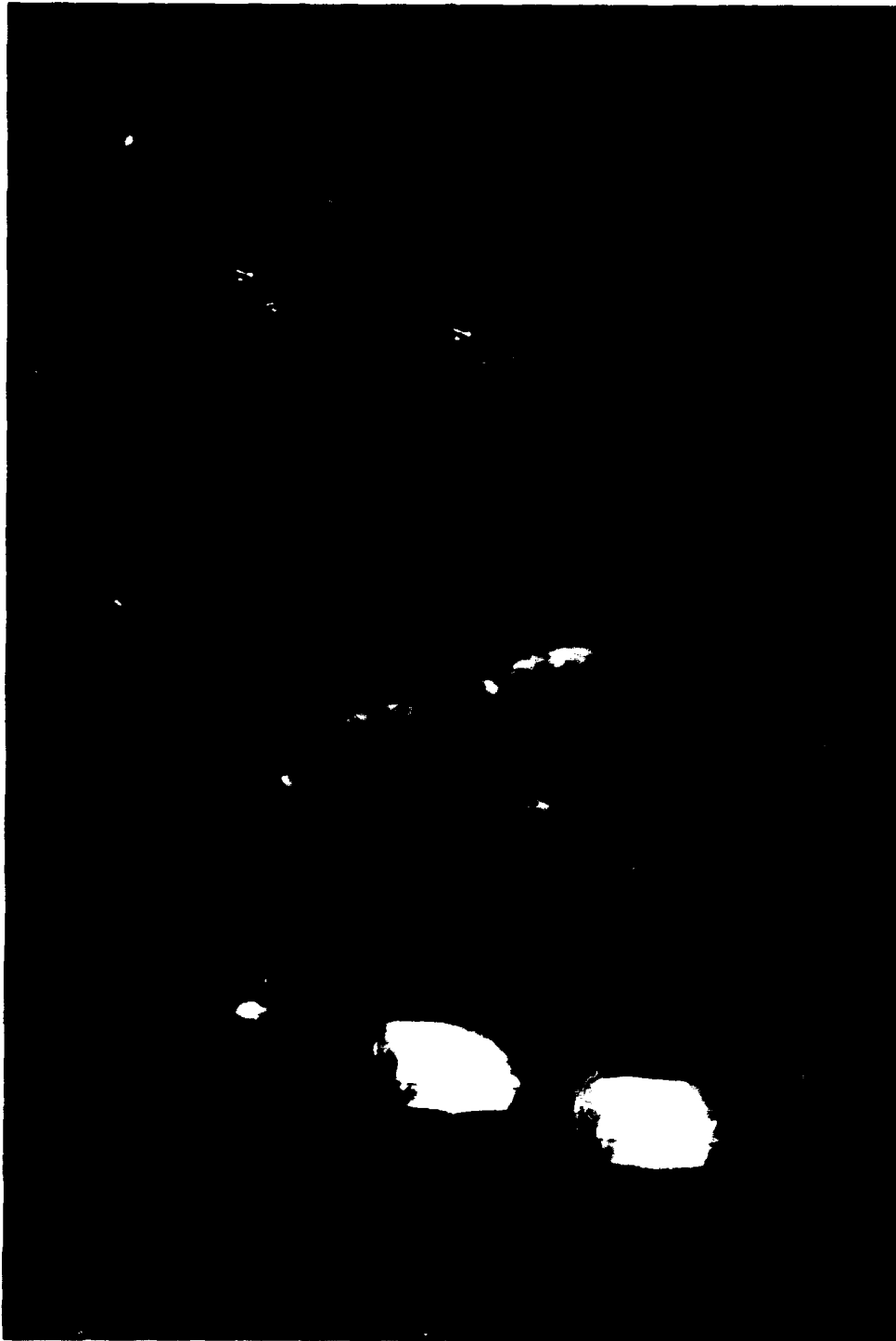


Figure 11. Cordin photograph, Shot 2449, $z = 10$ m,
Ar operation, overhead 45-deg view,
used target.

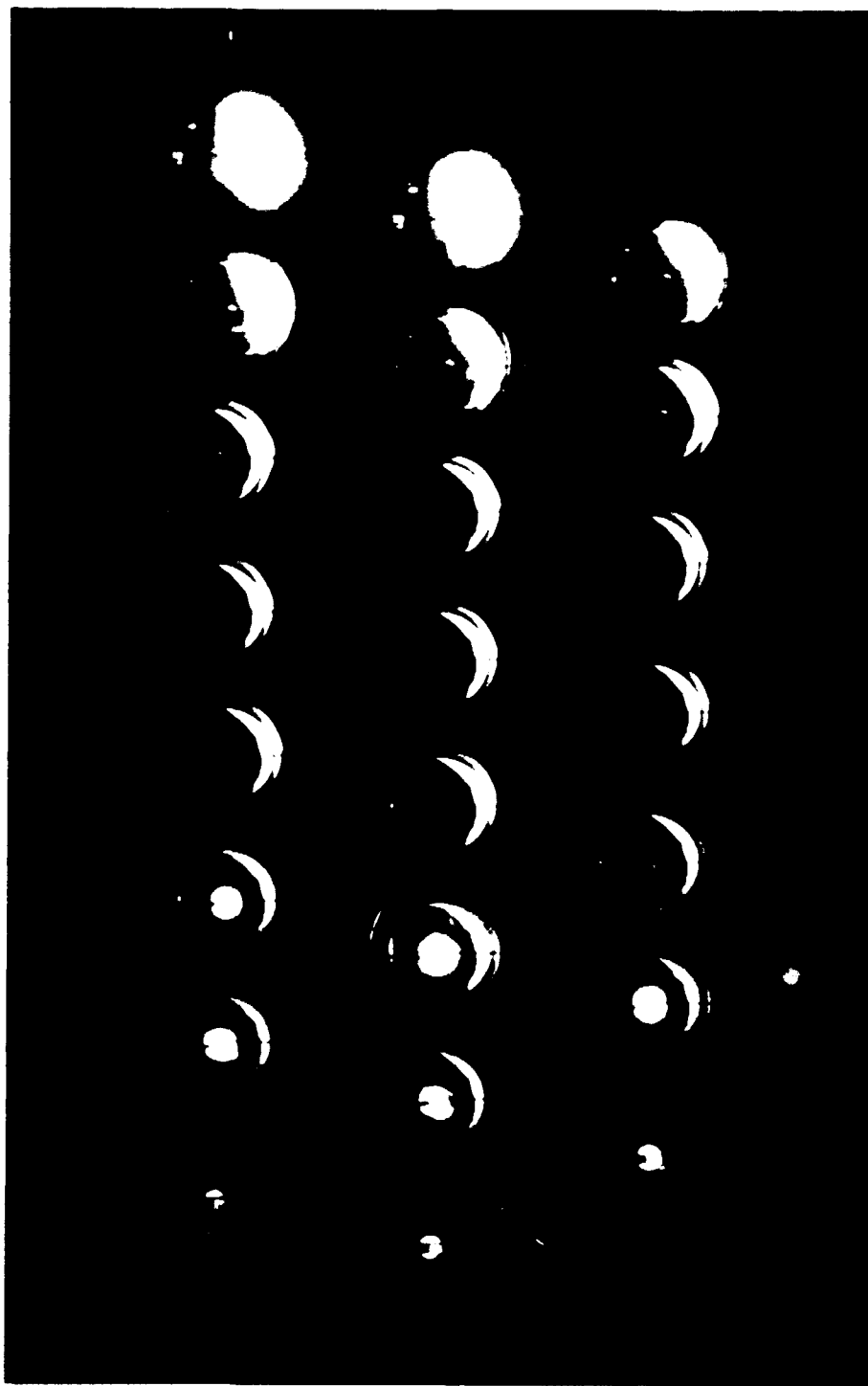


Figure 12. Cordin photograph, Shot 2538, $z = 10$ m, Ar operation, rear direct view, blow-through target.

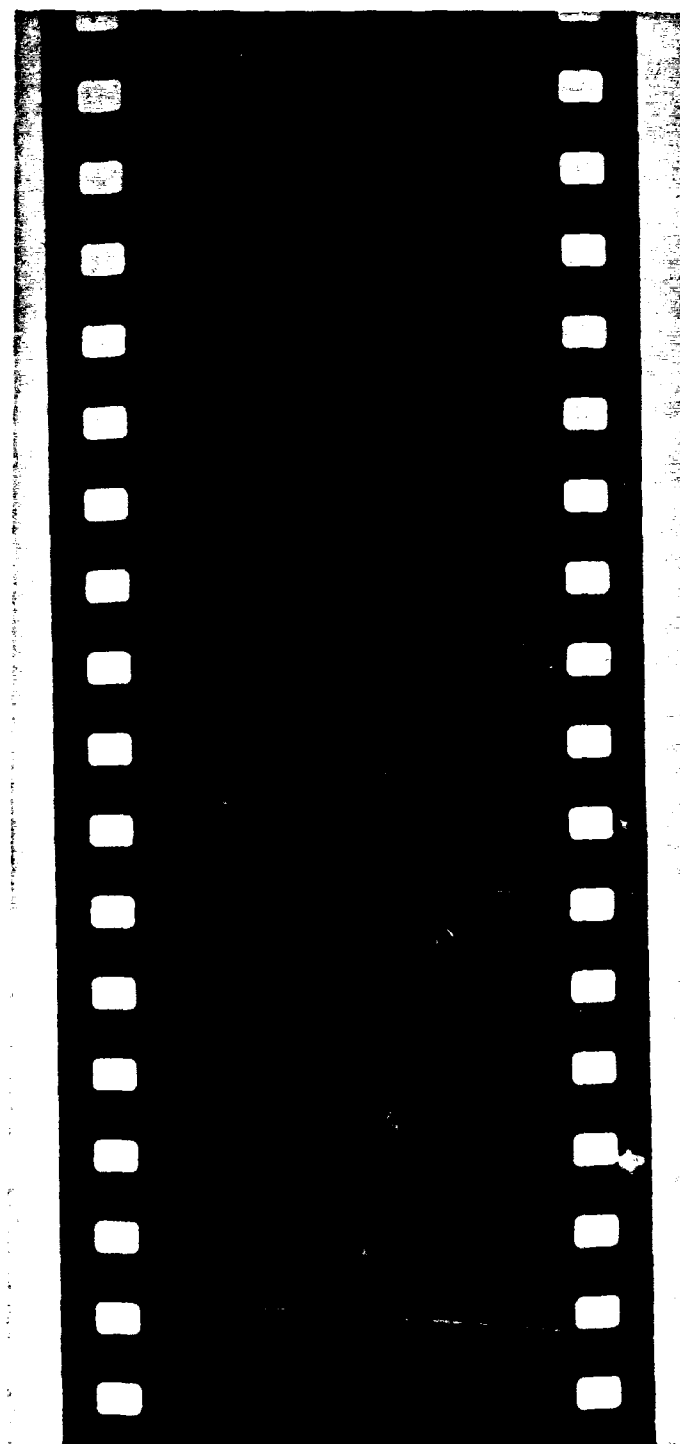


Figure 13. Cordin 200- μ s streak photograph,
Shot 2538.

Figures 12 and 13 show 8- μ s frames and an \sim 200- μ s streak of a rear view of a blow-through target, mounted 10 m from the coaxial gun. While most of the coaxial gun shots, including those in Figures 3 through 11, were driven by a 126- μ F, 18-kV, 20-kJ discharge, Shot 2538 was driven by a 252- μ F, 18-kV, 40-kJ discharge. The gun was operated with Hydrogen (H). As is evident in Figure 12, the first frame is already luminous. It is believed that the coaxial gun discharge started during or slightly before the first frame, and the luminosity is gun discharge light reaching the camera by travelling between the drift tube and the circular target. The target was a circular metal plate with a central circular hole covered by 0.7- μ m-thick Al foil. The first evidence of foil penetration is in frame 14 (plasma beam TOF = 112 μ s, corresponding to velocity \sim 90 km/s). This foil is significantly penetrated in frame 16 (TOF = 128 μ s, velocity \sim 80 km/s).

The MCP cameras used ITT F4111 MCP tubes, which have an 18-mm-dia sensitive area. These tubes are available from ITT Electro-optics Products Division, Fort Wayne, Indiana (Dr John Cuny). The MCP input to output voltage is adjustable from \sim 200 to \sim 700 V, with corresponding luminous gain ranging from \sim 5 to \sim 10,000. The MCP output to phosphor voltage is \sim 5 kV. The cathode to MCP voltage is \sim 200 V and (in pulsed gated mode) is provided by a small charged cable discharge, with gate (on) time equal to twice the electrical length (length divided by two-thirds speed of light) of the cable. The MCP tube photocathode, used in transmission mode, is type S-20. The phosphor is type P-20 and is optically coupled via a fiber optic faceplate to pressure mounted Polaroid film (Type 612). The camera resolution at the film is \sim 20 line pairs/mm. The camera structure includes a 50-mm, f/1.2 lens and a biasing and triggering package that requires a 600- to 700-V bias input, a charged cable connection, and a 10-V trigger input. This package includes a pot to adjust MCP bias (i.e., gain), batteries, a 5-kV supply, a battery charging connection, toggle switches for on/off and DC/pulsed mode operation. The biasing and triggering package were designed and built by Dr Steve Seiler of R&D Associates, Washington Research Laboratories, Alexandria, Virginia. To obtain reliable and successful triggering of the MCP cameras, isolation transformers were used on the 600- to 700-V bias power supplies and inductive isolators on the bias connections; or 600-V batteries were used. For triggering, fiber-optic-links or inductive isolators were used.

A photograph of an MCP camera is shown in Figure 14. The MCP camera views used are illustrated in Figure 15. Low camera gains (pot setting = 8 corresponding to gain ~60), were typically used, a neutral density (ND) 1.5 filter, and a 45-cm charged cable to get reasonable exposures of the self-luminous plasma beam. The use of photodiode signals for guidance in choice of camera trigger timing was important.

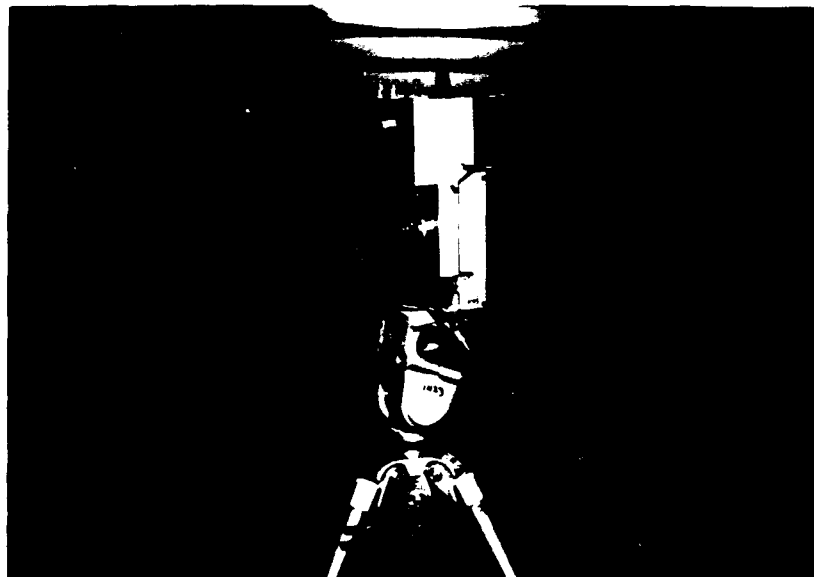
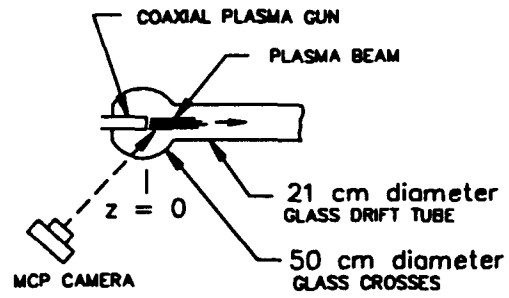


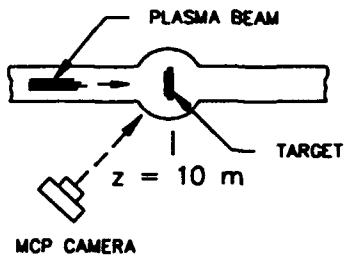
Figure 14. Microchannel plate camera.

Some MCP photographs of the plasma beam exiting the coaxial gun muzzle are shown in Figure 16. The image is contained in a circle 18 mm in diameter. The bright, irregular circle surrounding the image is due to contact pressure effects on the Polaroid film, which is pressed into contact with the MCP tube fiber optic faceplate. The exposed regions outside that circle are due to light leak. The view is an ~45 deg rear view of the gun muzzle taken through the cylindrical glass drift tube.

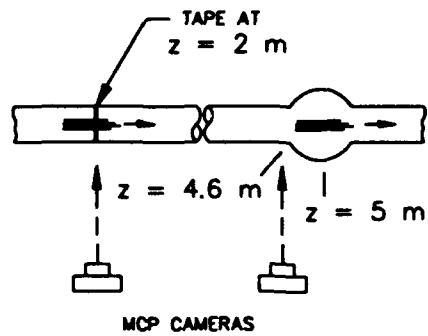
Some MCP photographs of a target illuminated by the plasma beam light are shown in Figure 17. The target had a complex structure, half anodized and half shiny Al sheet, with a slit and hole for possible rear diagnostics, and with a hole in the Al sheet for an ~0.7- μ m-thick Al foil covering it. This



(a) Gun muzzle

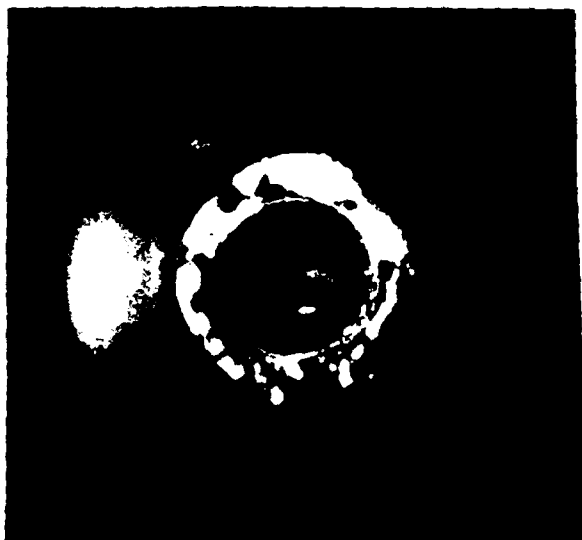


(b) Target at $z \approx 10 \text{ m}$

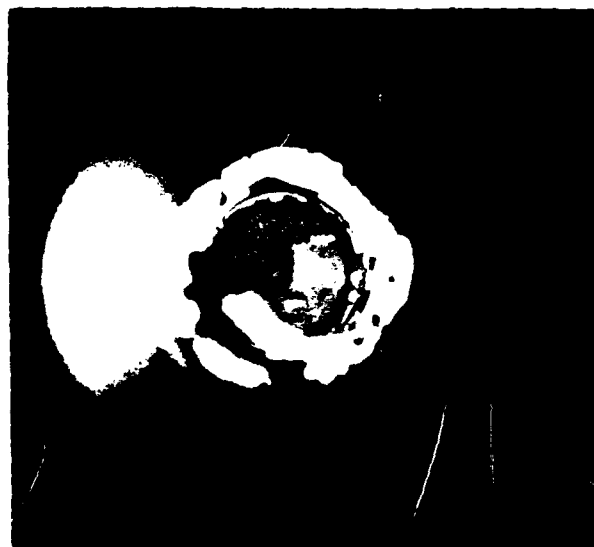


(c) Self-luminous plasma beam

Figure 15. The MCP camera views.

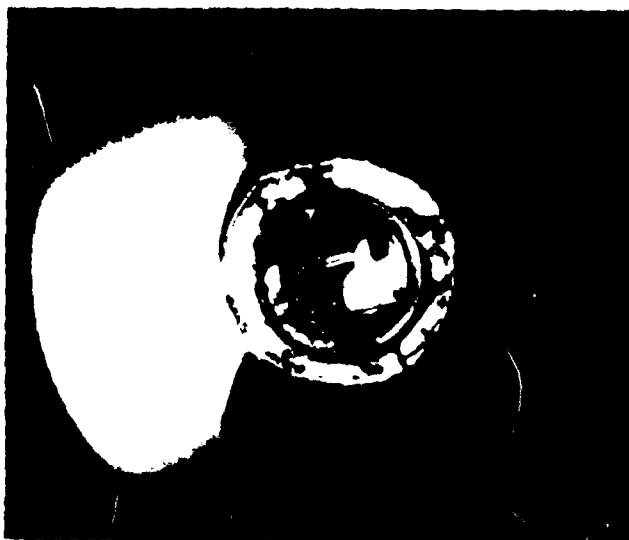


2441

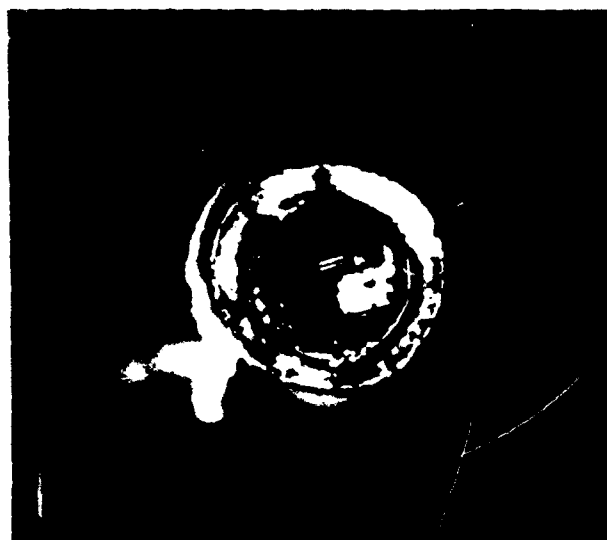


2444

Figure 16. Some MCP photographs of coaxial gun muzzle emission.



2448 Fresh Target



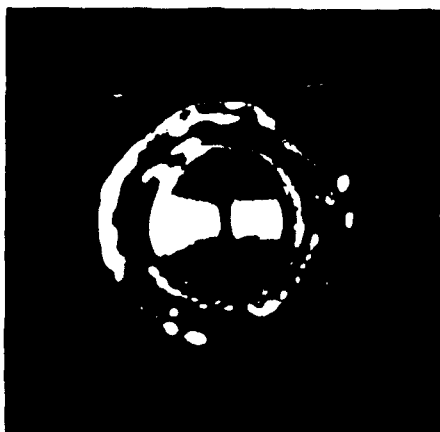
2450 Used Target

Figure 17. Some MCP photographs of target, $z = 10$ m, $t = 60$ μ s.

target was located at 10 m from the plasma gun in an ~50-cm spherical glass cross connected to the ~21-cm-dia cylindrical glass drift tube. The view is an ~45-deg view of the gun side of the target, taken through the glass cross. The hole for the foil is evident in the used target photograph (Shot 2450) and is not evident in the fresh target photograph (Shot 2448). These photographs were taken 60 μ s after the plasma gun (self-break) discharge initiated. The self-break occurred at an approximately reproducible time after the gun puff valve fired. The MCP camera gate time was monitored with a Tektronix CT-3 signal pickoff. These photographs indicate there is insufficient plasma beam energy and momentum to damage the foil target prior to 60 μ s after the gun fires. Thus the damaging portion of the plasma beam has a velocity <160 km/s. This is consistent with Cordin camera data (Figs. 10 and 11), which indicate that the velocity for the portion of the plasma beam giving rise to the peak impact luminosity is 80 to 90 km/s.

Some MCP photographs of the self-luminous plasma beam, taken with a perpendicular view through the 21-cm inner dia cylindrical glass drift tube, are shown in Figure 18. The dark strip transverse to the drift tube axis is a position marking tape located 2 m from the coaxial gun muzzle. The ~5- to 10-ns exposures were taken at 20 to 30 μ s after gun self-break. The times are indicated for each photograph, as well as the shot numbers and gas used. In both Figures 18 and 19, the plasma beam appears to have some MHD-like instabilities. That is, the radial location of the center of the plasma beam seems to vary with axial position. Recall that 8- μ s Cordin framing photographs (Figs. 3-5) suggested transverse wandering of the plasma beam. The observed presence of azimuthal magnetic field consistent with up to 1.5 kA of axial current, combined with this photographic evidence of plasma beam instabilities, transverse wandering and oscillation about the drift tube axis, suggests magnetic field guiding, focusing or cushioning from the drift tube walls. As discussed in a separate section, the observed fields and inferred currents are a factor of 3 to 10 low for simple quasi-steady pressure balance confinement.

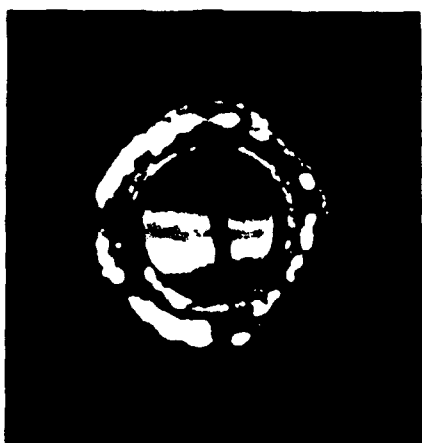
Some MCP photographs of the leading edge of the luminous plasma beam, referred to as beamheads were obtained. These are shown in Figure 20. The MCP photographs of plasma beams generated by a plasma gun with an alumina insulator



2495 He 2 m, 30 μ s



2511 Ar 2 m, 25 μ s

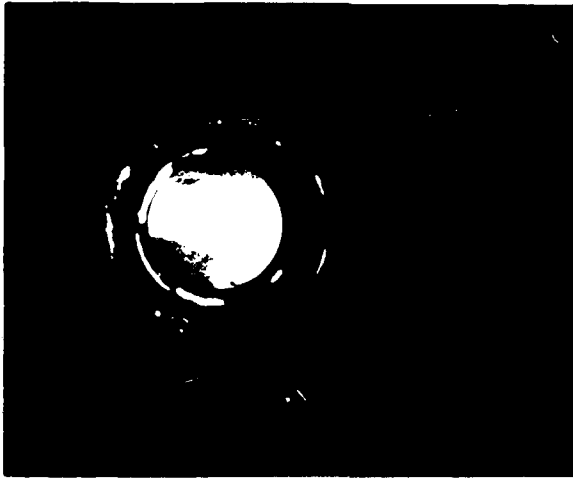


2509 Ar 2 m, 30 μ s

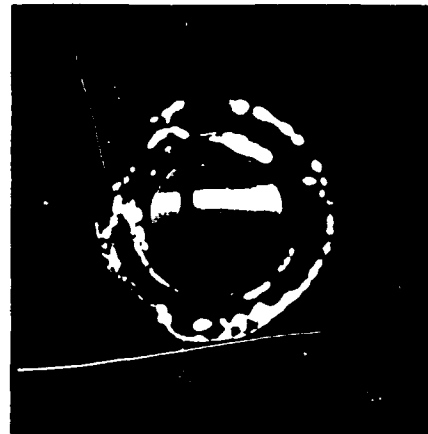


2521 Ar 2 m, 20 μ s

Figure 18. Some MCP photographs of self-luminous plasma beams for He, Ar operation, $z = 2$ m, $t = 20$ to 30μ s.



2468 5 m



2522 2 m, 20 μ s

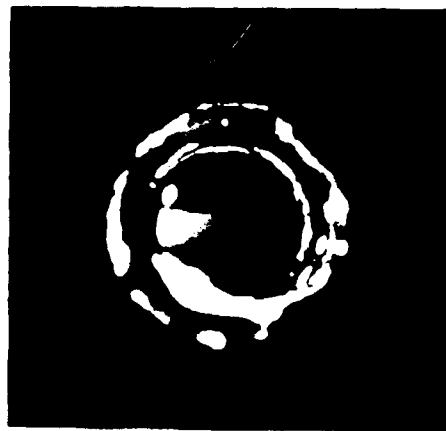
Figure 19. Some MCP photographs suggesting instabilities.

appear more granular and turbulent than MCP photographs of beams generated by a gun with a quartz insulator. Figure 21 shows MCP photographs for alumina insulator shots. The previous MCP photographs shown were for quartz insulator shots.

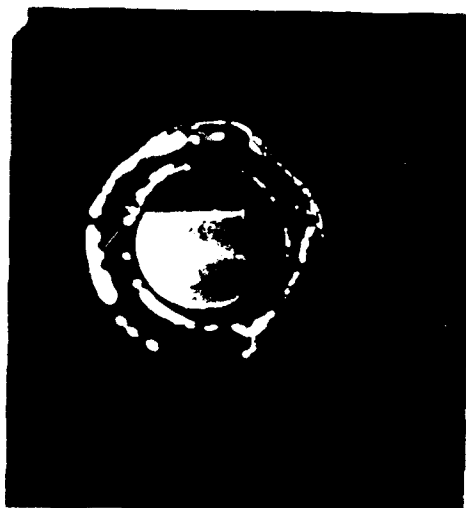
The TRW Model 1D IC camera photographs, examples of which are shown in Figures 22 through 25, show a diffuse plasma filling the center half of the drift tube, and the walls lit up, consistent with rotating mirror and MCP camera photographs. The IC photographs also show the plasma beam to be somewhat off-center.



2514 2 m, 20 μ s

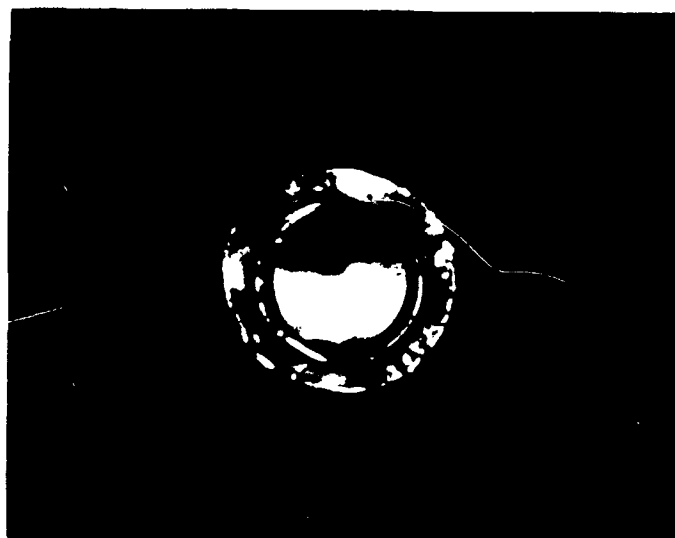


2515 2 m, 20 μ s

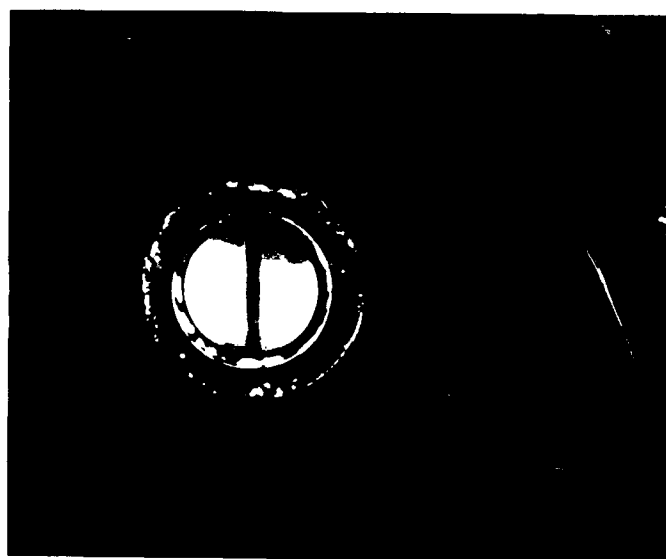


2526 Ar (196 μ F, 18 kV)
2 m, 20 μ s

Figure 20. Some MCP photographs of beamheads, $z = 2$ m, $t = 20$ μ s.



MCP-2 3.9 m, 65 μ s



MCP-3 4.6 m, 75 μ s

Figure 21. Some MCP photographs of beam in Shot 2505 (aluminum insulator) suggesting turbulence, granular structure.

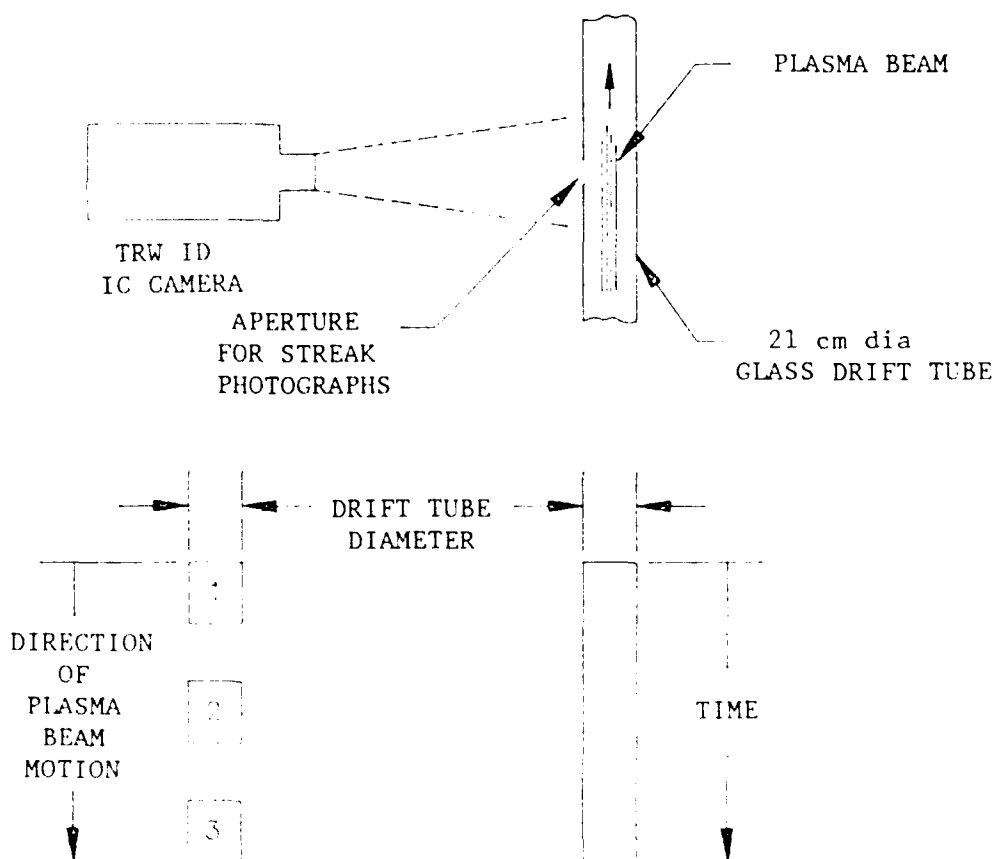


Figure 22. The TRW IC camera view (top), frame sequence (lower left), and streak photograph description.

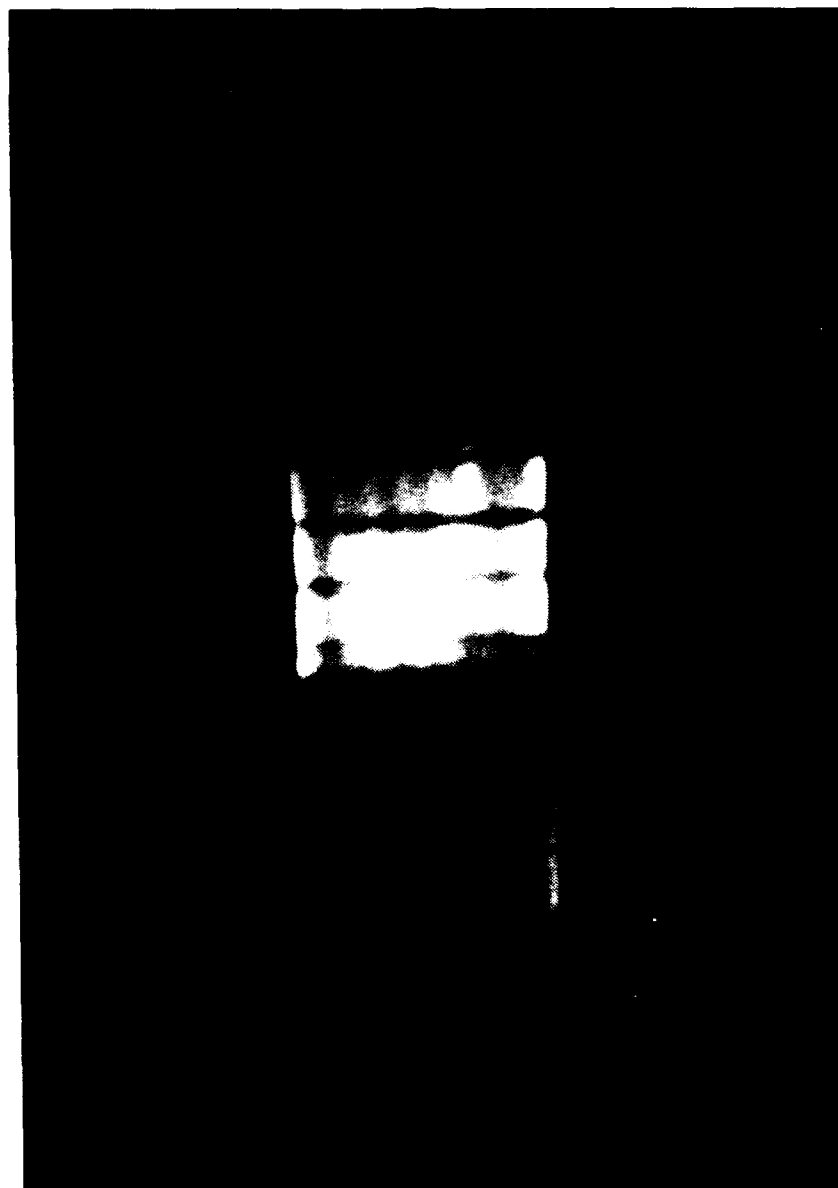


Figure 23. The IC framing photographs, Shot 2501, $z = 8$ m, alumina insulator, Ar operation; $1\text{-}\mu\text{m}$ pressusres at 70, 75, 80 μs after fiducial.

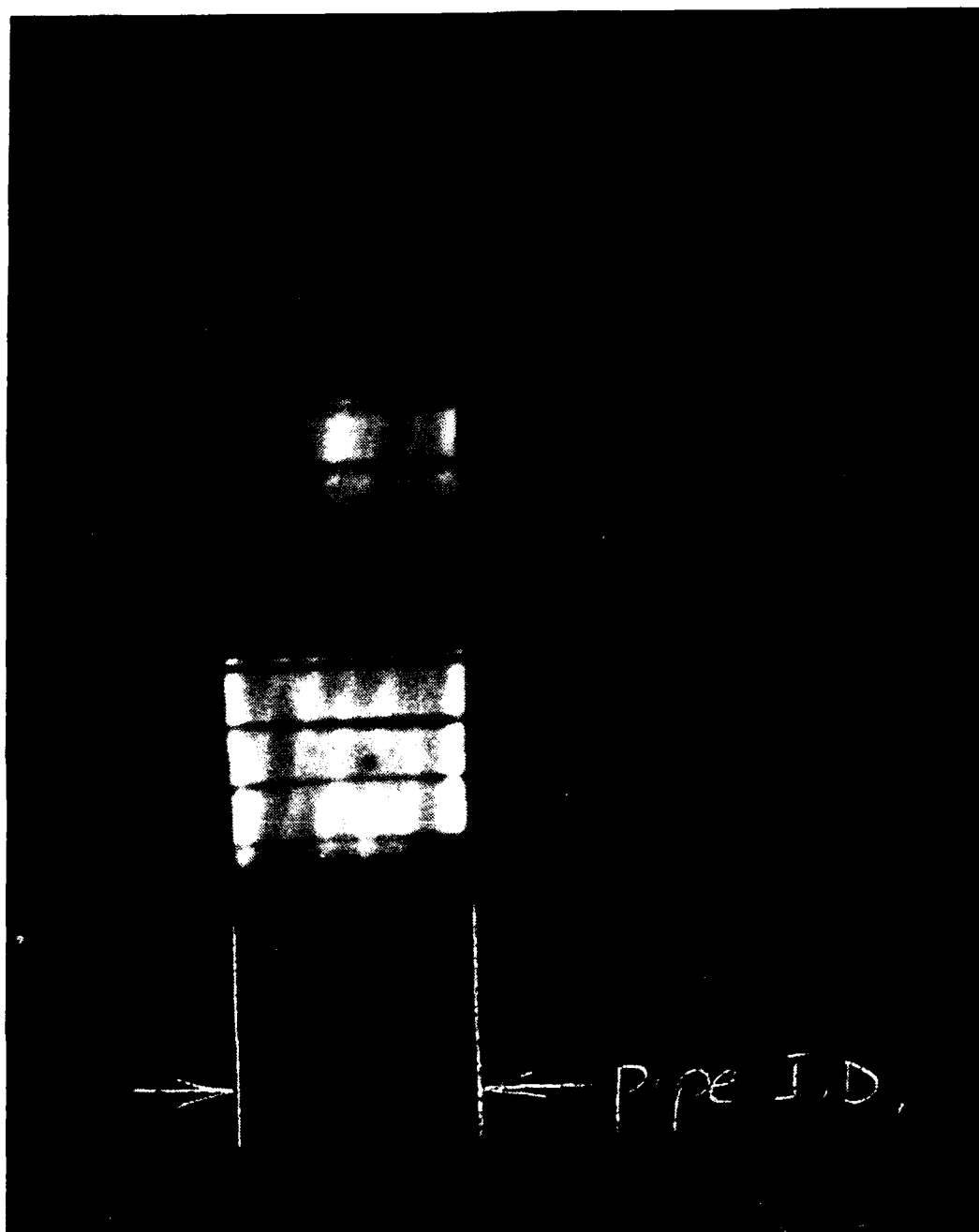


Figure 24. The IC framing photographs, Shot 2502, $z = 9$ m, alumina insulator, Ar operation. 1- μ s exposures at 70, 75, 80 μ s after fiducial.

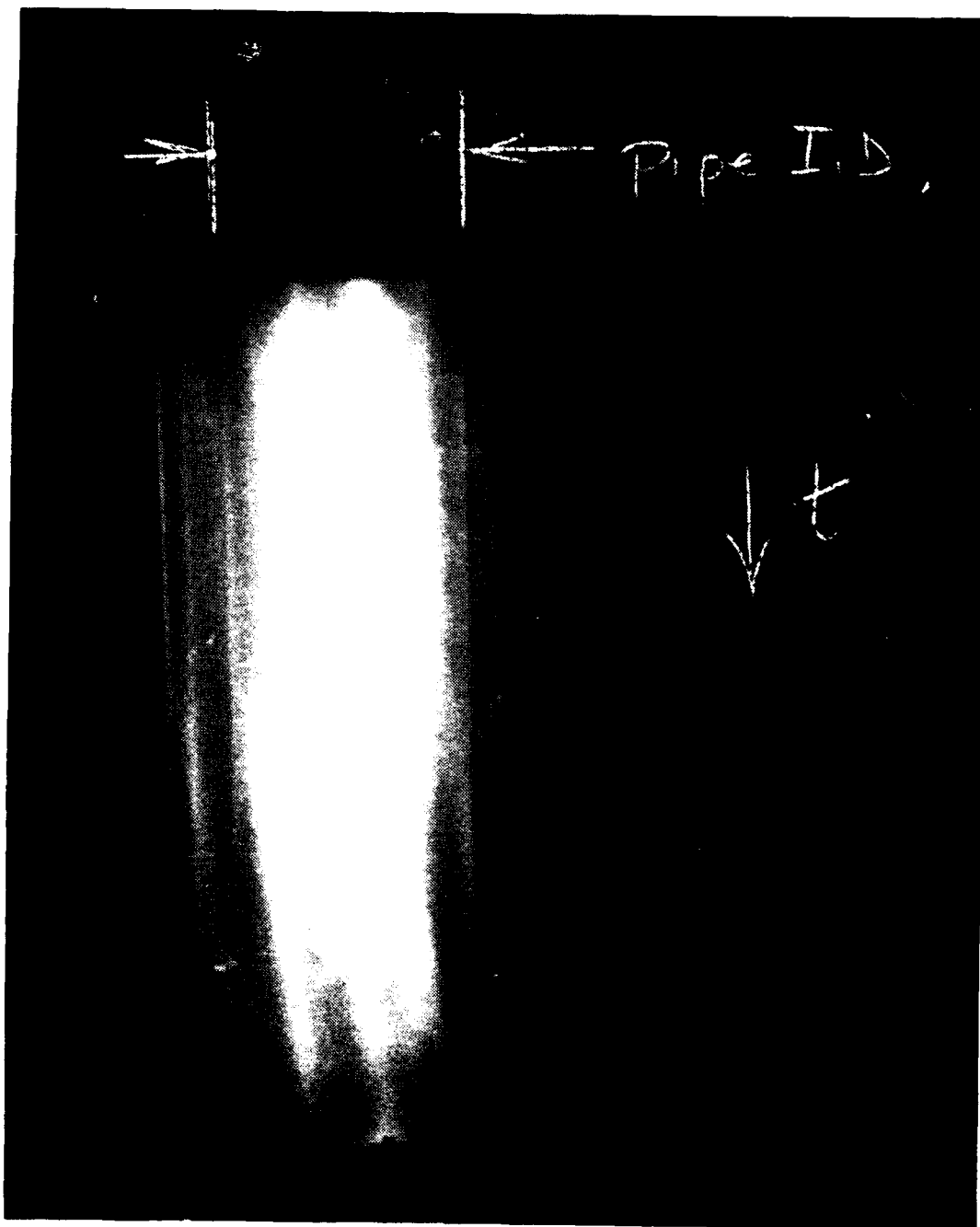


Figure 25. The IC camera 10- μ s streak photograph, Shot 2506, quartz insulator, Ar operation.

OPTICAL AND VACUUM ULTRAVIOLET PHOTODIODE DATA

The optical photodiode data of both the plasma beam luminosity and plasma beam target interaction luminosity were obtained. Vacuum Ultraviolet (VUV) photodiode data of the plasma beam target interaction luminosity were also obtained. The optical photodiodes had S-5 and S-20 photocathodes. They were placed to view the plasma beam through the glass drift tube. Typically, one was placed at 5 m and one at 8 m from the coaxial gun muzzle just outside the drift tube. The photodiode at the 5-m location looked through the spherical glass junction or cross in the drift tube. On some shots, this 5-m cross contained a target. The VUV photodiode, commonly called an X-ray photodiode (XRD), was mounted on the spherical glass cross port at 10 m from the coaxial gun muzzle, looking at target impact luminosity. This XRD was connected to the vacuum and was generally used unfiltered. The XRD response function (bare Al photocathode) is shown in Figure 26. When filtered, this response peaks in the ultrasoft to soft X-ray range. When unfiltered, the XRD response peaks at 16 eV with >10 percent of peak response from ~10 to ~45 eV. The target to XRD distance was ~50 cm, and the XRD sensitive diameter was ~5 cm. The 1-cm XRD anode screen to cathode gap was biased to 1 kV. The photodiode and XRD bias and signal cables included inductive isolators.

The optical photodiode data gave self-luminous plasma beam velocity distribution information via TOF. Examples are given in Figures 27 (Shot 2501) and 28 (Shot 2526). The TOF velocities obtained from the peaks of pairs of such photodiode signals were generally in the 70- to 90-km/s range for Ar, and 90- to 100-km/s range for H. The use of target impact luminosity (Fig. 28) instead of plasma beam self-luminosity did not obviously change these TOF velocities. This was done to check for the possibility of a fast neutral (nonluminous) beam. Inferred TOF velocities are substantially the same whether using pairs of photodiode traces or a single trace with the ~10- μ s gun discharge as zero time.

When photodiode traces were observed with sensitive oscilloscope settings, so peak signals were off scale, earlier peaks in luminosity were observed on some 20-kJ Ar and most 30- to 40-kJ H shots. These peaks should not be confused with the ~zero TOF peaks correlated with the ~600 kA gun current signal (Fig. 29).

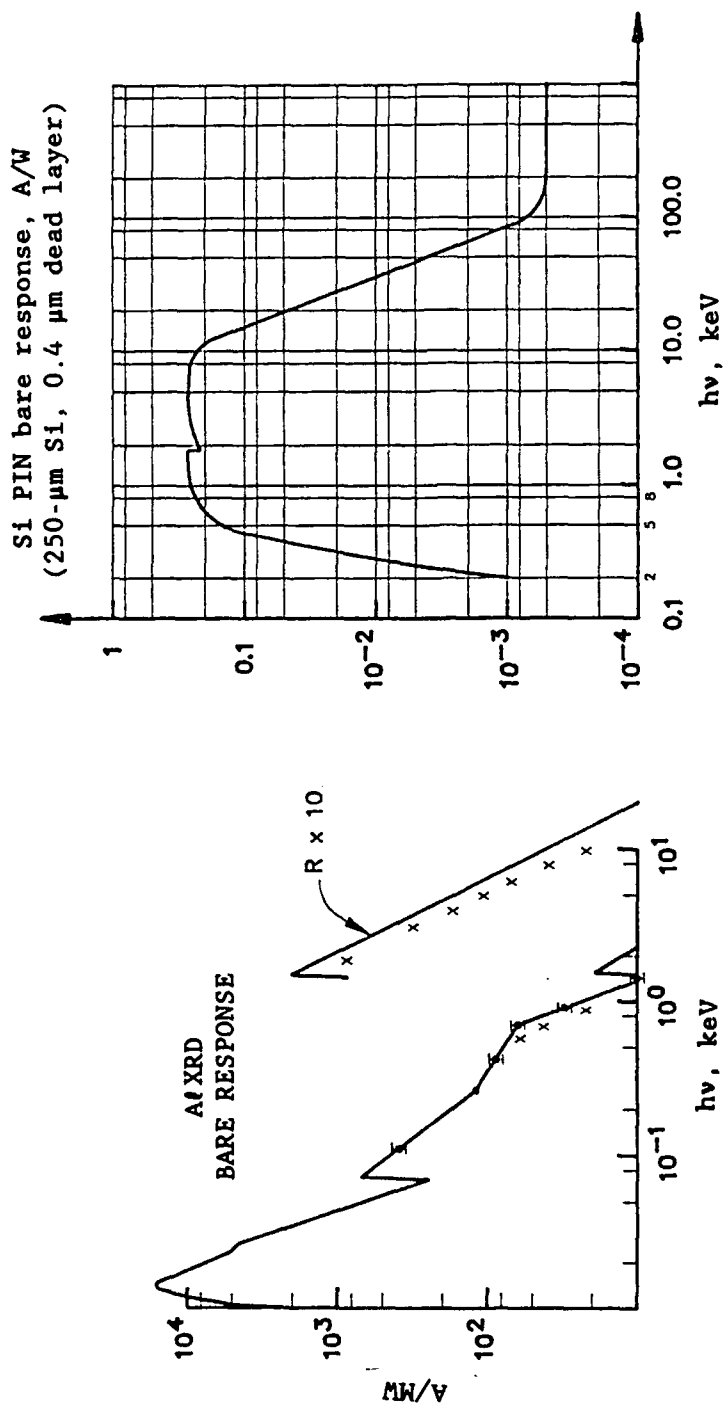


Figure 26. Response functions for bare Al photocathode (XRD) and Si PIN.

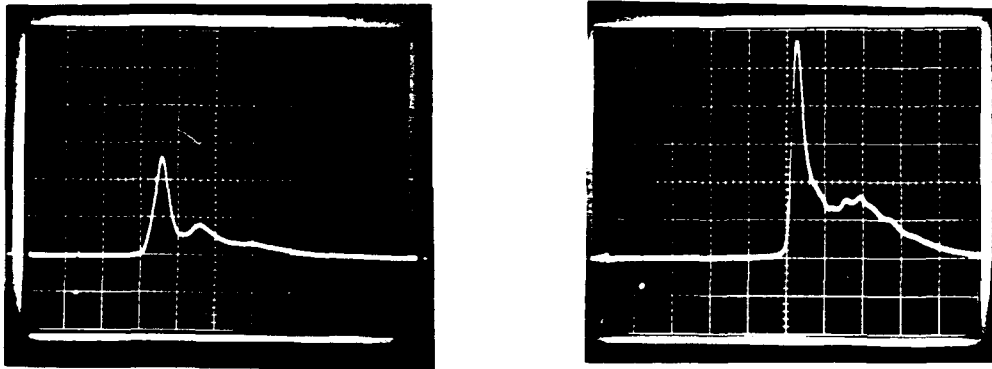


Figure 27. Optical photodiode signals for Shot 2501; $z = 5, 8$ m, $20 \mu\text{s}/\text{division}$; signal peaks at $48, 82 \mu\text{s}$ after fiducial suggest velocity ~ 88 km/s.

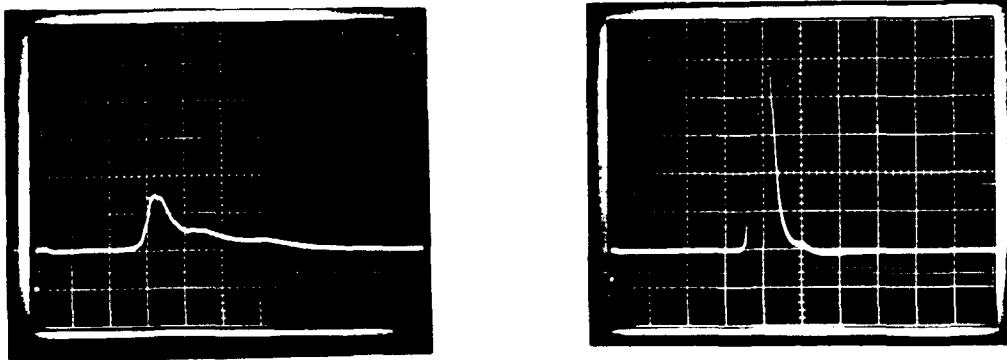


Figure 28. Optical photodiode signals for Shot 2526; $z = 5$ m (plasma beam) and $z = 15$ m (beam - target luminosity); $z = 5$ and 15 -m traces at 20 and $50 \mu\text{s}/\text{division}$, respectively; signal peaks at $64, 200 \mu\text{s}$ past fiducial suggest velocity ~ 74 km/s.

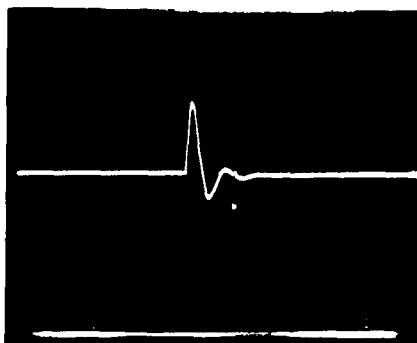
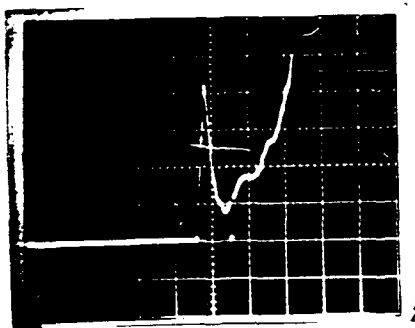


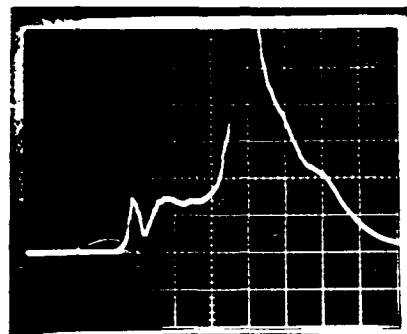
Figure 29. Coaxial gun integrated Rogowski coil current signal; 20 μ s/division; peak current \sim 600 kA.

The small \sim zero TOF luminosity peak, present in all signals observed on sensitive oscilloscope settings, is believed to be caused by reflected gun discharge light. The additional early peaks, which are called precursors or fast beam component signals, have TOF velocities (at precursor signal peak) of typically 200 to 250 km/s. Examples are shown in Figure 30 for both target impact and self-luminosity cases. Target impact luminosity does not exceed self-luminosity for these precursor pulses. As discussed in the section on interferometry, the density and mass of such precursors is 3 to 4 orders of magnitude less than the main (slow) plasma beam component, and this was with target impact enhancement. The luminosity of these precursors is typically 2 orders of magnitude smaller than that of the main plasma beam.

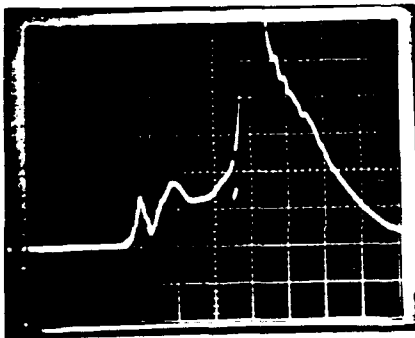
The XRD signals of target impact luminosity, shown in Figure 30, again give TOF velocities in the 70- to 90-km/s range for Ar (and He) gun operation. Some XRD data, such as that for Shot 2451, shown in Figure 31, showed small (up to few \times 0.1 V) early negative signals as well as the large (2 to 4 V) positive signals at later time. These early negative signals are believed to be due to photoelectrons produced at the target by VUV emission from the plasma beam, or from beam--drift tube wall collisions.



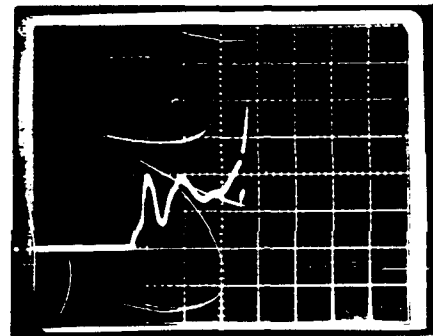
SHOT 2536



SHOT 2538

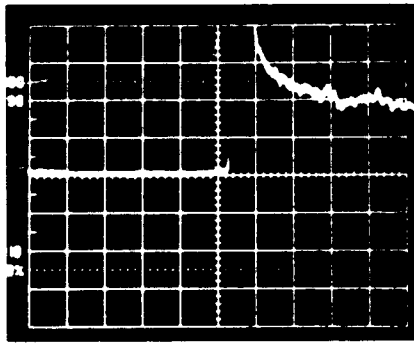


SHOT 2539

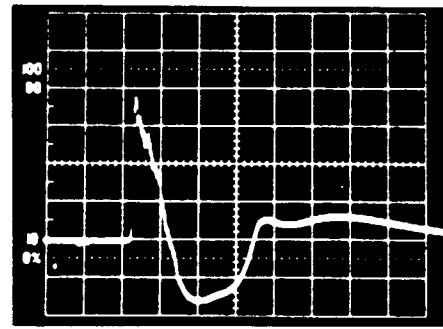


SHOT 2540

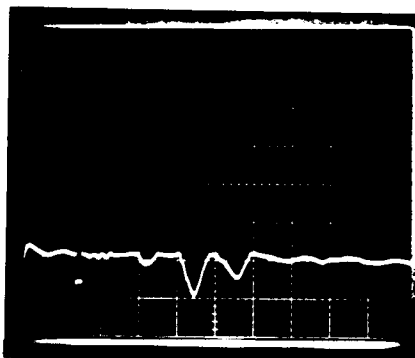
Figure 30. Optical photodiode signals showing evidence of fast plasma beam component (precursor): 20 μ s/division; $z = 5$ m; H operation.



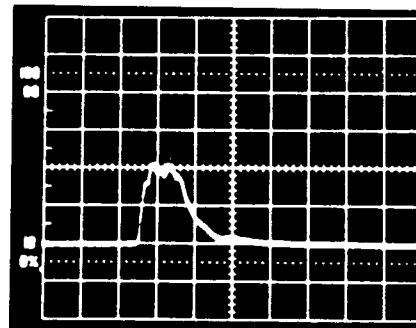
SHOT 2436



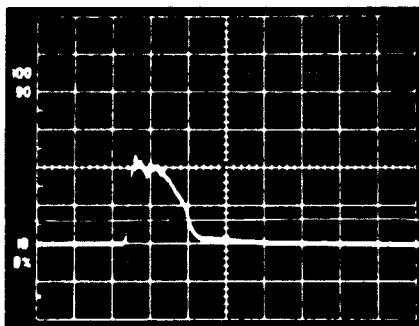
SHOT 2451



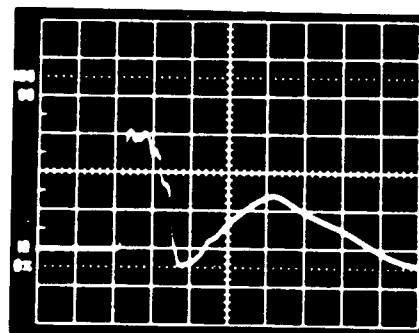
SHOT 2451 SENSITIVE SCALE



SHOT 2460



SHOT 2463



SHOT 2466

Figure 31. The XRD traces. $z \approx 10$ m, observing beam - target luminosity. Shot 2436: 1 V, 20 μ s/division, no magnet. Shot 2451: 1 V, 50 μ s/division, and 0.1 V, 10 μ s/division, no magnet and no inductive isolator. Shots 2460, 2463, and 2466. 1 V, 50 μ s/division, magnet and inductive isolator.

Such photoelectrons may be accelerated toward the 1-kV biased XRD anode mesh, passing through the mesh toward the XRD cathode, giving a negative signal. Placing a sweeping magnetic field ~ 1 kG between the target and the XRD eliminates these negative signals. Such a magnet was used for all shots after and including Shot 2460. Inductive isolators, used for all XRD data except Shots 2448 to 2459, appeared to suppress ± 0.02 V "noise". The XRD data obtained with inductive isolators and sweeping magnets generally showed a small, prompt positive signal (essentially zero TOF), which is believed to be caused by reflected VUV from the gun discharge (it tracks the discharge current), and a larger delayed positive signal (110 to 140- μ s TOF) which is interpreted as target impact luminosity. There is no clear XRD evidence for a faster beam component (i.e., early positive signals above noise). Some (questionable) XRD evidence for a fast beam component is shown in Figure 32. This was obtained in a preliminary experiment three months before the main series of experiments. If the small signal at ~ 20 μ s (XRD at 10 m) is in fact due to a fast beam component, its luminosity is 2 to 3 orders of magnitude less than the main peak.

Attempts to observe higher photon energy target impact radiation with filtered XRDs (>150 eV and >1 keV) and with filtered Silicon (Si) PIN detectors (>1 keV, response function shown in Figure 26) gave null results.

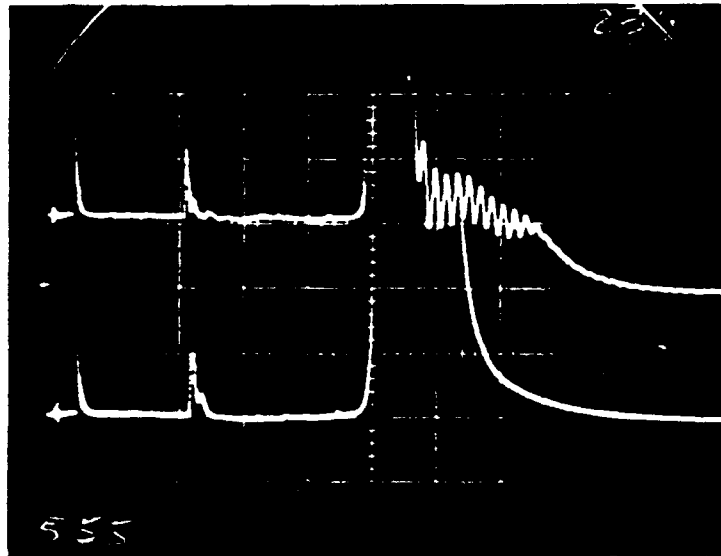


Figure 32. Upper trace: XRD signal. Lower trace: photo-diode signal. Both traces looking at beam - target luminosity at $z = 10$ m; 2 V, 50 μ s/division; gun current starts ~ 105 μ s; possible XRD evidence for fast beam component ~ 15 μ s after gun current starts.

MAGNETIC FIELD MEASUREMENTS

INTRODUCTION

Personnel from the WL were tasked to find the parameters of plasma beams generated at GRC. One of the methods used was to observe axial currents and any associated azimuthal magnetic fields (if any). This method used Rogowski coils (to measure current directly) and coils of wires to measure induced voltages created by changing magnetic fields. The results of using these kinds of methods to examine the GRC plasma beams are discussed.

This section contains the following: a simple magnetic field theory; a description of magnetic field probe coils and selected results from magnetic field measurements; discussion of magnetic pressure balance and beam parameters; and a discussion of results.

MAGNETIC FIELD MEASUREMENT THEORY

A coil of wire can be used to determine a line current under several simplifying assumptions. If a current flows linearly (in the axial direction), it generates an azimuthal magnetic field. Since the magnetic field is represented in the literature by the B vector notation, it is often called a B -field. This convention will be used throughout this section. Using this notation, the azimuthal B -field is indicated by B_θ . The azimuthal magnetic field B_θ is related to the current I by the relation in Equation 1.

$$B_\theta = \frac{\mu_0}{2\pi r} I \quad (1)$$

In this equation, μ_0 is the permeability of free space and r is the perpendicular distance between the point where the B -field and the axis of symmetry are measured.

The magnetic field will create a voltage in a coil of wire oriented in an appropriate direction. The voltage is related to the relation given in Equation 2.

$$V = - \frac{\mu_0 n A}{2\pi r} \frac{dI}{dt} \quad (2)$$

In Equation 2, the voltage V is induced in the loop of N turns and A cross-sectional area (perpendicular to the magnetic field B). The voltage is related to the time derivative of the current (dI/dt).

The magnetic field probes are not usually operated in a time differentiated mode in the experiments; they are integrated to observe the magnetic field and the current. In the system fielded at GRC, the signal was integrated with passive (RC) integration. The relation between the induced loop voltage and the axial current due to the azimuthal B-field is given in Equation 3

$$V = - \frac{1}{RC} \frac{\mu_0 n A}{2 \pi r} I \quad (3)$$

where the passive integration time constant is RC .

Because the passive RC integration introduces a voltage droop (due to the RC decay of the source voltage), the voltage must be numerically corrected. This corrected voltage is given in Equation 4

$$V_{corr} = \int \left(V + RC \frac{dV}{dt} \right) dt \quad (4)$$

where V_{corr} is the corrected voltage, V is the measured source voltage and dV/dt is the time differential of the measured voltage.

Equations 2 through 4 assume the position of the current is known and the current path can be described analytically to generate relations between current and induced magnetic fields. If, however, the relation between the current and the magnetic field is not explicitly known, the relation between the voltage and the induced magnetic field can still be valid. This relation is shown in Equation 5

$$V = - \frac{n A}{RC} B \quad (5)$$

where the values of n , A , B and RC have been previously defined.

EXPERIMENTAL MAGNETIC FIELD MEASUREMENTS

The B-dot probes were used to determine the current at the 5- and 10-m stations of the GRC experimental system. There were two B-dot probe designs. The first B-dot probe design had a pair of circular coils of wire (with four turns each) of opposite polarity (so the measured B-dot probe signals would be of opposite sign). With this reversed polarity pair of probes, the inductive and electrostatic signals can be distinguished, allowing unambiguous identification of the signal and (unintended) noise components. The B-dot probe pairs 3A/3B and 4A/4B were of this circular design. The second design had a pair of opposite polarity loops made from small gauge coaxial cable. The effective area of this design was defined by the rectangular shape of 1.3-cm width and the 2.6-cm length of the coil. The B-dot probe pair 6A/6B was made with this second (rectangular) design. All B-dot probes were mounted in 0.75-in outer diameter (OD) glass tubes inserted into the vacuum of the GRC experimental system through a Wilson seal. Mounting the B-dot probe packages through the Wilson seal allowed the position of the B-dot probe pairs to be changed axially and radially. Such mounting allowed the B-dot probe orientation to be sensitive to either the azimuthal field component, B_θ , or the axial field component, B_z . For the GRC system, it was expected (and observed) that $B_\theta \gg B_z$. The radial position of the magnetic field probes was usually 3 in (7.5 cm) from the drift tube axis.

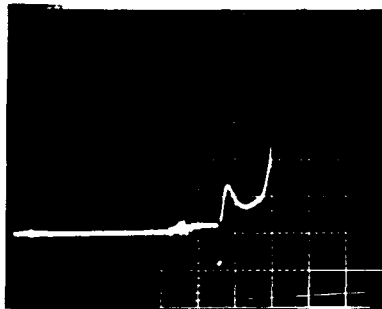
The noted B-dot probe pairs (3A/3B, 4A/4B and 6A/6B) were mounted in the GRC experimental system at different places at different times dependent on the experiment to be fielded. After 19 September, the B-dot probe pair 6A/6B was mounted at the 5-m station. The B-dot probe pairs 3A/3B and 4A/4B were mounted at the 10-m station. The B-dot probe pair 6A/6B was mounted so the coil was at the center line of GRC system. After 19 September, the B-dot probe pair 3A/3B was mounted at the center line of the experimental system and B-dot probe pair 4A/4B was mounted 2 in above the centerline location of 3A/3B and 1.25 in to the right of 3A/3B. Before 19 September, B-dot probe pairs were mounted at the center of the GRC experimental system at the 5- and 10-m stations.

The B-dot probes are calibrated in a spark gap system using a large capacitor of known capacitance. In this system, breakdown voltage is measured and the voltage response of the B-dot probes are recorded. For consistency and error reduction, several shots are made on the calibration system for each B-dot probe to be calibrated. The B-dot probe sensitivities were then calculated from this series of data. Two of the three B-dot probe pairs (3A/3B and 6A/6B) were calibrated with this system. Calculated B-dot probe calibrations are consistent and yield statistical variations (standard deviations) of <5 percent. The third B-dot probe pair (4A/4B) is assumed to be equivalent to the other probe of the same design (3A/3B) within 10 percent.

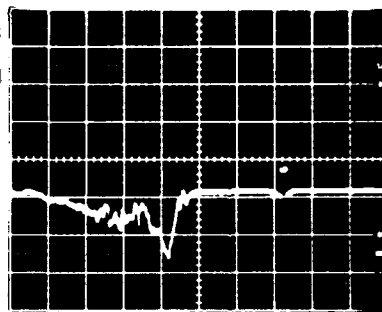
It should be noted the results reported here are subject to the assumptions reported in the subsection on magnetic field measurement theory.

A comparison of the results of the voltage responses for the photodiode and a B-dot probe (3A) mounted to measure the B_0 field at the 5-m station can be seen in Figure 33. These show the correlation of precursor signals and (assumed) plasma luminosity and magnetic field signals. These data were for Shot 2500 taken on 13 September. The gas used in this shot was Ar at 30 psig. Charge voltage was 18 kV on a 126- μ F capacitor bank. The start of gun current (evident as the damped oscillatory perturbations in the trace) occurs at 90 μ s. The fiducial occurs at 110 μ s and the photodiode precursor peak occurs at 115 μ s. The main light pulse goes off-scale at 140 μ s. In Figure 33b, the effects of an axial current are shown. This trace is triggered at the start of the gun current. The precursor and the fiducial are coincident at 27 μ s. The main B_0 field begins at 52 μ s. The magnetic field peaks at 12 μ s after current rise to a maximum magnetic field of 1.3 mT. This peak magnetic field corresponds to a current (under the stated assumptions) of 430 A. These assumptions include cylindrical symmetry, a centered beam, a current distribution inside the probe radius and a return current external to the probe radial position.

Figure 34 shows the signals for a coaxial B-dot probe pair (3A/3B) at the 5-m station. These data were for Shot 2513 taken on 14 September. The gas used in this shot was Ar at 30 psig. Charge voltage was 18 kV on a 126- μ F capacitor bank. Noise is minimal in these traces because fiber optic signal

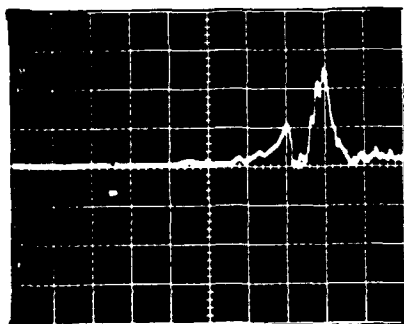


(a) Photodiode voltage response;
0.2 V/division.



(b) B_0 probe response for B3A;
53- μ s RC integrator;
240 A/division. (7.0×10^{-4}
T/division.)

Figure 33. Correlation of luminosity and magnetic field precursor and main signal responses taken at 5-m station. Both time bases 20 μ s/division.



(a) B_0 probe response for B3B;
46.8- μ s RC integrator;
250 A/division. (6.2×10^{-4}
T/division.)



(b) B_0 probe response for B3A;
53- μ s RC integrator;
240 A/division. (7.0×10^{-4}
T/division.)

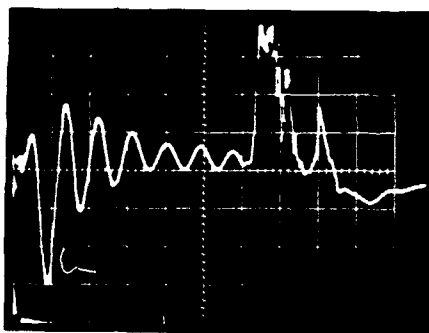
Figure 34. Reversed pair of B_0 probe signals
taken at 5-m station. Both time
bases 10 μ s/division. Fiber optic
coupling of signal.

links were used to transmit the voltage signals to the oscilloscopes. Both signals are triggered by start of gun current. The fiducials occur at 25 μ s and precursor magnetic signals can be seen at 90 μ s. The B_0 fields (and assumed axial currents) are seen to peak at 70 and 80 μ s. In Figure 34a, the peak magnetic fields are 1.3 mT (at 70 μ s) corresponding to an axial current of 530 A and 2.6 mT (at 80 μ s) for an axial current of 1.0 kA. In Figure 34b, the peak magnetic fields are 0.7 mT (at 70 μ s) for an assumed axial current of 240 A and 1.7 mT (at 80 μ s) for an assumed axial current of 580 A.

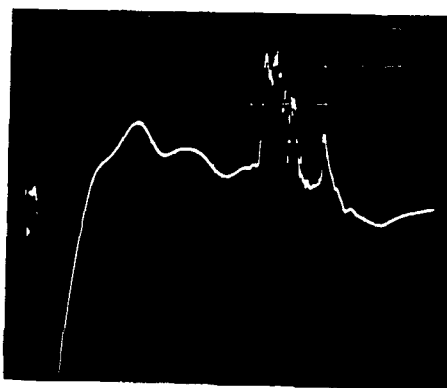
Figure 35 shows the signals for a coaxial B-dot pair (3A/3B) at the 10-m station. These data were for Shot 2524 taken on 20 September. The gas used was Ar at 30 psig. Charge voltage was 12.3 kV on a 252- μ F capacitor bank. Electromagnetic (EM) noise is evident due to the lack of fiber optic transmission of the signals. Both signals are triggered by start of gun current. No fiducials are present. Figure 35b was inverted at the oscilloscope. Current is seen to begin at 106 μ s and yields a peak magnetic field of 1.3 mT for an assumed current of 500 A occurs at 108 μ s. A smaller peak of 0.6 mT for an assumed current of 200 A occurs at 160 μ s.

Figure 36 shows the signals for an azimuthal B_0 signal and an axial B_z signal taken at the 10-m station. These data were taken for Shot 2525 on 20 September. The gas used was Ar at 30 psig. Charge voltage was 12.7 kV on a 252- μ F capacitor bank. Again EM noise is evident due to the lack of fiber optic signal transmitters. Both signals are triggered by the start of gun current. Again, fiducials are not present due to equipment limitations. In Figure 36a, axial current and azimuthal magnetic field, B_0 , are seen to begin at 124 μ s and peak at 134 μ s and 140 μ s. The peak magnetic field is 1.2 mT for an assumed axial current of 300 A. In Figure 36b, voltage from axial magnetic probe, B4B (measuring B_z), is displayed. Although the signal is noisy, a B_z signal structure is evident from 134 to 150 μ s (corresponding to the time of the B_0 signal). Figure 36b is inverted at the oscilloscope. No current calibration data are available for the axial current, but the peak B_z signal is about 0.4 mT.

Figure 37 shows a comparison of noise traces and the largest azimuthal magnetic field and axial currents observed during the series of experiments.

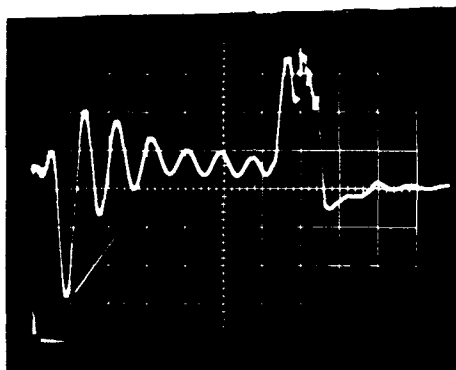


(a) B_0 probe response for B3B;
27- μ s RC integrator;
140 A/division. (3.6×10^{-4}
T/division.)

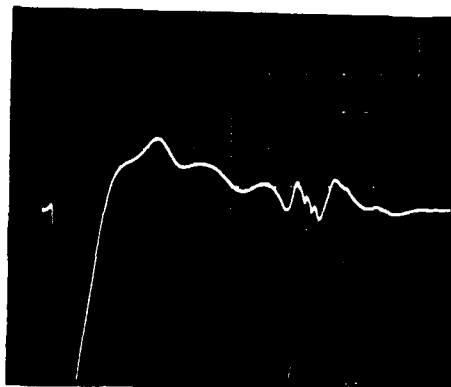


(b) B_0 probe response for B3A;
27- μ s RC integrator;
120 A/division. (3.6×10^{-4}
T/division.) Signal inverted
at oscilloscope.

Figure 35. Reversed pair of B_0 probe signals
taken at 10-m station. Both time
bases 20 μ s/division.

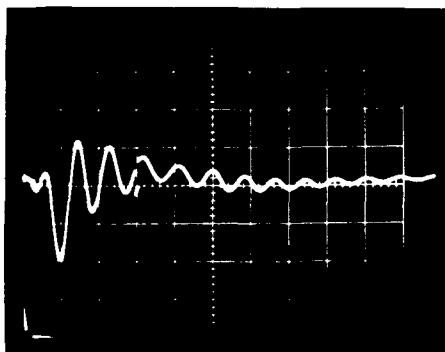


(a) B_θ probe response for B3B;
27- μ s RC integrator;
140 A/division. (3.6×10^{-4}
T/division.)

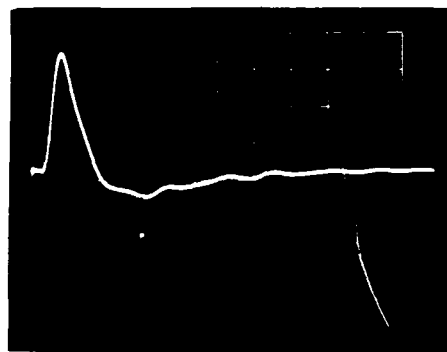


(b) B_z probe response for B4B;
27- μ s RC integrator;
5 mV/division; no current
calibration. (3.6×10^{-4}
T/division.)

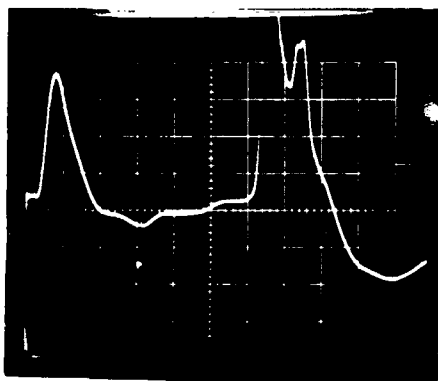
Figure 36. Magnetic probe signals taken at 10-m
station. Both time bases 20 μ s/
division.



(a) B_θ response for B3B for
Shot 2540; 27- μ s RC
integrator; 140 A/division.
(3.6×10^{-4} T/division.)



(b) B_θ response for B4B for
Shot 2540; 27- μ s RC
integrator; 270 A/division.
(7.1×10^{-4} T/division.)



(c) B_θ response for B4B for
Shot 2538; 27- μ s RC
integrator; 270 A/division.
(7.1×10^{-4} T/division.)

Figure 37. Correlation of noise signals with large B_θ
signal taken at 10-m station. All time
bases 20 μ s/division.

Figures 37a and 37b are taken from Shot 2540 and Figure 37c from Shot 2538. Both shots were fired on 21 September. The gas in both shots was Ar at 30 psig. The charge voltage was 16 kV on a 126- μ F capacitor bank. Some EM noise is evident, again, due to lack of fiber optic signal coupling. All signals were taken at the 10-m station. The main difference in these two traces is an interfering diagnostic was inserted into the beam at the 5-m station on Shot 2540 (thus obscuring the diagnostics at the 10-m station). On Shot 2538, the obscuring diagnostic was not inserted into the beam region. In all other physical respects, these two shots are the same. All traces were triggered by the rise of gun current. In Figure 37a, the fiducial occurs at 60 μ s. The sensitivity to azimuthal magnetic field is 0.36 mT/division and to an assumed axial current is 140 A/division. Only noise is evident in Figure 37a. In Figure 37b, the fiducial occurs at 60 μ s. The voltage peak at 18 μ s is a noise signal. The magnetic field sensitivity is 0.71 mT/division and current sensitivity is 270 A/division. In Figure 37c, the axial current and azimuthal magnetic field are displayed. As in Figure 37b, the noise signal peaks at 18 μ s and the fiducial is at 60 μ s. As in Figure 37b, the azimuthal magnetic field sensitivity is 0.71 mT/division and the current sensitivity is 270 A/division. The axial current rises at 124 μ s to a maximum that goes off-scale. This off-scale peak magnetic field peak is excess of 4.0 mT for an axial current of 1.5 kA. There is a second peak, at 150 μ s, of 3.2 mT for an axial current of 1.2 kA.

When Rogowski coils were mounted around the glass vacuum vessel, only currents at minimum detectable levels (on the order of 200 A or smaller) were measured. All return current is presumed to be inside the vacuum vessel. Fast photography shows a luminous sheath on the internal surface of the GRC vacuum vessel suggesting a return current layer. These results are consistent with the results of the axial B-dot probe measurements. For the entire series of experiments, axial currents measured with B-dot probes were generally <1 kA. On one shot, Shot 2538, at the 10-m station, a maximum current of 2 kA was measured. As previously stated, the validity of this interpretation depends on the validity of the assumptions of cylindrical symmetry and radial current distribution.

MAGNETIC PRESSURE BALANCE

It was experimentally observed that the luminous portion of the plasma was constrained within some fractional diameter of the vacuum drift tube. Visible light observations using 8- μ s framing, 10-ns framing and 200- μ s streak photographs indicated a visible or incandescent envelope smaller than the vacuum vessel inner diameter. Interferometric data also indicated a rapid decrease of density as a function of radial beam position. If the axial current is of sufficient magnitude, it generates an azimuthal magnetic field to restrict the plasma radius. This restriction would come from the balance of the transverse kinetic plasma pressure and the magnetic field pressure. In a complete analysis, this balance (which ignores radiative effects) is the Bennett condition. A complete presentation of the Bennett condition is given in Reference 3.

For a simple analysis of the balanced plasma condition, assume a plasma density profile, $n(r)$ given in Equation 6.

$$n(r) = \begin{cases} n_0, & 0 \leq r \leq R_0 \\ 0, & R_0 < r \end{cases} \quad (6)$$

where n_0 is the uniform plasma density and R_0 is the plasma radius. Using this definition of density, the plasma density J is described in Equation 7

$$J(r) = \begin{cases} n_0 e v_D a_z, & 0 \leq r \leq R_0 \\ 0, & R_0 < r \end{cases} \quad (7)$$

where v_D is the effective plasma velocity and a_z is the axial unit vector.

The plasma current $I(r)$ is related to the plasma current density $J(r)$. It can be obtained by the integration over the surface transverse to the axial flow. The current $I(r)$ is given in Equation 8.

$$I(r) = \begin{cases} e n_0 v_D (\pi r^2), & 0 \leq r \leq R_0 \\ e n_0 v_D (\pi R_0^2), & R_0 < r \end{cases} \quad (8)$$

It should be noted that the plasma drift velocity $v_D = v_i - v_e$ is not identical to the plasma beam velocity.

In an equilibrium condition, the magnetic pressure (which inhibits radial expansion) will balance the plasma thermal pressure (which promotes plasma radial expansion). If neutral gas particles are present, they are assumed to be uniformly dispersed within the vacuum vessel and provide no pressure differential anywhere within volume of the vacuum vessel. Thus, in this analysis, the pressure effects of neutral particles will be ignored.

The MHD balance for this condition is given in Equation 9.

$$\mathbf{J} \times \mathbf{B} = \nabla P = \nabla(n_i k T_i + n_e k T_e) \quad (9)$$

where P is the plasma pressure, n is the species number density, k is the Boltzmann constant and T is the species temperature. The subscripts i and e refer to the positively charged ions and the (negatively charged) electrons, respectively.

In cylindrical coordinates, Equation 9 is given in Equation 10.

$$\mathbf{J} \times \mathbf{B} = k \frac{\partial}{\partial r} (n_i T_i + n_e T_e) \mathbf{e}_r \quad (10)$$

No axial variation in the beam and beam azimuthal symmetry are also assumed. Inserting values for J and B at the plasma edge yields the relation in Equation 11.

$$\left(\frac{I}{\pi R_0^2} \right) \mathbf{e}_z \times \left(\frac{\mu_0 I}{2 \pi R_0} \right) \mathbf{e}_\theta = k \frac{d}{dr} (n_i T_i + n_e T_e) \mathbf{e}_r \quad (11)$$

If one assumes that $T = T_e = T_i$ and $n_0 = n_i + n_e$ and simplifies the relation, the result is Equation 12.

$$I^2 = \frac{2 \pi^2 R_0^3 k T}{\mu_0} \frac{dn_0}{dr} \quad (12)$$

For simplistic assumptions, dn_0/dr goes to infinity and an approximation for dn_0/dr must be made for this relation to be evaluated. The smallest value for dn_0/dr can be approximated by $dn_0/dr = \Delta n_0/\Delta r = n_0/R_0$. Equation 12 then transformed into Equation 13.

$$I^2 = \frac{2 \pi^2 R_0^2 n_0 k T}{\mu_0} \quad (13)$$

From this relation, one can calculate an equilibrium current, I_{eq} . These data are displayed in Table 1. The radial positions are chosen to be 25, 50, 75 and 100 percent of the maximum possible plasma radius (10.5 cm).

The plasma equilibrium radius is not a constant but is dependent on the plasma parameters. The Bennett relation shows this variation. From Reference 4, the appropriate descriptive equations are given below (Eqs. 14-17).

$$n(r) = \frac{n^*}{(1 + n^* b r^2)^2} \quad (14)$$

$$b = \frac{\mu_0 e^2 v^2}{8 k (T_e + T_i)} \quad (15)$$

$$N_l = \frac{n^* \pi R_0^2}{1 + n^* b R_0^2} \quad (16)$$

$$I_B^2 = \frac{8 \pi N_l k (T_e + T_i)}{\mu_0} \quad (17)$$

where n^* becomes the peak plasma density ($n_e = n_i$) at $r = 0$, b is the characteristic Bennett scaling parameter, N_l is the linear plasma density and Equation 17 describes the Bennett equilibrium relation. In these relations, the plasma drift velocity, v_0 , is used. The relation between the plasma drift velocity and the ion drift velocity v_i and the electron drift velocity v_e is $v_0 = v_i - v_e$.

For limits in the calculations, it should be noted the plasma may be no larger than the vacuum vessel inner radius, 10.5 cm. It can be shown in the effectively infinite linear plasma density, $N_{l\infty}$, occurs when $N_l = \pi/b$ which provides an upper bound for R_0 , if not otherwise constrained.

The denominator of the linear plasma density will strongly affect the behavior of the limiting Bennett current I_B . If $n^* b R_0^2 \ll 1.0$, $N_l = n^* \pi R_0^2$. If $n^* b R_0^2 > 1.0$, $N_l = N_{l\infty}$.

Table 1. Calculated equilibrium current (assuming $kT = 1.0$ eV).

Plasma Radius R_0 (cm)	Plasma Density n_0 (cm^{-3})	Equilibrium Current, I_{eq} (A)
2.63	10^{10}	4.16×10^0
2.63	10^{11}	1.32×10^1
2.63	10^{12}	4.16×10^1
2.63	10^{13}	1.32×10^2
2.63	10^{14}	4.16×10^2
2.63	10^{15}	1.32×10^3
2.63	10^{16}	4.16×10^3
2.63	10^{17}	1.32×10^4
5.25	10^{10}	8.33×10^0
5.25	10^{11}	2.63×10^1
5.25	10^{12}	8.33×10^1
5.25	10^{13}	2.63×10^2
5.25	10^{14}	8.33×10^2
5.25	10^{15}	2.63×10^3
5.25	10^{16}	8.33×10^3
5.25	10^{17}	2.63×10^4
7.68	10^{10}	1.25×10^1
7.68	10^{11}	3.95×10^1
7.68	10^{12}	1.25×10^2
7.68	10^{13}	3.95×10^2
7.68	10^{14}	1.25×10^3
7.68	10^{15}	3.95×10^3
7.68	10^{16}	1.25×10^4
7.68	10^{17}	3.95×10^4
10.5	10^{10}	1.67×10^1
10.5	10^{11}	5.27×10^1
10.5	10^{12}	1.67×10^2
10.5	10^{13}	5.27×10^2
10.5	10^{14}	1.67×10^3
10.5	10^{15}	5.27×10^3
10.5	10^{16}	1.67×10^4
10.5	10^{17}	5.27×10^4

An evaluation of $n^*bR_0^2$ is required for a complete evaluation of I_B . Assuming a maximum peak plasma density of 10^{16} cm^{-3} , a maximum plasma radius of 0.5 cm, we have

$$n^*bR^2 = 2.77 \cdot 10^{-4} \frac{v_D^2}{k(T_e + T_i)} \quad (18)$$

where v_D is the plasma drift velocity (in meters per second) and kT_e , kT_i are temperatures in electronvolts. Assuming $kT_e = kT_i = 1 \text{ eV}$, the relation is

$$n^*bR^2 = 1.39 \cdot 10^{-4} v_D^2 \quad (19)$$

If the plasma drift velocity v_D is $<250 \text{ m/s}$ (where the maximum value of $n^*bR_0^2$ for the described system is ~ 10 percent), then the denominator term can be approximated by 1.0 and the Bennett relation becomes

$$I_B^2 = \frac{8\pi^2 R_0^2 n^* k(T_e + T_i)}{\mu_0} \quad (20)$$

and the numbers in Table 2 result. Equation 20 is similar in form to the equilibrium relation of Equation 12. The equation for this case of the Bennett equilibrium where $n^*bR_0^2 \ll 1.0$ is the same as that obtained for surface axial current confinement of a uniform cylindrical plasma column.

For evaluation of the v_D restriction, allow a 2-kA current (the maximum observed current), a typical plasma electron density of $5 \times 10^{15} \text{ cm}^{-3}$, a plasma beam radius of 10.5 cm and the definition of $J = ne\langle v_D \rangle$ where $\langle v_D \rangle$ is the averaged drift velocity. The magnitude of the averaged drift velocity becomes 72 m/s and is less than the 10-percent value given before. It can reasonably be assumed that the term $(1 + n^*bR_0^2)$ can be ignored. It can also be reasonably assumed that since the averaged drift velocity is small compared to the bulk plasma velocity, plasma charge separation is small.

Using the Bennett relation of Equation 20, Table 2 is generated. As before, radii are chosen to correspond to 25, 50, 75 and 100 percent of the maximum possible plasma radius. The plasma ion and electron temperatures are assumed to be 1.0 eV.

Table 2. Calculated Bennett current (assuming $kT_i = kT_e = 1.0$ eV).

Plasma Radius R_0 (cm)	Peak Plasma Density n^* (cm^{-3})	Bennett Current, I_B (A)
2.63	10^{10}	1.18×10^1
2.63	10^{11}	3.72×10^1
2.63	10^{12}	1.18×10^2
2.63	10^{13}	3.72×10^2
2.63	10^{14}	1.18×10^3
2.63	10^{15}	3.72×10^3
2.63	10^{16}	1.18×10^4
2.63	10^{17}	3.72×10^4
5.25	10^{10}	2.36×10^1
5.25	10^{11}	7.45×10^1
5.25	10^{12}	2.36×10^2
5.25	10^{13}	7.45×10^2
5.25	10^{14}	2.36×10^3
5.25	10^{15}	7.45×10^3
5.25	10^{16}	2.36×10^4
5.25	10^{17}	7.45×10^4
7.88	10^{10}	3.53×10^1
7.88	10^{11}	1.12×10^2
7.88	10^{12}	3.53×10^2
7.88	10^{13}	1.12×10^3
7.88	10^{14}	3.53×10^3
7.88	10^{15}	1.12×10^4
7.88	10^{16}	3.53×10^4
7.88	10^{17}	1.12×10^5
10.5	10^{10}	4.71×10^1
10.5	10^{11}	1.49×10^2
10.5	10^{12}	4.71×10^2
10.5	10^{13}	1.49×10^3
10.5	10^{14}	4.71×10^3
10.5	10^{15}	1.49×10^4
10.5	10^{16}	4.71×10^4
10.5	10^{17}	1.49×10^5

Comparing the data from Tables 1 and 2, it is seen that the values for limited current differ by a factor of $2\sqrt{2}$. The plasma pressure balance equation is a function of the form of the density function, $n(r)$, and of the current distribution, $I(r)$.

Fast photography and interferometry both suggest the plasma beam radius is 5 cm. Results from interferometry and optical spectroscopy indicate the average plasma density is 10^{15} cm^{-3} and the peak plasma density is $<10^{16} \text{ cm}^{-3}$. Optical spectroscopy indicates a plasma temperature of 1 eV. These results indicate the beam current required for Bennett equilibrium (beam confinement) is from 3 to 20 kA.

DISCUSSION

The observed azimuthal magnetic fields and the interpreted axial currents, typically 1.0 kA and always <2.0 kA, are a factor of 3 to 20 less than that required for simple magnetic confinement/equilibrium (Bennett equilibrium). This conclusion is based on the assumptions of cylindrical beam symmetry, a centered beam, a radial current distribution contained within the magnetic probe radius and a return current outside the magnetic probe radius. Even though observed magnetic field is too small to maintain Bennett equilibrium, such fields can assist in centering the plasma beam. An uncentered beam (where $r \neq 0$) will encounter compressed magnetic field between the beam and the drift tube wall.

The magnetic probes were inserted through a 50-cm dia spherical cross/diagnostic station and not through the 21-cm dia drift tube walls. Inertial confinement effects (where the thermal velocity is much less than beam velocity) are sufficient for the plasma beam to traverse the 50-cm cross with no significant expansion and no radial drift. Radial beam drift oscillations (where the plasma beam drifted radially and returned to center) were, however, observed in fast photographic data in the drift regions of the GRC vacuum vessel.

Fruitful areas for future research include measurement of the radial current distribution, $I(r)$, and testing the effect of larger diameter drift tubes.

INTERFEROMETRY ON THE WL/GRC EXPERIMENTS

INTRODUCTION

Direct time resolved measurements of the integral of the free e^- density along a single line through the plasma beam emitted from the GRC plasma gun were taken as part of the WL/GRC experimental series using interferometry at three different wavelengths. The function of interferometry is to measure phase shift of a beam of EM radiation traversing a medium relative to a reference beam or oscillator. A double pass optical interferometer using either a CO_2 or a HeNe laser and a separate single pass millimeter wave interferometer was used. With this wide range of wavelengths, listed in Table 3, a wide range of density measurements was available, as will be explained below.

Table 3. Interferometric parameters for the WL/GRC experiment.

System	Wavelength λ (cm)	Cutoff Electron Density, n_c (cm^{-3})	Line Averaged Electron Density for a Phase Shift of 2π , \bar{n}_l (cm^{-3})
HeNe	6.33×10^{-5}	2.79×10^{21}	8.39×10^{15}
CO_2	1.06×10^{-3}	9.94×10^{18}	5.01×10^{14}
mm wave	3.33×10^{-1}	1.01×10^{14}	3.19×10^{12}

The dispersion relation for EM radiation propagating in a cold unmagnetized plasma is

$$\omega^2 = \omega_p^2 + c^2 k^2 \quad (21)$$

where

$$\omega_p^2 = 3.18 \times 10^9 n \quad [cgs] \quad (22)$$

with n being the free electron density. Temperatures and magnetic fields present in the experiments were well below levels for which corrections terms for these properties are required (Ref. 5). The electron densities n_c for

which the angular frequencies of the three radiation sources equal ω_p are listed in Table 3. Interferometry cannot be performed above these (cutoff) densities using the respective sources since there are no propagating (real k) solutions. In practice, inhomogeneities in the plasma result in lower limits. If the phase shift of the plasma traversing beam varies significantly over the sampled beam cross-section, the interference signal will be washed out by a large distribution of phase shifts being received simultaneously.

For $n \ll n_c$, a useful approximation is derivable from the dispersion relation. In this limit, the phase shift ϕ_p of the beam (in radians) due to the plasma is proportional to the line averaged electron density \bar{n} along the beam path (Ref. 6):

$$\bar{n} = \frac{1}{L} \int_0^L n \, dy = \frac{3.55 \times 10^{12}}{pL\lambda} \phi_p \quad [cgs] \quad (23)$$

Here, p is the number of times the beam passes through the plasma (once for the millimeter system and twice for the optical system) and L is the length along which the density is averaged. The length, L , will be taken to be 21 cm, the diameter of the plasma drift tube. For the three wavelengths, the values of \bar{n} which result in one order of shift ($\bar{n} = \bar{n}_1$ for $\phi_p = 2\pi$) are listed in Table 3. Values of $\bar{n} = \bar{n}_1/20$ were resolvable using the respective systems, in practice.

This section will be concluded with a general description of the nature of the signal output from the interferometer receivers and how \bar{n} may be calculated therefrom. Ideally, given a constant amplitude, plasma traversing beam mixed with its local oscillator or reference beam, the receiver signal is

$$V = \frac{1}{2} [V_+ - V_-] [1 + \cos(\phi_p + \phi_0)] + V_- \quad (24)$$

where ϕ_0 is the vacuum phase angle and V_+ and V_- are the signal levels at maximum and minimum interference, respectively. One property of this equation which is particularly relevant to signal interpretation is that a measurement of $V = V(t)$, by itself, does not uniquely determine $\phi_0(t)$, and, therefore, \bar{n} , since the arccosine is a multivalued function. Whenever $\phi_p + \phi_0$ equals an integer multiple of π , it is unclear whether \bar{n} continues on to increase or

integer multiple of π , it is unclear whether \bar{n} continues on to increase or decrease without additional information. With the millimeter wave system, this information was supplied by recording V simultaneously with two values of ϕ_0 differing by $\pi/2$. Although this option was not available with the optical system, ambiguities were usually resolvable either by recording data with different values of ϕ_0 or by correlating the HeNe signal with the CO_2 signal to form a consistent interpretation. Both these methods assume reproducibility.

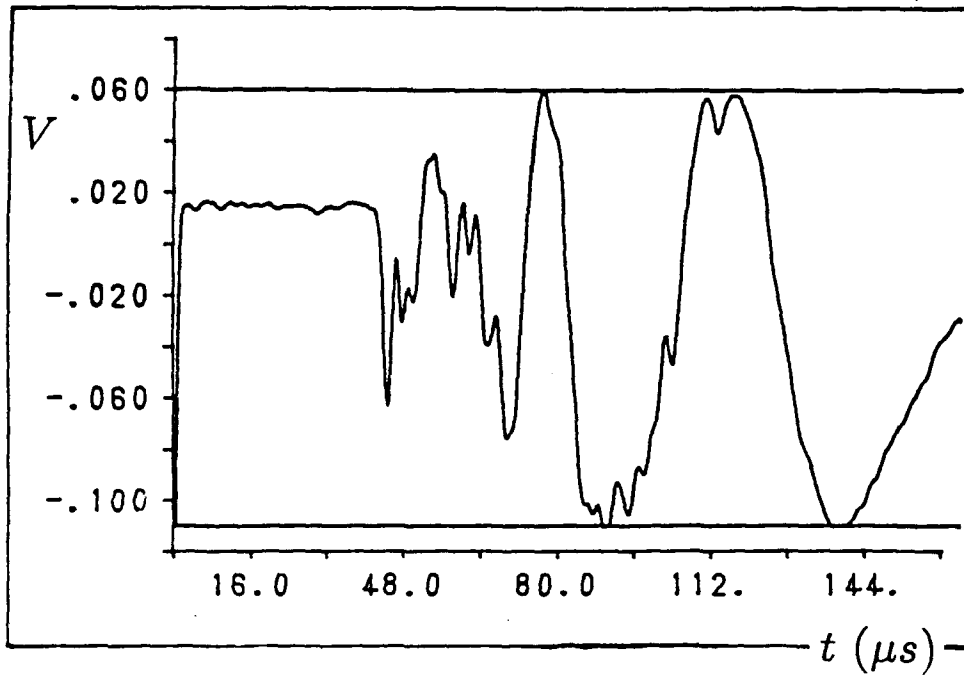
RESULTS

An example of a CO_2 interference signal and the calculated \bar{n} trace are illustrated in Figure 38. The shot number is in the bottom right corner of each graph. The receiver signal, Figure 38a, was chosen for display because it has both a multiple order phase shift and an interval during which it cannot be interpreted due to plasma inhomogeneities. Signal interpretation is particularly complicated by these two effects. This signal was taken at $z = 5$ m down range of the plasma gun with the laser beam orthogonally intersecting the z axis of the glass drift tube. In the graphs, as well as in the rest of this section, time $t = 0$ corresponds to the start of gun current, as determined by a Rogowski coil signal from the gun current feed. The gun current supply was, in this case, a 126- μF capacitor bank charged to 18 kV (20 kJ). The plenum gas was Ar pressurized to 30 psi.

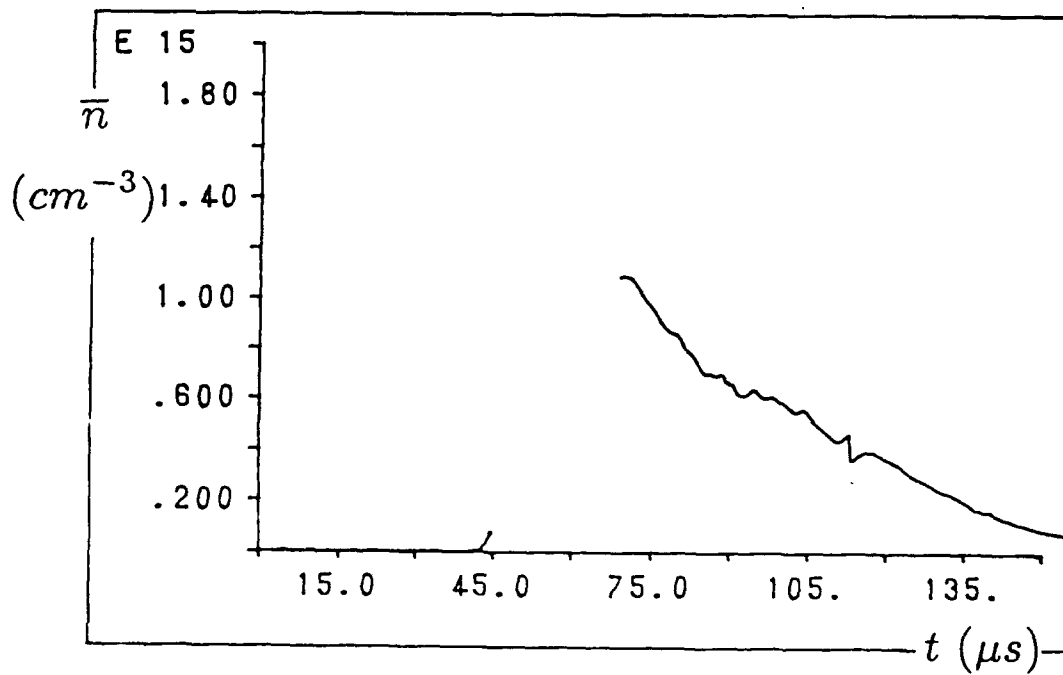
Figure 38a shows the signal bounded between horizontal lines at V_+ and V_- . Since the current pulse driving the plasma is only 15 μs , the beam velocity at any time t significantly >15 μs may be approximated by

$$v = z/t \quad (25)$$

For earlier times, Equation 25 is still useful for establishing a lower bound on v . The beam is first detectable with this instrument at 45 μs , giving an inferred maximum velocity of 110 km/s for anything with $\bar{n} > 3 \times 10^{13} \text{ cm}^{-3}$, the detection threshold for the device. The signal between 45 and 70 μs is impossible to interpret, but data using the HeNe laser under similar conditions indicate that \bar{n} peaks in this region and then slowly falls off. This fall-off is apparent in the signal after 70 μs , resulting in over two periods of oscillation.



(a) Interference signal.



(b) Calculated \bar{n} .

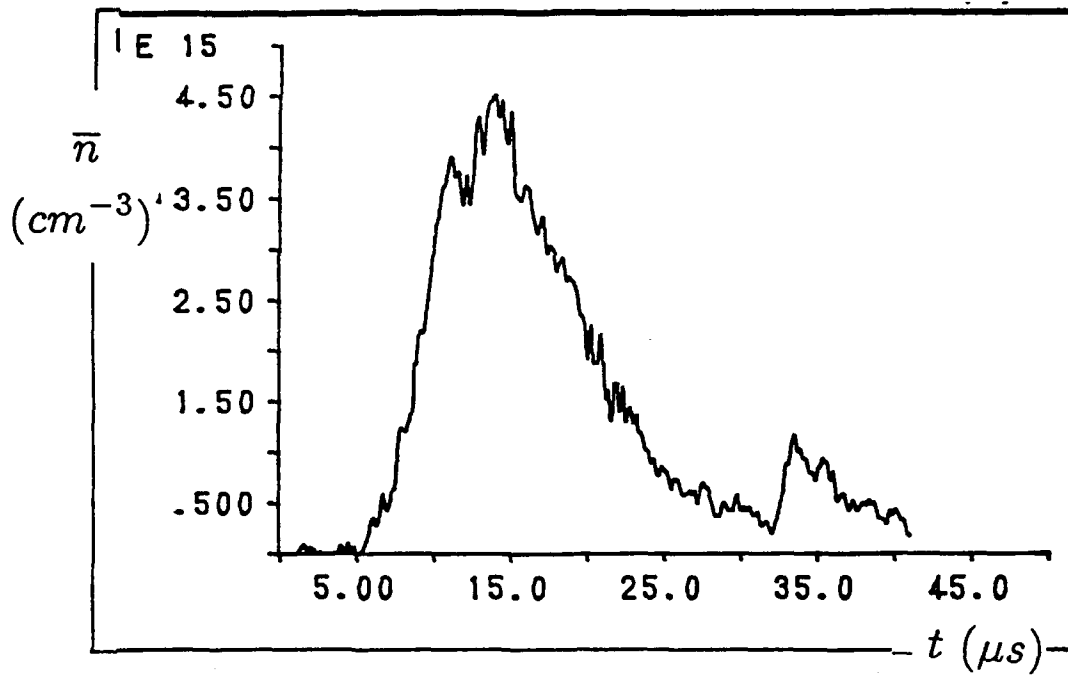
Figure 38. Sample CO_2 interference signal and calculated \bar{n} taken at 5-m station through center port. 20 kJ bank Ar plenum.

The HeNe signals never exceeded $\phi_p = 2\pi$ due to its lower sensitivity, except for measurements taken directly across the muzzle of the gun. Interpretation of down range HeNe data was, therefore, much simpler. Measurements at the muzzle, though, have proven uninterpretable. Figure 39 shows \bar{n} as determined from a HeNe signal for the same machine parameters as Figure 38 but at $z = 0.7$ m. Figure 39a is taken with the laser on axis and Figure 39b was taken 6.4 cm off axis for a different shot. There appears in both graphs two distinct local maxima with the first being much greater in density and velocity. The first peak is a factor of 3 lower off axis, implying that it is collimated. The slower component, traveling at only 20 km/s, has the same density off axis showing no indication, therefore, of collimation.

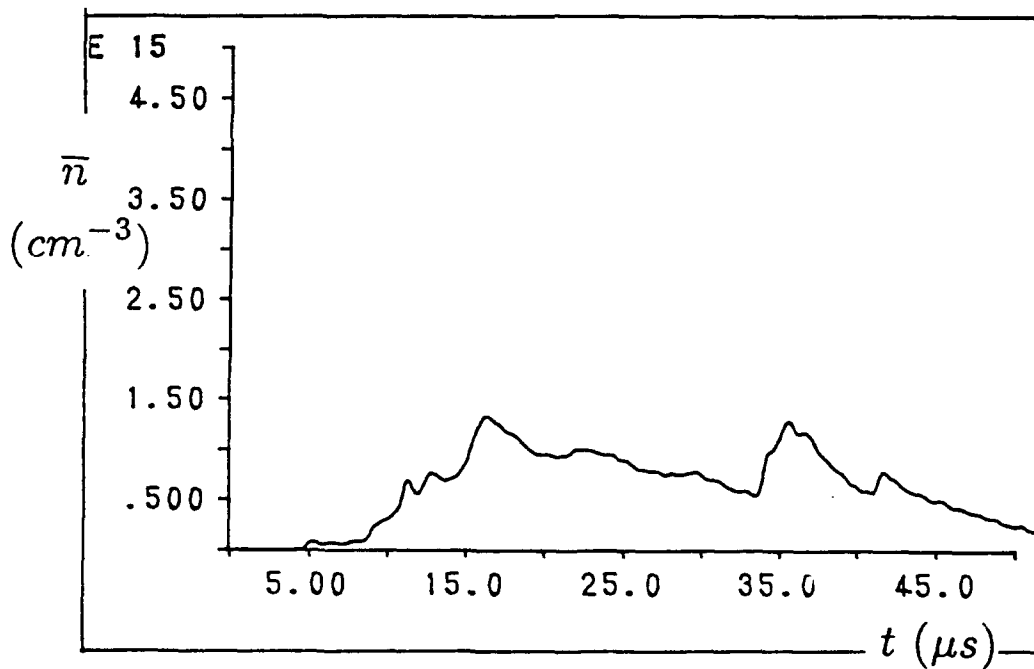
Figure 40 shows more data from the 5-m station. The machine parameters are the same, except the axially centered \bar{n} in Figure 40a (higher plot), calculated this time from HeNe data, was taken for a shot which used He at 42 psi as the plenum gas. Comparison with the Ar plenum data of Figure 38b, though, shows that there is not a great deal of difference, at least during the time domain when the signal is reducible. This is consistent with spectroscopic results indicating that much of the plasma beam consists of Si ablated from the gun's quartz insulator. The \bar{n} using the Ar plenum, though, does appear to begin to rise earlier, implying faster component. The lower trace, also rising earlier, was taken 6.4 cm off center, like Figure 39b, using the CO₂ laser. The order of magnitude lower density off axis shows that the degree of collimation has not noticeably deteriorated at this range.

Considerable effort was made to observe and quantify any precursor plasma arriving earlier than the main mass because of its implied higher velocity. The millimeter system, with a noise level of $\bar{n} = 2 \times 10^{11} \text{ cm}^{-3}$, was useful for this purpose. Figure 40b shows an example of what was often observed with this device prior to 45 μs at the 5-m station. The signal first clearly rises above the noise at about 20 μs , implying a velocity of $v \geq 250 \text{ km/s}$, albeit at densities 3 orders of magnitude lower than the main mass. The signal is abruptly cut off at 45 μs as the main mass begins to arrive.

The interferometry data allow estimates to be made of the time histories of plasma beam power dE/dt and mass flow rate dm/dt , and the time integrated

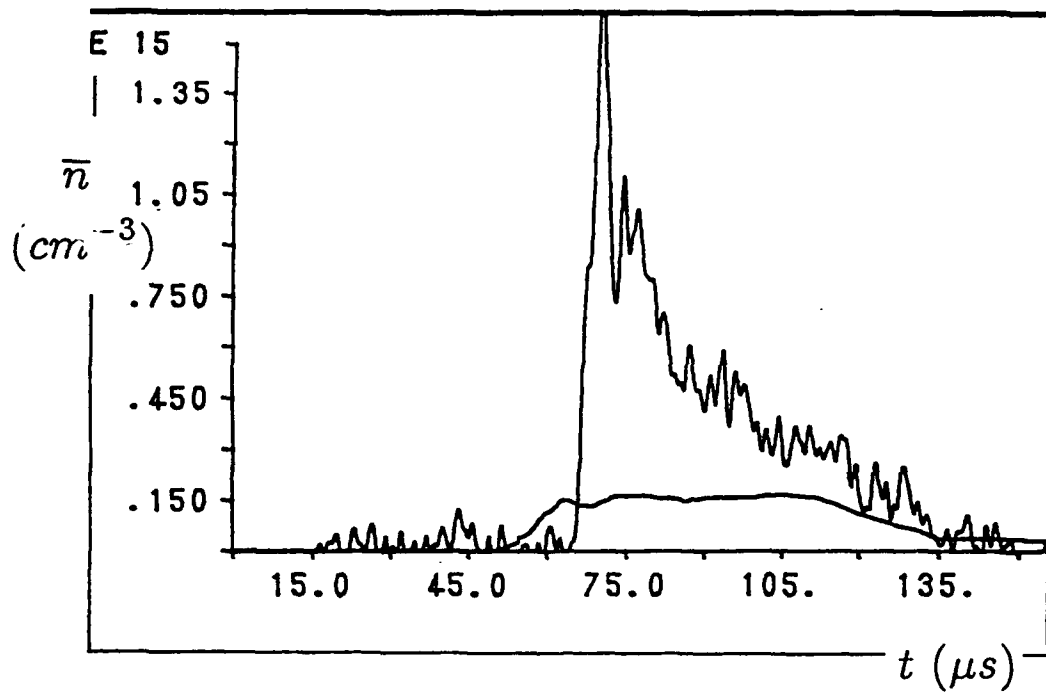


(a) Center port.

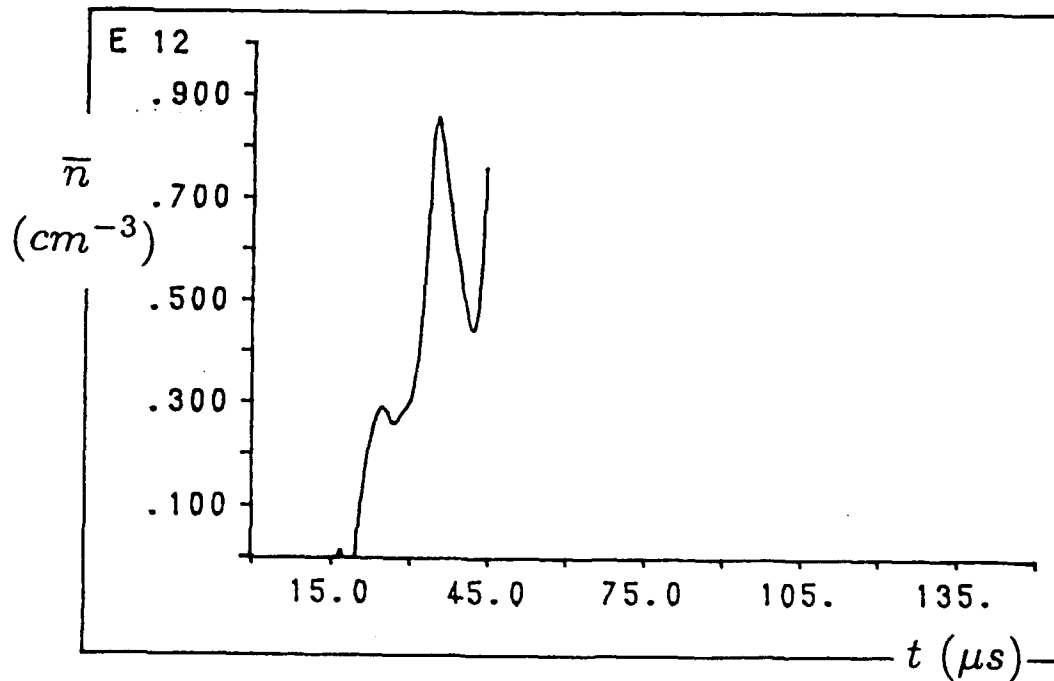


(b) 6.4 cm off-axis.

Figure 39. The \bar{n} from HeNe signal at 0.7-m station through center port and port 6.4 cm off-center. 20 kJ bank with Ar plenum.



(a) \bar{n} from on-center HeNe signal (upper trace) and from off-centered CO_2 signal.



(b) Centered \bar{n} from millimeter wave signal (using He as the gas plenum gas).

Figure 40. Interferometry results at 5-m station.

properties of total energy E , mass m , and momentum $p = (2mE)^{1/2}$, given some simplifying assumptions. The assumptions, followed by a brief justification and/or qualification of each, are as follows:

- $v = z/t$. As already mentioned, this gives a reasonable beam velocity estimate only for $t \gg 15 \mu s$ at the 0.7-m station. Otherwise, only a lower bound can be established.
- $R = 6.4 \text{ cm}$ = the characteristic radius of the plasma beam, which is assumed to be rotationally symmetric. This value appears reasonable since the \bar{n} measurements 6.4 cm off axis at $z = 0.7$ and 5 m correspond to about one e-fold drop.
- $n = L\bar{n}/2R$ interior to R and 0 exterior to R . Here, n is electron density and \bar{n} refers to an on axis measurement of its line average. This relationship follows from Equation 23 if one assumes, for simplification purposes, that n is radially (but not axially or temporally) uniform interior to R , with only vacuum exterior to R .
- $\bar{m}_i = 4.65 \times 10^{-23} \text{ g} = 28 \text{ amu}$ = the mean ion mass. Spectroscopic evidence indicates that the principle constituent of the plasma is Si. The other possible constituents have lower atomic masses, with the result that this assumption may give an overestimate of the beam power.
- $\bar{Z} = 1$ = the mean ionization state of the ions. Spectroscopic evidence indicates that the Si observed is mostly singly ionized.

With $\rho = \bar{n}\bar{m}_i/\bar{Z}$ being the beam's mass density interior to R , derivable from the above assumptions are

$$\frac{dm}{dt} = (\pi R^2) \rho v = \frac{\pi R L \bar{n} \bar{m}_i z}{2 \bar{Z} t} \quad (26)$$

and
$$\frac{dE}{dt} = \frac{1}{2} \frac{dm}{dt} v^2 = \frac{\pi R L \bar{n} \bar{m}_i z^3}{4 \bar{Z} t^3} \quad (27)$$

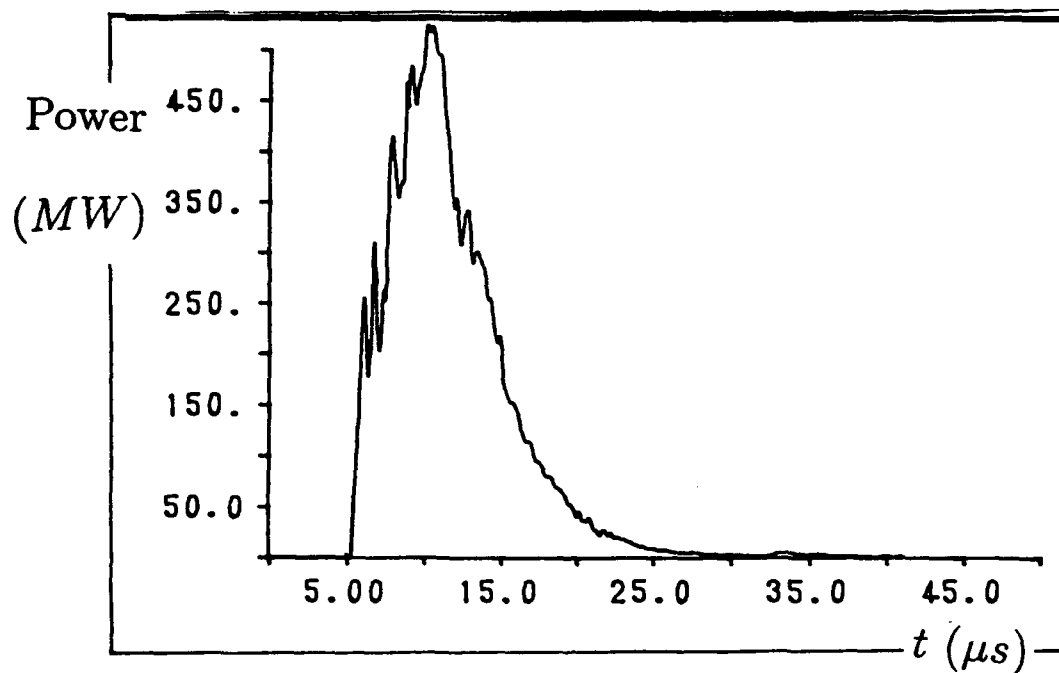
Figures 41a and Figure 41b plot the beam power at 0.7 and 5 m, respectively, using the capacitor bank with energy $\frac{1}{2}CV^2 = 20$ kJ. These plots were derived from the \bar{n} plots of Figures 39a and Figure 40a, respectively. The time integrated properties are listed in Table 4. Provided the assumptions are sufficiently correct, the 0.7-m values represent a lower bound in mass, energy, and momentum because of the constraints on the first assumption ($v = zt$). Even so, mass and energy conservation of the beam between 0.7 and 5 m appears fairly good, indicating minimal plasma loss to the walls of the drift tube. One noteworthy observation is the apparent conversion efficiency of capacitative energy ($\frac{1}{2}CV^2$) to beam energy E of about 20 percent. This should be of particular significance for potential space propulsion applications. A word of caution is warranted, though. A population of lighter ions, unresolvable in the spectroscopic data, could mean that the actual beam energy is lower. This possibility needs more study. Included in Table 4 are the parameters for the plasma precursor plotted in Figure 40b, for comparison. Its contribution to the beam energy is negligible, under the assumptions, despite its greater velocity.

Table 4. Inferred time integrated plasma beam properties.

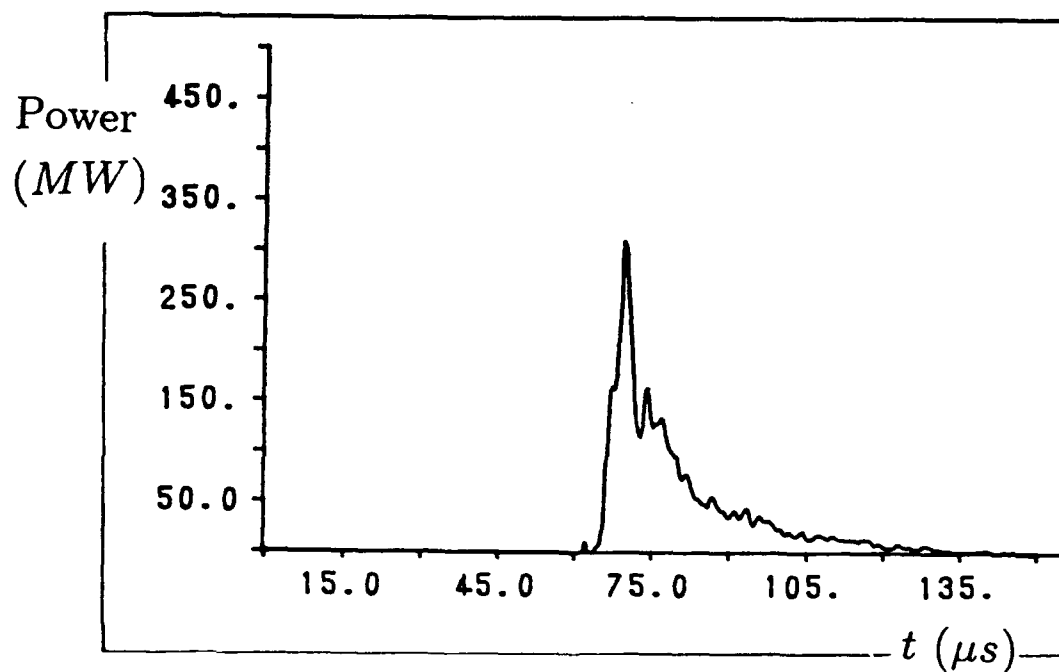
Shot No.	$\frac{1}{2}CV^2$ (kJ)	Plenum Gas	z (m)	m (mg)	E (kJ)	p (N · s)
2474	20	Ar	0.7	5.0	3.9	0.20
2496	20	He	5.0	3.7	3.4	0.16
2506*	20	Ar	5.0	4×10^{-4}	3×10^{-4}	1.5×10^{-5}
2534	40	H ₂	5.0	10.4	12.9	0.27

*precursor only, from millimeter wave system

Late in the experiments, the plasma gun capacitance was increased to 252 μ F, resulting in an increase in bank energy to 40 kJ, and the plenum gas was changed to 30 psi H₂. The \bar{n} and power histories calculated from an on axis HeNe signal taken at 5 m are shown in Figure 42. There are little

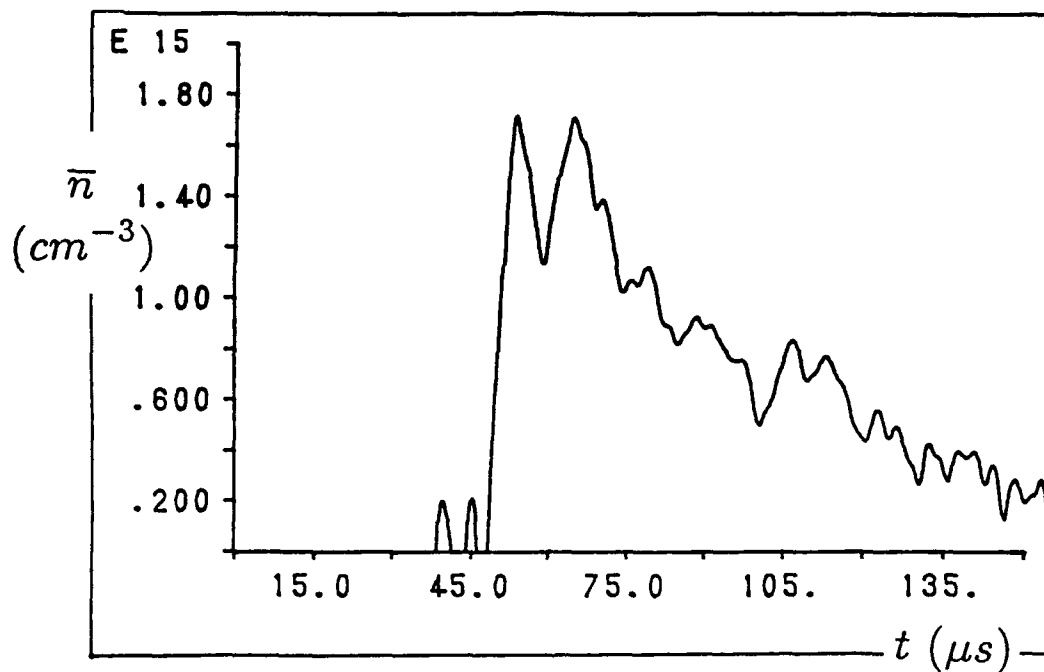


(a) Power at 0.7 m, inferred from Figure 39a.

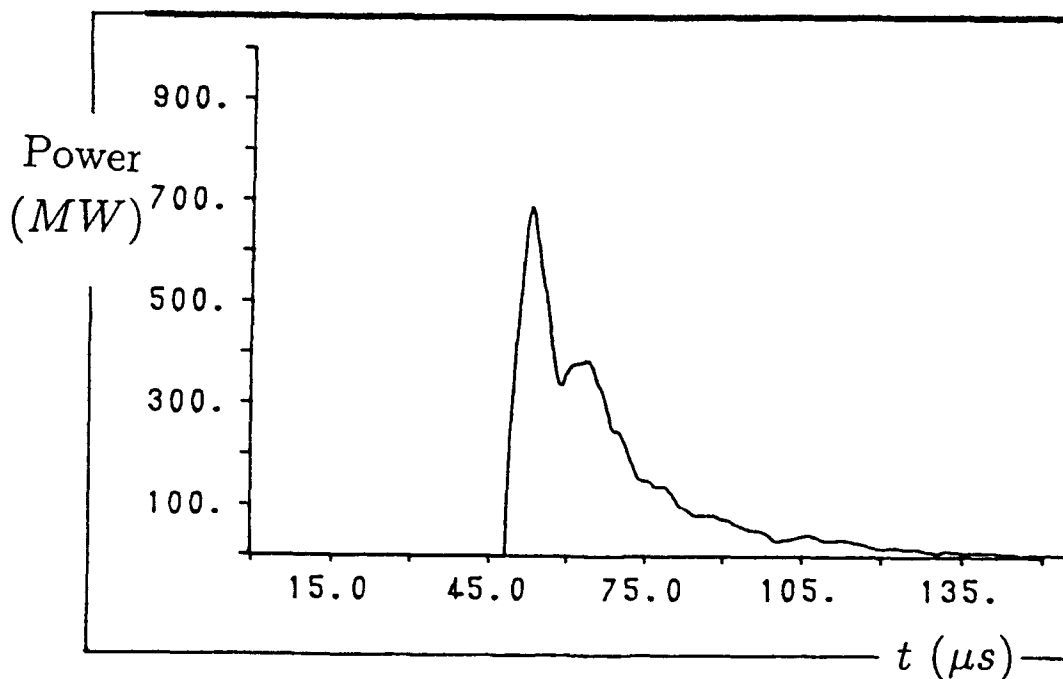


(b) Power at 5 m, inferred from Figure 40a.

Figure 41. Beam power.



(a) Centered \bar{n} .



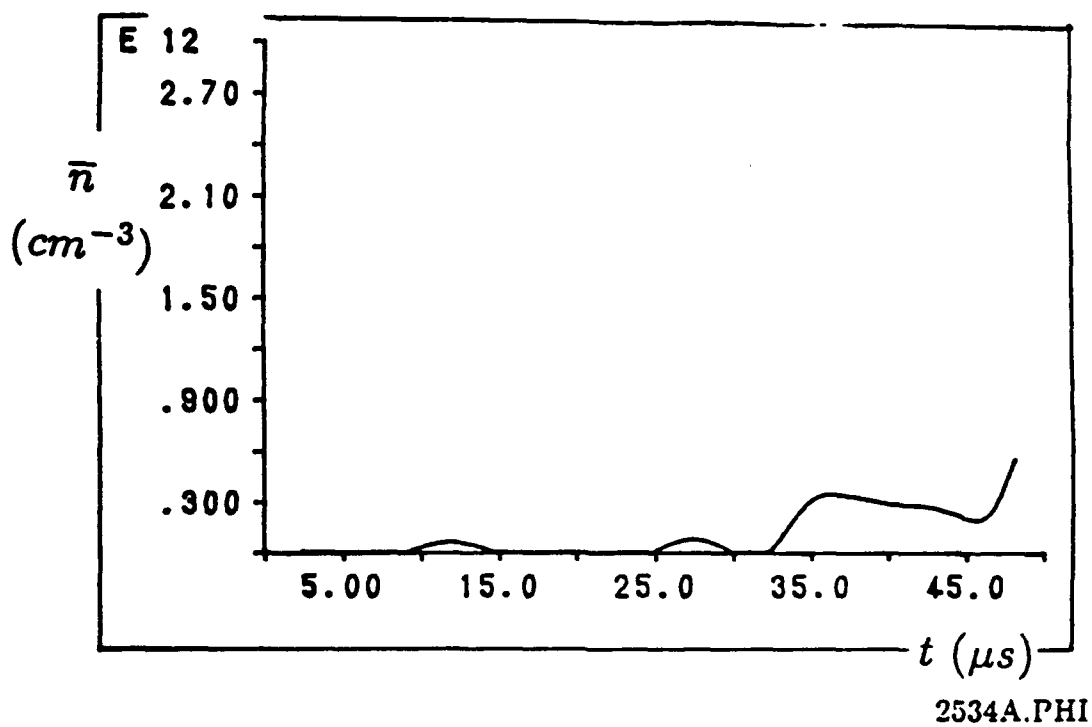
(b) Inferred power.

Figure 42. Centered \bar{n} and inferred beam power from HeNe signal at 5 m. The 40 kJ bank with H_2 plenum.

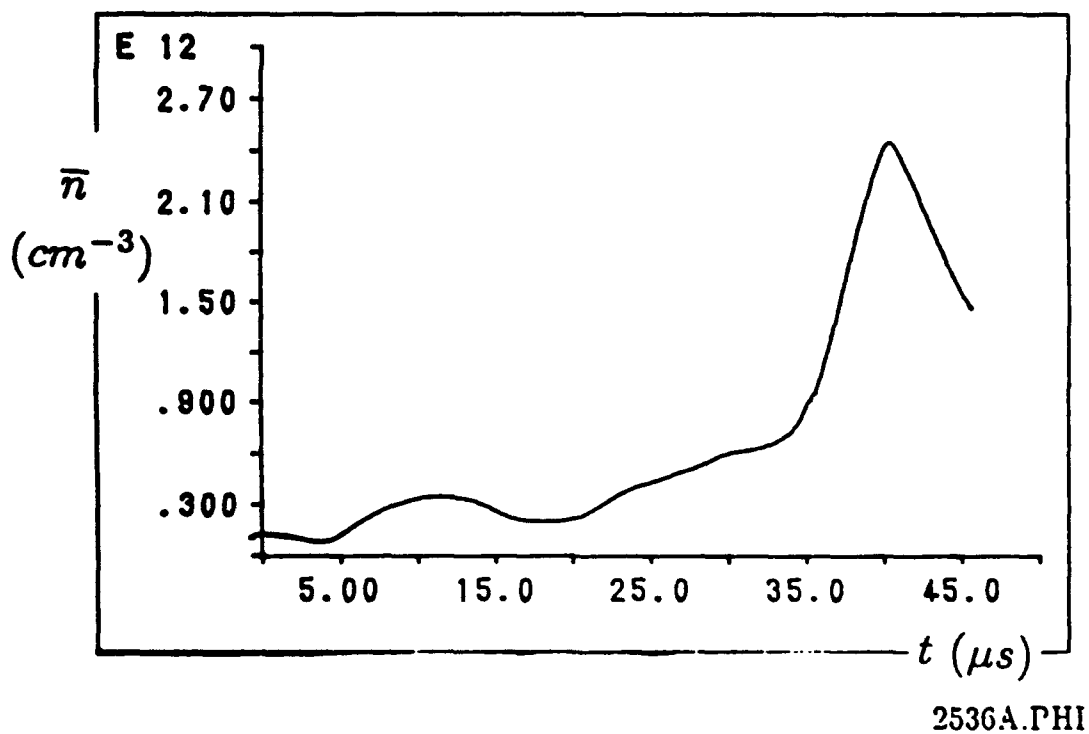
interpretable off axis interferometric data to determine if the plasma had the same degree of collimation, so the second assumption is only tentative. Nonetheless, the time integrated properties, listed in Table 4, indicate that a reasonable conversion efficiency is maintained, or possibly even improved, as the bank energy is increased, although the plasma velocity itself does not increase.

There was some controversy about the significance of the precursor measurements. It was pointed out that the interferometer was blind to neutrals and that, even if ionized, a sufficiently fast beam might carry significant energy even if its density was below the noise level. Because of the great interest in the possibility of such a beam, a simple experiment was performed to look for it using the 40-kJ bank with the H₂ plenum. A plastic target was placed orthogonal to, and centered on, the plasma beam at a range of 5 m and the millimeter interferometer radiation was transmitted through it at a 45-deg angle. Any neutrals striking the target in <50 μ s would be ionized, and additional ions would be ablated from the target. In this way, if any appreciable fraction of bank energy was deposited on target, n_e would be exceeded and the millimeter signal would cut off.

The signal did not cut off and \bar{n} was interpretable up to the usual 45 μ s before the main plasma arrived. The results of this experiment, along with an \bar{n} plot of the precursor as it appeared with the same machine parameters, but no target, is shown in Figure 43. There is an enhancement of the signal due to the target, and there is even a significant rise above noise as early as 10 μ s, providing evidence for a component with $v \geq 500$ km/s, but the energy deposition is very small compared to the slower plasma.



(a) Without a plastic target.



(b) Transmitting through a plastic target.

Figure 43. The \bar{n} from millimeter wave signal at 5 m.

OPTICAL SPECTROSCOPY

OMA DIAGNOSTIC SETUP

The OMA system for these experiments was an EG&G PARC (Princeton Applied Research) Model 1460V, comprising a Model 1234 Spectrograph, a Model 1254E Silicon Intensified Target Vidicon Detector, a Model 1211 High Voltage Pulse Generator, a Model 1301 High Speed Optical Trigger Detector, a Model 1216 Multichannel Detector Controller, and a Model 1215 OMA II Console. The OMA system is shown in the block diagram of Figure 44. Note that because of sensitivity of the electronics to power line transients and electromagnetic pulse (EMP), the entire system was placed inside a Faraday cage with power line filter; data and trigger signals were brought in via fiber optic links.

The spectrograph was manufactured by Jarrell Ash (Monospec 27) and features a crossed Czerny-Turner configuration for excellent stray light reduction. It is stigmatic so that incident spatial information in the vertical direction along the entrance slit is maintained through the system and focused at the exit plane. This capability was used to simultaneously record up to three distinct spectra. The spectrograph has a turret grating mount which holds three different diffraction gratings. Any of these can be moved into position without realigning the optical system. The gratings used are listed in Table 5 with the corresponding dispersions and resolutions for a 25- μm

Table 5. Grating specifications.

Grating (1/mm)	Range (\AA)	Dispersion ($\text{\AA}/\text{channel}$)	Resolution (\AA)
150	3000	6.00	12.0
1200	375	0.75	01.5
1800	250	0.50	01.0

entrance slit (50- and 100- μm slits were also available). Reflection efficiency curves, supplied by Thermo Jarrell-Ash, for the three gratings are

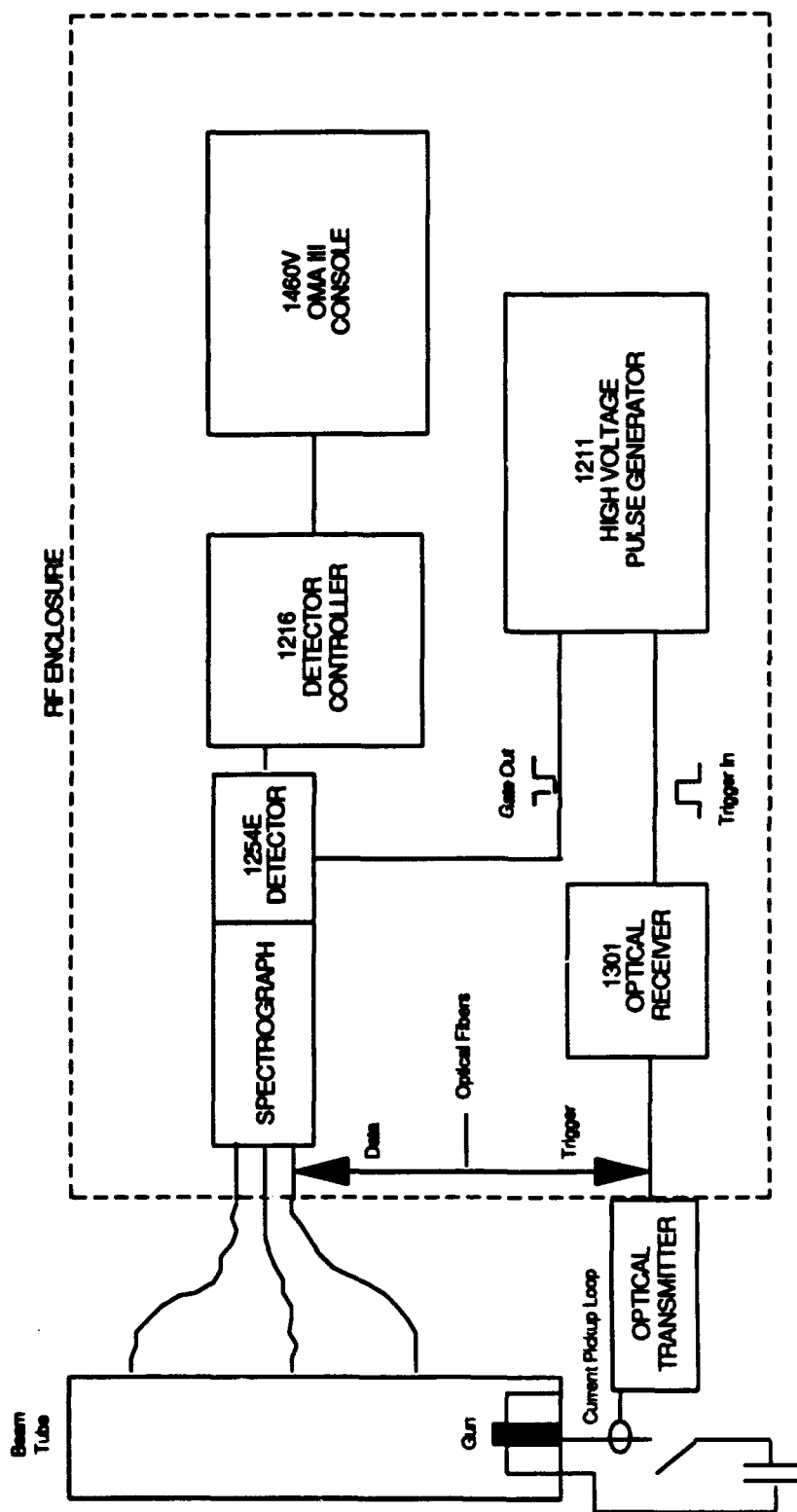


Figure 44. The OMA system configuration block diagram.

shown in Figures 45 through 47. The spectrograph has a focal length of 275 mm and an effective aperture of $f/3.8$. An optical alignment was performed prior to the measurements to ensure optimum performance.

The detector is an Si intensified target vidicon mounted at the spectrograph exit plane. A schematic of the detector is shown in Figure 48. Incident photons are coupled through a fiber optic faceplate to an extended red response S-20 photocathode. Photoelectrons are accelerated and focused through an aperture and imaged onto a 16-mm-dia Si target. The target contains a microscopic array of millions of photodiodes--approximately one every 8 μm . The diodes have a common cathode and isolated anodes which are selectively addressed by a scanning electron beam. Initially, the beam charges the diodes. As accelerated photoelectrons strike the target, electron-hole pairs are created which deplete the stored charge. When the beam rescans the depleted region, charging current (which is proportional to the depleted charge) flows and is sensed and integrated by the electronics. The scanning beam has a spot size of 25 μm , and scans a 12.5- x 12.5-mm area, resulting in an array of 512 horizontal channels by 512 vertical tracks. With the OMA console and the detector controller, the channels and tracks may be grouped for display. For example, a horizontal group size of 2 and a vertical group size of 16 produces a lower resolution array of 256 channels by 32 tracks. A typical response curve for the 1254E detector is shown in Figure 49.

The detector may be operated repetitively (continuously) or pulsed. Pulsed operation is achieved by manually setting a hardware switch on the detector, so that focusing voltage is applied by a separate high voltage pulser, and setting a software switch to the 1211 pulser position in the OMA configuration menu. The 1211 pulser supplies a negative pulse of about 500 to 1500 V, with width variable from about 50 ns to 1 ms. The gating pulse occurs after a delay externally set on the pulser (+200-ns fixed internal delay) from a trigger pulse. In the experiments, the trigger pulse was produced from a current sensor on the gun discharge circuit and coupled to the 1211 through a fiber optic transmitter/receiver link. The receiver was the EG&G 1301 unit.

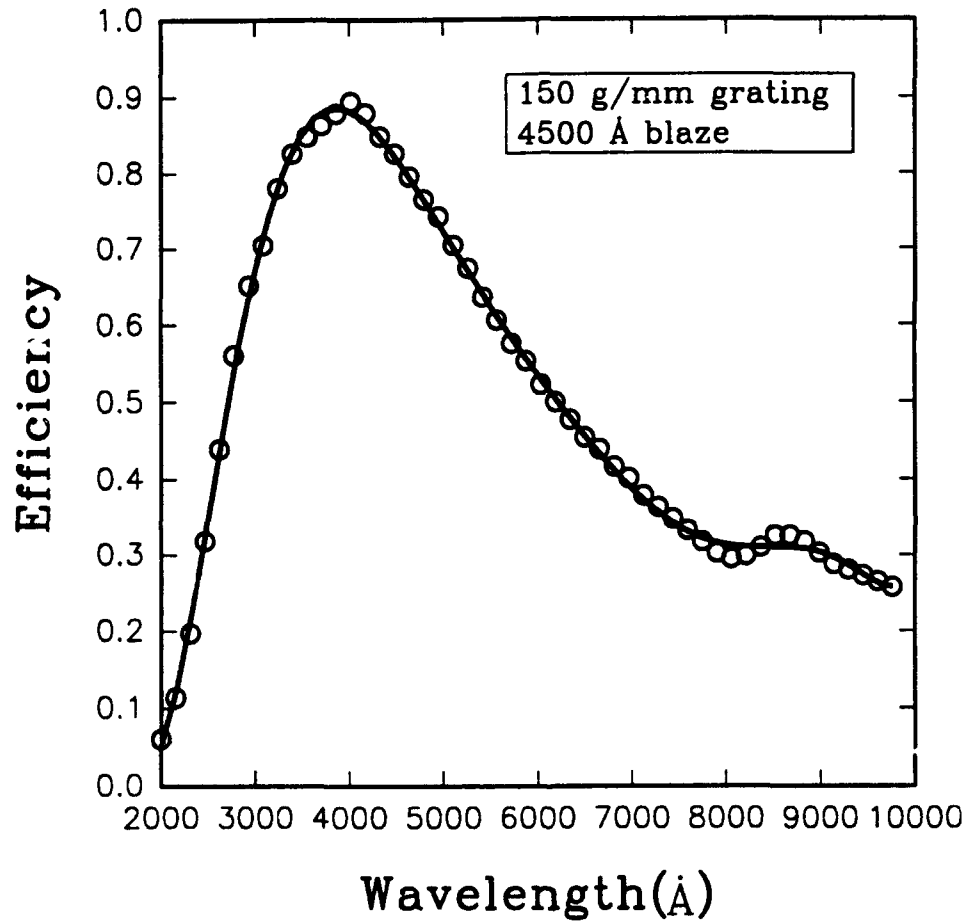


Figure 45. 150 l/mm grating reflection efficiency curve.

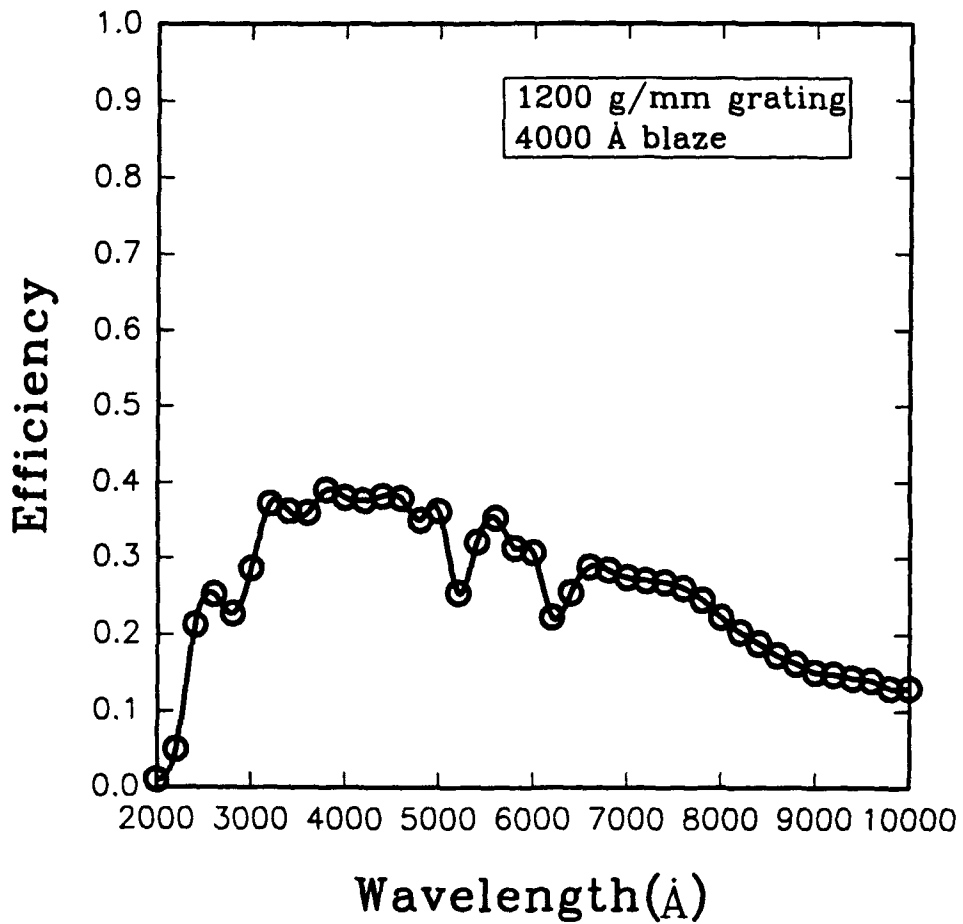


Figure 46. 1200 1/mm grating reflection efficiency curve.

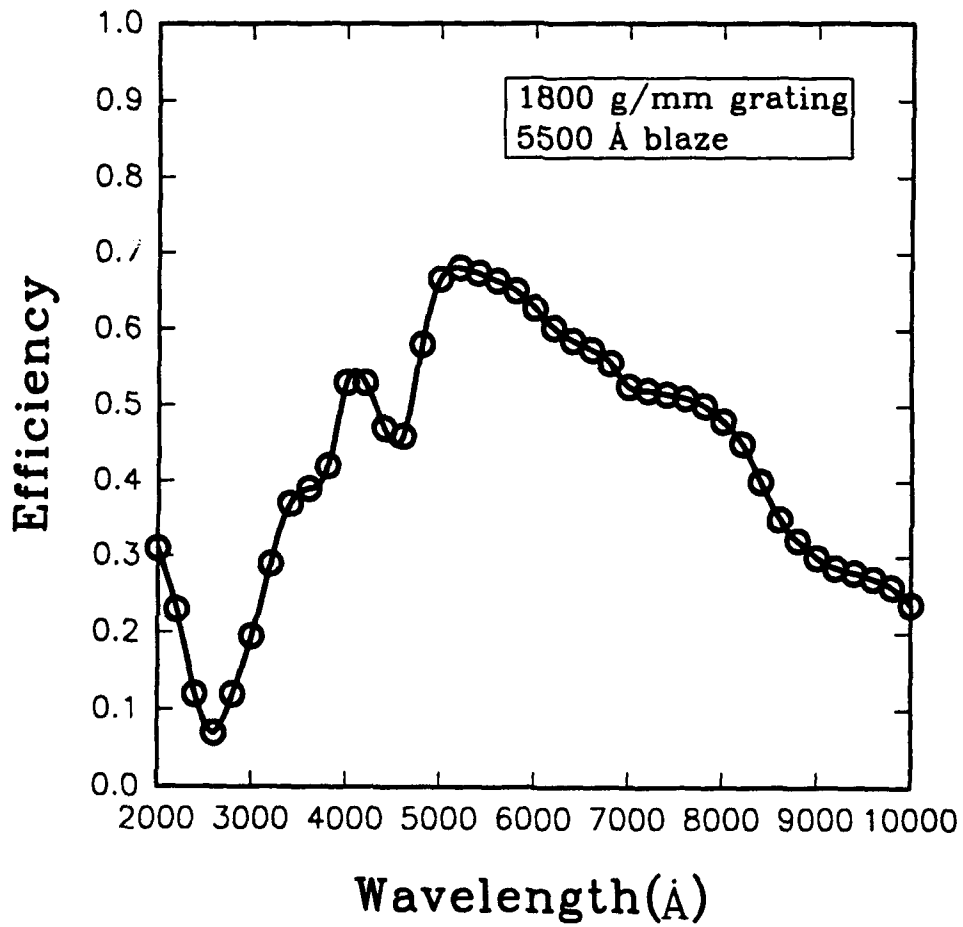


Figure 47. 1800 l/mm grating reflection efficiency curve.

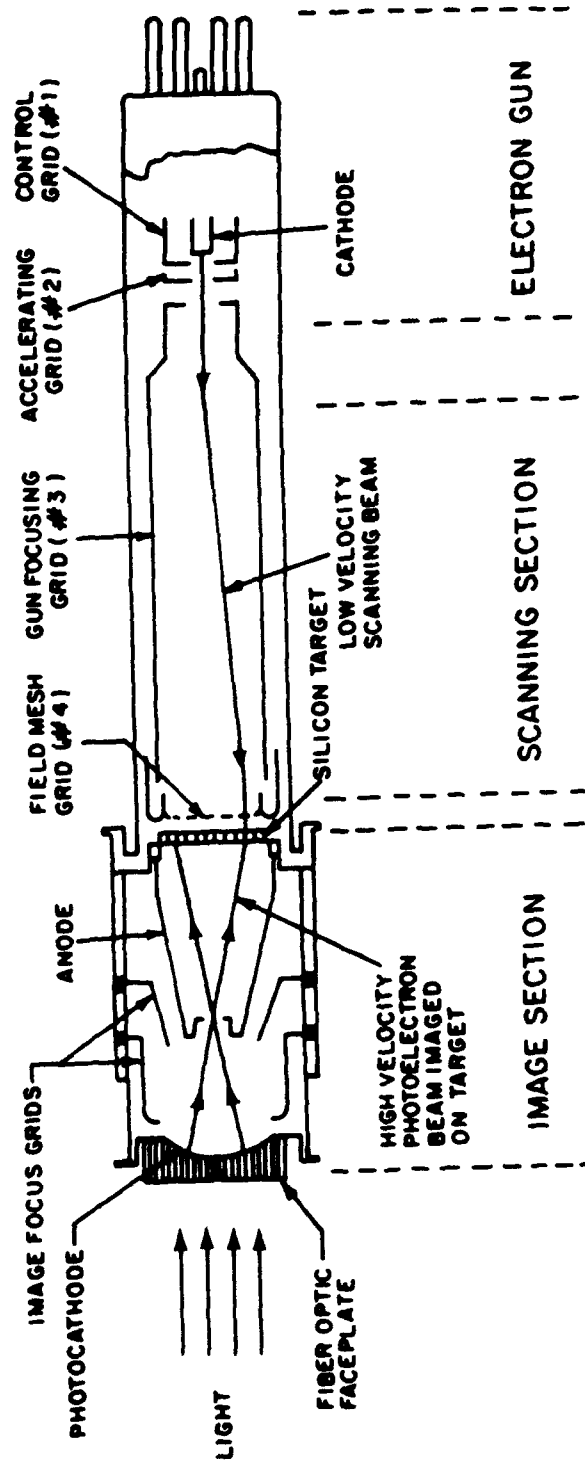


Figure 48. Silicon intensified tube (SIT) vidicon detector.

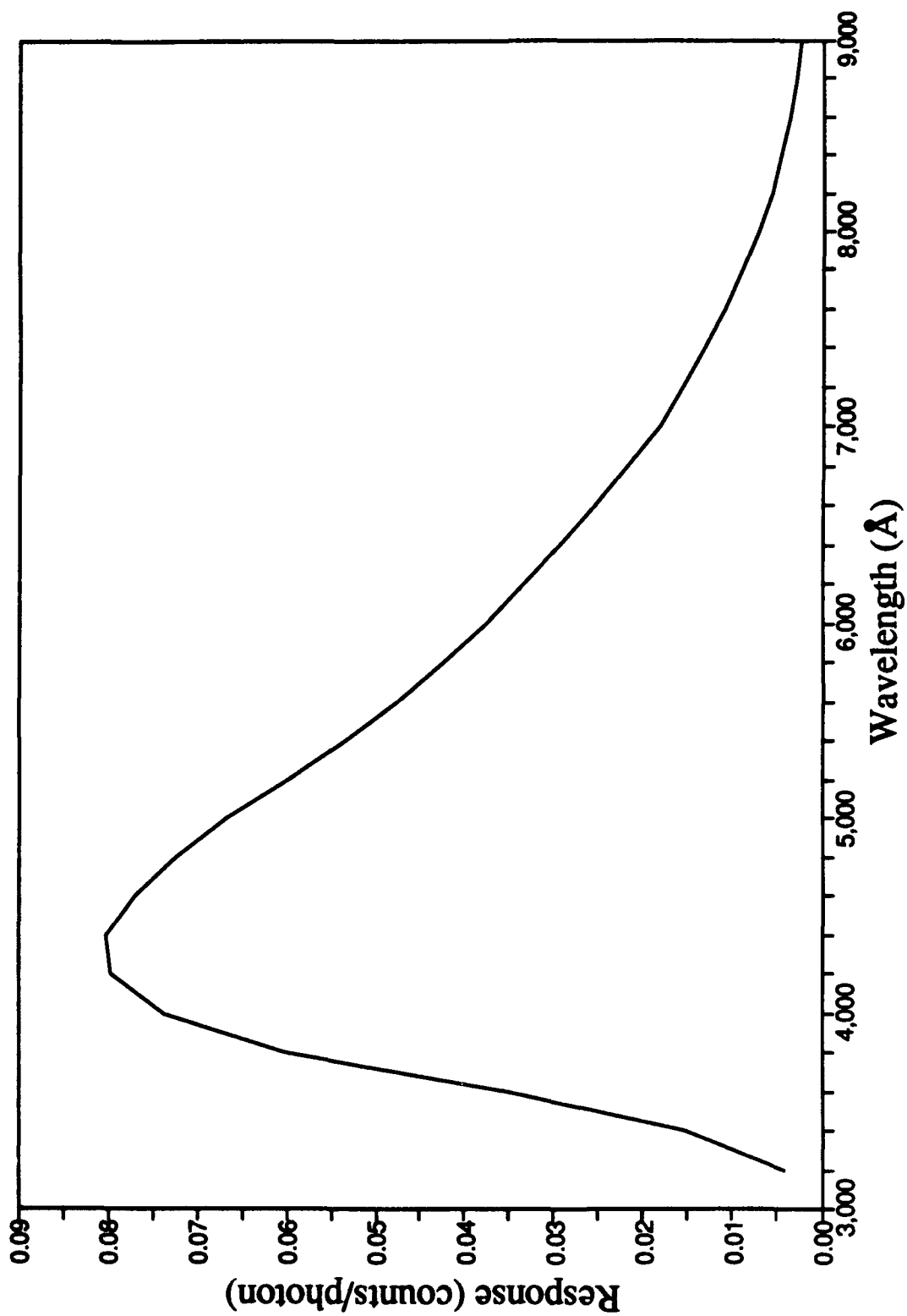


Figure 49. Detector response function.

Prior to acquiring data, a comprehensive electrical alignment of the detector controller was performed, as outlined in the 1216 manual.

The OMA software has several different preprogrammed data acquisition modes to accommodate a variety of applications. Mode 19 was used for the measurements. In this mode, the detector is armed, then waits for the gating pulse. Upon triggering, the data are scanned according to the specified channel/track configuration in the scan menu and are temporarily stored. Then, the controller cycles through a number of dummy scans and accumulates a background record, *in situ*, after the experiment is over. It subtracts (pixel for pixel) from the data record and stores the result, automatically corrected for background.

For this application, three fused silica optical fibers were set up for data acquisition. They were fed into the RF enclosure through a 0.5-in dia, 6-in-long copper waveguide. At the spectrograph, they were mounted to a holder plate in a linear array. The holder was built with a micrometer translation stage and rotation stage, so that the output from each fiber could be accurately proximity focused onto the entrance slit. The input ends were deployed, without any focusing optics, at axial locations of 0.0, 0.3, 0.5, 1, 3, 5, or 10 m down range from the gun muzzle along the beam tube. The fibers were usually oriented perpendicular to the tube axis at radial distances of 0.15 m (tube wall), 0.6 m (tube support structure), or 1.5 m (remote). Other mounting positions at the 5-m axial location included a radial view at 1 m through a laser interferometer port and a tangential (to the tube inside wall) view.

To calibrate the display channels in terms of wavelength, known lines from Oriel calibration lamps (Hg, A, Xe, Kr) and H Geisler tubes were used. The OMA software allowed fitting the calibration line wavelengths to either a linear or cubic polynomial in detector channel number by the method of least squares. Spectral data thus could be displayed as intensity (counts) versus either channel number or wavelength. Hardcopy of the data was generated using a Hewlett Packard 7475 plotter.

RESULTS AND ANALYSIS

Spectral Features

Line Identifications. A typical time-integrated broad-band spectrum at 5 m with Ar as the working gas is shown in Figure 50. The well-known wavelength tables of Striganov and Sventitskii (Ref. 7) were used to identify the features. At first, the expected Ar transitions were not evident. Although the features in Figure 50 appeared to fit the Si II (standard notation is I - neutral atom, II - singly ionized, III - doubly ionized, etc.) spectrum, the high-resolution (1800 l/mm) grating was used to verify the identification of dominant lines. For example, Figure 51 shows a high-resolution spectrum in the vicinity of the feature at 6355 Å. One can see the fully resolved Si II 4s-4p multiplet at 6347.1 Å (1/2-3/2) and 6371.4 Å (1/2-1/2). Because of the high intensities, the detector is saturated in this spectrum, but similar spectra at lower sensitivity show the two lines in precisely the 2:1 expected intensity ratio from statistical weights and transition probabilities (Ref. 8). Figure 52 shows the Si II 4p-5s multiplet at 5978.9 Å (3/2-1/2) and 5957.6 Å (1/2-1/2). In general, the strongest lines also included other Si II transitions, as shown in Figure 50, the H Balmer lines H_α at 6562.8 Å (Fig. 53) and H_β at 4861.3 Å (Fig. 54), Si III 4s-4p lines at 4560.1 Å and 5739.7 Å, the O I 3s-3p lines at 7773.4 Å, and occasionally C II 3s-3p lines at 6579.7 Å. Note that no Ar transitions were clearly identified when Ar was the working gas.

Silicon Contamination. The predominance of Si II lines in the spectra suggested strong Si contamination from the gun insulator (quartz is just SiO_2). However, some coworkers pointed out that it may have originated in the walls of the Pyrex beam tube (primarily SiO_2 , with lesser amounts of B_2O_3). To determine the source of Si contamination, two experiments were performed which pointed to the insulator with a high degree of certainty. For the first experiment, one of the fibers was positioned to look tangentially at just the inside of the beam tube wall. The second fiber was positioned radially, but looking through an interferometer port, which was recessed and symmetric with respect to the beam axis and precluded seeing any of the tube wall. The third fiber was positioned radially, looking through the tube wall and axis. The axial position for all three fibers was the 5-m station. For this experiment,

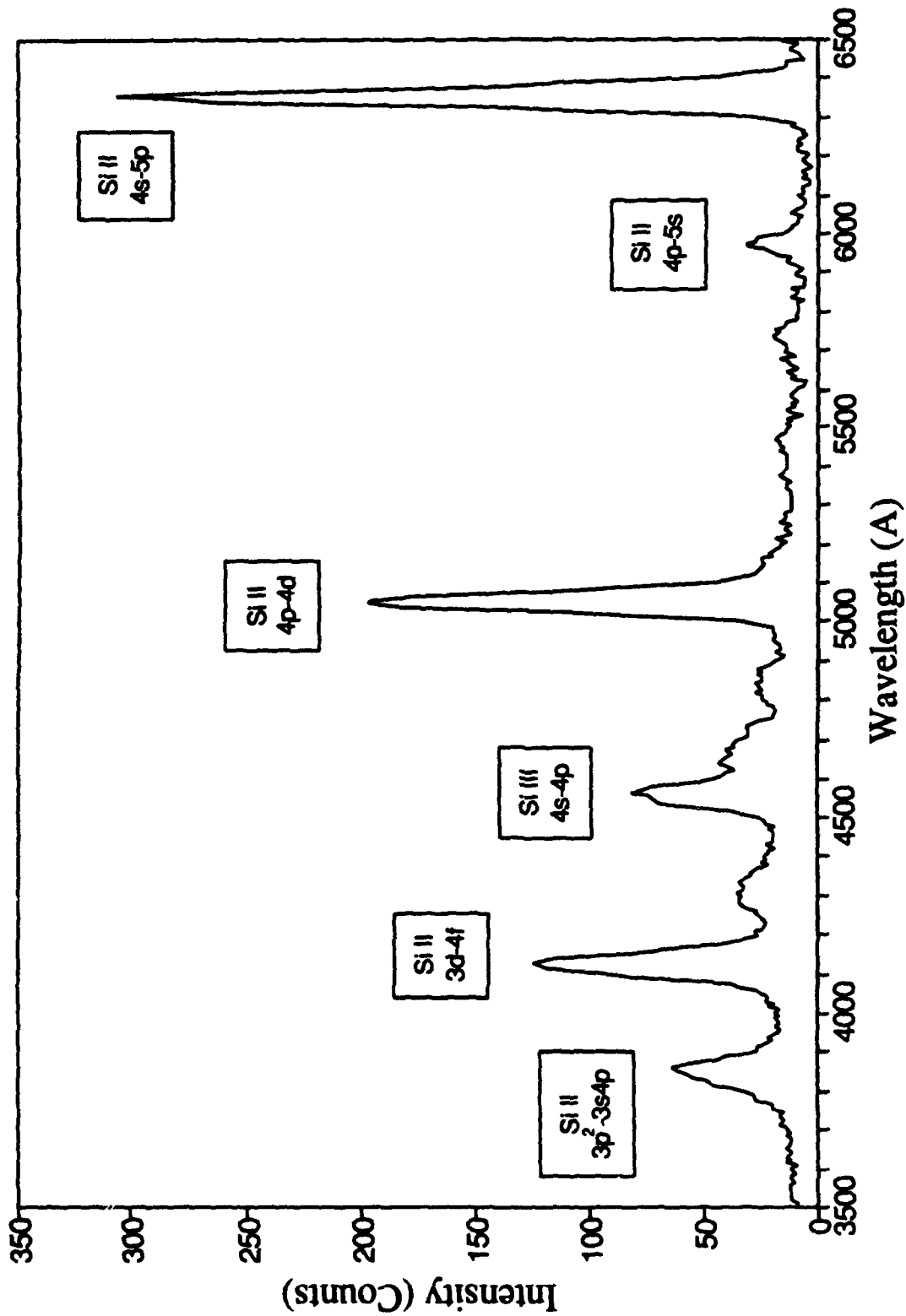


Figure 50. Typical time-integrated Ar spectrum at 5 m.

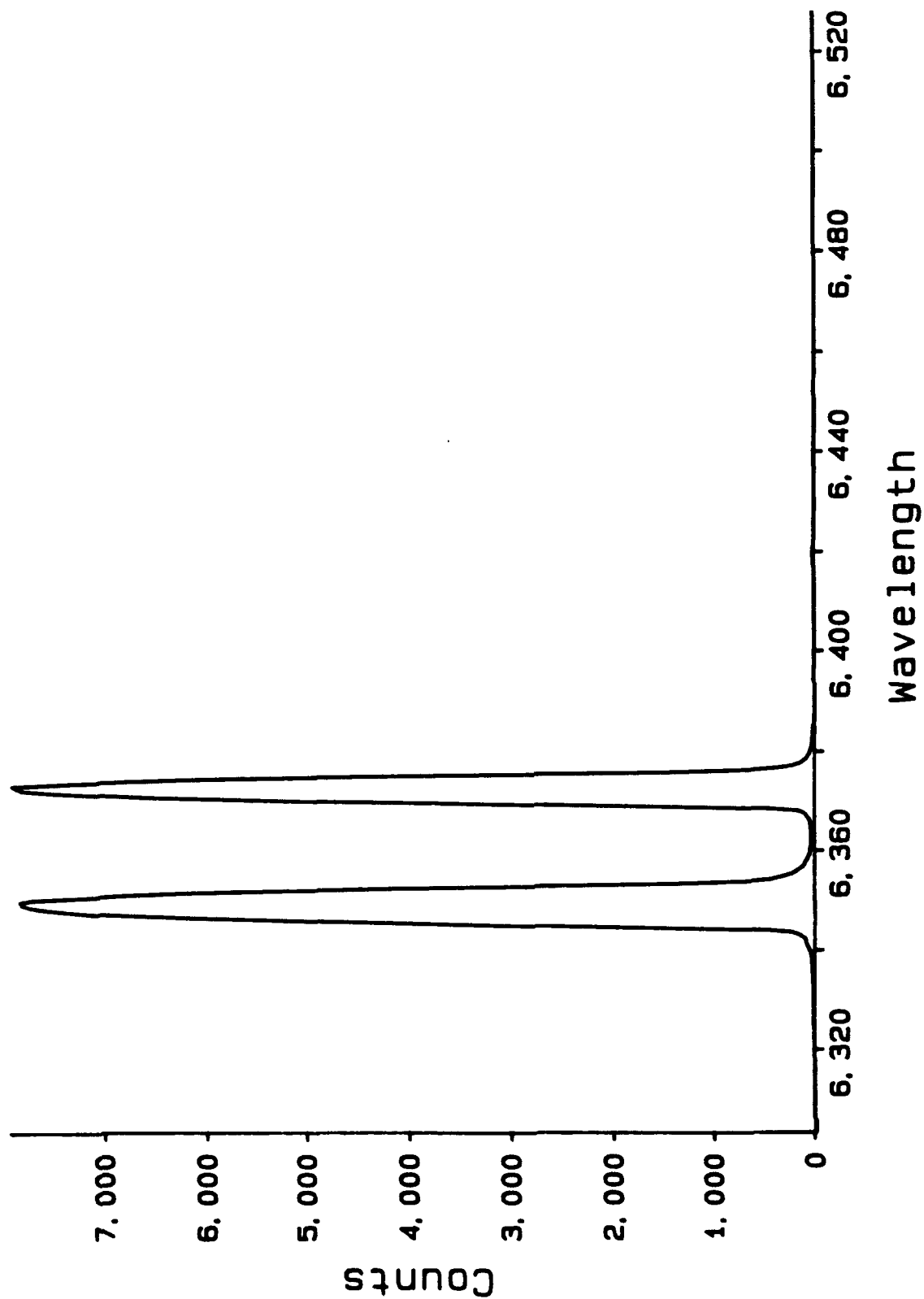


Figure 51. High-resolution spectrum of the Si II 4s-4p multiplet.

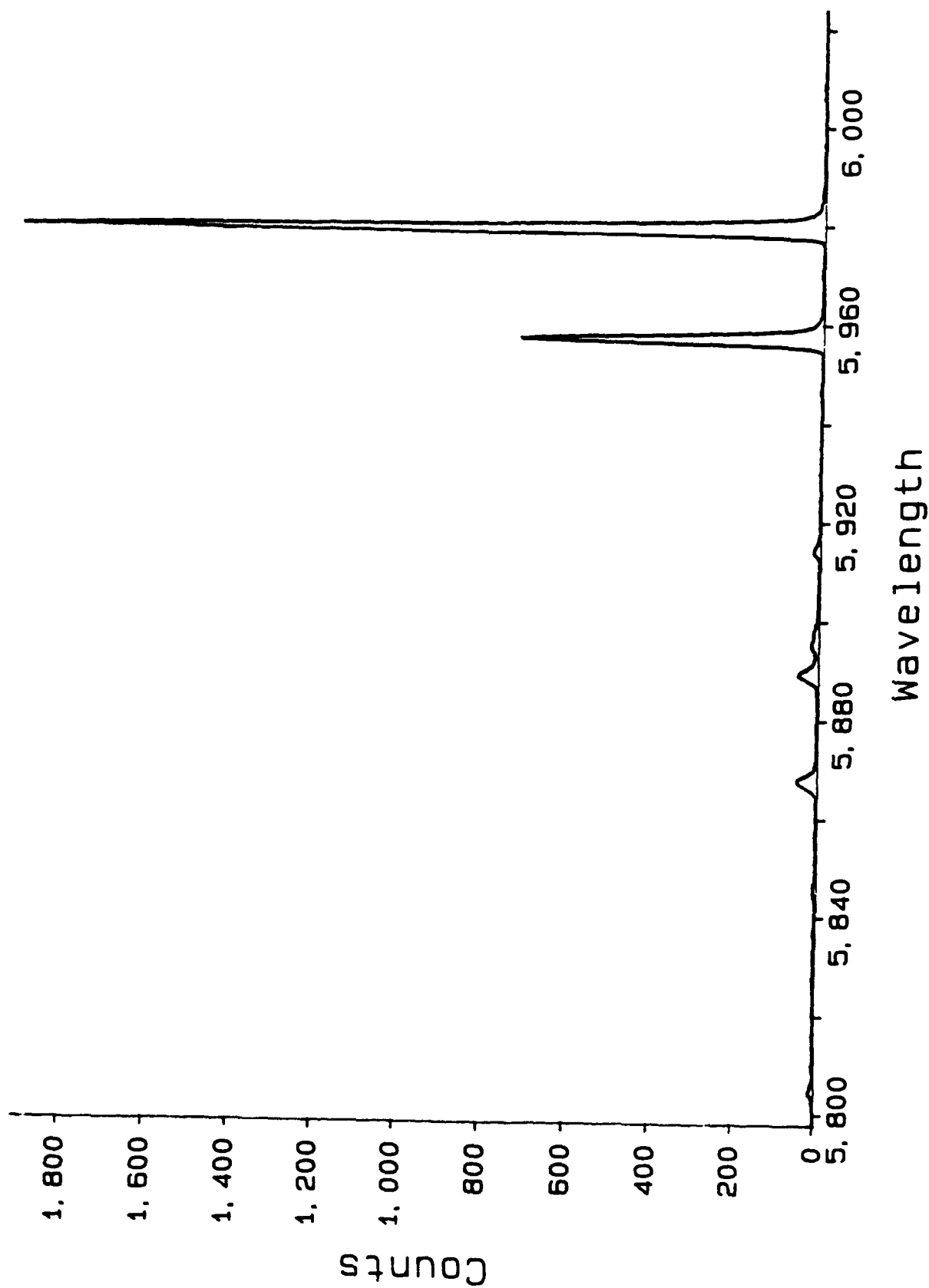


Figure 52. High-resolution Si II 4p-5s multiplet.

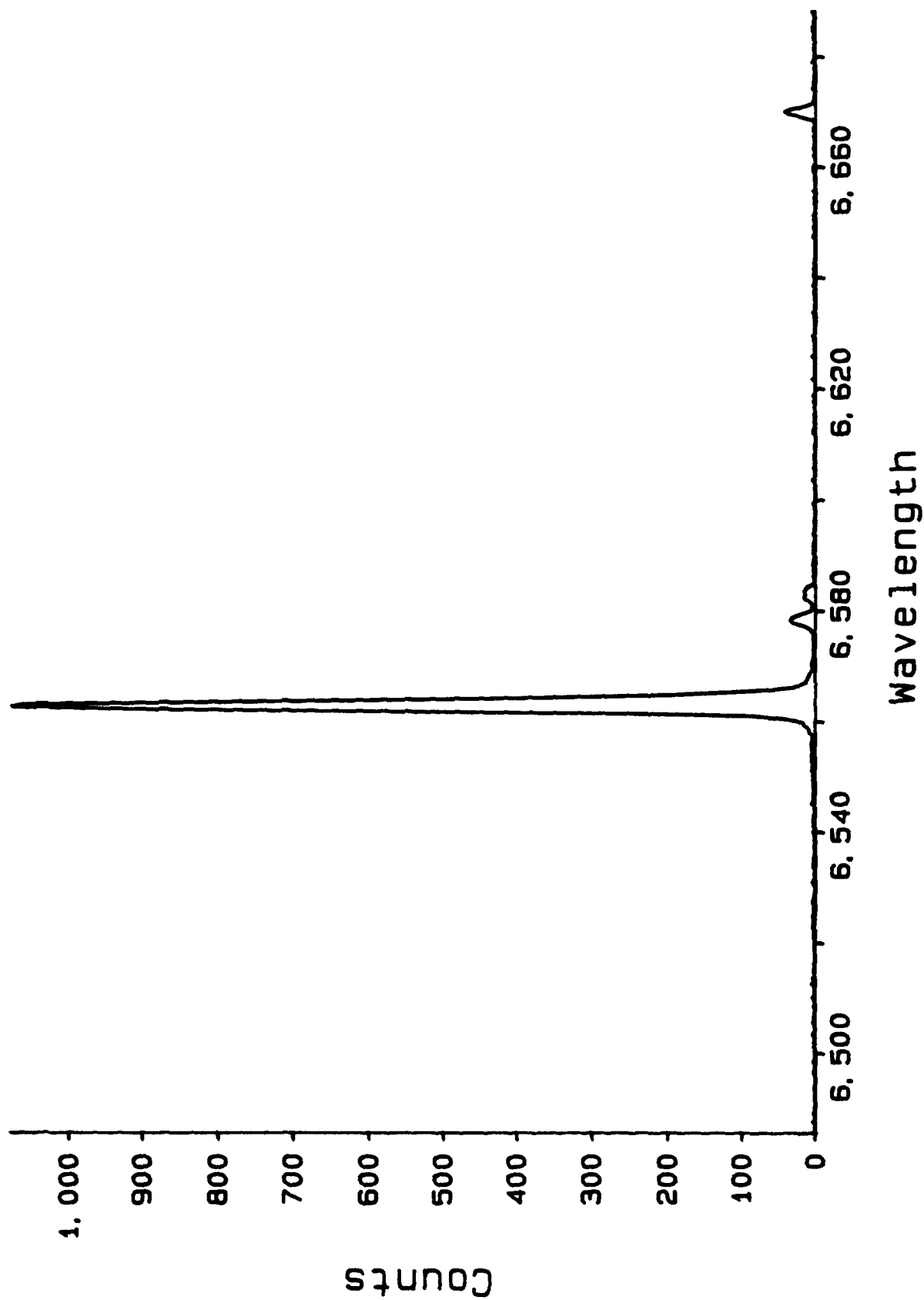


Figure 53. High-resolution H α spectrum.

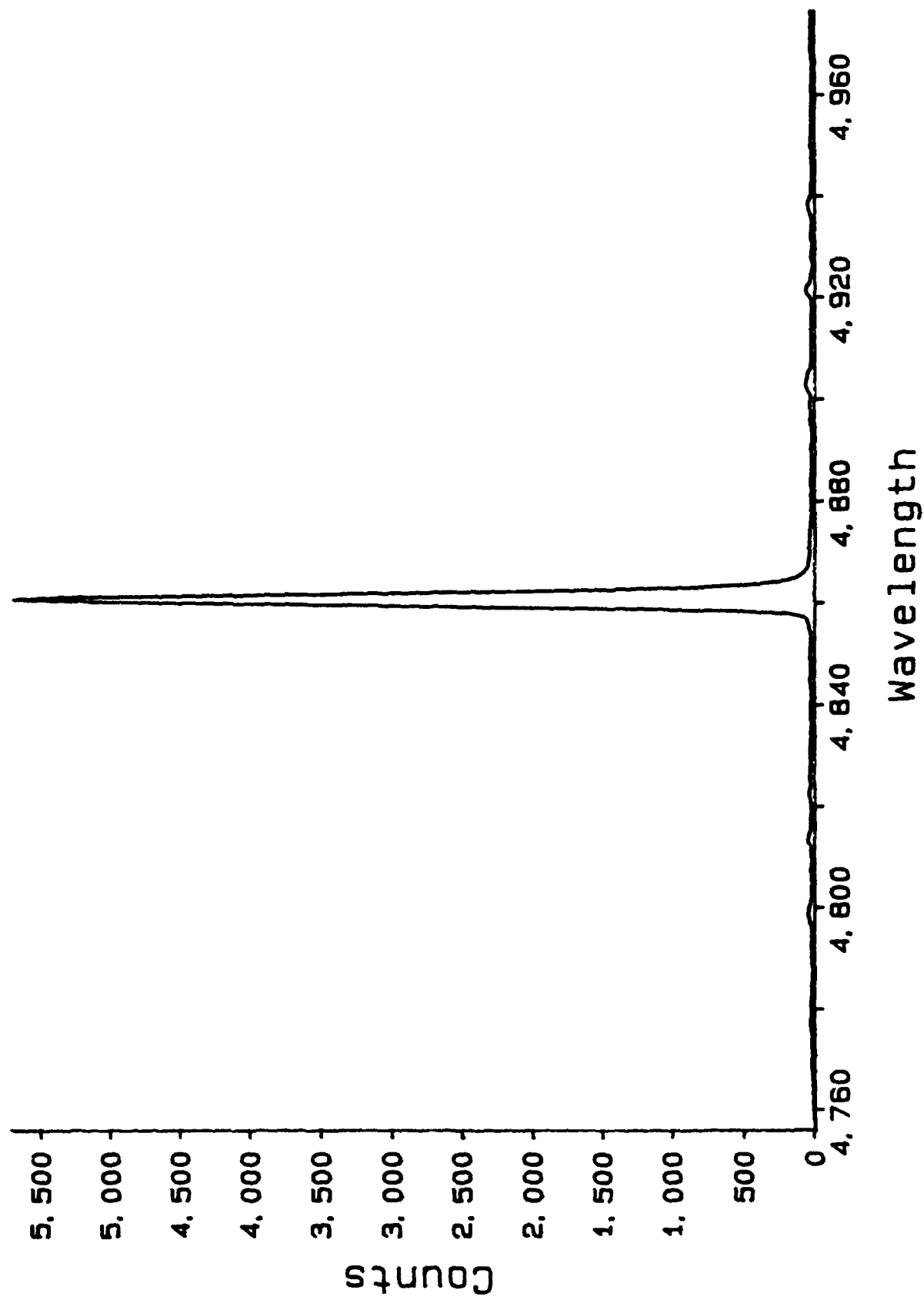


Figure 54. High-resolution H_β spectrum.

He was the working gas. Figures 55 through 57 (#2496) show the respective spectra taken 80 μ s after current rise with a 1- μ s exposure (near the peak in luminosity at 5 m). One can see that Si II and Si III lines are dominant in the spectrum taken through the interferometer port. The H_α and O I lines are clearly stronger for the fibers that "see the wall." An insulator made of alumina (Al_2O_3) was available and was installed for some shots for comparison with the quartz. Figure 58 (#2504T2) shows a spectrum taken with alumina insulator and Ar gas at 5 m, between 60 and 80 μ s. The strongest features are now the H_α and Al III 4s-4p lines at 5705.9 Å. Thus, it is believed with a high degree of certainty that the Si line radiation seen down range emanates from accelerated insulator material.

Load Gas Comparisons. One result of the spectral measurements was the insensitivity of the characteristic spectrum to working gas. For example, Figures 59 and 60 compare time-integrated broad-band spectra for Ar and He, respectively, at 5 m. The detectors are saturated for the strongest lines in both spectra, but a one-to-one correspondence in features can be seen, and these features are due to Si, H, and O. The same correspondence can be seen between Figure 55 for He at 80 μ s and 5 m, and Figure 61 for Ar and the same conditions. Neither time-integrated nor late-time spectra were recorded for H shots for comparison. However, some comparison can be made between Ar and H for relatively early times near the gun. Figure 62 shows a broad-band spectrum for Ar from 0 to 10 μ s at 0.3 m in front of the gun. Figure 63 shows a corresponding spectrum for H (5-10 μ s at the same location). Note that the two Si II transitions at 6355 and 5972 Å are somewhat saturated in both spectra. Again, almost all features match, with Si II and Si III dominating.

Early Time Characteristics. Some photodiode and interferometer signals suggested that there may have been a plasma precursor accelerated away from the gun ahead of the bulk of the density and luminosity. These erratic occurrences were never observed with the OMA because of its inherent single-frame mode of operation. It was hypothesized that the precursors could, in fact, be the ionized gas accelerated out of the gun before insulator flash-over. A number of spectra with Ar gas with 1- to 10- μ s time resolution between 0 and 10 μ s was recorded, at the gun muzzle, to look for characteristic line emission. These broad-band spectra did not show any clear Ar lines. In particular, the Ar II lines at 6642 Å are both relatively strong and well isolated; they were never observed.

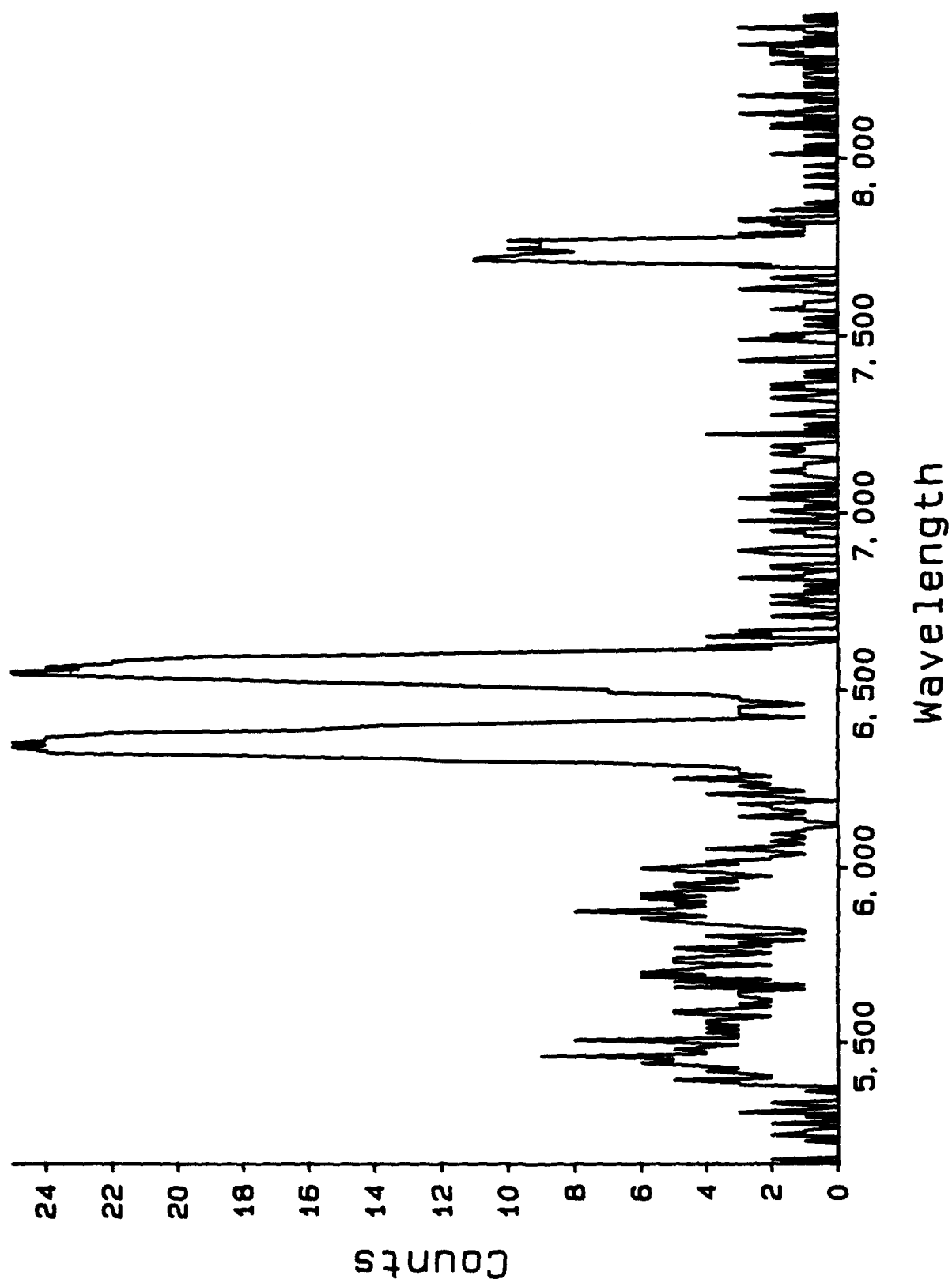


Figure 55. Tangential view at 5 m.

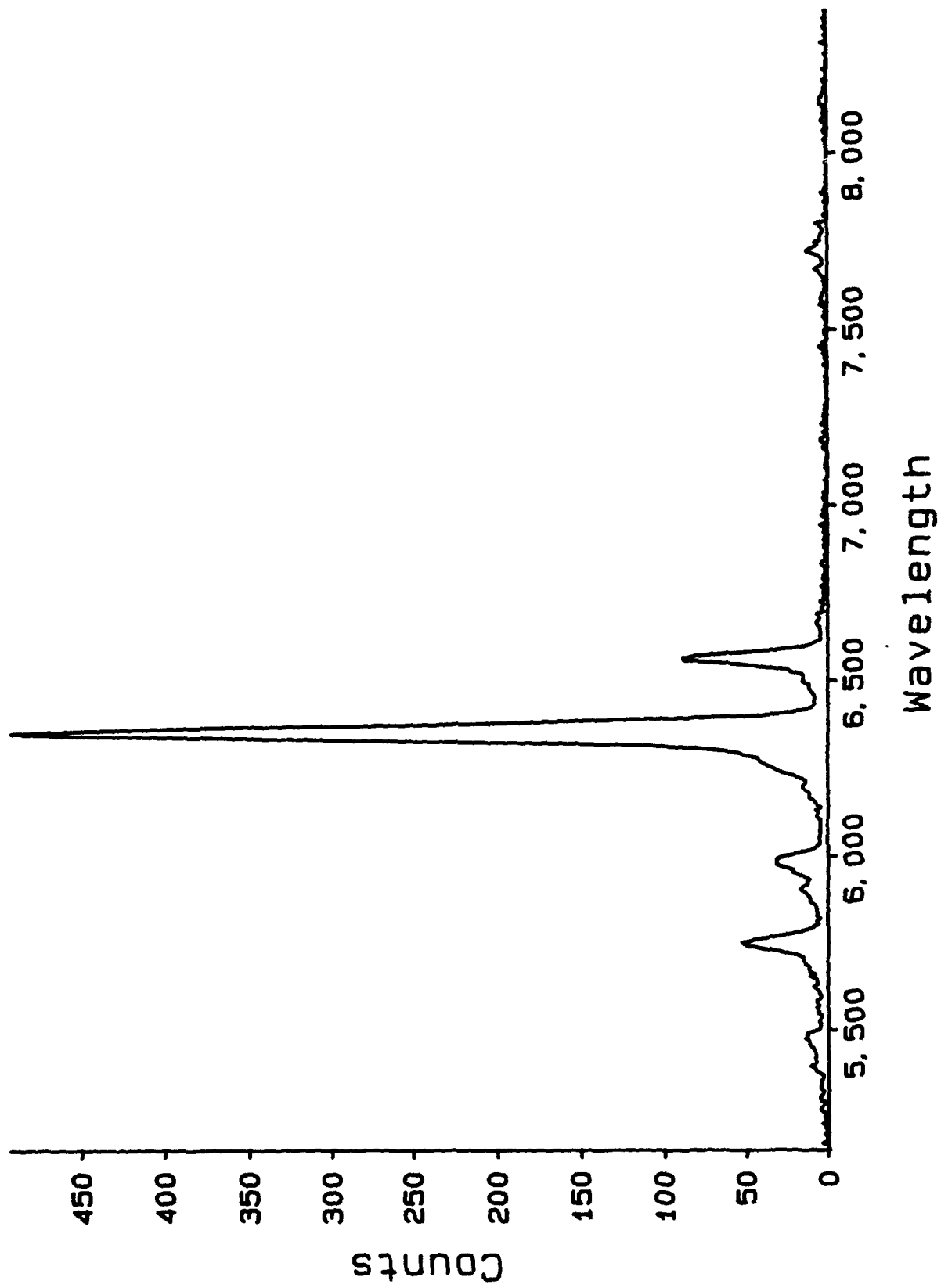


Figure 56. Interferometer port (no wall) view, at 5 m.

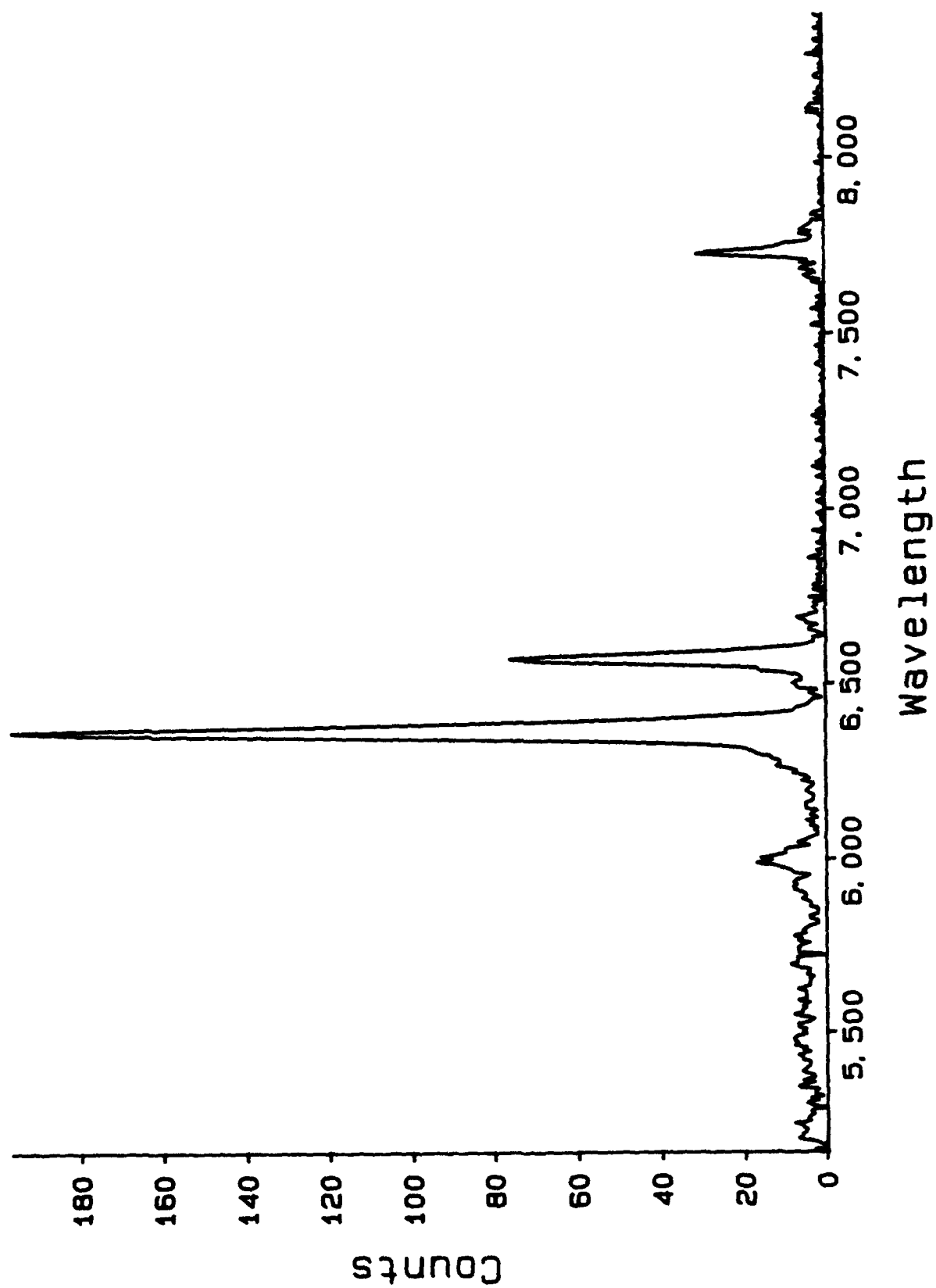


Figure 57. Radial (wall) view at 5 m.

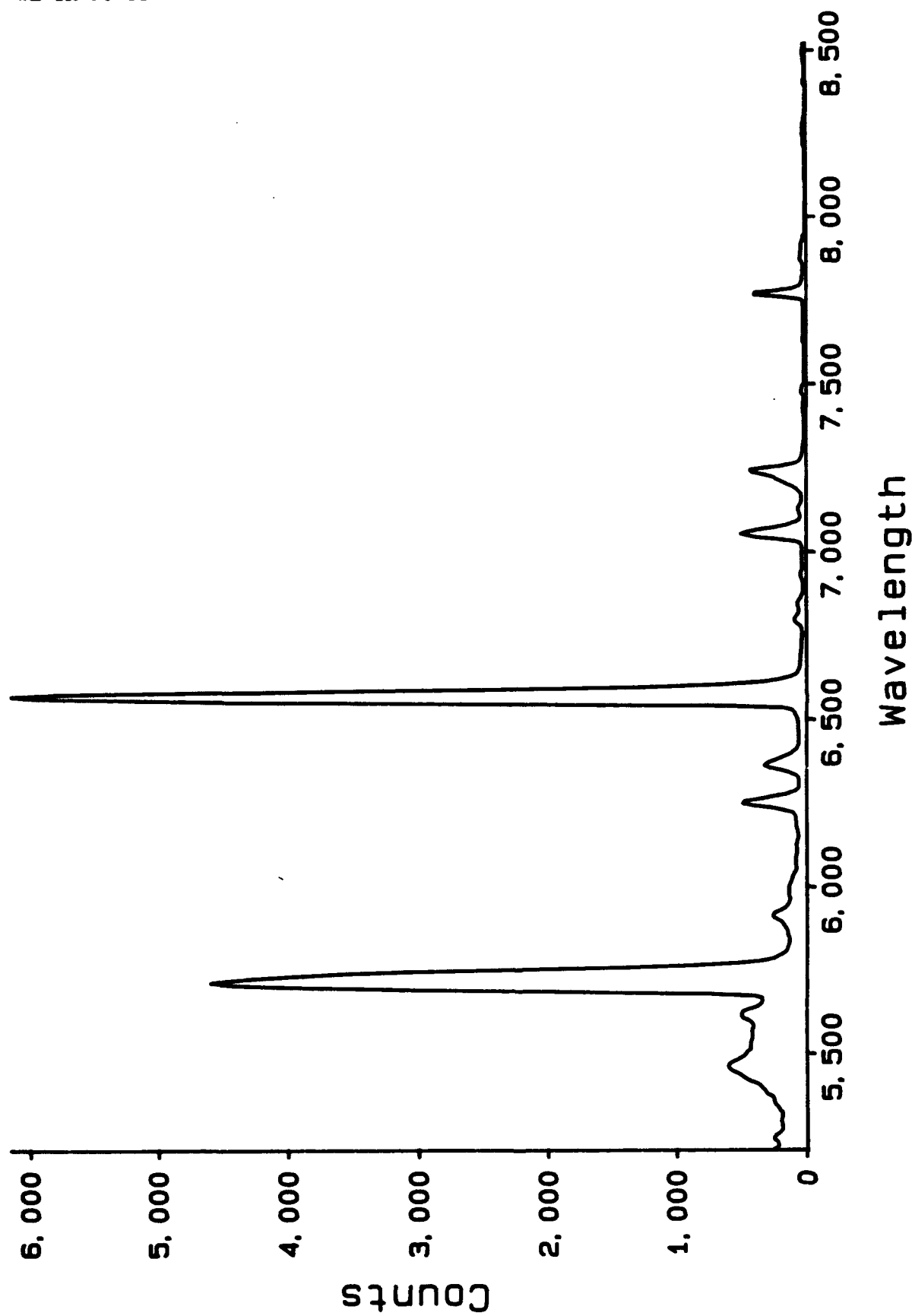


Figure 58. Broad-band spectrum at 5 m with alumina insulator.

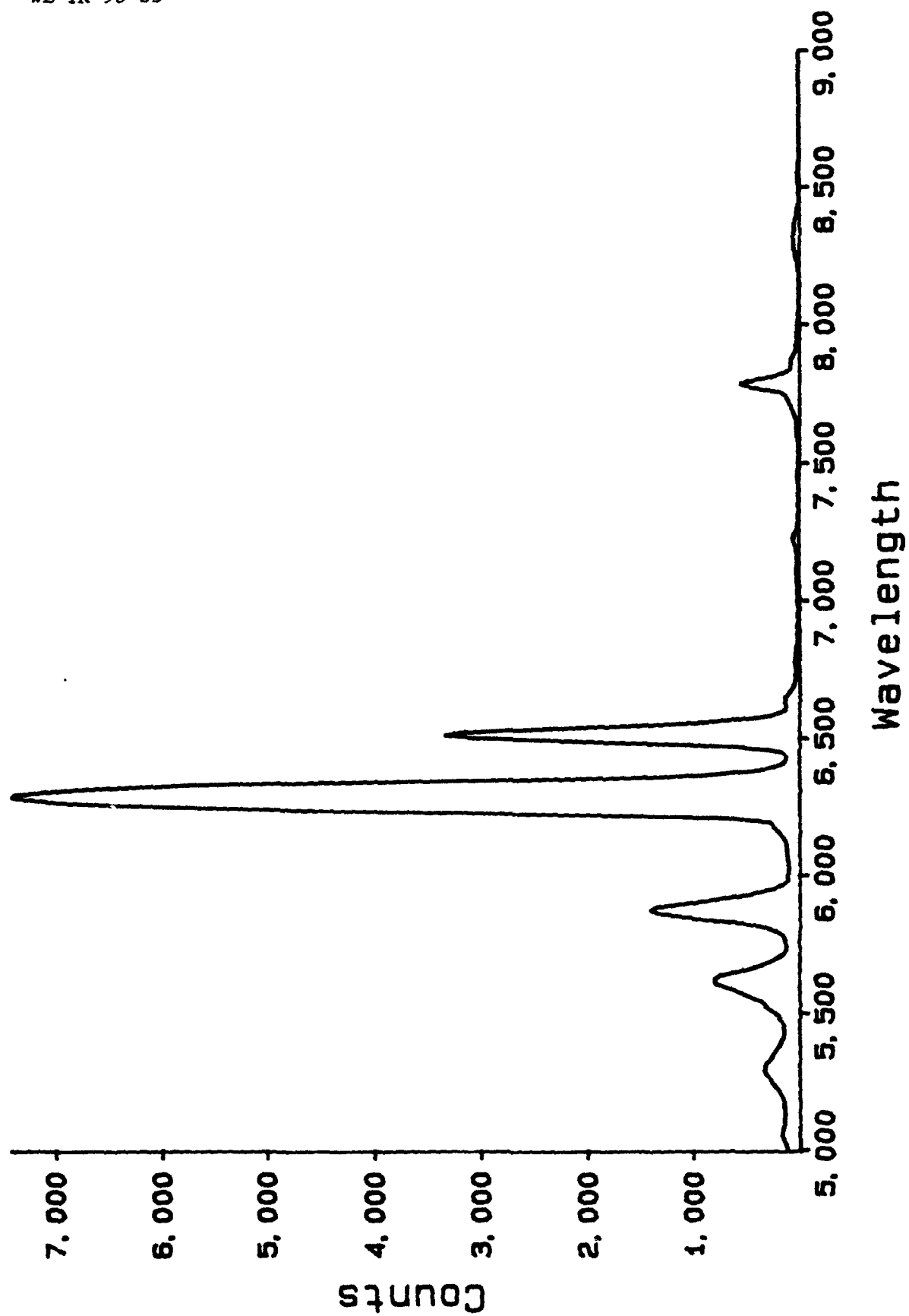


Figure 59. Broad-band Ar load spectrum at 5 m and 80 μ s.

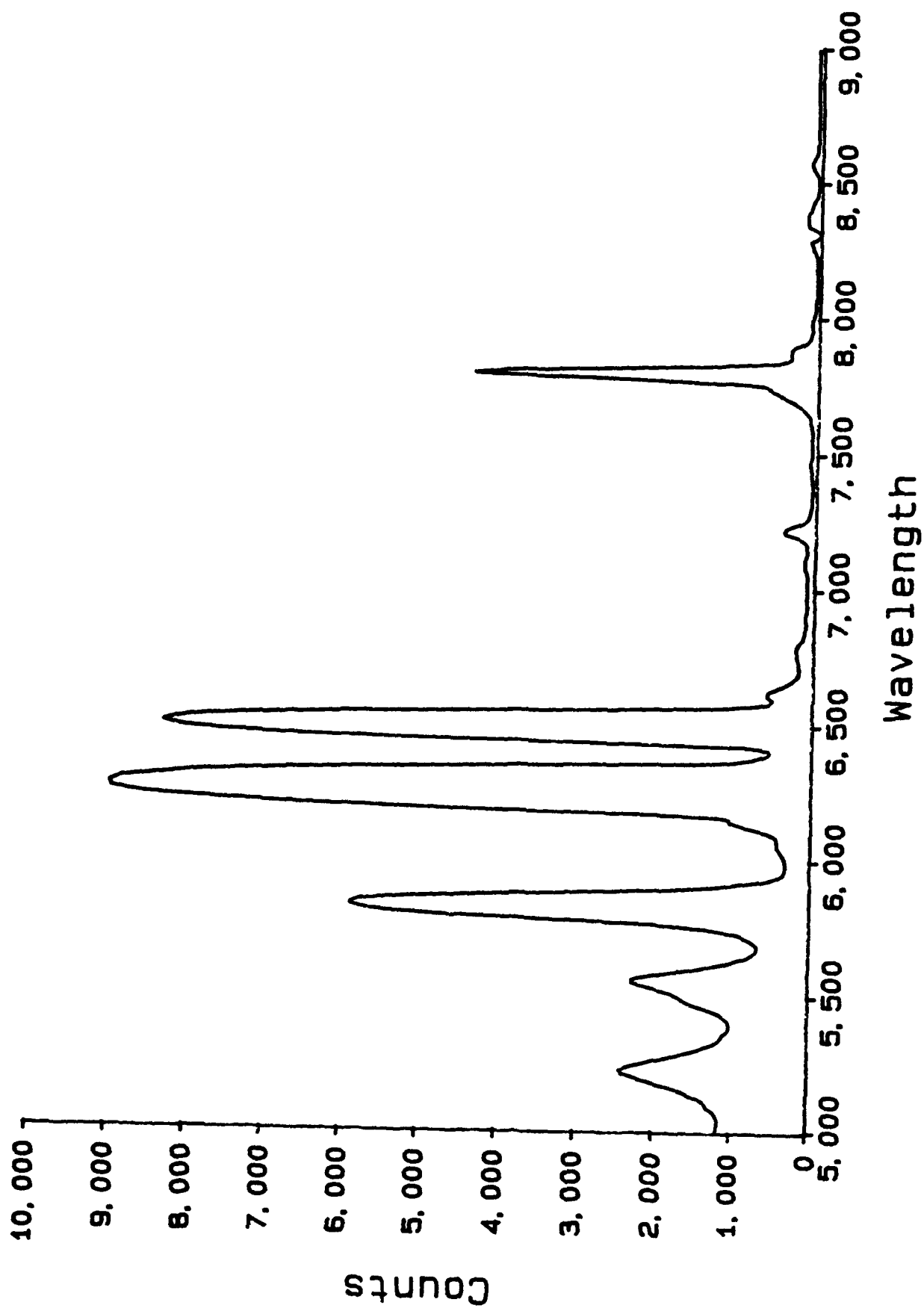


Figure 60. Time-integrated broad-band Ar load spectrum at 5 m.

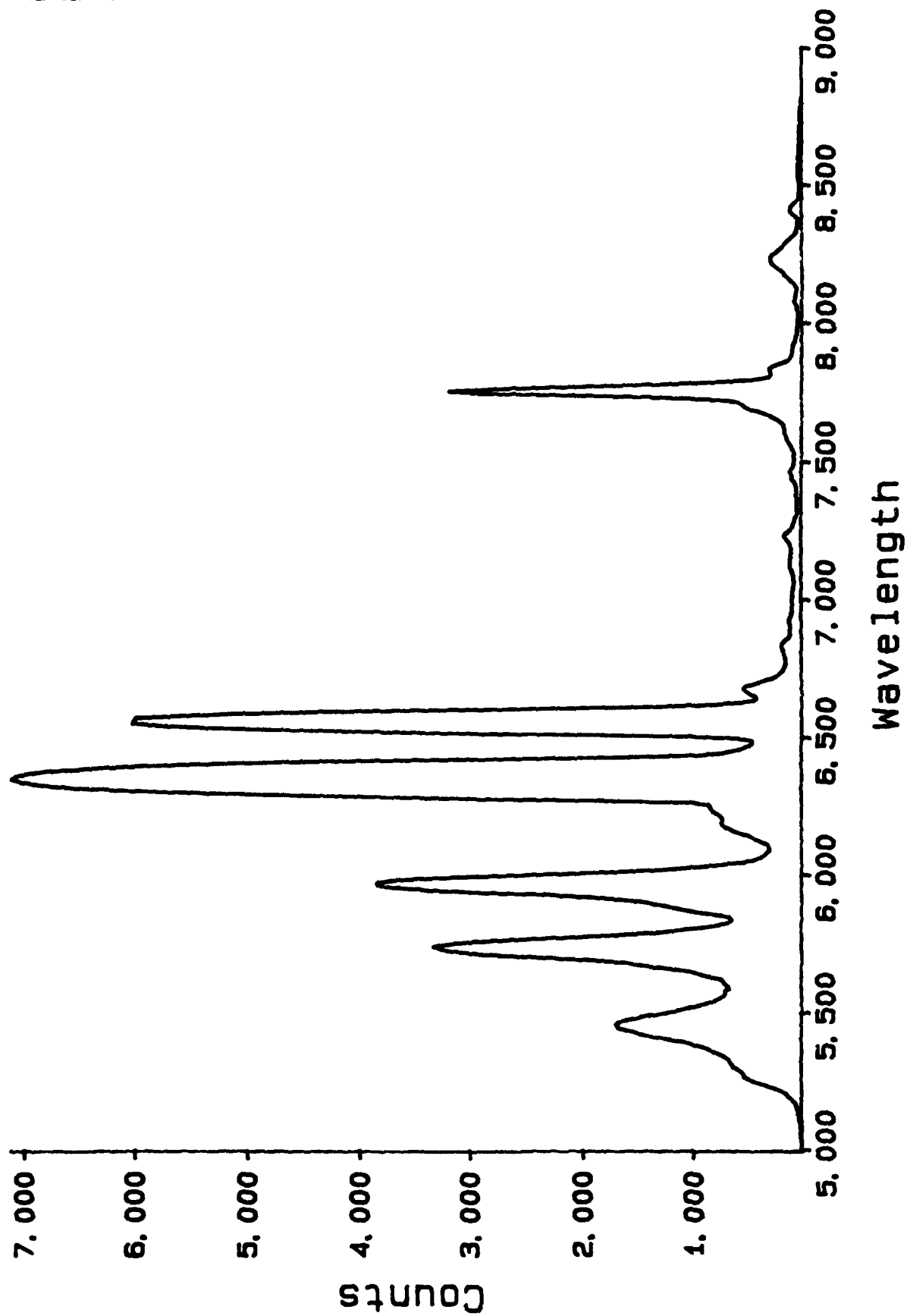


Figure 61. Time-integrated broad-band He load spectrum at 5 m.

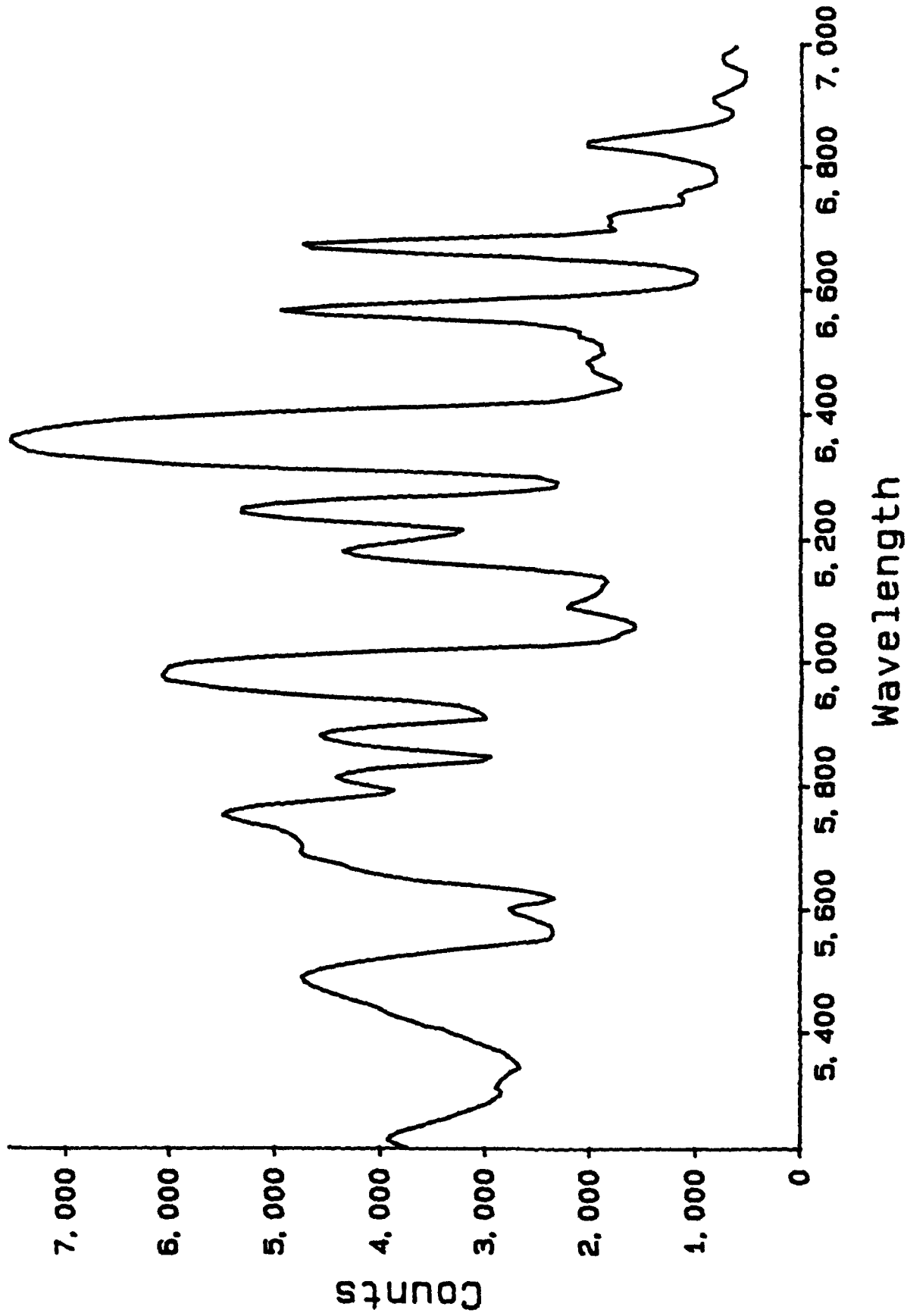


Figure 62. Broad-band Ar load spectrum, 0-10 μ s, 0.3 m.

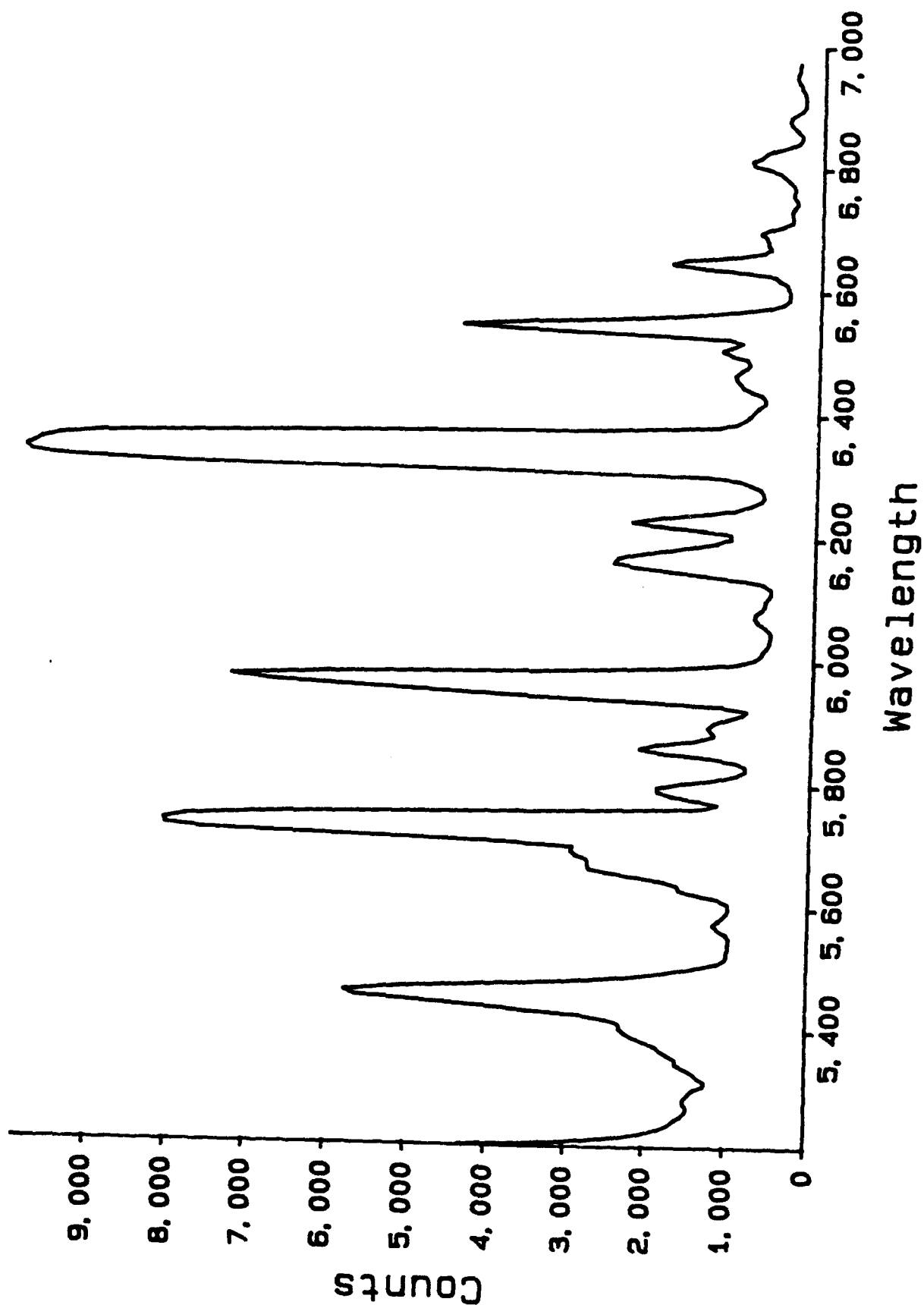


Figure 63. Broad-band H load spectrum, 5-10 μ s, 0.3 m.

Plasma Parameter Estimation

T_e From Relative Line Intensities. It is well known that under local thermodynamic equilibrium (LTE) conditions, the population density of excited states with respect to the ground state for a given specie is just the Boltzmann factor times the relative statistical weights,

$$\frac{N_i}{N_o} = \left(\frac{g_i}{g_o} \right) \exp\left(\frac{-(E_i - E_o)}{kT_e} \right) \quad (28)$$

where E is the energy of the state, g is the statistical weight, k is Boltzmann's constant, and T_e is the electron temperature. The line intensity ratio for two transitions beginning in two different excited states of the same specie and ionization state, then, is

$$\frac{I_{lj}}{I_{kl}} = \frac{(E_l - E_j)}{(E_k - E_l)} \left(\frac{A_{lj}}{A_{kl}} \right) \exp\left(\frac{-(E_l - E_k)}{kT_e} \right) \quad (29)$$

where A is the transition probability, and the intensities are weighted by the energy of the transitions.

The ratio of the intensity of the Si II 4p-5s transition to the intensity of the Si II 4s-4p transition was used to estimate the temperature of the gun plasma as a function of time and axial position for Ar gas and quartz insulator. For these estimates, broad-band spectra were taken at $z = 0, 5$, and 10 m, for gate widths of $20 \mu s$ in $20\text{-}\mu s$ steps. The results are shown in Figure 64. Note that the line-integrated intensities were corrected for detector response and grating efficiency. The intensities are radially- and azimuthally-integrated values. One can see that the characteristic temperatures are on the order of 1 eV and exhibit a decrease as time progresses at a given position. Also, the temperatures are somewhat higher at the gun. The validity of the LTE assumption is discussed below in subsection CRE Model Analysis, Excitation and Ionization Equilibrium.

N_e From Stark Broadening. Stark broadening of spectral line profiles is due to perturbations in the local electric fields by charged particles (Ref. 9).

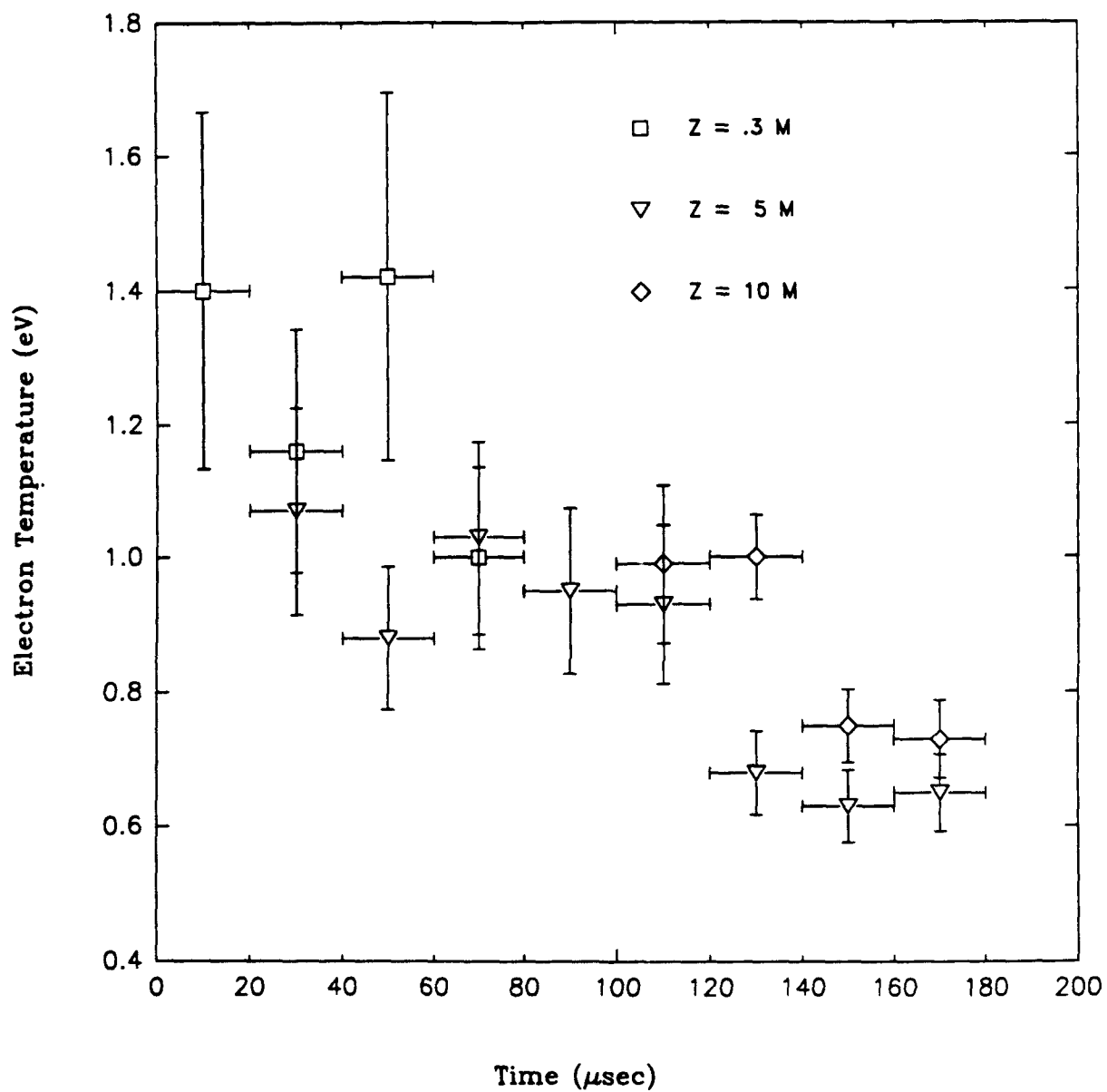


Figure 64. Time history of electron temperature for LTE model.

Thus, the higher the density, the greater the broadening. The theory is quite well-developed for the Balmer series in H and has been compared favorably to experiment. The H_β line width exhibits a particularly simple and sensitive dependence to electron density (Fig. 65), is essentially independent of temperature over the range of 0.5 to 5 eV, and is therefore a nearly ideal density diagnostic. Since evidence of H was seen in nearly all coaxial gun plasma spectra, the H_β line was isolated for some shots. Figure 54 is one example, taken for Ar gas and alumina insulator at 5 m from 50 to 150 μ s. The FWHM of the line is not significantly greater than the instrumental resolution, so that for this shot one can place an upper bound on the electron density of $\sim 10^{15} \text{ cm}^{-3}$. The greatest broadening seen was $\sim 8 \text{ \AA}$, for an H shot at 20-22 μ s, just in front of the gun. This width corresponds to an electron density of $\sim 6 \times 10^{15} \text{ cm}^{-3}$. Note, however, that if the H is not well mixed with the rest of the plasma, or if the electron temperature is not uniform throughout the volume sampled, N_e inferred from the H_β line width may not be representative of the entire volume.

Lines from other species also may be sensitive to pressure. For example, the Si II 4f-6d multiplet at 6680 has an FWHM of $\sim 12 \text{ \AA}$ at an electron density of 10^{17} cm^{-3} , independent of temperature, and has a shift of about 13 \AA , with relative temperature insensitivity. Both width and shift are linearly dependent on the density (Ref. 10). Other sensitive transitions in Si II are the 4d-nf and 5p-ns lines. When these lines were observed, their widths and shifts were generally insignificant ($< 10 \text{ \AA}$), so no quantitative inferences could be made other than the electron densities were $< 10^{17} \text{ cm}^{-3}$.

CRE Model Analysis

Excitation and Ionization Equilibrium. The LTE line intensity ratio analysis described above presupposes that the plasma electron velocities have a Maxwellian distribution, that collisional transitions (excitation and deexcitation) dominate radiative transitions and that the plasma is optically thin to its radiation (that is, the probability of radiation absorption by the plasma is negligible, so that all radiation emitted escapes the plasma directly). Furthermore, the LTE model assumes that time scales for variation

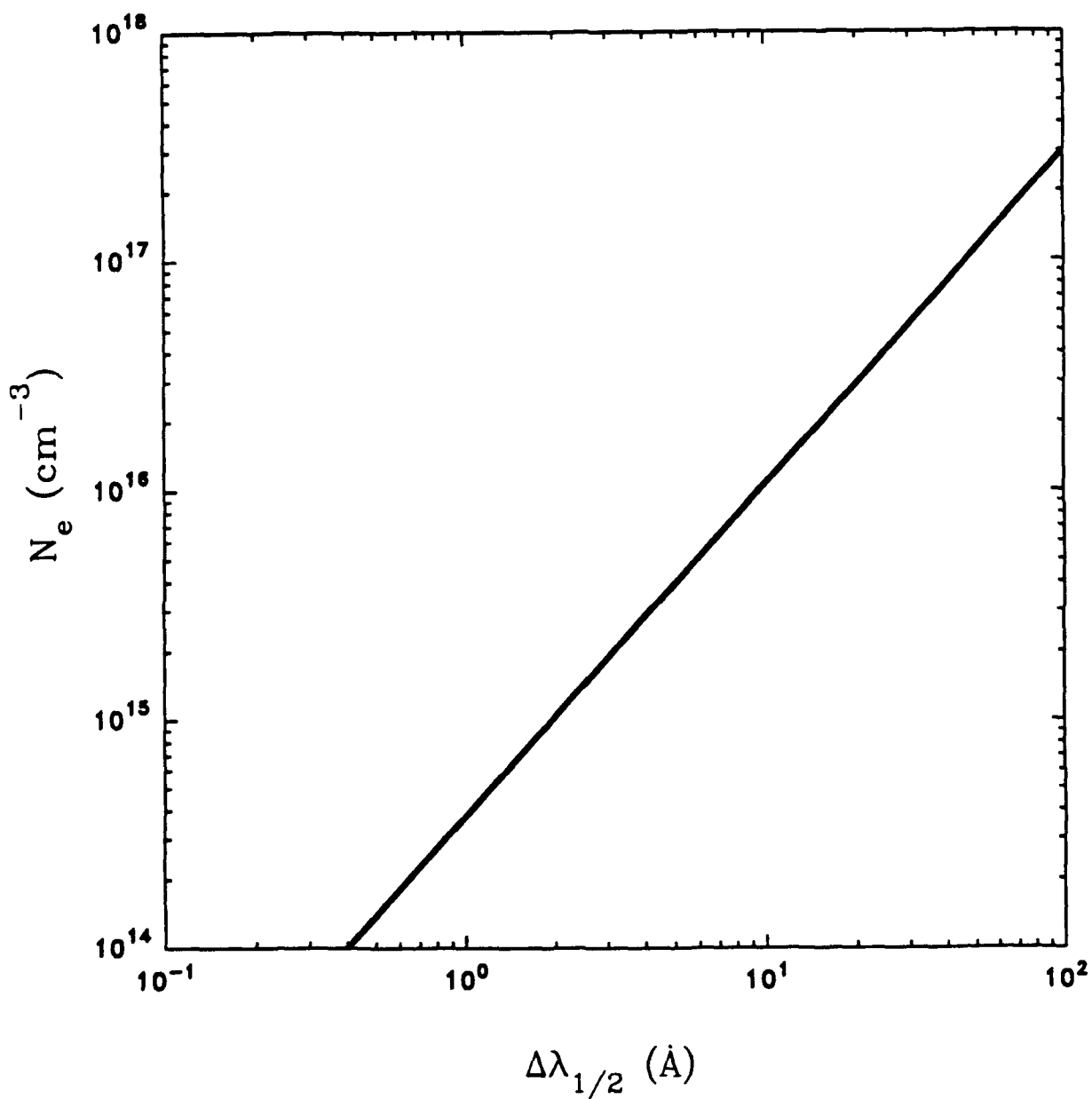


Figure 65. Scaling of the FWHM of H_β with electron density.

of the plasma parameters are longer than collisional transition times, so that the plasma--at least locally--remains in equilibrium. A necessary, but not sufficient, criterion for validity of the LTE approximation may be expressed quantitatively by comparing collisional to radiative transition rates. Several authors have proposed the criterion for validity of LTE (Refs. 11-13).

$$N_e \text{ (cm}^{-3}\text{)} \geq 1.5 \times 10^{14} \chi^3 \sqrt{T_e} \quad (30)$$

where the energy difference between two levels, χ , and the electron temperature, T_e , are in electronvolts. For the coaxial gun plasmas, the temperatures and densities are roughly 1-2 eV and 10^{13} - 10^{15} cm $^{-3}$, respectively, and typical transition energies are 2 eV. Therefore, LTE criteria for excitation levels within a particular ionization state cannot be expected to be satisfied just from collisional versus radiative transition considerations.

Given that the plasma electron temperature is of order 1 eV and electron density is in the range 10^{12} cm $^{-3}$ to 10^{16} cm $^{-3}$, to what degree can one expect equilibrium between successive ionization states? The ionization relaxation time for various species is estimated. In general, a given ion may experience ionizing collisions with particles, photoionization, collisional recombination, and radiative recombination. The collisions may be with electrons, ions, or neutral atoms or molecules. For the temperature and density regime of interest, only electron collisions are important (Ref. 14). Similarly, although radiative recombination can be significant, photoionization usually is not.

Thus, the ionization rate equation for a species with ionization state Z ($Z = 0$ corresponds to the neutral atom) may be simplified to

$$\frac{dN(Z)}{dt} = N_e [-S(Z)N(Z) - \alpha(Z)N(Z) + S(Z-1)N(Z-1) + \alpha(Z+1)N(Z+1)] \quad (31)$$

where S is the collisional ionization coefficient, and the recombination coefficient

$$\alpha(Z) = \alpha_r(Z) + N_e \alpha_3(Z) \quad (32)$$

contains a radiative recombination term and a three-body recombination term. Whereas the relaxation to excitation equilibrium occurs on the time scale of radiative transitions (typically 10^{-8} s) or faster, the relaxation from higher to lower ionization states occurs on recombination time scales.

In the gun, one expects considerable collisional ionization, and even step-wise collisional ionization to highly ionized states. Neglecting collisional momentum transfer to the neutral atoms, one can speculate that the plasma emerging at the gun muzzle does not contain neutral species except as they are created by recombination processes. The following simple expressions for the recombination rate coefficients (Refs. 15-16), have been used to calculate the relaxation time constants for singly ionized to neutral species.

$$\alpha_r(Z) = 5.2 \times 10^{-14} Z \left(\frac{E_\infty^Z}{T_e} \right)^{1/2} \left[0.43 + \frac{1}{2} \ln \left(\frac{E_\infty^Z}{T_e} \right) + 0.469 \left(\frac{E_\infty^Z}{T_e} \right)^{-1/2} \right] \text{ cm}^3/\text{s} \quad (33)$$

$$\alpha_3 = 8.75 \times 10^{-27} T_e^{-9/2} \text{ cm}^6/\text{s} \quad (34)$$

The results are relatively insensitive to atomic specie over the ranges of temperature and density of interest. Representative figures for H are shown in Table 6. One can see that for temperatures of order 1 eV and densities of order 10^{14} cm^{-3} , the relaxation times are considerably longer than the experiment time scales. This means that it is not probable that the plasma attains any kind of ionization equilibrium, and therefore inferences of plasma parameters based on assumed equilibria are generally invalid.

Table 6. Hydrogen ($\text{H}^+ \rightarrow \text{H}^0$) relaxation times.

n_e (cm^{-3})	T_e (eV)				
	0.2	0.5	1.0	2.0	5.0
10^{12}	7.5×10^{-2}	1.2×10^0	2.6×10^0	4.5×10^0	9.2×10^0
10^{13}	8.1×10^{-4}	3.9×10^{-2}	2.2×10^{-1}	4.4×10^{-1}	9.2×10^{-1}
10^{14}	8.2×10^{-6}	4.9×10^{-4}	8.0×10^{-3}	3.8×10^{-2}	9.2×10^{-2}
10^{15}	8.2×10^{-8}	5.0×10^{-6}	1.1×10^{-4}	1.6×10^{-3}	8.7×10^{-3}
10^{16}	8.2×10^{-10}	5.0×10^{-8}	1.1×10^{-6}	2.4×10^{-5}	5.8×10^{-4}

Collisional Radiative Equilibrium (CRE) Model. The CRE model used to analyze gun plasmas is a relatively simple one. Basically, it is assumed that the various excited states of a given ionization state are in equilibrium, with the important transition processes being collisional excitation, collisional deexcitation, and radiative deexcitation. Photoexcitation is specifically ignored; that is, it is assumed the plasma is optically thin.

The radiative deexcitation rate from state k to state i is just given by the product of the upper excited state number density and the Einstein transition probability, $N_k A_{ki}$.

The collisional excitation rate from state i to state k is given by

$$X_{ik}(T_e) = 3.644 \times 10^{-14} N_e N_i \frac{g_k}{g_i} \frac{A_{ki} \langle g \rangle}{(kT_e)^{1/2} E_{ki}^3} \exp\left(-\frac{E_{ki}}{kT_e}\right) \text{ cm}^{-3} \text{ s}^{-1} \quad (35)$$

where $E_{ki} = (E_k - E_i)$, in electronvolts, g_k and g_i are the statistical weights, and the Gaunt factor, $\langle g \rangle$, is well approximated by (Ref. 17)

$$\langle g \rangle = 0.2 + 0.551 \ln(1 + T_e/E_{ji}) \quad (36)$$

The corresponding collisional deexcitation rate between the same two levels can be determined from the principle of detailed balancing to be

$$Y_{ki}(kT_e) = 3.644 \times 10^{-13} N_e N_k \frac{A_{ki} \langle g \rangle}{(kT_e)^{1/2} (E_{ki})^3} \text{ cm}^{-3} \text{ s}^{-1} \quad (37)$$

In equilibrium, the collection of rate equations for the various excited states form a linear algebraic system, which can be solved in terms of the ratio of state densities to ground state density. A computer program was written in the "C" language for running on PCs and is included as an Appendix at the end of this report. The Appendix contains a listing of the program and tabular output for the Si II system. A Grotrian diagram of the Si II excitation structure and energy values are shown in Figures 66 and 67 (Ref. 18). The transition probabilities appearing in each of the rate coefficients were taken from various reports in the literature. It is noteworthy that the relative excited state densities are much more sensitive to the energy levels

than the transition probabilities. For example, cases were run with variations in the A_{ki} of ± 50 percent, and density variations of only ± 10 percent resulted.

At the temperatures and densities characteristic of the coaxial gun plasmas, and for the lower lying states from which the strongest radiative transitions originate, the inclusion of radiative depopulation mechanisms can have a significant effect on the relative populations. For example, Figure 68 is a Boltzmann plot of selected level populations for Si II at $kT_e = 5$ eV. One can see dramatic departures from LTE at electron densities as high as 10^{16} cm^{-3} for the population of the $4f$ state, especially.

The sensitivity of certain levels to the electron density can be used to zero in on a region in $T_e - N_e$ parameter space which fits many line intensities in a spectrum. An example of such a sensitivity is the ratio of $4p^1P^o$ to $4p^3P^o$ states in Si III, as shown in Table 7.

Table 7. Si III $4p^1P^o$ to $4p^3P^o$ state density ratio.

T_e (eV)	N_e (cm^{-3})					
	10^{12}	10^{13}	10^{14}	10^{15}	10^{16}	10^{17}
0.5	7.1×10^1	7.6×10^0	9.7×10^{-1}	4.5×10^{-1}	3.9×10^{-1}	2.7×10^{-1}
0.7	6.8×10^1	8.8×10^0	1.1×10^0	5.0×10^{-1}	4.4×10^{-1}	3.0×10^{-1}
1.0	4.6×10^1	9.3×10^0	1.3×10^0	5.4×10^{-1}	4.8×10^{-1}	3.2×10^{-1}
1.2	3.5×10^1	9.1×10^0	1.4×10^0	5.6×10^{-1}	5.0×10^{-1}	3.3×10^{-1}
1.5	2.4×10^1	8.6×10^0	1.4×10^0	5.8×10^{-1}	5.3×10^{-1}	3.4×10^{-1}
2.0	1.7×10^1	7.6×10^0	1.5×10^0	5.9×10^{-1}	5.5×10^{-1}	3.6×10^{-1}
2.5	1.3×10^1	6.9×10^0	1.5×10^0	6.0×10^{-1}	5.5×10^{-1}	3.6×10^{-1}
3.0	1.1×10^1	6.3×10^0	1.5×10^0	6.0×10^{-1}	5.5×10^{-1}	3.7×10^{-1}
4.0	8.7×10^0	5.6×10^0	1.5×10^0	5.9×10^{-1}	5.5×10^{-1}	3.7×10^{-1}
5.0	7.6×10^0	5.1×10^0	1.5×10^0	5.9×10^{-1}	5.4×10^{-1}	3.7×10^{-1}

S, II GROTRIAN DIAGRAM (13 electrons, $Z=14$)
(All Sequence, Configuration: $1s^2 2s^2 2p^3 3s^2 n$, Doublet System)

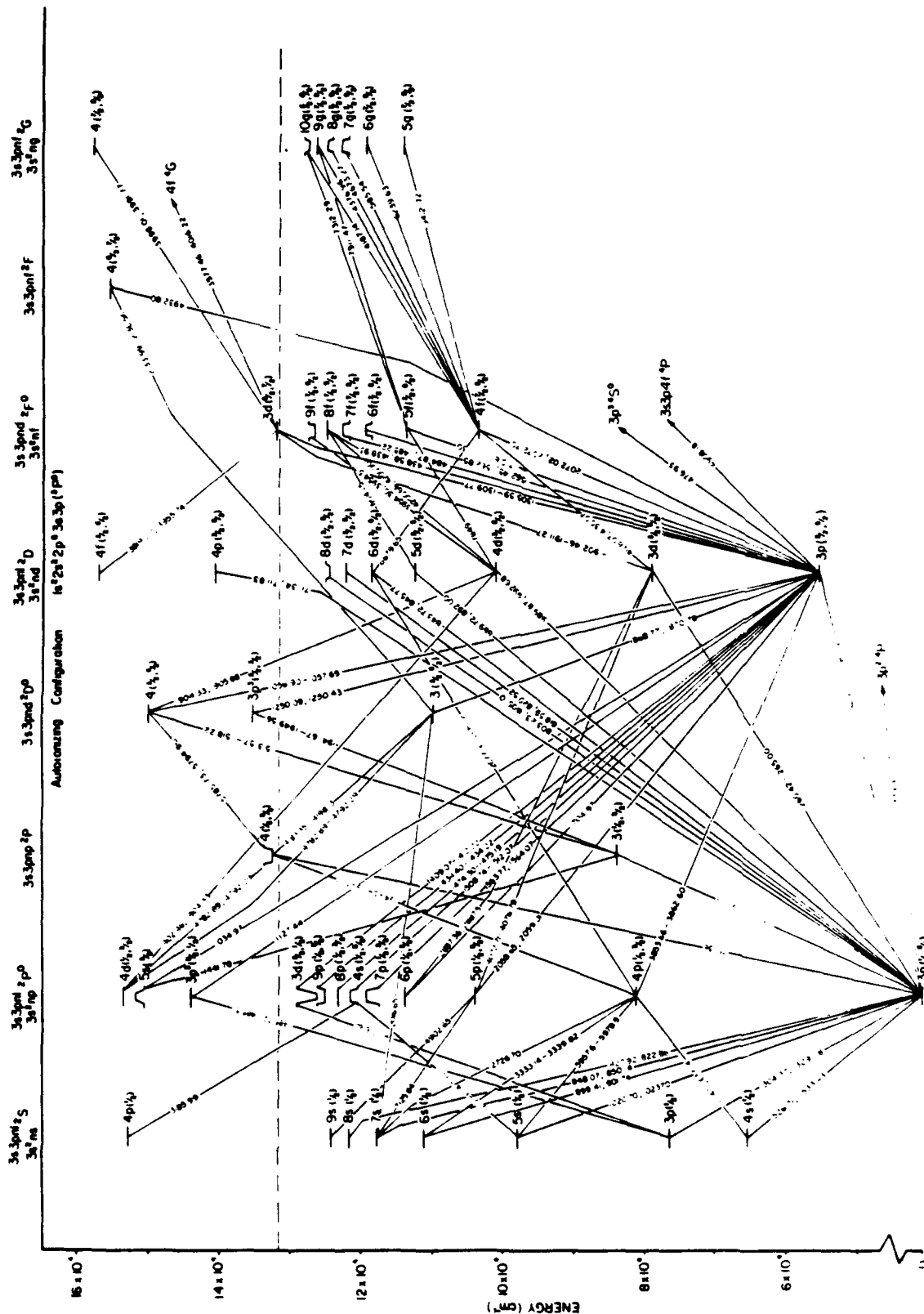


Figure 66. Grotrian diagram of the S I II system (from Ref. 18).

Si II ENERGY LEVELS (13 electrons, Z = 14)
(AII Sequence, Configuration $1s^2 2s^2 2p^6 3s^2 n$, Doublet System)

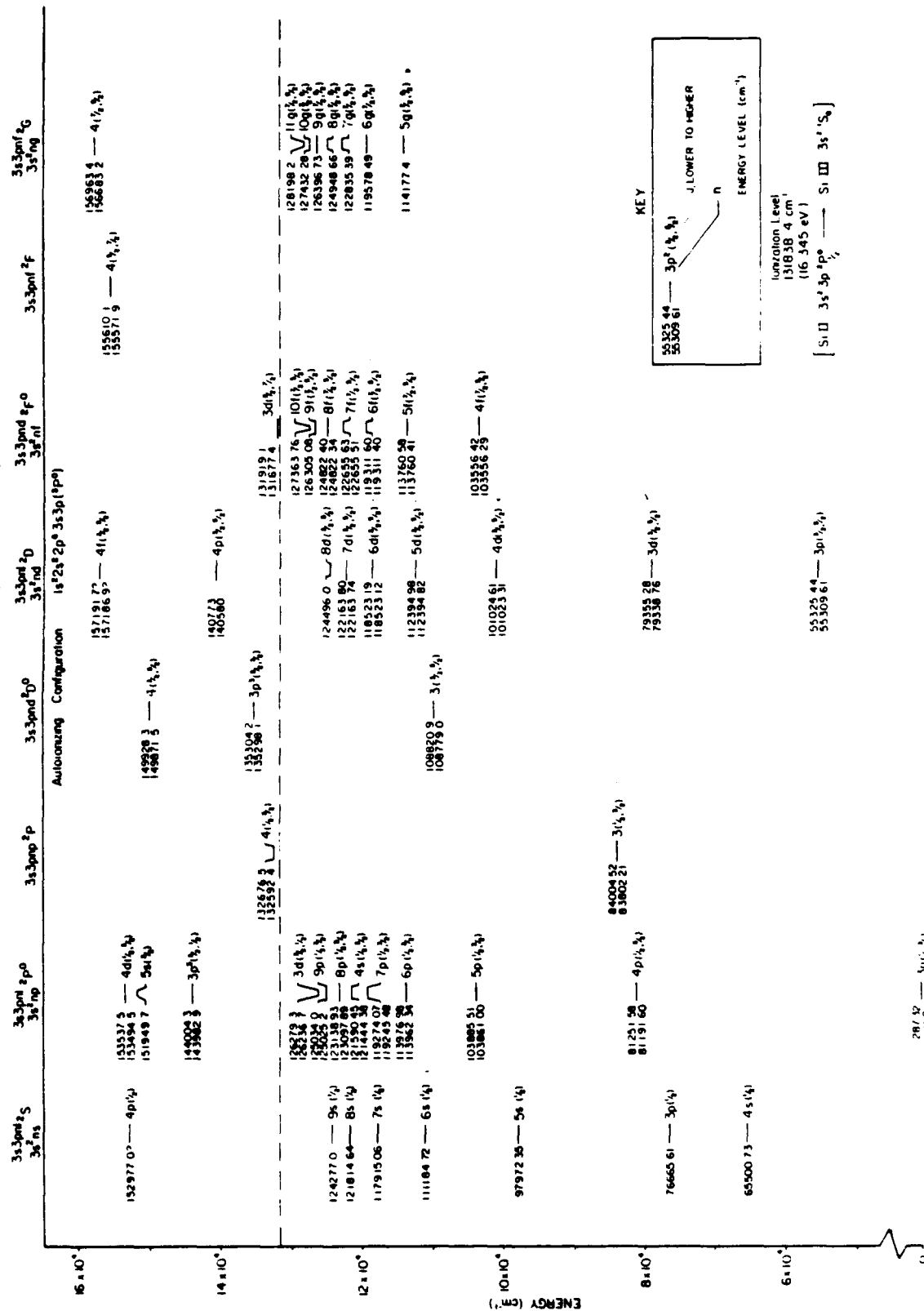


Figure 67. Energy levels for the Si II system (from Ref. 18).

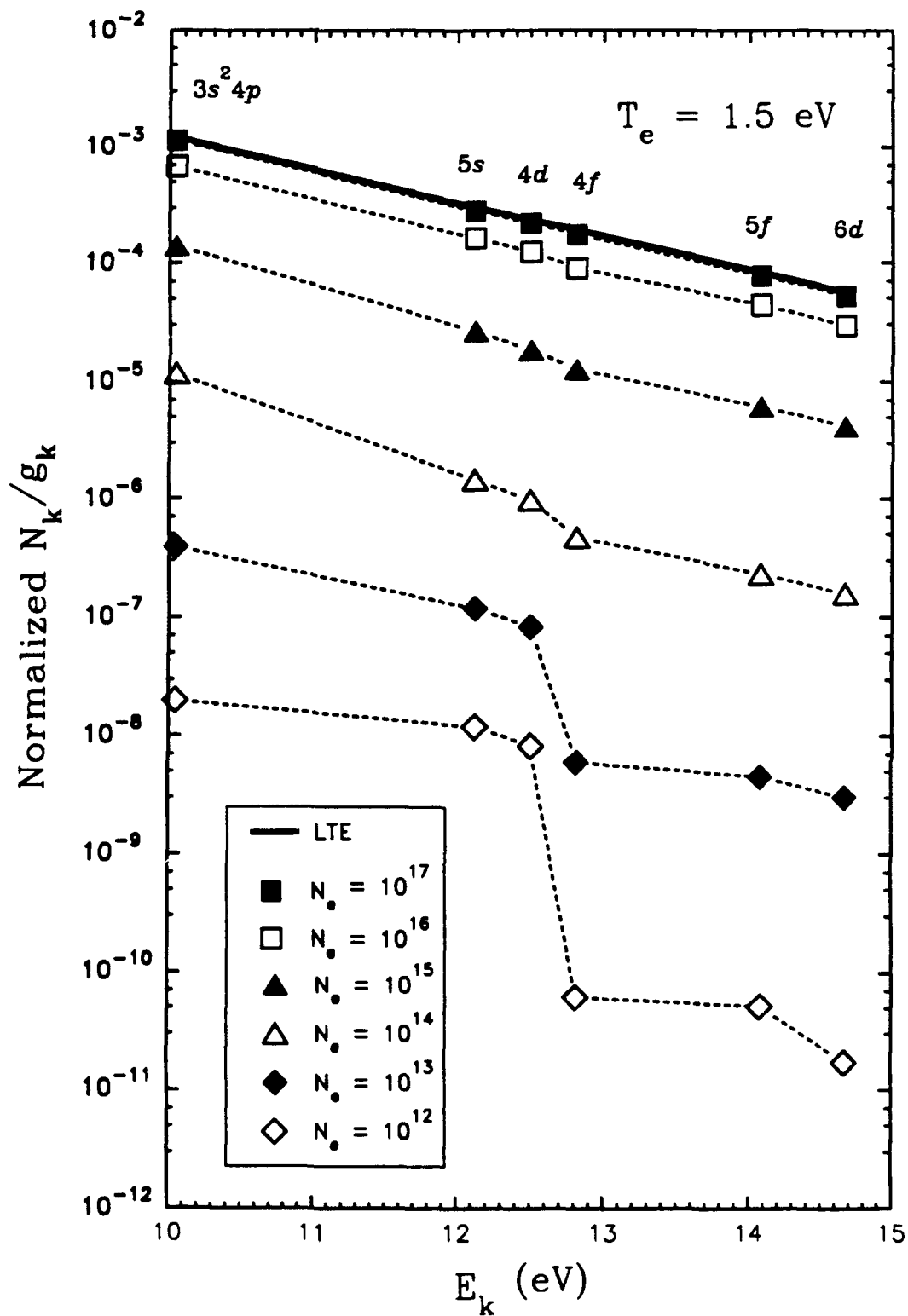


Figure 68. Boltzmann plot of CRE calculations for Si II at 5 eV.

The CRE model results for Si II and Si III was used to reanalyze the spectra from which the temperature history was determined (Fig. 66). From the Si III line ratios and Table 7, it was determined that the electron density is $\sim 10^{14} \text{ cm}^{-3}$ for most of the spectra. The electron temperature was then calculated from the ratio of intensities of the 4p-5s and 4s-4p multiplets and the CRE results from the tables in the Appendix. The results are plotted in Figure 69. A comparison with the LTE analysis of Figure 64 shows that the CRE temperatures are ~ 50 percent higher.

The value of having a model which takes into account the variation of excited state densities with electron density as well as temperature was seen more clearly by fitting several Si II line intensities to the CRE results. In this case, the reduced chi square values of the fits for various temperatures and densities were computed. The goodness of fit is indicated in Table 8, where the reduced chi square values for the various fitting parameters are tabulated. One can discern a distinct minimum for $N_e = 10^{15} \text{ cm}^{-3}$ and $T_e = 1.5 \text{ eV}$.

Table 8. Goodness of CRE fit to Si II line intensity data.

	1.2 eV	1.5 eV	2.0 eV
10^{13} cm^{-3}			1.96E-2
10^{14} cm^{-3}	6.32E-2	3.65E-2	1.03E-2
10^{15} cm^{-3}	2.46E-2	3.86E-3	3.02E-2
10^{16} cm^{-3}	8.33E-3	8.87E-3	
10^{17} cm^{-3}	6.90E-3		

Relative Abundance Estimates. Although an ionization equilibrium model cannot be invoked, one can make estimates of the relative ground state abundances of different species based on line intensities. For example, for Ar II, a relatively strong and spectrally isolated transition occurs at 6642 Å, with upper and lower states j and i , respectively. The intensity of this transition is compared with an observed strong Si II transition, say from state l to state k . Then, the ratio of Ar II ground state density to Si II ground state density is given by

$$\frac{N_0^{\text{Ar II}}}{N_0^{\text{Si II}}} = \left[\frac{(I/\eta A)_{ji}^{\text{Ar II}}}{(I/\eta A)_{lk}^{\text{Si II}}} \right] \left[\frac{(N_l/N_0)^{\text{Si II}}}{(N_j/N_0)^{\text{Ar II}}} \right] \quad (38)$$

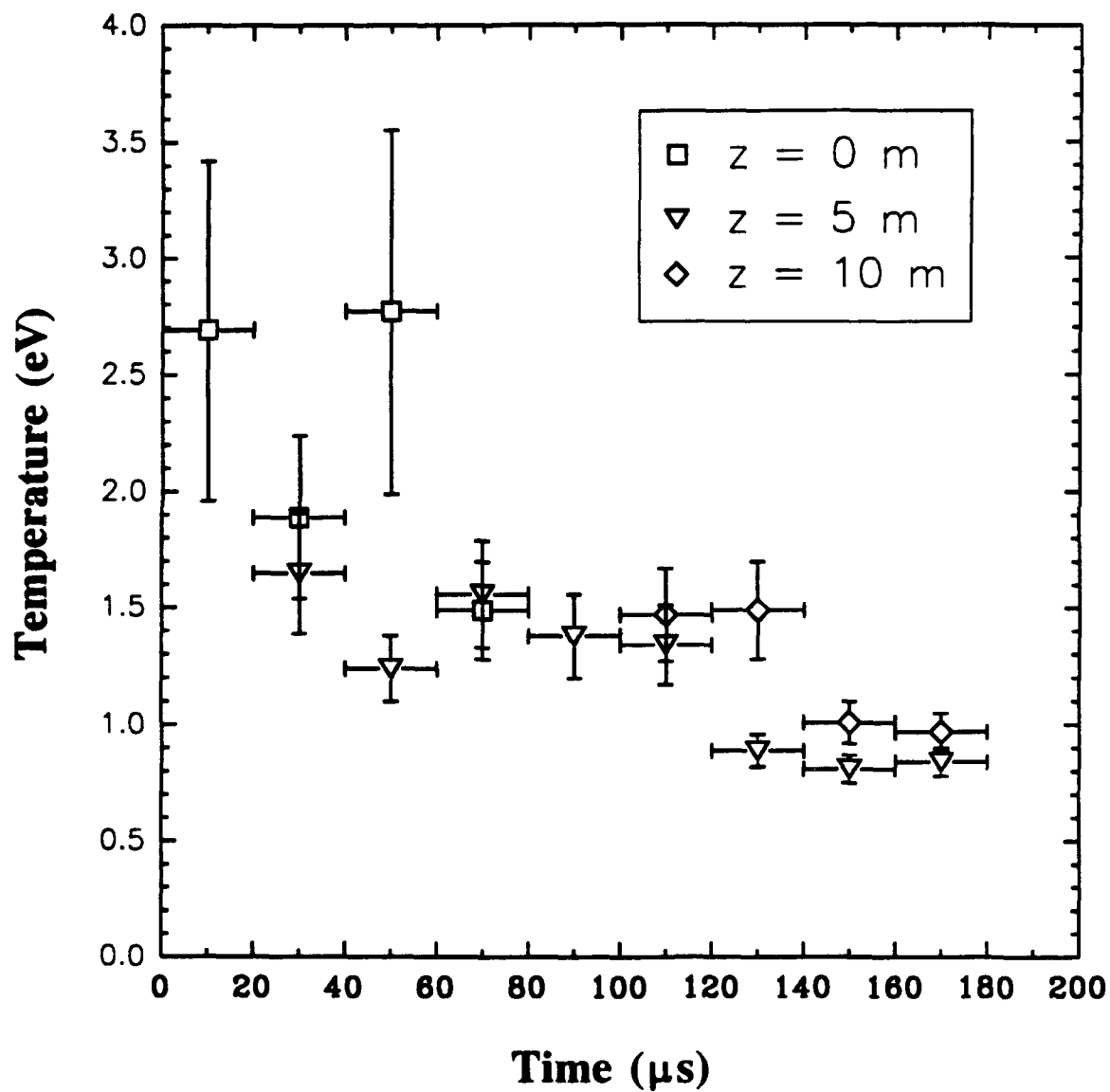


Figure 69. Temperature history from CRE model assuming $N_e = 10^{14} \text{ cm}^{-3}$.

The first factor on the right incorporates the overall detector response efficiency, η . The second factor is the relative population density of the upper state calculated from the CRE model. For Si II the 4s-4p transition was used at 6355 Å. Since the Ar II 6642 Å transition was never observed in any spectra, and the signal-to-noise ratio for the measurements was of order 10^3 , the relative abundance ratio was calculated based on a line intensity ratio of 10^{-3} . The results are shown in Table 9.

Table 9. Ratio of Ar II to Si II for line intensity ratio of 10^{-3} .

T_e (eV)	N_e (cm ⁻³)					
	10^{12}	10^{13}	10^{14}	10^{15}	10^{16}	10^{17}
0.5	9.0×10^6	6.8×10^6	5.3×10^6	3.4×10^6	1.4×10^6	5.1×10^5
0.7	7.1×10^4	3.5×10^4	2.5×10^4	1.6×10^4	7.0×10^3	2.4×10^3
1.0	2.5×10^3	7.7×10^2	4.5×10^2	2.8×10^2	1.3×10^2	4.4×10^1
1.2	7.4×10^2	1.8×10^2	9.5×10^1	5.5×10^1	2.7×10^1	9.3×10^0
1.5	2.2×10^2	4.5×10^1	2.0×10^1	1.1×10^1	5.5×10^0	2.0×10^0
2.0	6.7×10^1	1.2×10^1	4.3×10^0	2.1×10^0	1.1×10^0	4.1×10^{-1}
2.5	3.3×10^1	5.4×10^0	1.7×10^0	7.5×10^{-1}	4.2×10^{-1}	1.6×10^{-1}
3.0	2.1×10^1	3.2×10^0	9.0×10^{-1}	3.8×10^{-1}	2.2×10^{-1}	8.8×10^{-2}
4.0	1.2×10^1	1.7×10^0	4.2×10^{-1}	1.6×10^{-1}	9.8×10^{-2}	4.0×10^{-2}
5.0	8.3×10^0	1.2×10^0	2.6×10^{-1}	9.9×10^{-2}	6.1×10^{-2}	2.5×10^{-2}

One can see that for the temperatures and densities inferred from the previous analyses, the absence of the Ar II line could still correspond to relative abundances of Ar II greater than Si II by an order of magnitude or more. This conclusion is explained by the high excitation energies (nearly 20 eV) of the ionized Ar, compared to 10-12 eV for ionized Si. Other similar calculations were carried out for H I, O I, and Si III with respect to Si II. These calculations yielded relative abundances of $\sim 10^0$, 10^1 , and $>10^3$, respectively.

Based on the estimates of relative specie abundances, we can bracket Z_{eff} of the plasmas between 1 and 2. Similarly, the effective mass number of the plasma is ~ 30 .

Conclusions

For all experimental parameters, locations, and times, the optical spectra were dominated by line emission from Si. Silicon II (singly ionized) lines at 6355, 4130, 5051, and 5972 Å were consistently strongest. Silicon III lines were also evident, but generally at lower intensities. Next in prevalence was the neutral H H_α line at 6563 Å. Hydrogen was identified whether it was the working gas or not. Next in strength were neutral O lines, especially at 7773 Å. In some high-resolution spectra, low-intensity carbon II lines were seen. Although Ar was the working gas for most of the experiments, no Ar lines could be unambiguously identified.

The Si seen in the spectra was found to originate from the gun insulator, which was made from quartz (SiO_2), rather than the beam tube wall. When an alumina (Al_2O_3) insulator was substituted, the Si lines were replaced by Al lines. An independent test, in which an optical fiber probe was not allowed to see the inside of the beam tube wall, still showed an abundance of ionized Si.

The intensity of optical emissions at a given downstream position peaked in time after gun current rise. In general, the time-position relationship indicated the highest intensity portion of the plasma travelling at an axial speed of roughly 50-80 km/s. The fastest inferred speed of detectable emitting plasma was between 100 and 150 km/s. The optical intensity variations seen by the OMA were consistent with those seen by photodiode detectors, although in some cases the photodiodes also registered low-intensity precursors corresponding to somewhat higher speeds.

An LTE analysis was applied to a pair of Si line intensities to estimate electron temperature as a function of time and distance downstream. These analyses indicated a roughly monotonically decreasing temperature with time at any position, and peak temperature at the gun being slightly greater than downstream peak temperatures. The range of inferred temperatures was between 0.5 and 2.0 eV.

The LTE assumption, although simplifying analysis, is generally invalid. For some shots, the $H\ H_\beta$ line at 4861 Å was recorded. For these shots, significant line broadening was not observed, indicating an upper bound on electron density of $\sim 10^{15}\text{ cm}^{-3}$. This estimate is consistent with average densities inferred from interferometry. At such low densities, and temperatures of order 1 eV, LTE is not satisfied for most levels giving rise to optical line radiation.

To improve the estimates of plasma parameters based on line intensity ratios, a CRE analysis model was developed. This model was applied to Si II, and the results showed significant departure from LTE, for the states bearing the strongest line intensities, for densities of order 10^{14} - 10^{15} cm^{-3} and temperatures of order 1 eV. When applied to the Si III system, the model showed that a particular level population ratio ($3s4p^1P^\circ$ - $3s4p^3P^\circ$) was sensitive only to density. Spectra which showed lines from both states exhibited a density of slightly more than 10^{14} cm^{-3} .

The model, although preliminary, has been used to estimate the relative abundances of observed plasma species. It turns out that because of the higher excitation energies and lower transition probabilities of Ar II compared to Si II, the absence of Ar II lines in the spectra does not preclude its existence. The best that can be done is to estimate an upper bound on the ratio of Ar II to Si II of 100:1 for the nominal plasma temperature and density. At the same parameters, the equilibrium ionization state ratio (Ar II to Ar I) is $<10^{-2}$. A similar relative abundance calculation for A I has yet to be carried out. For Ar shots, the ratio of H I to Si II at 5 m was 1:1 within half an order of magnitude. Similarly, the ratio of O I to Si II at 5 m increased from ~4:1 at 30 μs to ~40:1 at 210 μs . The relative abundance of Si III with respect to Si II was also estimated. At 5 m, Si III was at least 4 orders of magnitude more prevalent than Si II early in time (30 μs) and dropped monotonically until no Si III was discernible after 130 μs (corresponding still to as much as 1000:1 doubly ionized to singly ionized). Taking into consideration the relative abundances of the species observed the effective charge was estimated to be between 1 and 2, and the effective mass to be ~30.

For shots late in the experimental series, with H as the working gas, the spectra still exhibited strong Si line radiation with no change in relative strength of H Balmer series lines. Ionized H emits only continuum radiation, so the relative abundance of ionized H could not be estimated. However, the H I to Si II, and the Si III to Si II ratios cited above are generally valid for H shots as well as Ar shots.

Based on the spectroscopic observations and analysis, it appears that insulator material was an important contribution to the gun plasma for virtually all operating conditions. It was noted that in the earliest studies by other investigators, clean operation of coaxial guns could not be achieved with breech gas injection (Ref. 8). Only when injection occurred through the center electrode, well away from the insulator, did successful operation result.

TARGET IMPACT RADIATION CALCULATIONS

INTRODUCTION

The physical state of a propagating plasma beam may be characterized by specifying the values of a number of physical attributes that it possesses. Of particular interest are its temperature, (mean translational) velocity, and density; and, in addition, if the beam resembles a finite length circular cylinder, its length and diameter. All of these properties may be measured experimentally in some manner; however, it may turn out, because of the large number of variables involved, that a particular experimental value of some quantity of interest is consistent with many different states of the beam. In such situations, it is frequently useful to perform computational simulations of the experiment in which all but one of the large number of variables referred to above are fixed and the variation of the particular quantity of interest, as the value of the remaining parameter (variable) varies, is studied. In this way, a particular experimentally measured value of the quantity of interest can be correlated with a particular value of this remaining parameter (at specified values of the other variables). It is in this context that calculations have been performed in conjunction with the experiments addressed in this report.

To be more specific, one of the experimental diagnostic techniques used for the series of experiments under consideration is the following: measure the radiation output resulting from the impact of an Ar plasma beam on an Al foil (or sheet) target; then use this measured radiation output to infer properties of interest of the beam. This inference is complicated by the fact that this radiation is a function of some combination of the beam's size (length [L] and diameter [D]), temperature (T), velocity (v), and density (ρ). In general, a given radiation output (to the precision to which it can be measured) may not correspond to a unique quintuple (L,D,T,v, ρ). However, if four of these five attributes are fixed, then one does expect to see a measurable variation in the radiation output as the fifth parameter varies, and one should then be able to correlate radiation output with the value of this fifth parameter. In particular, we studied the variation of radiation output resulting from beam impact on a 1-mm-thick Al target as a function of ρ , with all of the

other four parameters (L, D, T, v) remaining fixed at values representative of those obtained by experimental measurements. In this way, theoretically computed results were obtained for beam density versus radiation output and hence for beam density itself given an experimental value of radiation output.

THEORETICAL/COMPUTATIONAL ISSUES

The computational model of the target impact experiment is illustrated in Figure 70. A cylindrical Ar plasma of length L centimeter and diameter 10 cm and having equilibrium temperature 1 eV, speed v cm/ μ s, and density ρ g/cm³ impacts a 1-mm-thick, room temperature (0.025 eV) Al sheet, with velocity perpendicular to the sheet and L , v , and ρ assuming fixed values for each of five cases under study ($L = 10$ or 20, $v = 8$ or 100, $\rho = 6.63 \times 10^{-10}$ to 6.63×10^{-7} , corresponding to number densities of 10^{13} to 10^{16} cm⁻³); the radiation output from this interaction is then ascertained.

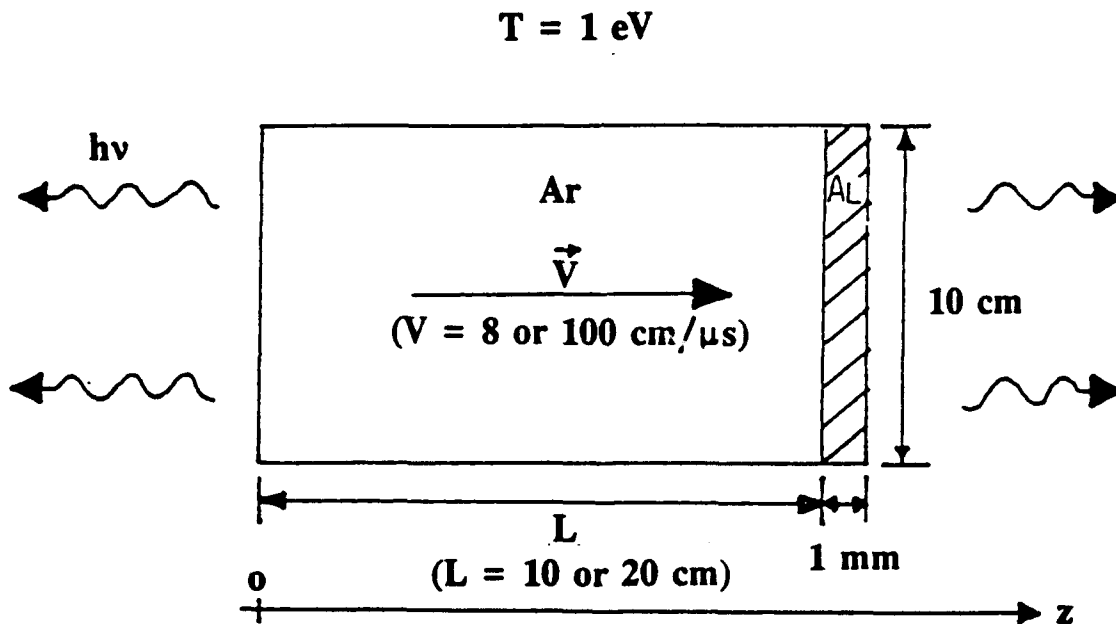


Figure 70. The computational model.

The above description is far from complete; there are many details involved, and while it would not be warranted here to go into them in great depth, some discussion is appropriate. These issues are discussed in the remainder of this section.

The gross classification of the computational tool (the LASNEX code) used for the calculations is: one-dimensional (1-D), three-temperature (3-T) radiation hydrodynamics (hydro) using Lagrangian hydro, S_{M} radiation transport, tabular equation-of-state data (SESAME), and analytic/tabular opacities (XSN/cold opacity tables). There are other radiation hydrodynamics codes for which the descriptors are different from those above. The adequacy (or inadequacy) of the particular choices with respect to the experiment being modelled are discussed below.

Geometry

The choice was made to use a 1-D slab geometry. This means the hydrodynamic quantities $q(x,t)$ (x is spatial position, t is time) depend only upon the z coordinate (the z axis being the axis of symmetry of the problem) and the radiation intensity $I(x,v,\Omega)$ (v is the radiation frequency, Ω is the unit vector specifying direction) depends only upon z and upon the angle that Ω makes with the z axis (i.e., only upon $\mu = \Omega \cdot k$ where k is the unit vector in the z direction). The choice of 1-D geometry was made because, even though precise modelling of the experimental measurements requires a 2-D calculation (the radiation was measured at -90 deg to the z axis, at the z location of the A1 sheet), 1-D calculations are much less expensive to perform than 2-D ones and one can learn from 1-D if 2-D calculations are worth doing (e.g., one can learn if there is sufficient variation of radiation output with variation of beam density). In fact, the 1-D calculations indicate that 2-D calculations are worth doing (see subsection on Methodology and Results); and if this investigation had been pursued further, these calculations would have been done.

The shortcoming of a 1-D calculation vis-a-vis the present experiment is, computationally, no radiation is allowed to leak from the sides of the cylindrical plasma (which is where the measurements were done). The reason why this is so, is as follows (Fig. 71). Suppose some radiation were allowed to leak out the side, say at point A; i.e., $I(z_A, v, \mu) > 0$. Then, if point B has the same z coordinate as point A, we must have by the 1-D assumption that $I(z_B, v, \mu) = I(z_A, v, \mu)$ so that $I(z_B, v, \mu) > 0$. But this means radiation enters

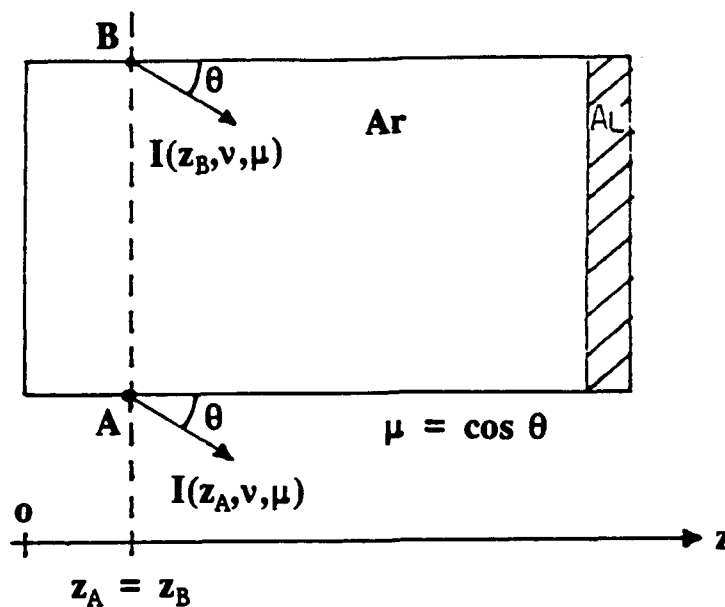


Figure 71. Radiation leakage in a 1-D calculation.

the problem from the exterior of the plasma at point B, which is a contradiction. Therefore $I(z_A, \nu, \mu)$ must be 0, i.e., no radiation can leak out the side at point A. But A is an arbitrary boundary point. On the other hand, the 1-D calculation gives an indication of the total radiation leaking from the 2-D problem and so gives an upper bound on the radiation that should be seen off to the side.

Local Thermodynamic Equilibrium

A 3-T treatment of radiation hydrodynamics was used, and a discussion of the issues associated with this choice follows.

A 1-T treatment of radiation hydrodynamics implicitly assumes all species of particles (material and photons) present in the problem are in LTE at one and the same locally dependent temperature (so Maxwellian, Boltzmannian, Sahaian, and Planckian distributions, each at that temperature, obtain). For this assumption to be valid, it is necessary (but not sufficient) that the collisional and radiative interactions involved (which are the mediators of the tendency toward equilibrium) have relaxation time scales much shorter than the time span of interest in the situation under study. If such is not the case,

then deviations from LTE are significant and a 1-T code cannot correctly handle the physics of the problem.

A first level of deviation from LTE behavior (so-called non-LTE behavior) can be considered to be one in which each material particle species is locally in self-equilibrium, so each such species can be described locally by a single (self-equilibrium) temperature; but the self-temperatures of the different species are different from each other. In addition, a local temperature is ascribed to the radiation field according to $E = a_r T$, where E is the local radiation energy density and a_r is the usual radiation constant; but note that there is no assumption here that the radiation field is locally Planckian. For a plasma consisting of electrons, ions, and photons, this model entails three temperatures and a code which takes this into account (by using three separate energy evolution equations) is called 3-T. The next level of deviation from LTE behavior can be considered to be one in which the particle species are not even in self-equilibrium and so the plasma is not even accurately described by a collection of self-temperatures. In this case, kinetic rate equations for the time-dependent distributions of the electron level populations in the various material species must be coupled to the equation of radiative transfer, which governs the time evolution of the radiation field, and the whole system solved simultaneously to produce a correct treatment of the physics.

The reason for including the above discussion is that the problem under consideration is in the non-LTE regime so some version of a non-LTE treatment is required. But which one? The code used has both 3-T and kinetic rate equation treatments. Thus, a particular set of parameters was selected for the general problem for which the deviation from LTE was expected to be most severe and this set was run using both treatments. The results were essentially identical. Therefore it was concluded that the 3-T treatment was adequate and, since it is less expensive to run, this is the choice made to run all of the cases.

Hydrodynamics

This section discusses some of the hydrodynamic issues related to the calculations. The reader may well wonder why hydrodynamics should be an issue in a

calculation in which only the radiation output is of real interest. The answer is the radiation and the hydro are coupled, i.e., they influence each other. More specifically, in this situation the radiation momentum and energy densities are comparable to those of the material fluid and so contribute to the momentum and energy equations of motion of the fluid, thus significantly influencing its flow. Reciprocally, the specifics of the flow determine the local values of fluid thermodynamic parameters (e.g., v and T) upon which the opacities that govern the transport of radiation depend.

The hydrodynamics used for the calculations was Lagrangian. This implies the grid associated with the fluid for the purposes of numerical computation of the flow moves along with the fluid mass and contrasts with Eulerian hydro, in which the grid remains stationary during the flow, and with adaptive hydro, in which the grid moves ("adapts") with the fluid (not necessarily with the fluid mass but, possibly with some other feature of the fluid, e.g., pressure gradient). The advantage of moving grid techniques is they put more grid lines "where the action is" and therefore allow more numerical accuracy than would otherwise be practical in those regions. For the type of problem under study, one in which mass, momentum, and energy gradients are very large in certain regions of the problem, Lagrangian or adaptive hydro are the techniques of choice; since the code (which was chosen based on its composite of features) is well-tested only for Lagrangian hydro, that is what was used.

Lagrangian hydro imposes a requirement on grid selection which heavily influences the spatial resolution of our solution. It turns out that in Lagrangian hydro, the masses of neighboring grid cells need to be comparable (i.e., no different from each other than a factor of about 2) to get meaningful results. (This is because in the numerical computations, averages of properties of neighboring cells are formed and if the mass of one of the neighbors is significantly different from that of the other, then one cell unduly dominates the average and this leads to erroneous inferences.) In our problem, the juxtaposition of a tenuous Ar plasma had to be considered, in the density range of roughly 5×10^{-7} to 5×10^{-10} g/cm³, with a relatively much more massive Al sheet with density 2.7 g/cm³. This leads to density ratios for the two neighboring cells across the Ar-Al interface (Fig. 70) of $\sim 5 \times 10^6$ to 5×10^9 (Al to Ar) so these two cells on either side of the interface must

have width ratios of at most 4×10^{-7} to 4×10^{-10} (Al to Ar) for a mass ratio ≤ 2 . Thus, if the interface Ar cell is 1 cm wide then the interface Al cell must be 4×10^{-7} to 4×10^{-10} cm wide. Cells of such small width pose two problems: (1) Since atomic dimensions are on the order of 10^{-8} cm, it is not clear that cells of such width have enough (physical) particles in them for a hydrodynamic approximation to be valid. It is also not clear that it makes sense to ascribe macroscopic properties (e.g., density, opacity, and heat capacity) to such cells: (2) Numerically, the Courant condition associated with cells of such small width is such as to make the allowable time steps in time marching of the hydro evolution equations extremely small and hence to make a numerical computation extremely time consuming (the hydro used in this code is explicit). Making Ar cells much smaller than about 1 cm only exacerbates the above problems. So the spatial resolution in the Ar region is limited initially (i.e., at problem time zero) to about 1 cm (in fact, the width was chosen to be about 0.5 cm). As the flow evolves, these Ar cells become much narrower and thus spatial resolution is enhanced. Note also the spatial resolution in the Al is much finer: the 1-mm Al width must be divided into 25-30 cells to get neighboring mass ratios ≤ 2 .

The choice of grid spacing was one of compromises. It was chosen to ignore the possible physical deficiencies alluded to in (1) above in favor of the numerical mass ratio requirement. Also, the Courant condition timestep limitation alluded to in (2) above was mitigated to some extent by subcycling many times through the hydrodynamic part of the calculation during each computational main cycle.

One final issue that needs to be addressed is as follows. While those choices which qualify the nature of the hydrodynamic aspects of the calculations have been explained to some extent, an even more basic choice has not been explained: why hydrodynamics at all, as opposed to a kinetic type calculation? In other words, are the basic assumptions required for the validity of the hydrodynamic approximation valid in our situation? The answer is yes and no; that is, the answer is yes for the slow beam cases and no for the fast beam cases. This is explained further.

The reader will recall the calculations are two-fluid ones, with the electron fluid assumed to be in LTE with local temperature T_e and the ion fluid assumed to be in LTE with local temperature T_i , with $T_e \neq T_i$ in general at any given location. The implication is both the electron-electron (e-e) collision times and the ion-ion (i-i) collision times are very short compared to problem time scales of interest; therefore, on this latter time scale each fluid is in effect always in self-equilibrium. For the slow beam, essentially all radiation is emitted from the interaction region in about 2 μ s, while e-e collision times are never greater than about 30 ps in the Ar or Al vapor (variations are both spatial and temporal) and i-i collision times are essentially never $>0.1 \mu$ s there, so the criteria are well-satisfied for the electron fluid and very marginally satisfied for the ion fluid. On the other hand, for the fast beam, essentially all radiation is emitted from the interaction region in about 200 ns, while e-e collision times may get as large as 125 ns in the Ar and 2 μ s in the Al vapor; and the i-i collision times may get as large as 90 μ s in the Ar and 45 μ s in the Al vapor. In this case, the criteria are grossly violated in both the electron and ion fluids. The basic reason for these differences in the two cases is collision times are proportional to $T^{3/2}/n$ (where n is species number density) and the fast beam has lower particle densities and produces much higher interaction temperatures than the slow beam.

One may well ask: If hydrodynamic calculations for the fast beam are invalid, why were they done? The answer is that it was not absolutely clear the calculations would be invalid (i.e., the temperatures would be so high and the densities would be so low) before the computations were done, although a simple calculation predicts the "temperature" in the hot Ar stagnation layer to be approximately

$$T = v^2/2C_v = 0.347 [A/(Z + 1)] v^2 \text{ (eV)} \approx 7 \text{ keV} \quad (39)$$

where v is beam velocity in centimeters per microseconds, C_v is heat capacity, A is mass number, and Z is atomic number. However, the computations having been done, it was worthwhile to discuss them and present the results, as long as they exist, along with the appropriate disclaimers.

Radiation

We ultimately chose to use an S_5 discrete ordinate treatment of radiation transport. This choice immediately raises two questions: why transport (as opposed to diffusion) and why S_5 (as opposed to, say, S_3 or S_7 ; or P_N or Monte Carlo)?

The answer to the first question is as follows. It is certainly true that a diffusion treatment of radiation is less intricate--and less expensive to run--than a transport treatment and is certainly adequate for radiation in the diffusion regime. However, the present problem under study is not one in the diffusion regime. A particular set of parameters for the general problem was selected and the set was run using both a diffusion treatment and an S_N treatment, with $S = 3, 5$, and 7 . The diffusion results differed significantly from even those of the S_3 calculation (the least accurate of the S_N 's [S_1 is just diffusion and is not regarded as real S_N]); so the diffusion treatment was discarded for the general problem. Further, there was a significant variation in results from $N = 3$ to $N = 5$ but not much variation from $N = 5$ to $N = 7$; so $N = 5$ (being less costly than $N = 7$) was chosen. To complete the answer to the second question, it is pointed out that a possible extension of these calculations to 2-D was anticipated and the code has both a 1-D and a 2-D S_N treatment; on the other hand, P_N is only a 1-D technique. Lastly, Monte Carlo is much more expensive to run than S_N and the nature of the problem (simple geometry) did not warrant use of the former. Thus, S_5 was chosen.

At this point, some comments concerning the choice of opacities for the radiation transport are in order. The opacities used were the standard ones provided for in our code. These come from an analytic formula (so-called XSN opacities) for photon energies >20 eV and from tables (so-called cold opacity tables) for photon energies <20 eV. In general, cold opacity data (below, say, 10 eV) are not known with a high degree of confidence, so these tabular data suffer from the same defect; but they are generally available. In this situation it turns out that no more than 25 percent (and often significantly less) of the radiation output is at or below 10 eV. Additionally, since the same opacities were used consistently for all of the calculations, the relative results from case to case should be correct.

Finally, it should be noted that some calculations were performed using another set of opacities to get a feeling for the magnitude of the variations that might be expected as a result of changing opacities. The results are these: the total output radiation was essentially the same when using either set of the differing opacities, with reasonable agreement of spectral shapes >10 eV; spectral shapes <10 eV differed significantly (sometimes differing by orders of magnitude at a given energy <1 eV). However, since the experiments measured output radiation in the 10-50 eV range, it was felt that the differences in opacities in the two opacity sets are not important from our point of view.

Other Issues

Having pointed out in some detail what was done, some of the apparent limitations embodied in the computational model are discussed next.

Target Modelling. The gas-dynamic model of the Al target which was used is not the correct one if one is interested in the dynamics of the target during impact (with a view towards target failure). The target is a solid and should be treated (at least approximately) with elastic-plastic hydrodynamics incorporating material strength and spallation effects. However, the time scale of these effects is somewhat longer (many microseconds) than the time interval during which significant radiation emission occurs, so our gas-dynamic model of the target (which, incidentally, does take into account phase transitions, i.e., melt and vaporization which are important for the radiation calculation since they affect temperature) is adequate. This apparent modelling limitation is then of no concern here.

Interface Physics. Computationally, the mode of energy transfer from the plasma beam to the target is thermal conduction and radiative transfer from the extremely hot stagnation layer adjacent to the front face of the Al sheet to the relatively cooler Al itself. In fact (i.e., physically), penetration of the Al by beam electrons and ions, and subsequent deposition of their kinetic energy at the surface, plays a role in this energy transfer process. This feature is not taken into account in the modelling process and nothing has been done to estimate the relative magnitude of this effect; however, it

is expected to be unimportant in those beam density regimes where hydrodynamics are valid. The impact here would be to modify the time-dependent temperature profile at the Ar-Al interface and, thus, also the radiation output.

Magnetic Fields. Although the Ar plasma beam contains embedded magnetic field, the calculations were performed without considering such field. In principle, this field has two macroscopic effects: (1) it causes the beam radius to be smaller than it would otherwise be without the field present; and (2) it adds some rigidity to the beam by enhancing its hydrodynamic pressure with so-called magnetic pressure (given by $B^2/2\mu_0$ [MKS]). Concerning the first point, the beam radius used in the model was inferred from experimental measurements and so already reflected the beam pinching effect of the magnetic field. Concerning the second point, beam measurements also revealed a beam current (in the z direction), I_z , of about 1 kA. This implies a magnetic field of magnitude $B_\theta = \mu_0 I_z r / 2\pi r_0^2$ (MKS) inside the beam (of radius r_0) at a radial distance r from the beam axis of symmetry, and a maximum field anywhere inside the beam of $B_{\theta, \max} = \mu_0 I_z / 2\pi r_0$. For $r_0 = 5$ cm, this gives $B_{\theta, \max} = 0.004$ T and a magnetic pressure of 6.4 Pa. Since the hydrodynamic pressures in the interaction region of the beam are at least 10^7 Pa, the magnetic pressure contribution is negligible.

METHODOLOGY AND RESULTS

As indicated at the beginning of the section on Theoretical/Computation Issues, five cases were studied: three for slow beams ($v = 8$ cm/ μ s) and two for fast beams ($v = 100$ cm/ μ s). These cases are specified in more detail in Table 10. The parameters chosen for the computations were those dictated by the experimental measurements. The beam length of 10 cm was appropriate to the actual fast beam situation, but such was not the case for the slow beam, it being on the order of 1 m long. However, modelling a 1-m beam is computationally cost prohibitive (computer time required scaling directly with beam length) so for the slow beam $L = 10$ cm and $L = 20$ cm were studied to ascertain the affect of beam length variation on radiation output.

The desired output from the calculations is luminosity, which is the fraction of initial total beam energy radiated away as a result of target interaction,

Table 10. Cases studied.

Case					
	I	II	III	IV	V
v (cm/ μ s)	8	8	8	100	100
n (cm ⁻³)	10^{16}	10^{16}	10^{15}	10^{14}	10^{13}
ρ (g/cm ³)	6.63×10^{-7}	6.63×10^{-7}	6.63×10^{-8}	6.63×10^{-9}	6.63×10^{-10}
L (cm)	10	20	10	10	10
$E_{\text{beam}}^{\text{initial}}$ (kJ)	1.634	3.310	0.159	2.450	0.254

in broad spectral ranges. To ensure the interaction was observed for a long enough time (i.e., the calculation was run for a long enough time) to allow essentially all radiation that was going to escape to actually do so, the radiation output fraction was tabulated as a function of time. The initial guess was the problem should be run 50 percent longer than the unimpeded beam run-in time, which run-in time is 100 ns for the fast beam and 1.25 μ s (2.50 μ s, respectively) for the 10-cm (20-cm, respectively) slow beam. Table 11 shows this is quite accurate for both slow and fast beams. Since the fast beam cases were not run as long as they might have been (another 20-50 ns would have sufficed), the fast beam results were extrapolated to 88.3 percent total luminosity in case IV and to 16.6 percent total luminosity in case V. The luminosities in several broad spectral ranges for cases I through V are given in Table 12.

Several features of these data are discussed. Firstly, concerning the beam length effect, one can see that for the 10^{16} cm⁻³, 8 cm/ μ s slow beam (cases I and II), doubling the beam length increases the total luminosity by only $(6.1/43.3) \times 100 = 14$ percent. Even more relevant for us, the luminosity in the 10- to 56-eV energy range increases by only $(1.8/34.8) \times 100 = 5$ percent upon doubling the beam length. This can be attributed to the fact that, for longer beams, the rear portion of the beam never gets to interact very strongly (if at all) with the Al target because this portion is repelled by the hot rebounding front portion of the beam which has already interacted with the target. Based on the above result, it is expected a further doubling of the

Table 11. Luminosity as a function of time.

Radiated Energy (% of $E_{\text{beam}}^{\text{initial}}$) for Case:					
Time (μs)	I	II	III	IV	V
1.250	41.7	18.1			
1.375	42.8	20.5	30.8		
1.500	43.1	23.1	31.5		
1.625	43.2	25.7	31.8		
1.750	43.3	28.4	32.0		
1.875	43.3	31.3	32.1		
2.000		34.5			
2.250		41.5			
2.500		47.6			
2.750		48.9			
3.000		49.2			
3.250		49.3			
3.500		49.3			
3.625		49.4			
3.760		49.4			
Time (ns)					
100				59.6	6.2
110				72.3	9.6
120				78.4	12.1
130				82.2	13.9
140				84.2	15.1
150				85.3	15.8
160				86.1	16.2
170				86.7	16.4
180				87.2	16.5
				(88.3)	(16.6)

Table 12. Luminosities for various broad spectral ranges.

Radiation Energy (% of $E_{\text{beam}}^{\text{initial}}$) for Case:					
Photon Energy Range (eV)	I	II	III	IV	V
0 - ∞ (total)	43.3	49.4	32.1	87.2	16.5
				(88.3) ^a	(16.6) ^a
1.00 - 1.78	0.092	0.21	0.094	0.039	0.023
1.78 - 5.62	2.0	3.62	2.15	1.26	0.62
5.62 - 10.0	4.85	7.37	5.25	3.90	1.72
10.0 - 56.2	34.8	36.6	24.4	46.9	13.75
≥ 56.2	1.53	1.54	0.18	35.0	0.36

^aExtrapolated value (see Table 11)

beam length from 20 to 40 cm would produce almost no increase in the luminosity. So calculations with 10-cm beams should give luminosities (at least in the 10- to 56-eV range) that are within 5 percent of those for 1-m beams.

Secondly, there is a significant decrease in luminosity associated with an order of magnitude decrease in density (from 10^{16} to 10^{15} for the slow cases [I and III] and from 10^{14} to 10^{13} for the fast cases) for 10-cm beams (and thus, in the slow case, for 1-m beams). So luminosity differences should be a reliable indicator of density differences. On the other hand, while there is high confidence in the calculated values of the luminosity for the slow beams, there is uncertainty in the calculated values of the luminosity for the fast beams as discussed at length earlier; we do believe, however, the trend of rapidly decreasing luminosity with decreasing beam density for fast beams.

Finally, note that while all of the Ar gas serves as a source of radiation, only a thin hot layer of Al (on the order of 0.1-mm-thick) serves as such a source. For the slow beams, the radiation temperature in the Ar and in the Al vapor are similar; but for the fast beams, the radiation temperature in the thin Al layer rapidly (within 10 ns) becomes and stays about 30 percent hotter than that in the Ar for the duration of significant radiation emission.

MAGNETOHYDRODYNAMIC SIMULATIONS OF GRC/CHENG DEFLAGRATION GUN

INTRODUCTION

Computer simulations of the GRC deflagration gun have been performed to develop a general understanding of the operation of the gun and the propagation of plasma in the drift tube. The simulations solve the single-fluid MHD equations in the appropriate geometries. The magnetic boundary condition at the breech is determined by solving circuit equations that are coupled to the problem. The initial mass distribution is taken from a separate calculation that models neutral gas flowing into the gun from the valve that is behind the breech. The MHD simulations demonstrate the deflagration process within the gun, but they do not model the ablation of insulator material. They show nonnegligible magnetic field being carried with the plasma. As it spills into the drift tube, this magnetic field pushes plasma to the glass wall of the tube, and it focuses a column off the end of the inner conductor. Confinement of this column is clearly due to the magnetic field.

MHD THEORY AND DEFLAGRATION

An MHD treatment of a plasma considers it to be a single fluid even though it contains positively charged ions, negative electrons, and neutral atoms. The approximations that are made in deriving the MHD equations are formally valid when the collection of particles is neutral on the length scales of interest, the gyroradii of the particles' motion about the magnetic field lines are small compared to the dimensions of the problem, and the period of the particles' rotation is small compared to the duration of phenomena in the problem. Also, the particles are assumed to have a Maxwellian velocity distribution. Collisions and gyration about the magnetic field lines tend to make the distributions Maxwellian.

The derivation of the MHD equations starts by taking velocity moments of the kinetic equations for the ion and electron species to produce fluid equations for each. Using the quasi-neutrality assumption, the mass and momentum equations are combined to give the set of single-fluid equations (Ref. 19). Conservation of mass is expressed by the continuity equation,

$$\frac{\partial \rho}{\partial t} + \nabla \cdot (\rho \bar{\mathbf{v}}) = 0 \quad (40)$$

where ρ is the mass density, and $\bar{\mathbf{v}}$ is the fluid velocity. The momentum conservation equation is

$$\rho \frac{\partial \bar{\mathbf{v}}}{\partial t} + \rho (\bar{\mathbf{v}} \cdot \nabla) \bar{\mathbf{v}} = -\nabla P + \bar{\mathbf{J}} \times \bar{\mathbf{B}} \quad (41)$$

The pressure, P , is a scalar when the velocity distribution is Maxwellian. The last term on the right side of the equation represents the force due to the magnetic field; $\bar{\mathbf{J}}$ is the current density, and $\bar{\mathbf{B}}$ is the magnetic induction.

Maxwell's Equations are used to solve for the time-dependent development of the magnetic field. The displacement current is taken to be negligible (Ref. 20) and is omitted from Ampere's Law. The Generalized Ohm's Law is used to determine the electric field. It comes from multiplying each of the species fluid equations--from which the momentum equation is derived--by the species charge, dividing by the species mass, and then adding the two. Some of the resulting terms are much more significant than others in laboratory plasmas, and the most common simplification is

$$\bar{\mathbf{E}} = -\nabla \times \bar{\mathbf{B}} + \eta \bar{\mathbf{J}} \quad (42)$$

where $\bar{\mathbf{E}}$ is the electric field and η is the plasma resistivity. The first term on the right side by itself would describe a perfectly conducting fluid where magnetic field is frozen to the fluid. The second term accounts for the diffusive behavior that results from electron-ion collisions. Besides these two, the Hall term, $(\bar{\mathbf{J}} \times \bar{\mathbf{B}})/en$ with e the elementary unit of charge and n the electron number density, may also be important. When collisions are not frequent, it accounts for the separation of the electron fluid motion from the ion fluid motion.

The internal energy must also be considered. It is easiest to list the processes that affect it. Ohmic heating is a source from the magnetic field diffusion. Compressive work, radiative transport, thermal conduction, and

viscous work also affect the internal energy. Finally, an equation of state based on internal energy and density determines the scalar pressure.

One of many possible behaviors of an MHD fluid is deflagration. This is true even for a highly simplified set of equations in one dimension. Figure 72 illustrates the behavior. Fluid enters from the left with high density, high

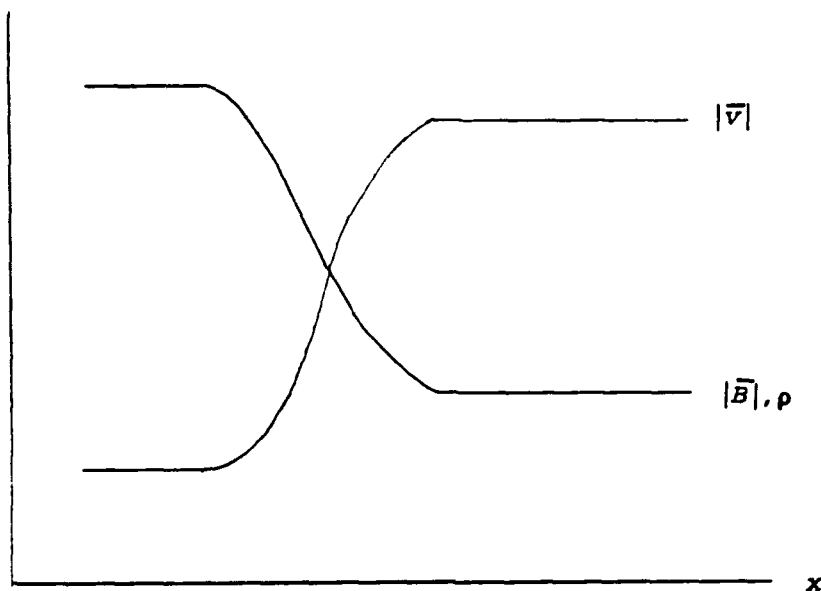


Figure 72. One-dimensional MHD deflagration.

magnetic field, and low velocity. Positive velocity is to the right, and the magnetic field is perpendicular to the velocity. There is a current discharge in the middle that reduces the magnetic field while accelerating the fluid. The fluid leaves on the right with a reduced density, magnetic field and an increased velocity. That, simply, is an MHD deflagration.

BREAKDOWN

The GRC deflagration gun does not use a switch in the circuit. Instead, while the gun and drift tube are under vacuum, the capacitor is charged placing a potential across the gun electrodes. The plenum valve is opened and breakdown occurs spontaneously when gas enters the gun. Although there are many ionization mechanisms, the breakdown in the gun starts with Townsend or avalanche ionization (Ref. 21). Stray electrons are accelerated by the

electric field and collide with neutral gas atoms causing them to ionize, making more electrons available. This process grows in an exponential fashion allowing the gas to conduct current.

To get the initial conditions for the breakdown process, and for the rest of the simulation, gas inflow and electrostatic calculations have been performed. The gas calculations were run on the 2-D MHD code, MACH2, developed by Mission Research Corporation (MRC), Albuquerque, New Mexico under contract by the WL. A number of simplifications were used. Viscosity and thermal conduction are neglected. Also, there is a set of 3-D holes in the inner conductor of the real gun through which the gas must flow to enter the barrel. These have been idealized in the calculation as a 2-D opening. Figure 73 is the computation mesh for the gas calculation and represents the evacuated region from the valve at the bottom to the muzzle of the gun at the top. The center-line on the left of the mesh is in the axial direction.

The valve is a solenoid armature and moves away from the gun barrel when current is passed through its coil. This opens a gap allowing gas to flow radially inward at the bottom of the evacuated region. The opening time has been estimated at 40 μ s. This has been simulated by putting a flow-through boundary condition at the appropriate location and ramping the density linearly from nothing to a steady state at 40 μ s. The steady-state conditions are based on density and temperature relations for 1-D converging nozzles. With a 45-psia plenum at room temperature, the H nozzle conditions are 0.16-kg/m³ density and 0.022-eV temperature at its local sound speed of 1.2 km/s; the velocity of the gas at the flow-through boundary is directed radially inward.

The gas from the boundary crashes on axis then expands upward into the evacuated gun. At the time that breakdown spontaneously occurs, experiments with H show a 60- μ s delay from the time the valve is actuated, the gas is continuing to expand upward, but there is not much mass in the gun itself (Figs. 74 and 75). Only 23 μ g are above the breech, and most of that is near the inner conductor.

DEFLAGRATION GUN (GAS INFLOW) 83

IDEAL MESH

1ST X = 0.00E+00
 X INC = 1.00E-02
 1ST Y = 0.00E+00
 Y INC = 5.00E-02

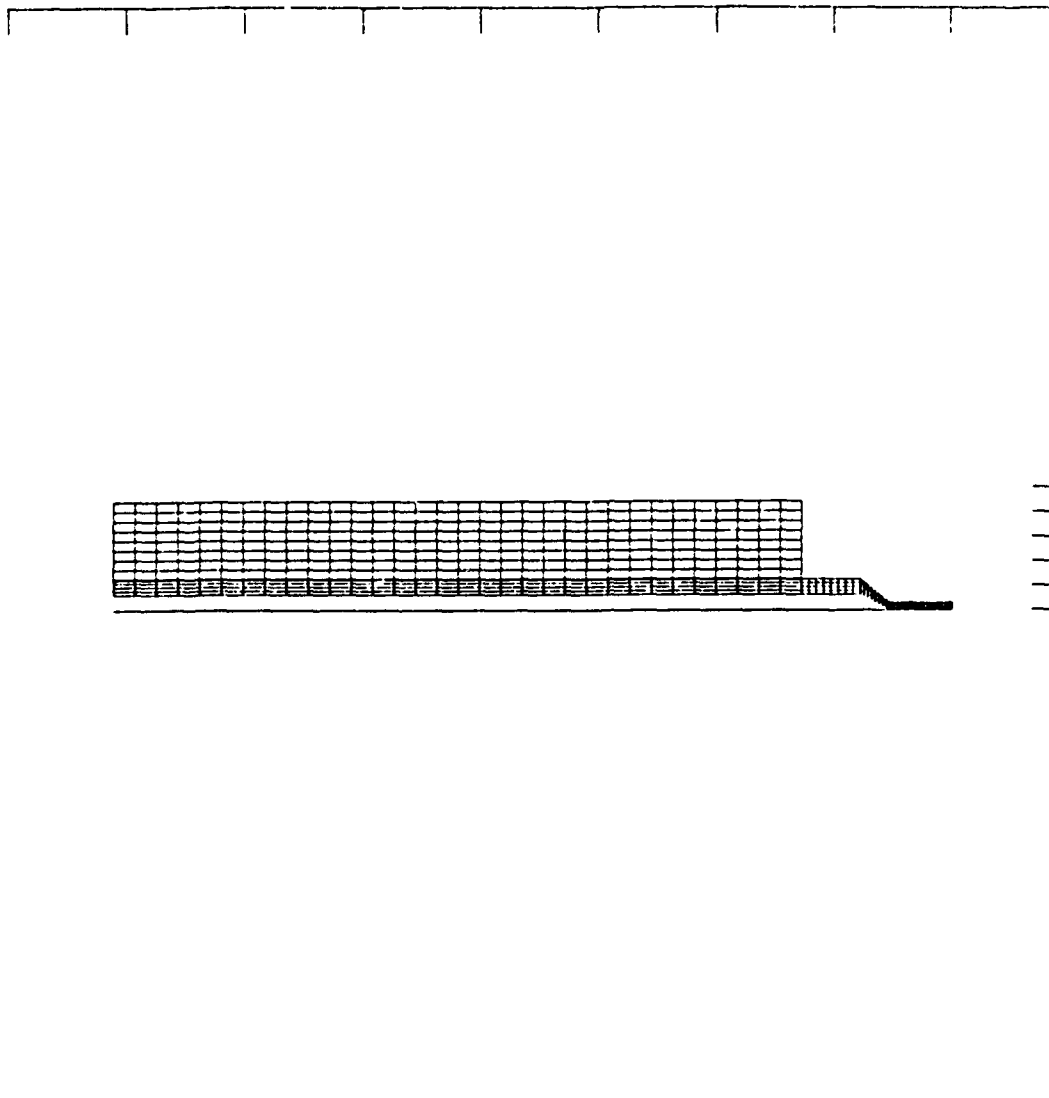


Figure 73. Computation mesh for the neutral gas calculation.

DEFLAGRATION GUN (GAS INFLOW) 83
T = 6.008E-05 CYCLE = 823
DENSITY

-- 6.1E-09 A= 5.7E-08 B= 5.4E-07
C= 5.0E-06 D= 4.7E-05 E= 4.4E-04
F= 4.1E-03 G= 3.8E-02 +/- 3.6E-01

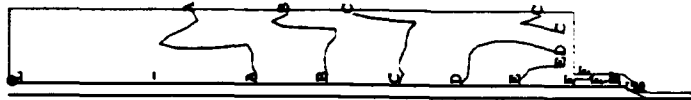


Figure 74. Mass density of neutral gas 60 μs from valve actuation.

DEFLAGRATION GUN (GAS INFLOW) 83
T = 6.008E-05 CYCLE = 823
PRESSURE

-- 7.7E-04 A= 1.0E-02 B= 1.3E-01
C= 1.7E+00 D= 2.2E+01 E= 2.9E+02
F= 3.7E+03 G= 4.8E+04 +/- 6.3E+05

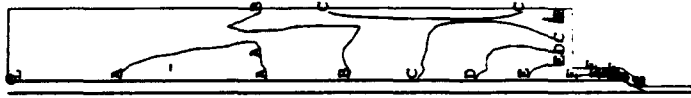


Figure 75. Hydrostatic pressure of neutral gas 60 μs from valve actuation.

An electrostatic calculation has been performed to find the initial electric field distribution. The finite element code, FLUX2D from Magsoft, was used to solve Laplace's equation for the potential. Figure 76 shows the problem region. The open space is vacuum, and the shaded region is the quartz insulator with ϵ_r set to 4.3. The entire right boundary from the top right corner of the open regions to the bottom right corner of the insulator is given a potential of 18 kV, and the entire left boundary from the top left corner of the open region to the bottom left corner of the insulator is at ground. The results show a slight compression of the equipotential lines in the open space between the insulator and the inner conductor (Fig. 77). The compression is small, and the electric field, E , there and all along the inner conductor is ~ 10 kV/cm.

In general, avalanche ionization increases with E/P , where P again is the scalar pressure of the gas. However, P must be large enough so the mean free path for an electron is at least within the dimensions of the experiment. Cobine gives the mean free path for an electron as $1/(AP)$, where A for diatomic H is 5.0 collisions/(cm Torr) (Ref. 21). Using the E contour of the pressure plot (Fig. 75) and converting to Torr, the mean free path near the gas inlet is 1.5 mm which is small enough to expect collisions there. In contrast, the C contour corresponds to a mean free path of 24 cm. The objective is not to pinpoint an exact location for breakdown, there are too many approximations for that, but it is reasonable to say it occurs near the breach.

MHD CALCULATIONS

To solve the MHD equations for the gun behavior after breakdown, again the MACH2 computer code was used. It has many physical models and advanced numerical techniques, and not all are used here. For these simulations, the hydrodynamics routine is time-centered and solves its equations implicitly. The multigrid acceleration technique is used for diffusion of the magnetic field. The computational mesh is fixed in space, and a second-order van Leer advection routine transports quantities across it.

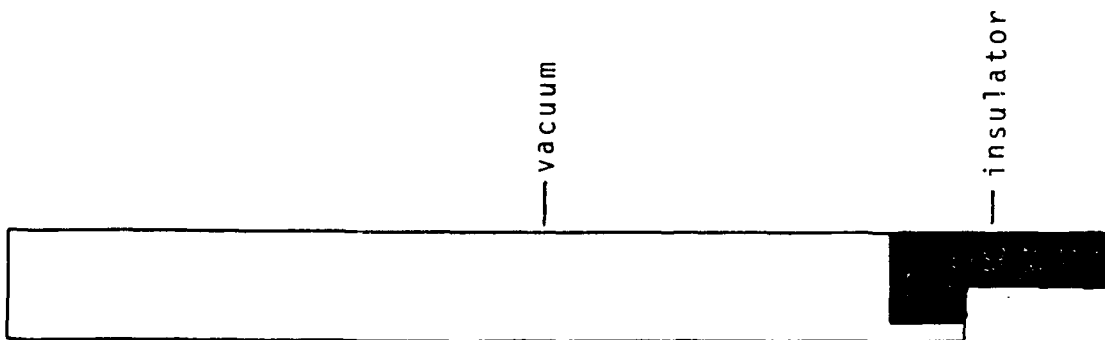


Figure 76. Problems region for the electrostatic calculation.

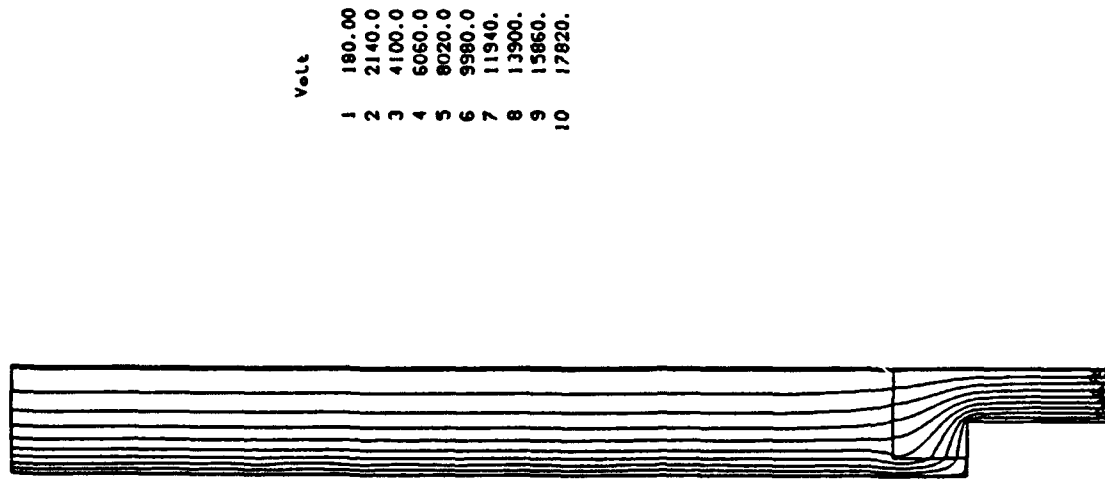


Figure 77. Equipotential lines.

Besides using large routines to solve the conservation equations, other information is necessary for the remaining unknowns. First, an ideal gas equation of state is used. This is reasonable for H, particularly at the low densities involved. Second, the plasma resistivity comes from the Spitzer formulation that models Coulombic collisions between electrons and ions. Third, the radiation of energy is handled by an analytical cooling model developed by J. Buff of MRC. It considers line radiation from neutral H, Bremsstrahlung radiation from the free electrons, and radiation from O impurities (Ref. 22). Finally, an accurate prediction of temperatures was not expected, so the thermal conduction routine was not used. Therefore, of the processes that could influence internal energy, only compressive work, Ohmic heating, and radiative cooling are modelled.

The calculations presented in this report all use H as the working fluid, although most of the experiments at GRC have used Ar. Many calculations had been run on Ar, producing similar behavior as the H, but the approximations are not as reasonable. The heat capacities from the ideal gas equation of state are too simple, and tabular information is not readily available for the low densities involved. Also, MACH2 cannot handle an appropriate radiation treatment for the Ar. Other fundamental assumption like small ion Larmor radii lose credibility, too. However, like the calculations, experiments with different gases appear to behave the same, so the more realistic H calculations are presented to show more detail.

The circuit model in the code is a source of magnetic flux at a specified boundary. The magnetic induction is consistent with the current flowing through the circuit, and it enters the problem by diffusion or by advection of conducting material. The bank capacitance, initial bank voltage, circuit inductance and resistance (outside the calculational region) are set. The time dependent current is found from circuit equations, taking the induced electromotive force (emf) at the boundary into account. Figure 78 is the computation mesh for one of the MHD calculations. The lower section is the gun, and the circuit connection is indicated. In these calculations, the connection only extends across the open gas feed between the inner conductor and the insulator. It does not extend to the outer conductor. This has been done to account for insulator ablation which can complete the circuit to the outer conductor without actually modelling the complicated process.

DEFLAGRATION GUN 110

IDEAL MESH

1ST X = 0.00E+00

X INC = 2.00E-02

1ST Y = 0.00E+00

Y INC = 1.00E-01

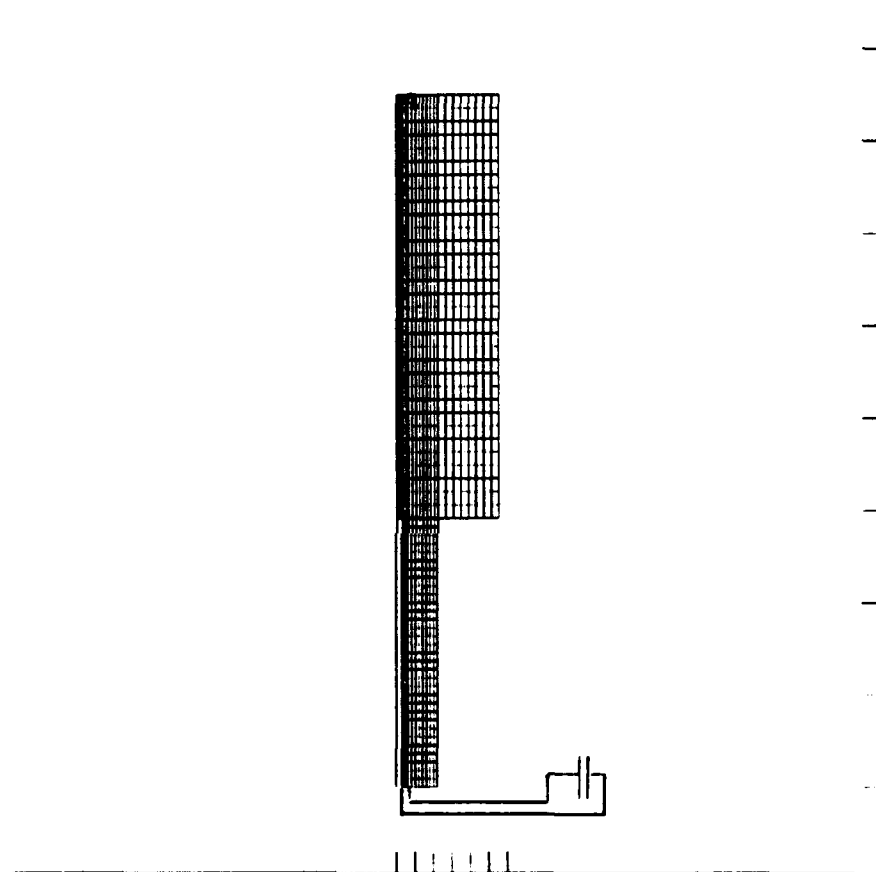


Figure 78. Computation mesh for the MHD calculation.

There are at least two observations that indicate insulator ablation influences the discharge significantly. First, the spectroscopy analysis discussed earlier shows that a large fraction of the plasma in the drift tube is actually insulator material and not working fluid. Second, the current traces from experiments show a stationary discharge. The inductance estimates from those traces almost match estimates from shorted discharges where a metal plate was placed on the insulator. If the ablation did not occur, the discharge would lift off the insulator. A changing inductance would then be apparent in the current trace. This is not an impossibility, but it is not observed. By connecting the circuit across the gas feed only, the simulation reproduces the stationary discharge, but it does not reproduce the acceleration of insulator material.

Referring again to Figure 78, the upper section corresponds to the first 45 cm of the drift tube, and the calculational mesh there extends from the axis to the glass tube. The magnetic field boundary conditions at the top and on the boundary extending from the muzzle of the gun to the tube are von Neumann conditions to represent open boundaries. The mass distribution from the gas calculation (Fig. 74) is copied into the lower section of this mesh, and the density at the open feed boundary is set to $2.5 \times 10^{-3} \text{ kg/m}^3$. At the start of the MHD calculation, all of this mass is considered fully ionized and given a temperature of 0.5 eV. This essentially forces the main discharge to occur at the breech, which again is consistent with the inductance measurements.

This simulation uses the bank parameters of the Ar experiments with H as the working fluid. Those parameters are 126 μF of bank capacitance, 3 m Ω of external resistance, and 45 nH of external inductance. The circuit current peak is 620 kA at 2.9 μs , and it passes through zero at 8.1 μs . The potential in the bank passes through zero at 4.8 μs . These numbers match the Ar experiments well.

Figures 79, 80, and 81 show the behavior of the simulation in both the gun and the drift tube from 1.5 to 3.5 μs . (When a second set of contour levels is shown above the figure, they correspond to the contour lines in the drift tube only.) Current discharges along the breech, accelerating the plasma and reducing the magnetic field; this is the deflagration. Contours of enclosed

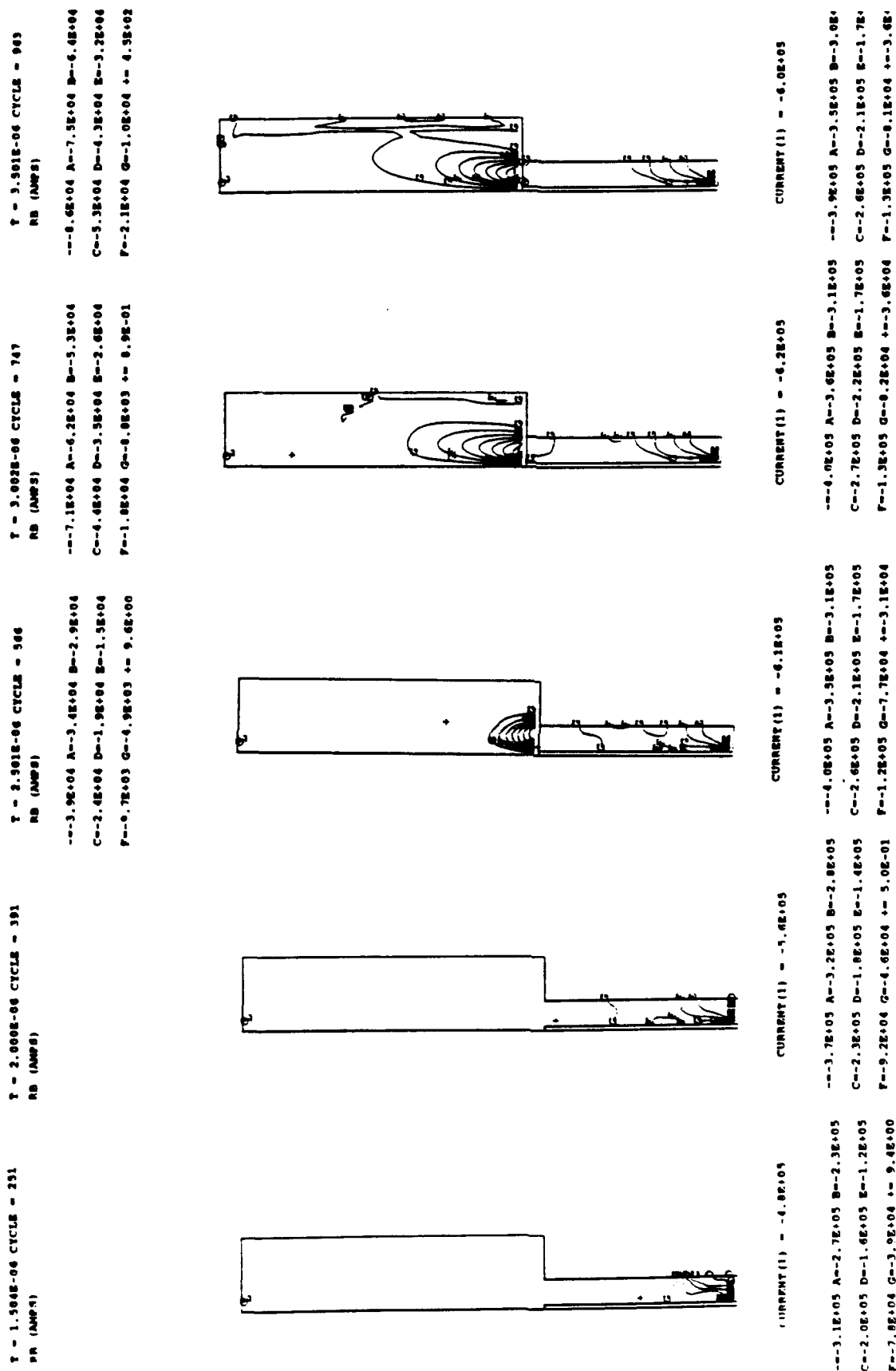


Figure 79. Enclosed current contours from the MHD calculation.

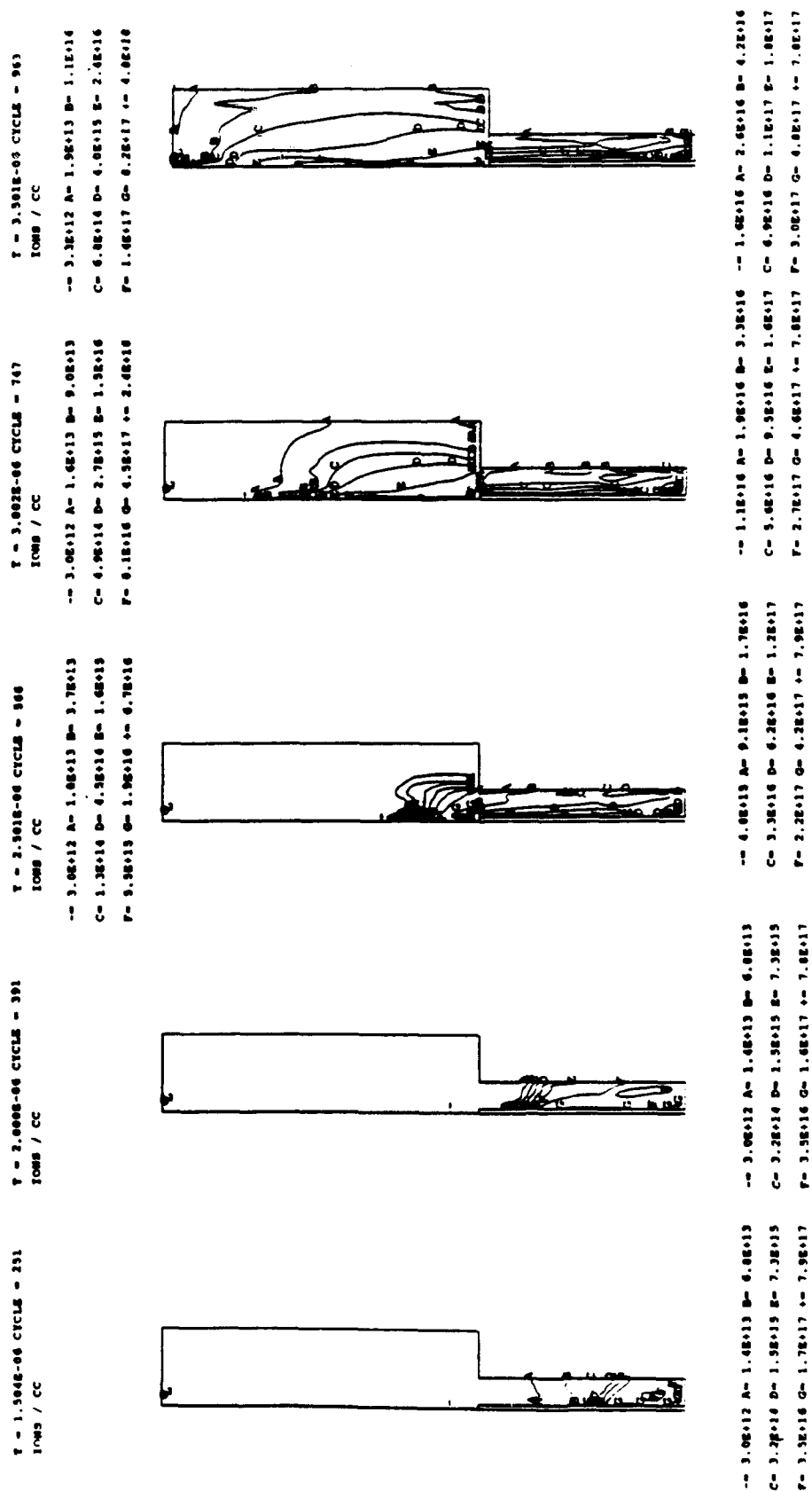


Figure 80. Ion number density from the MHD calculation.

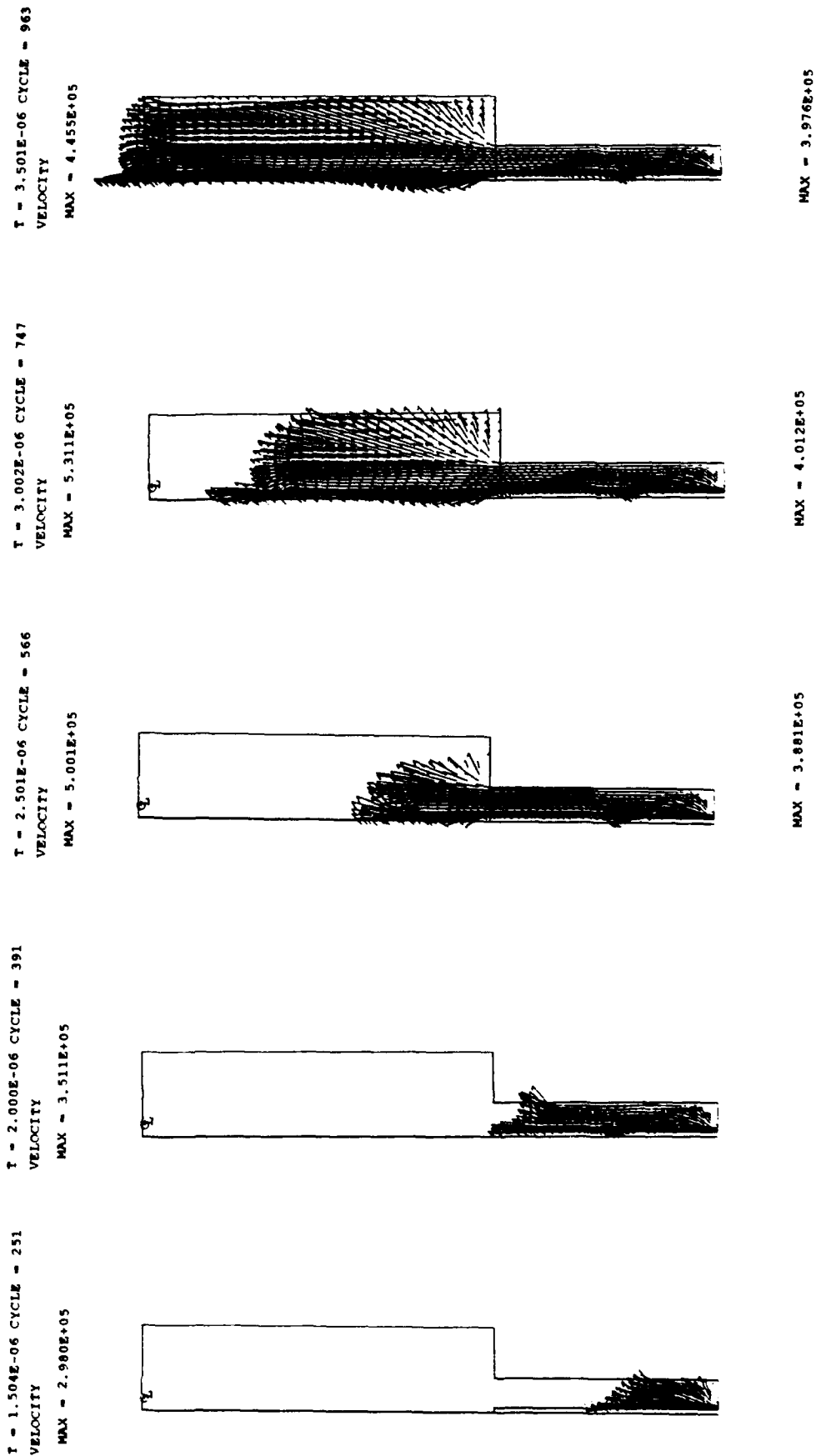


Figure 81. Fluid velocity from the MHD calculation.

current (azimuthal magnetic induction multiplied by radius in units of amperes) are shown in Figure 79. There is a small amount of current, i.e., magnetic induction, that advances with the accelerated plasma (Figs. 80 and 81). Note that it is roughly an order of magnitude less than the current flowing through the circuit, but it is still not negligible.

This reduced magnetic induction seems to play an important role in the behavior of the plasma in the drift tube. The $\bar{J} \times \bar{B}$ force is always perpendicular to the contour lines of enclosed current. As the plasma leaves the gun, this force pushes material at large radii towards the drift tube wall. It also pushes material at small radii inward towards the axis. The confinement that results is illustrated in the plots of number density (Fig. 80). The presence of magnetic induction in the plasma is consistent with the experimental B-dot probe measurements taken in the drift tube. It is also consistent with the MCP camera photographs of the beam that suggest magnetic instabilities. Finally, both the MCP and IC photographs show current on the wall of the drift tube. The simulation shows how plasma from the gun carries this current.

There has been some conjecture that the plasma propagates down the tube as a plasmoid--its current being detached from that in the gun. The integrated B-dot signals show magnetic induction falling after the plasma passes. Reversed current in the plasma must accompany the decreasing induction. The current contours at 9.5 μ s also support this idea (Fig. 82). The contours that are concave upward indicate partial detachment of the exiting plasma.

The temperatures from the simulation also warrant examination. A series of temperature plots are shown in Figure 83. The Ohmic heating and the radiative cooling balance rather well. Excepting the hot spot at the leading edge of the beam that reaches a fixed ceiling of 40 eV, most temperatures stay between 1 and 10 eV. This is also fairly consistent with the experimental spectroscopy information. Even though the heating and cooling mechanisms may not model the actual ones in the experiment--recall that a substantial fraction of the plasma in the experiment is not working fluid, obtaining reasonable temperatures is good for the credibility of the simulations. First, temperature is a factor in the ion gyro or Larmor radii as it determines the

DEFLAGRATION GUN 110
 T = 9.501E-06 CYCLE -2723
 RB (AMPS)

--2.0E+04 A--1.7E+04 B--1.5E+04
 C--1.2E+04 D--1.0E+04 E--7.5E+03
 F--5.0E+03 G--2.5E+03 +-6.5E-01
 --2.5E+04 A--8.6E+03 B= 8.0E+03
 C= 2.5E+04 D= 4.1E+04 E= 5.8E+04
 F= 7.4E+04 G= 9.1E+04 +- 1.1E+05

CURRENT(1) = 1.7E+05

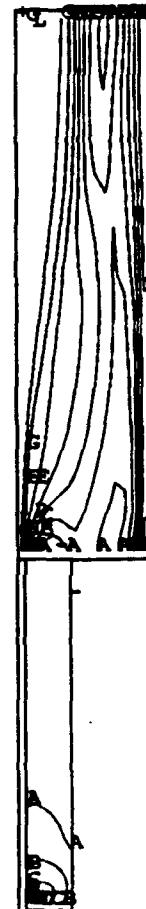


Figure 82. Enclosed current 9.5 μ s after breakdown.

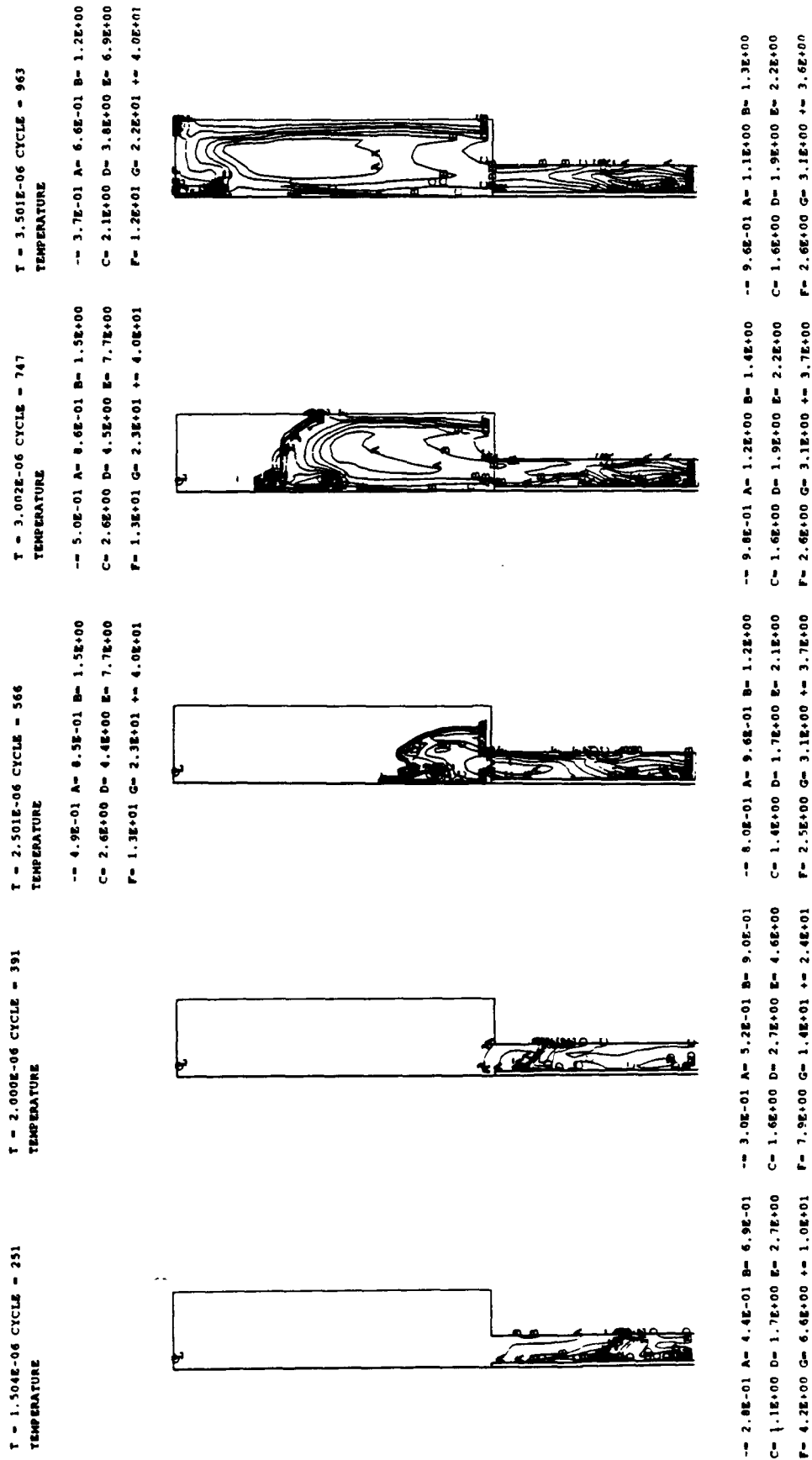


Figure 83. Temperature contours from the MHD calculation.

transverse particle velocity. Figure 84 is a plot of these radii at 3.5 μ s, and they are small, particularly in the gun where the acceleration occurs. The cyclotron period for the ions is small, too. The radii and temperatures halfway down the gun at this time give periods of <100 ns. This indicates that MHD is appropriate. The reasonable temperatures also produce reasonable resistivities from the Spitzer model. Finally, the hydrostatic pressure is not extreme. If it were, the hydrodynamics would be questionable; though, other calculations with extremely small or large temperatures exhibited the same deflagration behavior.

```

DEFLAGRATION GUN  110
T = 3.501E-06 CYCLE = 963
ION LARMOR RADIUS

-- 1.6E-04 A= 4.7E-04 B= 1.3E-03
C= 3.9E-03 D= 1.1E-02 E= 3.2E-02
F= 9.3E-02 G= 2.7E-01 += 7.8E-01
-- 1.9E-05 A= 2.9E-05 B= 4.3E-05
C= 6.6E-05 D= 1.0E-04 E= 1.5E-04
F= 2.3E-04 G= 3.5E-04 += 5.3E-04

```

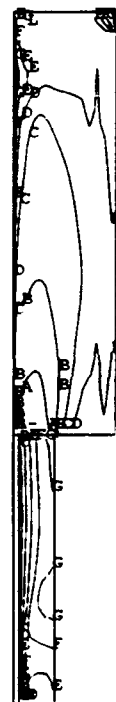


Figure 84. Ion Larmor radii at 3.5 μ s.

The effect of the Hall term in the Generalized Ohm's Law has not yet been discussed. A simulation of the gun with the Hall term was run and compared with the same simulation without the Hall term. The difference was minimal. The large number density of electrons from the fully ionized H made the magnitude of the Hall electric field small. With the center electrode negative, as it is in the experiment, and in a uniform electron number

density, this term tends to spread the discharge. This reduces the acceleration somewhat because the peak $\bar{J} \times \bar{B}$ force is reduced. The simulations without it represent a more ideal behavior with better coupling between the circuit energy and the ion kinetic energy. Regardless, the effect with H in the simulation is small.

DISCUSSION

The most important information from the calculations is how the plasma exits the gun and enters the drift tube. The magnetic field is responsible for the expansion of plasma to the wall of the tube and the focusing on the axis. This magnetic structure can then confine a beam and limit its divergence.

The largest shortcoming of the most recent calculation is the failure to simulate the ablation process. The experimental information of inductance and beam composition puts the insulator at center stage. Without modelling the ablation, the circuit only accelerates the working fluid. It produces a stream of plasma at hundreds of kilometers per second velocity. The velocity of this stream is close to what was observed in the faster, but less dense portion of the beam in the experiment. This faster component may come from the working fluid that is available in the gun at the time of breakdown, and the slower, denser component may arise from the ablated insulator material. The acceleration is still a deflagration process, but it is mostly insulator material that is deflagrating.

REFERENCES

1. Cheng, D. Y., "Plasma Deflagration and the Properties of a Coaxial Plasma Deflagration Gun," Nuclear Fusion, Vol. 10, No. 3, pp. 305-317, 1970.
2. Belikov, A. G., Goncharenko, V. P., Mishchenko, V. M., Safronov, B. G., and Slavaji, A. S., "Obtaining High Speed Plasmoids from a Coaxial Source," Zh. Tekh. Fiz. 34, p. 847, 1964.
3. Bennett, W. H., Physical Review, Vol. 98, No. 6, pp. 1584-1593, 15 June 1955.
4. Uman, M. A., Introduction to Plasma Physics, McGraw-Hill Book Company, New York, pp. 184-193, 1964.
5. Heald, M. A. and Wharton, C. B., Plasma Diagnostics with Microwaves, Wiley, p. 98, 1965.
6. Lochte-Holtgreven, ed., Plasma Diagnostics, American Elsevier Publishing Co., p. 607, 1968.
7. Striganov, A. R. and Sventitskii, N. S., Tables of Spectral Lines of Neutral and Ionized Atoms, IFI/Plenum, New York (translated from Russian), 1968.
8. Wiese, W. L., Smith, M. W., and Miles, B. M., Atomic Transition Probabilities, Vol. II, Publication NSRDS-NBS 22, National Bureau of Standards, October 1969.
9. Griem, H. R., Plasma Spectroscopy, McGraw-Hill, New York, 1964.
10. Griem, H. R., Spectral Line Broadening by Plasmas, Academic Press, New York, 1974.
11. Griem, H. R., Phys. Rev. 131, p. 1170, 1963.
12. Wilson, R., J. Quant. Spectrosc. and Radiat. Transfer 2, p. 477, 1962.
13. McWhirter, R. W. P., "Spectral Intensities," Plasma Diagnostic Techniques, edited by Huddleston R. H. and Leonard, S. L., Academic Press, New York, 1965.
14. Zel'dovich, Ya.B. and Raizer, Yu.P., Physics of Shock Waves and High-Temperature Hydrodynamic Phenomena, Vol. I, Academic Press, New York, ch. VI, 1966.
15. Seaton, M. J., "Radiative Recombination of Hydrogen Ions," Mon. Not. Roy. Astron. Soc., 119, p. 81, 1959.
16. Zel'dovich, Ya.B. and Raizer, Yu.P., Physics of Shock Waves and High-Temperature Hydrodynamic Phenomena, Vol. I, Academic Press, New York, p. 407, 1966.

REFERENCES (Concluded)

17. Hutchinson, I. H., Principles of Plasma Physics, Cambridge University Press, Cambridge, MA, p. 211, 1987.
18. Bashkin, S. and Stoner, J. O. Jr., Atomic Energy Levels and Grotian Diagram, Vol. I, North-Holland, Amsterdam, pp. 506-507, 1975.
19. Krall, N. A. and Trivelpiece, A. W., Principles of Plasma Physics, San Francisco Press, San Francisco, CA, 1986.
20. Jackson, J. D., Classical Electrodynamics, 2nd ed., Wiley, New York, NY, 1975.
21. Cobine, J. D. Gaseous Conductors, Dover, New York, NY, 1975.
22. Buff, J. S., Accretion Flows onto Galactic X-ray Sources, PhD Dissertation, University of Colorado, Boulder, CO, 1974.

APPENDIX

CRE C SOURCE CODE AND OUTPUT

```
/* si2.c source code */
```

```
/* Silicon II collisional radiative equilibrium */
/* written in Turbo C, ver. 2.0 */
```

```
#include <stdio.h>
#include <math.h>
#include <nrutil.h>
#include <nr.h>
#include <alloc.h>
#include <stdlib.h>
#include <string.h>
```

```
double Y(float Eu, float El, float Aul, float Te);
double X(float Eu, float El, float gu, float gl, float Aul, float Te);
```

```
main(int argc, char *argv[])
```

```
{
    FILE *fp;
    char fname[16];
    double **a, **awk, **alud, *b, *Ni;
    float c1, Ne, T, *g, *d, *Tvec, *E, **A;
    int *ndex, i, ii, iT, j, k, n, nT;
    n = 19; /* number of excited states */
    nT = 10; /* number of electron temperatures */
    a = dmatrix(1,n,1,n); /* rate coefficient matrix */
    awk = dmatrix(1,n,1,n); /* temporary working rate coefficient matrix */
    alud = dmatrix(1,n,1,n); /* lower upper decomposition matrix */
    A = matrix(0,n,0,n); /* transition probability matrix */
    d = vector(1,1); /* index variable for matrix inversions */
    E = vector(0,n); /* excitation energies */
    g = vector(0,n); /* statistical weights */
    Tvec = vector(1,nT); /* electron temperature array */
    b = dvector(1,n); /* ground state rate coefficient array */
    Ni = dvector(1,n); /* excited state normalized population array */
    ndex = ivector(1,n); /* index variable for matrix inversions */
    for (i=0; i<=n; i++) { /* initialize input arrays */
        for (j=0; j<=n; j++) {
            A[j][i] = 0;
        }
        g[i] = E[i] = 0;
    }
}
```

a2.c source code

```

*d = 0.;
c1 = 8065.5; /* inverse cm to eV conversion factor */
E[0] = 191./c1; /* ground state:  $3s^2(^1S)3p^2P^{\circ}$  */
E[1] = 43002./c1; /*  $3s3p^2^4P^{\circ}$  */
E[2] = 55319./c1; /*  $3s3p^2^2D^{\circ}$  */
E[3] = 65501./c1; /*  $3s^2(1S)4s^2S^{\circ}$  */
E[4] = 76666./c1; /*  $3s3p^2^2S^{\circ}$  */
E[5] = 79349./c1; /*  $3s^2(1S)3d^2D^{\circ}$  */
E[6] = 81232./c1; /*  $3s^2(^1S)4p^2P^{\circ}$  */
E[7] = 83837./c1; /*  $3s3p^2^2P^{\circ}$  */
E[8] = 97972./c1; /*  $3s^2(1S)5s^2S^{\circ}$  */
E[9] = 101024./c1; /*  $3s^2(1S)4d^2D^{\circ}$  */
E[10] = 103556./c1; /*  $3s^2(^1S)4f^2F^{\circ}$  */
E[11] = 103878./c1; /*  $3s^2(^1S)5p^2P^{\circ}$  */
E[12] = 111185./c1; /*  $3s^2(1S)6s^2S^{\circ}$  */
E[13] = 112395./c1; /*  $3s^2(1S)5d^2D^{\circ}$  */
E[14] = 113760./c1; /*  $3s^2(^1S)5f^2F^{\circ}$  */
E[15] = 113972./c1; /*  $3s^2(^1S)6p^2P^{\circ}$  */
E[16] = 114177./c1; /*  $3s^2(1S)5g^2G^{\circ}$  */
E[17] = 117915./c1; /*  $3s^2(1S)7s^2S^{\circ}$  */
E[18] = 118523./c1; /*  $3s^2(1S)6d^2D^{\circ}$  */
E[19] = 119312./c1; /*  $3s^2(^1S)6f^2F^{\circ}$  */

g[0] = 6;
g[1] = 12;
g[2] = 10;
g[3] = 2;
g[4] = 2;
g[5] = 10;
g[6] = 6;
g[7] = 6;
g[8] = 2;
g[9] = 10;
g[10] = 14;
g[11] = 6;
g[12] = 2;
g[13] = 10;
g[14] = 14;
g[15] = 6;
g[16] = 18;
g[17] = 2;
g[18] = 10;
g[19] = 14;

```

si2.c source code

```

A[1][0] = 6.45E3;      /* units: inverse seconds */
A[2][0] = .046E8;
A[3][0] = 6.67E8;
A[4][0] = 10.6E8;
A[5][0] = 25.0E8;
A[7][0] = 33.7E8;
A[8][0] = 10.3E8;
A[9][0] = 10.9E8;
A[6][1] = 1.18E4;
A[10][1] = 2.9E4;
A[6][2] = 0.98E8;
A[10][2] = 1.03E8;
A[6][3] = 0.65E8;
A[6][5] = 1.79E5;
A[10][5] = 2.11E8;
A[11][5] = 0.044E8;
A[14][5] = 0.71E8;
A[19][5] = 0.41E8;
A[8][6] = 1.41E8;
A[9][6] = 1.65E8;
A[12][6] = 0.46E8;
A[13][6] = 0.46E8;
A[17][6] = 0.24E8;
A[10][7] = 1.3E4;
A[11][8] = 0.129E8;
A[10][9] = 8.91E5;
A[11][9] = 2.22E6;
A[14][9] = 0.42E8;
A[19][9] = 0.26E8;
A[13][10] = 3.37E6;
A[18][10] = .014E8;
A[12][11] = 3.58E7;
A[13][11] = 3.45E7;
A[17][11] = .15E8;
A[18][11] = .13E8;
A[15][12] = 3.49E6;
A[14][13] = 4.89E5;
A[15][13] = 1.08E6;
A[19][13] = 8.42E6;
A[16][14] = 4.91E3;
A[18][14] = 2.34E6;
A[17][15] = 1.35E7;
A[18][15] = 1.11E7;
A[19][16] = 3.85E5;
A[19][18] = 2.25E5;

```


si2.c source code

```

Tvec[1] = 0.5;      /* units: eV */
Tvec[2] = 0.7;
Tvec[3] = 1.0;
Tvec[4] = 1.2;
Tvec[5] = 1.5;
Tvec[6] = 2.0;
Tvec[7] = 2.5;
Tvec[8] = 3.0;
Tvec[9] = 4.0;
Tvec[10] = 5.0;
strcpy(fname,argv[0]); /* define data output file */
fname[(strlen(argv[0])-3)] = 'A'; /* and open it */
fname[(strlen(argv[0])-2)] = 'S';
fname[(strlen(argv[0])-1)] = 'C';
if ((fp=fopen(fname,"w"))==NULL) {
    printf("can't open directory file\n");
    exit(1);
}
fprintf(fp,"Normalized (Ni/N0) Population Densities\n");
for (iT=1; iT<=10; iT++) { /* outermost loop - */
    T = Tvec[iT]; /* for each temperature */
    printf("\nT = %.1f eV",T);
    fprintf(fp,"\n");
    for (ii=12; ii<=17; ii++) { /* for each density loop */
        Ne = pow10(ii);
        printf("\nNe = %.1E cm(-3)\n",Ne);
        fprintf(fp,"%10.1f%10.1E",T,Ne);
        for (i=1; i<=n; i++) { /* initialize a,awk,alud,b,Ni */
            for (j=1; j<=n; j++){
                a[i][j] = awk[i][j] = alud[i][j] = 0.;
            }
            b[i] = Ni[i] = 0.;
            ndex[i] = 0;
        }
        for (k=1; k<=n; k++) { /* build rate coefficient matrix */
            b[k] = Ni[k] = X(E[k],E[0],g[k],g[0],A[k][0],T);
            for (i=0; i<k; i++) {
                if (!A[k][i]) continue;
                if (i>0) a[k][i] = awk[k][i] = -(X(E[k],E[i],g[k],g[i],A[k][i],T));
                a[k][k] += Y(E[k],E[i],A[k][i],T) + (A[k][i])/Ne;
            }
            for (i=k+1; i<=n; i++) {
                if (!A[i][k]) continue;
                a[k][k] += X(E[i],E[k],g[i],g[k],A[i][k],T);
                a[k][i] = awk[k][i] = -(Y(E[i],E[k],A[i][k],T) + (A[i][k])/Ne);
            }
            awk[k][k] = a[k][k];
        }
    }
}

ludcmp(awk,n,ndex,d); /* call lower upper decomposition */
for (k=1; k<=n; k++) {

```

```

        for (i=1; i<=n; i++) {
            alud[k][i] = awk[k][i]; /* save lu decomp matrix */
        }
    }
    lubksb(awk,n,ndex,Ni); /* call back substitution routine */
    mprove(a, alud, n, ndex, b, Ni); /* call iterative improvement routine */
    for (i=1; i<=ceil(n/5.); i++) {
        for (j=5*i-4; j<=5*i; j++) printf("N%d = %.3E ",j,Ni[j]);
        printf("\n");
    }
    for (i=1; i<=n; i++) fprintf(fp,"%10.3E",Ni[i]);
    fprintf(fp,"\n");
}
}
fclose(fp); /* close output file */
free_dmatrix(a,1,n,1,n); /* free memory */
free_dmatrix(awk,1,n,1,n);
free_dmatrix(alud,1,n,1,n);
free_matrix(A,0,n,0,n);
free_vector(d,1,1);
free_vector(E,0,n);
free_vector(g,0,n);
free_vector(Tvec,1,nT);
free_dvector(b,1,n);
free_dvector(Ni,1,n);
free_ivector(ndex,1,n);
}

double X(float Eu,float El,float gu,float gl,float Aul,float Te)
{
    double Y1, X1;
    float dE;
    dE = Eu - El;
    Y1 = Y(Eu,El,Aul,Te);
    X1 = (gu/gl)*Y1*exp(-dE/Te); /* collisional excitation rate coefficient */
    return(X1);
}

double Y(float Eu, float El, float Aul, float Te)
{
    double Y1;
    float C, dE; /* collisional deexcitation */
    C = 3.644E-13; /* rate coefficient */
    dE = Eu - El;
    Y1 = C*Aul*(.2+.551*log(1+Te/dE))/((pow(dE,3))*sqrt(Te));
    return(Y1);
}

```

si2.c source code

```

/* ludcmp.c */
/* performs lower-upper decomposition of matrix */

#include <math.h>

#define TINY 1.0e-20;

void ludcmp(a,n,indx,d)
int n,*indx;
float *d;
double **a;
{
    int i,imax,j,k;
    double big,dum,sum,temp;
    double *vv,*dvector();
    void nreerror(),free_dvector();

    vv=dvector(1,n);
    *d=1.0;
    for (i=1;i<=n;i++) {
        big=0.0;
        for (j=1;j<=n;j++)
            if ((temp=fabs(a[i][j])) > big) big=temp;
        if (big == 0.0) nreerror("Singular matrix in routine LUDCMP");
        vv[i]=1.0/big;
    }
    for (j=1;j<=n;j++) {
        for (i=1;i<j;i++) {
            sum=a[i][j];
            for (k=1;k<i;k++) sum -= a[i][k]*a[k][j];
            a[i][j]=sum;
        }
    }
}

```

si2.c source code

```

    big=0.0;
    for (i=j;i<=n;i++) {
        sum=a[i][j];
        for (k=1;k<j;k++)
            sum -= a[i][k]*a[k][j];
        a[i][j]=sum;
        if ( (dum=vv[i]*fabs(sum)) >= big) {
            big=dum;
            imax=i;
        }
    }
    if (j != imax) {
        for (k=1;k<=n;k++) {
            dum=a[imax][k];
            a[imax][k]=a[j][k];
            a[j][k]=dum;
        }
        *d = -(*d);
        vv[imax]=vv[j];
    }
    indx[j]=imax;
    if (a[j][j] == 0.0) a[j][j]=TINY;
    if (j != n) {
        dum=1.0/(a[j][j]);
        for (i=j+1;i<=n;i++) a[i][j] *= dum;
    }
}
free_dvector(vv,1,n);
}

#undef TINY

```

si2.c source code

```

/* lubksb.c */
/* performs backward substitution algorithm */

void lubksb(a,n,indx,b)
double **a,b[];
int n,*indx;
{
    int i,ii=0,ip,j;
    double sum;

    for (i=1;i<=n;i++) {
        ip=indx[i];
        sum=b[ip];
        b[ip]=b[i];
        if (ii)
            for (j=ii;j<=i-1;j++) sum -= a[i][j]*b[j];
        else if (sum) ii=i;
        b[i]=sum;
    }
    for (i=n;i>=1;i--) {
        sum=b[i];
        for (j=i+1;j<=n;j++) sum -= a[i][j]*b[j];
        b[i]=sum/a[i][i];
    }
}

```

si2.c source code

```

/* mprove.c */
/* iterative improvement of matrix solution */

void mprove(a,alud,n,indx,b,x)
double **a,**alud,b[],x[];
int n,indx[];
{
    int j,i;
    double sdp;
    double *r,*dvector();
    void lubksb(),free_dvector();

    r=dvector(1,n);
    for (i=1;i<=n;i++) {
        sdp = -b[i];
        for (j=1;j<=n;j++) sdp += a[i][j]*x[j];
        r[i]=sdp;
    }
    lubksb(alud,n,indx,r);
    for (i=1;i<=n;i++) x[i] -= r[i];
    free_dvector(r,1,n);
}

```

s12.c source code

Normalized (Ni/N0) Silicon II Excited State Population Densities							
	T_e :	0.5	0.5	0.5	0.5	0.5	0.5
<u>Config</u>	N_e :	1E+12	1E+13	1E+14	1E+15	1E+16	1E+17
3p ⁴ P	N1	4.22E-08	4.18E-07	3.88E-06	2.27E-05	4.39E-05	4.85E-05
3p ² D	N2	7.43E-10	7.42E-09	7.16E-08	5.24E-07	1.49E-06	1.87E-06
4s ² S	N3	6.98E-12	6.97E-11	6.81E-10	5.57E-09	2.09E-08	2.95E-08
3p ² S	N4	2.67E-13	2.67E-12	2.64E-11	2.35E-10	1.12E-09	1.81E-09
3d ² D	N5	6.17E-13	6.13E-12	6.12E-11	6.12E-10	3.10E-09	4.70E-09
4p ² P*	N6	1.52E-14	9.67E-13	2.40E-11	2.60E-10	1.20E-09	1.78E-09
3p ² P	N7	1.02E-13	1.02E-12	1.01E-11	9.28E-11	5.01E-10	8.96E-10
5s ² S	N8	5.56E-16	5.53E-15	6.56E-14	1.05E-12	6.06E-12	9.28E-12
4d ² D	N9	1.16E-15	1.12E-14	1.33E-13	2.36E-12	1.41E-11	2.18E-11
4f ² F*	N10	3.73E-17	2.73E-15	8.92E-14	1.77E-12	1.06E-11	1.63E-11
5p ² P*	N11	1.99E-16	3.15E-15	4.06E-14	7.06E-13	4.19E-12	6.44E-12
6s ² S	N12	1.13E-18	7.29E-17	1.92E-15	3.80E-14	2.28E-13	3.50E-13
5d ² D	N13	2.46E-18	2.17E-16	6.92E-15	1.40E-13	8.43E-13	1.30E-12
5f ² F*	N14	1.67E-18	1.94E-16	6.81E-15	1.40E-13	8.41E-13	1.30E-12
6p ² P*	N15	1.10E-18	9.20E-17	2.82E-15	5.69E-14	3.42E-13	5.27E-13
5g ² G	N16	1.94E-18	2.25E-16	7.90E-15	1.62E-13	9.75E-13	1.50E-12
7s ² S	N17	6.66E-20	1.03E-17	3.50E-16	7.13E-15	4.29E-14	6.60E-14
6d ² D	N18	1.98E-19	3.61E-17	1.46E-15	3.06E-14	1.84E-13	2.84E-13
6f ² F*	N19	1.93E-19	4.03E-17	1.68E-15	3.52E-14	2.12E-13	3.27E-13

Normalized (Ni/N0) Silicon II Excited State Population Densities							
	T_e :	0.7	0.7	0.7	0.7	0.7	0.7
Config	N_e :	1E+12	1E+13	1E+14	1E+15	1E+16	1E+17
3p ⁴ P	N1	7.95E-07	7.89E-06	7.38E-05	4.47E-04	9.02E-04	1.01E-03
3p ² D	N2	3.32E-08	3.35E-07	3.23E-06	2.18E-05	6.56E-05	9.12E-05
4s ² S	N3	6.36E-10	6.35E-09	6.20E-08	4.98E-07	1.98E-06	2.97E-06
3p ² S	N4	5.34E-11	5.33E-10	5.27E-09	4.76E-08	2.40E-07	4.04E-07
3d ² D	N5	1.49E-10	1.48E-09	1.48E-08	1.49E-07	7.90E-07	1.27E-06
4p ² P*	N6	5.32E-12	2.70E-10	6.57E-09	7.09E-08	3.47E-07	5.47E-07
3p ² P	N7	3.39E-11	3.39E-10	3.36E-09	3.10E-08	1.76E-07	3.32E-07
5s ² S	N8	4.98E-13	4.94E-12	5.72E-11	9.23E-10	5.73E-09	9.36E-09
4d ² D	N9	1.29E-12	1.23E-11	1.45E-10	2.60E-09	1.66E-08	2.72E-08
4f ² F*	N10	4.84E-14	3.53E-12	1.16E-10	2.33E-09	1.49E-08	2.44E-08
5p ² P*	N11	2.64E-13	4.14E-12	5.37E-11	9.48E-10	6.02E-09	9.86E-09
6s ² S	N12	2.42E-15	1.52E-13	4.19E-12	8.54E-11	5.49E-10	9.01E-10
5d ² D	N13	5.80E-15	4.99E-13	1.65E-11	3.44E-10	2.22E-09	3.63E-09
5f ² F*	N14	4.36E-15	4.92E-13	1.79E-11	3.77E-10	2.44E-09	4.00E-09
6p ² P*	N15	2.83E-15	2.33E-13	7.50E-12	1.56E-10	1.01E-09	1.65E-09
5g ² G	N16	5.20E-15	5.88E-13	2.14E-11	4.50E-10	2.91E-09	4.77E-09
7s ² S	N17	2.27E-16	3.46E-14	1.23E-12	2.58E-11	1.67E-10	2.73E-10
6d ² D	N18	7.00E-16	1.26E-13	5.37E-12	1.16E-10	7.48E-10	1.23E-09
6f ² F*	N19	7.21E-16	1.48E-13	6.51E-12	1.41E-10	9.11E-10	1.49E-09

Normalized (Ni/N0) Silicon II Excited State Population Densities							
	T_e :	1.0	1.0	1.0	1.0	1.0	1.0
<u>Config</u>	N_e :	1E+12	1E+13	1E+14	1E+15	1E+16	1E+17
3p ⁴ P	N1	7.12E-06	7.07E-05	6.65E-04	4.13E-03	8.67E-03	9.76E-03
3p ² D	N2	5.73E-07	5.93E-06	5.65E-05	3.14E-04	1.06E-03	1.67E-03
4s ² S	N3	1.84E-08	1.84E-07	1.78E-06	1.37E-05	5.76E-05	9.40E-05
3p ² S	N4	2.77E-09	2.77E-08	2.74E-07	2.50E-06	1.33E-05	2.33E-05
3d ² D	N5	8.89E-09	8.84E-08	8.85E-07	8.80E-06	4.86E-05	8.39E-05
4p ² P*	N6	5.37E-10	1.90E-08	4.33E-07	4.52E-06	2.34E-05	3.99E-05
3p ² P	N7	2.57E-09	2.56E-08	2.55E-07	2.37E-06	1.41E-05	2.79E-05
5s ² S	N8	7.94E-11	7.85E-10	8.90E-09	1.42E-07	9.41E-07	1.66E-06
4d ² D	N9	2.41E-10	2.29E-09	2.66E-08	4.72E-07	3.21E-06	5.69E-06
4f ² F*	N10	1.01E-11	7.39E-10	2.43E-08	4.84E-07	3.29E-06	5.82E-06
5p ² P*	N11	5.59E-11	8.69E-10	1.14E-08	2.00E-07	1.35E-06	2.40E-06
6s ² S	N12	7.31E-13	4.47E-11	1.29E-09	2.65E-08	1.82E-07	3.23E-07
5d ² D	N13	1.90E-12	1.59E-10	5.43E-09	1.14E-07	7.84E-07	1.39E-06
5f ² F*	N14	1.54E-12	1.69E-10	6.33E-09	1.34E-07	9.27E-07	1.64E-06
6p ² P*	N15	9.81E-13	7.97E-11	2.68E-09	5.62E-08	3.87E-07	6.86E-07
5g ² G	N16	1.88E-12	2.06E-10	7.73E-09	1.64E-07	1.13E-06	2.01E-06
7s ² S	N17	9.68E-14	1.46E-11	5.42E-10	1.15E-08	7.91E-08	1.40E-07
6d ² D	N18	3.10E-13	5.48E-11	2.44E-09	5.31E-08	3.67E-07	6.50E-07
6f ² F*	N19	3.33E-13	6.73E-11	3.09E-09	6.74E-08	4.65E-07	8.25E-07

Normalized (Ni/N0) Silicon II Excited State Population Densities							
	T_e :	1.2	1.2	1.2	1.2	1.2	1.2
Config	N_e :	1E+12	1E+13	1E+14	1E+15	1E+16	1E+17
3p 4P	N1	1.67E-05	1.66E-04	1.56E-03	9.78E-03	2.08E-02	2.36E-02
3p 2D	N2	1.76E-06	1.85E-05	1.73E-04	8.67E-04	3.11E-03	5.16E-03
4s 2S	N3	6.79E-08	6.79E-07	6.53E-06	4.86E-05	2.11E-04	3.59E-04
3p 2S	N4	1.28E-08	1.28E-07	1.27E-06	1.16E-05	6.28E-05	1.13E-04
3d 2D	N5	4.33E-08	4.31E-07	4.32E-06	4.25E-05	2.39E-04	4.27E-04
4p $^2P^o$	N6	3.43E-09	1.01E-07	2.19E-06	2.24E-05	1.19E-04	2.11E-04
3p 2P	N7	1.37E-08	1.37E-07	1.36E-06	1.27E-05	7.71E-05	1.56E-04
5s 2S	N8	5.66E-10	5.58E-09	6.27E-08	9.90E-07	6.78E-06	1.24E-05
4d 2D	N9	1.82E-09	1.73E-08	2.01E-07	3.52E-06	2.47E-05	4.53E-05
4f $^2F^o$	N10	7.95E-11	5.83E-09	1.93E-07	3.81E-06	2.66E-05	4.89E-05
5p $^2P^o$	N11	4.42E-10	6.85E-09	9.03E-08	1.58E-06	1.10E-05	2.03E-05
6s 2S	N12	6.65E-12	4.03E-10	1.19E-08	2.44E-07	1.73E-06	3.17E-06
5d 2D	N13	1.78E-11	1.48E-09	5.11E-08	1.07E-06	7.61E-06	1.40E-05
5f $^2F^o$	N14	1.49E-11	1.61E-09	6.14E-08	1.30E-06	9.25E-06	1.70E-05
6p $^2P^o$	N15	9.40E-12	7.59E-10	2.61E-08	5.47E-07	3.88E-06	7.14E-06
5g 2G	N16	1.84E-11	1.99E-09	7.56E-08	1.60E-06	1.14E-05	2.10E-05
7s 2S	N17	1.01E-12	1.51E-10	5.72E-09	1.21E-07	8.61E-07	1.58E-06
6d 2D	N18	3.28E-12	5.74E-10	2.61E-08	5.67E-07	4.04E-06	7.43E-06
6f $^2F^o$	N19	3.57E-12	7.16E-10	3.36E-08	7.32E-07	5.21E-06	9.59E-06

Normalized (Ni/N0) Silicon II Excited State Population Densities							
	T _e :	1.5	1.5	1.5	1.5	1.5	1.5
Config	N _e :	1E+12	1E+13	1E+14	1E+15	1E+16	1E+17
3p ⁴ P	N1	3.90E-05	3.88E-04	3.66E-03	2.30E-02	4.96E-02	5.70E-02
3p ² D	N2	5.51E-06	5.99E-05	5.36E-04	2.39E-03	9.13E-03	1.59E-02
4s ² S	N3	2.50E-07	2.50E-06	2.38E-05	1.71E-04	7.71E-04	1.37E-03
3p ² S	N4	5.88E-08	5.87E-07	5.82E-06	5.35E-05	2.97E-04	5.44E-04
3d ² D	N5	2.10E-07	2.09E-06	2.10E-05	2.03E-04	1.17E-03	2.17E-03
4p ² P*	N6	2.26E-08	5.46E-07	1.11E-05	1.10E-04	6.05E-04	1.12E-03
3p ² P	N7	7.27E-08	7.27E-07	7.22E-06	6.78E-05	4.20E-04	8.74E-04
5s ² S	N8	4.00E-09	3.94E-08	4.38E-07	6.86E-06	4.86E-05	9.29E-05
4d ² D	N9	1.37E-08	1.30E-07	1.50E-06	2.61E-05	1.88E-04	3.61E-04
4f ² F*	N10	6.20E-10	4.57E-08	1.52E-06	2.97E-05	2.14E-04	4.10E-04
5p ² P*	N11	3.46E-09	5.34E-08	7.11E-07	1.24E-05	8.93E-05	1.71E-04
6s ² S	N12	5.98E-11	3.59E-09	1.08E-07	2.22E-06	1.62E-05	3.12E-05
5d ² D	N13	1.66E-10	1.36E-08	4.78E-07	1.00E-05	7.35E-05	1.41E-04
5f ² F*	N14	1.43E-10	1.53E-08	5.91E-07	1.25E-05	9.19E-05	1.76E-04
6p ² P*	N15	8.91E-11	7.16E-09	2.52E-07	5.28E-06	3.87E-05	7.42E-05
5g ² G	N16	1.78E-10	1.89E-08	7.34E-07	1.56E-05	1.14E-04	2.19E-04
7s ² S	N17	1.03E-11	1.54E-09	5.99E-08	1.27E-06	9.31E-06	1.79E-05
6d ² D	N18	3.43E-11	5.94E-09	2.77E-07	6.01E-06	4.43E-05	8.49E-05
6f ² F*	N19	3.80E-11	7.53E-09	3.62E-07	7.89E-06	5.81E-05	1.11E-04

Normalized (Ni/N0) Silicon II Excited State Population Densities							
	T_e :	2.0	2.0	2.0	2.0	2.0	2.0
Config	N_e :	1E+12	1E+13	1E+14	1E+15	1E+16	1E+17
3p ⁴ P	N1	9.15E-05	9.13E-04	8.64E-03	5.38E-02	1.16E-01	1.37E-01
3p ² D	N2	1.83E-05	2.05E-04	1.68E-03	6.66E-03	2.68E-02	4.92E-02
4s ² S	N3	9.21E-07	9.21E-06	8.65E-05	5.92E-04	2.79E-03	5.23E-03
3p ² S	N4	2.69E-07	2.68E-06	2.66E-05	2.46E-04	1.40E-03	2.63E-03
3d ² D	N5	1.01E-06	1.01E-05	1.01E-04	9.65E-04	5.68E-03	1.10E-02
4p ² P*	N6	1.53E-07	3.03E-06	5.58E-05	5.33E-04	3.04E-03	5.89E-03
3p ² P	N7	3.84E-07	3.84E-06	3.82E-05	3.60E-04	2.28E-03	4.89E-03
5s ² S	N8	2.81E-08	2.76E-07	3.04E-06	4.71E-05	3.46E-04	6.93E-04
4d ² D	N9	1.02E-07	9.71E-07	1.12E-05	1.91E-04	1.43E-03	2.87E-03
4f ² F*	N10	4.77E-09	3.55E-07	1.19E-05	2.29E-04	1.71E-03	3.43E-03
5p ² P*	N11	2.67E-08	4.12E-07	5.55E-06	9.62E-05	7.18E-04	1.44E-03
6s ² S	N12	5.30E-10	3.16E-08	9.76E-07	2.00E-05	1.52E-04	3.05E-04
5d ² D	N13	1.52E-09	1.23E-07	4.43E-06	9.28E-05	7.05E-04	1.42E-03
5f ² F*	N14	1.36E-09	1.43E-07	5.63E-06	1.19E-04	9.07E-04	1.82E-03
6p ² P*	N15	8.32E-10	6.67E-08	2.41E-06	5.05E-05	3.83E-04	7.71E-04
5g ² G	N16	1.70E-09	1.79E-07	7.05E-06	1.49E-04	1.14E-03	2.28E-03
7s ² S	N17	1.04E-10	1.56E-08	6.21E-07	1.32E-05	1.00E-04	2.01E-04
6d ² D	N18	3.55E-10	6.07E-08	2.91E-06	6.32E-05	4.82E-04	9.69E-04
6f ² F*	N19	3.98E-10	7.81E-08	3.86E-06	8.42E-05	6.42E-04	1.29E-03

Normalized (Ni/N0) Silicon II Excited State Population Densities							
	T_e :	2.5	2.5	2.5	2.5	2.5	2.5
Config	N_e :	1E+12	1E+13	1E+14	1E+15	1E+16	1E+17
3p ⁴ P	N1	1.53E-04	1.53E-03	1.45E-02	8.88E-02	1.91E-01	2.32E-01
3p ² D	N2	3.92E-05	4.45E-04	3.35E-03	1.24E-02	5.09E-02	9.68E-02
4s ² S	N3	2.02E-06	2.02E-05	1.87E-04	1.24E-03	6.01E-03	1.17E-02
3p ² S	N4	6.68E-07	6.67E-06	6.62E-05	6.13E-04	3.54E-03	6.75E-03
3d ² D	N5	2.60E-06	2.60E-05	2.61E-04	2.45E-03	1.46E-02	2.92E-02
4p ² P*	N6	4.86E-07	8.62E-06	1.47E-04	1.37E-03	8.00E-03	1.60E-02
3p ² P	N7	1.04E-06	1.04E-05	1.03E-04	9.76E-04	6.27E-03	1.37E-02
5s ² S	N8	9.03E-08	8.85E-07	9.69E-06	1.49E-04	1.12E-03	2.31E-03
4d ² D	N9	3.41E-07	3.23E-06	3.71E-05	6.29E-04	4.80E-03	9.93E-03
4f ² F*	N10	1.61E-08	1.21E-06	4.09E-05	7.80E-04	5.93E-03	1.23E-02
5p ² P*	N11	9.01E-08	1.40E-06	1.90E-05	3.28E-04	2.50E-03	5.17E-03
6s ² S	N12	1.94E-09	1.16E-07	3.64E-06	7.47E-05	5.79E-04	1.20E-03
5d ² D	N13	5.69E-09	4.60E-07	1.68E-05	3.51E-04	2.73E-03	5.65E-03
5f ² F*	N14	5.22E-09	5.42E-07	2.17E-05	4.59E-04	3.57E-03	7.39E-03
6p ² P*	N15	3.15E-09	2.52E-07	9.28E-06	1.95E-04	1.51E-03	3.14E-03
5g ² G	N16	6.56E-09	6.81E-07	2.73E-05	5.78E-04	4.49E-03	9.31E-03
7s ² S	N17	4.12E-10	6.18E-08	2.52E-06	5.33E-05	4.14E-04	8.59E-04
6d ² D	N18	1.43E-09	2.43E-07	1.19E-05	2.58E-04	2.01E-03	4.17E-03
6f ² F*	N19	1.62E-09	3.15E-07	1.59E-05	3.47E-04	2.71E-03	5.61E-03

Normalized (Ni/N0) Silicon II Excited State Population Densities							
	T _e :	3.0	3.0	3.0	3.0	3.0	3.0
Config	N _e :	1E+12	1E+13	1E+14	1E+15	1E+16	1E+17
3p ⁴ P	N1	2.16E-04	2.17E-03	2.06E-02	1.23E-01	2.64E-01	3.28E-01
3p ² D	N2	6.72E-05	7.62E-04	5.33E-03	1.87E-02	7.82E-02	1.52E-01
4s ² S	N3	3.41E-06	3.41E-05	3.13E-04	2.03E-03	1.00E-02	1.99E-02
3p ² S	N4	1.23E-06	1.22E-05	1.22E-04	1.13E-03	6.57E-03	1.27E-02
3d ² D	N5	4.88E-06	4.88E-05	4.90E-04	4.55E-03	2.74E-02	5.59E-02
4p ² P°	N6	1.05E-06	1.74E-05	2.80E-04	2.56E-03	1.52E-02	3.10E-02
3p ² P	N7	2.02E-06	2.02E-05	2.01E-04	1.90E-03	1.23E-02	2.73E-02
5s ² S	N8	1.96E-07	1.92E-06	2.10E-05	3.20E-04	2.44E-03	5.16E-03
4d ² D	N9	7.60E-07	7.20E-06	8.25E-05	1.39E-03	1.07E-02	2.27E-02
4f ² F°	N10	3.60E-08	2.72E-06	9.28E-05	1.76E-03	1.36E-02	2.87E-02
5p ² P°	N11	2.02E-07	3.14E-06	4.29E-05	7.40E-04	5.73E-03	1.21E-02
6s ² S	N12	4.59E-09	2.75E-07	8.73E-06	1.79E-04	1.41E-03	2.99E-03
5d ² D	N13	1.37E-08	1.10E-06	4.07E-05	8.51E-04	6.70E-03	1.42E-02
5f ² F°	N14	1.27E-08	1.31E-06	5.32E-05	1.12E-03	8.87E-03	1.88E-02
6p ² P°	N15	7.59E-09	6.11E-07	2.28E-05	4.78E-04	7.77E-03	7.98E-03
5g ² G	N16	1.61E-08	1.66E-06	6.72E-05	1.42E-03	1.12E-02	2.38E-02
7s ² S	N17	1.02E-09	1.54E-07	6.38E-06	1.35E-04	1.07E-03	2.26E-03
6d ² D	N18	3.59E-09	6.09E-07	3.02E-05	6.57E-04	5.20E-03	1.10E-02
6f ² F°	N19	4.09E-09	7.95E-07	4.08E-05	8.90E-04	7.05E-03	1.49E-02

si2.c source code

Normalized (Ni/N0) Silicon II Excited State Population Densities							
	T_e :	4.0	4.0	4.0	4.0	4.0	4.0
Config	N_e :	1E+12	1E+13	1E+14	1E+15	1E+16	1E+17
3p ⁴ P	N1	3.35E-04	3.37E-03	3.21E-02	1.85E-01	3.91E-01	5.04E-01
3p ² D	N2	1.37E-04	1.53E-03	9.56E-03	3.16E-02	1.33E-01	2.66E-01
4s ² S	N3	6.62E-06	6.61E-05	5.97E-04	3.76E-03	1.89E-02	3.87E-02
3p ² S	N4	2.62E-06	2.62E-05	2.60E-04	2.42E-03	1.42E-02	2.78E-02
3d ² D	N5	1.07E-05	1.07E-04	1.08E-03	9.86E-03	5.99E-02	1.26E-01
4p ² P*	N6	2.79E-06	4.25E-05	6.28E-04	5.59E-03	3.39E-02	7.11E-02
3p ² P	N7	4.64E-06	4.64E-05	4.61E-04	4.37E-03	2.86E-02	6.44E-02
5s ² S	N8	5.18E-07	5.07E-06	5.50E-05	8.33E-04	6.47E-03	1.41E-02
4d ² D	N9	2.07E-06	1.96E-05	2.24E-04	3.73E-03	2.94E-02	6.39E-02
4f ² F*	N10	9.79E-08	7.48E-06	2.58E-04	4.86E-03	3.81E-02	8.28E-02
5p ² P*	N11	5.50E-07	8.63E-06	1.19E-04	2.05E-03	1.61E-02	3.51E-02
6s ² S	N12	1.33E-08	8.04E-07	2.60E-05	5.34E-04	4.28E-03	9.33E-03
5d ² D	N13	4.04E-08	3.28E-06	1.23E-04	2.57E-03	2.06E-02	4.49E-02
5f ² F*	N14	3.85E-08	3.95E-06	1.63E-04	3.44E-03	2.77E-02	6.03E-02
6p ² P*	N15	2.26E-08	1.83E-06	6.98E-05	1.47E-03	1.18E-02	2.57E-02
5g ² G	N16	4.87E-08	5.00E-06	2.06E-04	4.37E-03	3.51E-02	7.65E-02
7s ² S	N17	3.13E-09	4.81E-07	2.04E-05	4.32E-04	3.47E-03	7.57E-03
6d ² D	N18	1.13E-08	1.91E-06	9.70E-05	2.11E-03	1.70E-02	3.72E-02
6f ² F*	N19	1.29E-08	2.50E-06	1.32E-04	2.89E-03	2.33E-02	5.08E-02

Normalized (Ni/N0) Silicon II Excited State Population Densities							
	T_e :	5.0	5.0	5.0	5.0	5.0	5.0
Config	N_e :	1E+12	1E+13	1E+14	1E+15	1E+16	1E+17
3p 4P	N1	4.36E-04	4.41E-03	4.20E-02	2.34E-01	4.92E-01	6.53E-01
3p 2D	N2	2.14E-04	2.35E-03	1.36E-02	4.34E-02	1.84E-01	3.73E-01
4s 2S	N3	9.88E-06	9.87E-05	8.81E-04	5.44E-03	2.78E-02	5.78E-02
3p 2S	N4	4.15E-06	4.14E-05	4.11E-04	3.83E-03	2.27E-02	4.46E-02
3d 2D	N5	1.72E-05	1.73E-04	1.73E-03	1.57E-02	9.58E-02	2.04E-01
4p $^2P^o$	N6	5.01E-06	7.29E-05	1.02E-03	8.93E-03	5.47E-02	1.17E-01
3p 2P	N7	7.65E-06	7.65E-05	7.61E-04	7.21E-03	4.76E-02	1.08E-01
5s 2S	N8	9.29E-07	9.09E-06	9.81E-05	1.48E-03	1.16E-02	2.57E-02
4d 2D	N9	3.77E-06	3.59E-05	4.08E-04	6.76E-03	5.37E-02	1.19E-01
4f $^2F^o$	N10	1.77E-07	1.37E-05	4.78E-04	8.94E-03	7.07E-02	1.56E-01
5p $^2P^o$	N11	9.99E-07	1.58E-05	2.20E-04	3.77E-03	3.00E-02	6.65E-02
6s 2S	N12	2.49E-08	1.53E-06	5.00E-05	1.03E-03	8.33E-03	1.85E-02
5d 2D	N13	7.67E-08	6.27E-06	2.38E-04	4.98E-03	4.04E-02	8.97E-02
5f $^2F^o$	N14	7.43E-08	7.61E-06	3.18E-04	6.73E-03	5.47E-02	1.21E-01
6p $^2P^o$	N15	4.31E-08	3.53E-06	1.37E-04	2.87E-03	2.33E-02	5.17E-02
5g 2G	N16	9.43E-08	9.66E-06	4.04E-04	8.57E-03	6.96E-02	1.54E-01
7s 2S	N17	6.06E-09	9.45E-07	4.08E-05	8.67E-04	7.05E-03	1.56E-02
6d 2D	N18	2.21E-08	3.76E-06	1.95E-04	4.26E-03	3.47E-02	7.70E-02
6f $^2F^o$	N19	2.56E-08	4.95E-06	2.66E-04	5.84E-03	4.77E-02	1.06E-01